University of Kentucky
UKnowledge

Theses and Dissertations--Chemistry | Chemistry

2023

TRANSLATING CHEMISTRY, STRUCTURE, AND PROCESSING TO THE SOLID-STATE MORPHOLOGY AND FUNCTION OF ORGANIC SEMICONDUCTORS THROUGH COMPUTATIONAL MODELING AND SIMULATIONS

Chamikara D. Karunasena
University of Kentucky, chamikaradk@gmail.com
Author ORCID Identifier:
https://orcid.org/0000-0002-0631-9034
Digital Object Identifier: https://doi.org/10.13023/etd.2023.021

Right click to open a feedback form in a new tab to let us know how this document benefits you.

Recommended Citation

Karunasena, Chamikara D., "TRANSLATING CHEMISTRY, STRUCTURE, AND PROCESSING TO THE SOLID-STATE MORPHOLOGY AND FUNCTION OF ORGANIC SEMICONDUCTORS THROUGH COMPUTATIONAL MODELING AND SIMULATIONS" (2023). *Theses and Dissertations--Chemistry*. 173.
https://uknowledge.uky.edu/chemistry_etds/173

This Doctoral Dissertation is brought to you for free and open access by the Chemistry at UKnowledge. It has been accepted for inclusion in Theses and Dissertations--Chemistry by an authorized administrator of UKnowledge. For more information, please contact UKnowledge@lsv.uky.edu.

STUDENT AGREEMENT:

I represent that my thesis or dissertation and abstract are my original work. Proper attribution has been given to all outside sources. I understand that I am solely responsible for obtaining any needed copyright permissions. I have obtained needed written permission statement(s) from the owner(s) of each third-party copyrighted matter to be included in my work, allowing electronic distribution (if such use is not permitted by the fair use doctrine) which will be submitted to UKnowledge as Additional File.

I hereby grant to The University of Kentucky and its agents the irrevocable, non-exclusive, and royalty-free license to archive and make accessible my work in whole or in part in all forms of media, now or hereafter known. I agree that the document mentioned above may be made available immediately for worldwide access unless an embargo applies.

I retain all other ownership rights to the copyright of my work. I also retain the right to use in future works (such as articles or books) all or part of my work. I understand that I am free to register the copyright to my work.

REVIEW, APPROVAL AND ACCEPTANCE

The document mentioned above has been reviewed and accepted by the student's advisor, on behalf of the advisory committee, and by the Director of Graduate Studies (DGS), on behalf of the program; we verify that this is the final, approved version of the student's thesis including all changes required by the advisory committee. The undersigned agree to abide by the statements above.

Chamikara D. Karunasena, Student

Chad M. Risko, Major Professor

Dong-Sheng yang, Director of Graduate Studies

TRANSLATING CHEMISTRY, STRUCTURE, AND PROCESSING TO THE SOLID-STATE MORPHOLOGY AND FUNCTION OF ORGANIC SEMICONDUCTORS THROUGH COMPUTATIONAL MODELING AND SIMULATIONS

DISSERTATION

A dissertation submitted in partial fulfillment of the
requirements for the degree of Doctor of Philosophy in the
College of Arts and Sciences
at the University of Kentucky

By

Chamikara D. Karunasena

Lexington, Kentucky

Director: Dr. Chad Michael Risko, Professor of Chemistry

Lexington, Kentucky

2022

Copyright © Chamikara D. Karunasena 2022
https://orcid.org/0000-0002-0631-9034

ABSTRACT OF DISSERTATION

TRANSLATING CHEMISTRY, STRUCTURE, AND PROCESSING TO THE SOLID-STATE MORPHOLOGY AND FUNCTION OF ORGANIC SEMICONDUCTORS THROUGH COMPUTATIONAL MODELING AND SIMULATIONS

The immense synthetic design space and material versatility have driven the exploration and development of organic semiconductors (OSC) over several decades. While many OSC designs focus on the chemistries of the molecular or polymer building blocks, *a priori*, multiscale control over the solid-state morphology is required for effective application of the active layer in a given technology. However, molecular assembly during solid-state formation is a complex function interconnecting the building block chemistry and the processing environment. Insufficient knowledge as to how these aspects engage, especially at the atomistic and molecular scales, has so far limited the ability to predict OSC solid-state morphology, leaving Edisonian approaches as the stalwart methods. Therefore, through multiscale simulations combining atomistic quantum scale modeling and state-of-the-art molecular dynamics (MD) techniques, we aim to establish first principles understanding required to synthetically regulate solid-state morphology of organic semiconductors (OSC) as a function of molecular chemistry and processing. In turn, we try to understand the deceivingly simple yet complex mechanisms behind molecular aggregation and crystallization of OSC. Simultaneously, we develop semi-to-fully automated high-throughput schemes to automate the complex and labor-intensive analyses to generate data based on various crystal structures in different crystallization environments. Ultimately, we aim to bridge molecular-scale information revealed on solid-state physical organization, understood in the context of chromophore chemistry and the molecular environment, with the macro scale properties to uncover useful guidelines for rational design and morphology regulation of OSC systems.

KEYWORDS: Organic Semiconductor, Molecular Dynamics, Density Functional Theory

Chamikara Dinaruwan Karunasena

(Name of Student)

10/01/2022

Date

TRANSLATING CHEMISTRY, STRUCTURE, AND PROCESSING TO THE SOLID-STATE MORPHOLOGY AND FUNCTION OF ORGANIC SEMICONDUCTORS THROUGH COMPUTATIONAL MODELING AND SIMULATIONS

By
Chamikara D. Karunasena

Chad Michael Risko
Director of Dissertation

Dong-Sheng Yang
Director of Graduate Studies

10/01/2022
Date

ACKNOWLEDGMENTS

Reminiscing through the years, my journey as an international graduate student in the United States has been quite a blissful experience, and I have many to whom I am deeply indebted to for paving my way so clear through the hurdles. First and foremost, I would like to acknowledge my research advisor Professor Chad Risko for his excellence as a successful research advisor and a professor in chemistry, and I express my sincere gratitude and thanks for his outstanding mentorship throughout the years, which in my opinion is exactly what I needed to not only be the genuine enthusiast I am today with what I do, but also the future mentor that I am eagerly waiting to become.

I am most certainly thankful for the opportunity I had at the University of Kentucky (UK) to follow my dream pursuing an advanced degree in chemistry and I would like to thank all my committee members, Professors John Anthony, Kenneth Graham, Alexander Martin, and Earnest Bailey for their guidance. My sincere thanks also go to all the Professors and course instructors who conducted invaluable courses in chemistry at UK, and I would like to specifically acknowledge Professor Dennis Clouthier for turning quantum mechanics into something magical that really stuck with me for life, Professor John Anthony for his most inspiring course in organic electronics, and Professor Chris Richards for introducing me to the field of statistics in chemical sciences in the most fun way.

I am also thankful for all the group members who were around me for being amazing team players, making the whole experience in Risko Laboratory a one that I will cherish for the rest of my life. I would like to specifically extend my gratitude to Dr.

Shi Li and Dr. Sean Ryno for being the 'catalysts' of my molecular dynamics learning experience, who made the 'jump' easier across the barriers along the way. I would also like to thank my dearest colleagues Vinayak Bhat, Keerthan Rao, and Rebekah Duke for the stimulating conversations, exchanging expertise, and most importantly, for expanding my interests into the exciting new world of machine learning. My sincere thanks also go to Dr. Joel Bombile and Dr. Connor Callaway for their generous support as talented post-docs and great friends. I would also like to thank Dr. Zoran Bjelobrk, who has been an outstanding collaborator from ETH Zurich, Switzerland, and a 'guru' who assisted me to gallivant in the beautiful space of enhanced sampling molecular dynamics and advanced analysis techniques. I feel very lucky to have his guidance through the investigations of crystallization, which gave me the 'wings' I needed to explore the mysterious corners of this unknown world of science.

I cannot imagine myself achieving anything I boast of today through my academic path, without the wonderful teachers and advisors who carried the burden of teaching and mentoring me up to my bachelor's level in science. I would like to make this an opportunity to acknowledge the profound impact of I had during my undergraduate institute, University of Peradeniya in Sri Lanka, to push myself to the very limits as a young student and a resilient research scholar. I thank all the Professors and lectures for their exceptional contribution in making me knowledgeable in the areas of chemistry, biochemistry, and computer science. I would specifically like to express heartfelt gratitude to my undergraduate advisor Dr. Udayana Ranatunga for his exceptional mentorship during my final year research, as an incredibly humble young scholar who inspired me in the first place to pursue higher studies in the beautiful field

of computational chemistry. Among the many Professors who I found to be extremely talented at what they do, I would also like to specifically acknowledge Professors: Madhava Meegaskumbura, Veranja Karunaratne, Shelton Perera, Ratnayake Bandara, Vajira Seneviratne, Chandani Perera, and Gamini Rajapakse for the lifelong influence I gained from their demonstrated excellence in teaching and mentoring abilities. I would also like to thank all my schoolteachers and tuition instructors for the priceless education I received, that led me to me get through my ordinary levels and advanced levels examinations to gain entry into university.

As it goes without saying, I owe everything to my family for who and where I am today; although no words can really appreciate the hardships they went through so that I have this better life, I would like to express my love and thanks to my mother and father, as well as my brother and sister, for their untiring contributions that went above and beyond. I also feel extremely lucky to have found the love of my life – my beloved wife Hasanthi – so early in my life, who's devotion and solid partnership made everything worth fighting for through the roughest of the years, and I would like to thank her from the bottom of my heart for being all that she is, and my sincere wish is to see her shine and excel in everything she dream of becoming.

Although the list would only go on and on, I would also like to thank all my relatives and friends who rooted for me being supportive, and all the wonderful friends I met in Lexington including Solomon, Greg, Stephanie, Hannah, Rajeshwari, Joel and Christina, for the beautiful memories shared together, because of whom, Lexington, Kentucky, will forever be my second home.

TABLE OF CONTENTS

ABSTRACT OF DISSERTATION ii

ACKNOWLEDGMENTS iii

TABLE OF CONTENTS vi

LIST OF TABLES ix

LIST OF FIGURES x

CHAPTER 1. INTRODUCTION 1

1.1 Organic semiconductors as an emerging science 1

1.2 Crystallization of organic semiconductors 4

1.2.1 Understanding mechanisms of crystallization 5

1.2.2 Impact of supersaturation on crystallization 9

1.2.3 Thermodynamics and kinetics of nucleation and growth 10

1.2.4 Mechanisms of nucleation and growth of faceted crystallization 11

1.2.5. Solution growth and morphology evolution of OSC crystals 13

1.3 Objectives and outline of the dissertation 15

CHAPTER 2. COMPUTATIONAL METHODS 19

2.1 Overview of Concepts: Classical Mechanics and Molecular Dynamics 19

2.1.1 Molecular mechanics 19

2.1.2 Molecular dynamics 20

2.1.2.1 Nonbonded interactions through Lennard-Jones potential 22

2.1.2.2 Forcefields for representing organic molecular systems 23

2.1.2.3 Force field parameterization of molecules 24

2.1.2.4 Initial velocity generation and numerical integration of the equations of motion 25

2.1.2.5 Calculation of energy and average temperature 27

2.1.2.6 Periodic boundary conditions and minimum image convention 27

2.1.2.7 Statistical ensemble 28

2.1.2.8 Temperature control 29

2.1.2.9 Pressure control 29

2.1.2.10 General simulation protocol 30

2.1.3 Collective variables 31

2.1.4 Constant chemical potential molecular dynamics algorithm 31

2.1.5 Enhanced sampling through umbrella simulations 34

2.1.6 MD trajectory analysis techniques 35
2.1.6.1 Heat capacity 35
2.1.6.2 Mean square displacement 36
2.1.6.3 Radial distribution function 36
2.1.6.4 Potential of mean force 37
2.1.6.5 Weighted histogram analysis 38
2.1.7 MD software packages 38

2.2 Overview of Quantum Mechanics and Electronic-Structure Theory 39
2.2.1 The time-independent Schrödinger Equation 39
2.2.2 Born-Oppenheimer approximation 41
2.2.3 Density functional theory (DFT) 42
2.2.3.1 Approximate exchange-correlation functionals 44
2.2.4 Basis sets 48
2.2.4.1 Slater and Gaussian type orbitals 48
2.2.4.2 Basis set nomenclature 49
2.2.5 Polarizable continuum model for simulating solvent environment 51
2.2.6 Quantum theory of atoms in molecules 52
2.2.6.1 Critical points of electron density 52
2.2.6.2 Reduced density gradient of electron density 55
2.2.7 QM software packages 56

CHAPTER 3. ROLES OF INTRAMOLECULAR NONCOVALENT INTERACTIONS IN π -CONJUGATED MOLECULES ON STRUCTURE AND AGGREGATION 57

3.1 Introduction 57

3.2 Computational Methods 61

3.3 Results and Discussion 65
3.3.1 Determining existence of intramolecular noncovalent interactions 65
3.3.2 Determining nature and strength of intramolecular noncovalent interactions. 72
3.3.3 π-electron delocalization across rotatable bridging bonds 80
3.3.4 Summary: Impact of noncovalent intramolecular interactions on structure 85
3.3.5 The explicit role of solvent on the conformations of isolated oligomers in solution 86
3.3.6 Accounting for the inter-oligomer interactions: Effects on conformational ……..preferences in concentrated solutions 93
3.3.7 From conformational preferences to aggregation 103

3.4 Conclusions 115

CHAPTER 4. CRYSTALLIZATION OF HERRINGBONE PACKED MOLECULAR CRYSTALS FROM SOLUTION 117

4.1 Introduction 117

4.2 Methods 119

4.3 Results and Discussion 129
4.4 Conclusions 152

CHAPTER 5. THERMAL TRANSITIONS OF HERRINGBONE-PACKED ORGANIC SEMICONDUCTORS: INFLUENCE OF CHEMICAL MODIFICATIONS ON MELTING AND SOLIDIFICATION 154
5.1 Introduction 154
5.2 Methods 157
5.3 Results and discussion 159
5.4 Conclusions 188

CHAPTER 6. PERSPECTIVES 191
6.1 Synopsis and future considerations 191

REFERENCES 196
Chapter 1: References 196
Chapter 2: References 202
Chapter 3: References 205
Chapter 4: References 209
Chapter 5: References 212

VITA 215

LIST OF TABLES

Table 4.1 Steady state morphology of NDT crystal and relative surface areas predicted by the BFDH model 119

Table 4.2 Lattice parameters extracted from the crystallographic information file (CIF) at cell measurement temperature of 293 K, and the parameters obtained from molecular dynamics (MD) simulations at the same temperature..... 120

Table 4.3 Density restraint parameters used for crystallization simulations of homogenous solutions..... 123

LIST OF FIGURES

Figure 1.1. A diagrammatic illustration of common molecular stacking types observed in OSC crystal structures..... 2

Figure 1.2. Gibbs free energy associated with a growing spherical nucleus. The surface energy and bulk crystal free energy components are shown in solid lines and the dotted line indicate the overall energy. 7

Figure 1.3. Illustration of the 2D layer growth on top of the crystal surface, that follows the birth and spread of the 2D layer. 8

Figure 1.4. Comparison of heterogenous crystallization at the macroscale forming a droplet on top of the substrate surface (left) having contact angle θ, with the layer-wise crystal formation of on top of the substrate surface at molecular scale. 9

Figure 1.5 The three regimes of facet growth of crystals as a function of supersaturation. 12

Figure 1.6 Diagrammatic illustration of how fast-growing crystallographic faces (red arrows) are taken over by slow-growing faces (green arrows) during morphology evolution from steps 1 through 3. 14

Figure 2.1 Schematic diagram of the layout of the simulation box for implementation of CμMD procedure. The box is oriented horizontally along with the laboratory axis z 32

Figure 2.2 Modified layout of the simulation box adapt CμMD for NDT simulations allowing for only one growth region per simulation. 34

Figure 2.3 Schematic illustration of the colors used to indicate interaction types of the isosurface obtained by RDG analysis. 55

Figure 2.4 An example RDG against sign $(\lambda 2)\rho$ plot of FBT-TT molecular fragment (a), investigated in chapter 3 that reveals stronger attractive (blue), weak van der Waals (green), and repulsive (red) like forces found along the 0.5 isosurface (b) pointed out through colored dotted arrows. 56

Figure 2.1 Schematic diagram of the layout of the simulation box for implementation of CμMD procedure. The box is oriented horizontally along with the laboratory axis z 32

Figure 2.2 Modified layout of the simulation box adapt CμMD for NDT simulations allowing for only one growth region per simulation. 34

Figure 2.3 Schematic illustration of the colors used to indicate interaction types of the isosurface obtained by RDG analysis. 55

Figure 2.4 An example RDG against sign $(\lambda 2)\rho$ plot of FBT-TT molecular fragment (a), investigated in chapter 3 that reveals stronger attractive (blue), weak van der Waals (green), and repulsive (red) like forces found along the 0.5 isosurface (b) pointed out through colored dotted arrows. 56

Figure 3.1 Chemical structures of oligomers of interest. PT ≡ pyridyl-[2,1,3]thiadiazole; FBT ≡ fluorinated benzo[*c*][1,2,5]thiadiazole; biTh ≡ bithiophene; TT ≡ thieno[3,2-*b*]thiophene. 59

Figure 3.2 Three conformations for the central segments of the *D-A* oligomers considered in this work, with the corresponding notation scheme adopted to identify conformations. Each of these conformations is used as a starting point for different MD simulations. The green bonds represent the dihedral of the TT or biTh group with respect to the acceptor (either PT or FBT), whereas the red bonds represent the dihedral of the acceptor with respect to DTS. The arrows follow the direction of the sulfur atoms in the different aromatic groups and show the *anti*- (A) or *syn*- (S) orientations among these groups..... 60

Figure 3.3 Oligomer structures and fragment abbreviations. The colored bonds (red and green) correspond to the rotatable bonds among the fragments. Following established convention, we note that molecules 1, 2 and 3 are identified as PT-TT, BT-TT and FBT-TT for simplicity. 66

Figure 3.4 Torsional (dihedral) potential energy surfaces (PES) derived at the ωB97XD/6-31G(d,p) level of theory among select donor and acceptor moieties. 67

Figure 3.5 Potential energy surfaces (PES) for rotation among the noted fragments in gas phase as determined at the ωB97XD/6-31G(d,p) level of theory. The dotted lines with open symbols represent PES determined with the polarizable continuum model with the integral equation formalism variant (IEFPCM) simulating chlorobenzene solvent reaction field. The vertical dotted line references 90°. 68

Figure 3.6 Contour plots of the electron density for ωB97XD/6-31G(d,p)-optimized molecular fragments in the syn (top two rows) and anti (bottom two rows) configurations. Length units of X and Y axes are shown in Angstroms. The +3, -1 type (bond) critical points shown as orange dots (with paths shown by the brown straight lines) and +3, +1 (ring) type critical points are shown as yellow dots. Bonds that lie out of the plane are shown in dotted lines. The twist angle between D-A groups is annotated in blue. 71

Figure 3.7 RDG vs. sign(λ_2)ρ scatter plots for PT and FBT with either DTS (top) or TT (bottom) for the ωB97XD/6-31G(d,p) optimized *anti* orientations, highlighting the 0.5 isosurfaces of the sign(λ_2)ρ value 73

Figure 3.8 RDG vs. sign(λ_2) scatter plots for BT - DTS and BT – TT in the *anti* (top row) and *syn* (bottom row) orientations optimized at the ωB97XD/6-31G(d,p) level of theory 74

Figure 3.9 RDG vs. sign(λ_2) scatter plots for PT - DTS and PT – TT in the *anti* (top row) and *syn* (bottom row) orientations optimized at the ωB97XD/6-31G(d,p) level of theory 74

Figure 3.10 RDG vs. sign(λ_2) scatter plots for FBT - DTS and FBT – TT in the *anti* (top row) and *syn* (bottom row) orientations optimized at the ωB97XD/6-31G(d,p) level of theory 75

Figure 3.11 Diagramatic representation of intramolecular noncovalent interactions between rotatable fragments optimized in the *syn* (S) orientation, determined at ωB97XD/6-31G(d,p) level of theory. The noncovalent bonding interactions are identified through +3,-1 type bond critical points (BCP) of the electron density (shown by the green dashed lines). The repulsive interactions are shown in red shaded regions (identified thorugh RDG vs. sign(λ_2)ρ scatter plots). The annotated bar charts show the relative intramolecular noncovalent bonding interaction distances with respect to their BCP center, with orange and violet colors showing the overall electronegative and electropositive sides of the interactions. 76

Figure 3.12 Diagramatic representation of intramolecular noncovalent interactions between rotatable fragments optimized in the *anti* (A) orientation, determined at ωB97XD/6-31G(d,p) level of theory. The noncovalent bonding interactions are identified through +3,-1 type bond critical points (BCP) of the electron density (shown by the green dashed lines). The repulsive interactions are shown in red shaded regions (identified thorugh RDG vs. sign(λ_2)ρ scatter plots). The annotated bar charts show the relative intramolecular noncovalent bonding interaction distances with respect to their BCP center, with orange and violet colors showing the overall electronegative and electropositive sides of the interactions. 78

Figure 3.13 The ellipticity of electron density and bond length and variation of the bridging bond between acceptor and donor groups during dihedral rotation. The labeled structures that are colored to correspond to the conformations that give rise to higher bond ellipticities for the bridging bonds. The bond critical point paths 81

Figure 3.14 Electron density ellipticities of bonds labeled 1, 2, and 3 as the bond is rotated from *syn* optimized through 60°, 90°, 120°, to the *anti*-optimized angles for the acceptor-DTS (top) and TT-acceptor (bottom) fragments and ring critical points shown in dotted green lines and shaded regions, respectively 82

Figure 3.15 Mayer bond orders of bonds labeled 1, 2, and 3 as the bond is rotated from *syn* optimized through 60°, 90°, 120°, to the *anti*-optimized angles for the acceptor-DTS (top) and TT-acceptor (bottom) fragments 83

Figure 3.16 Model depicting the potential energy surface for rotation among π-conjugated moieties with contributions from the degree of double bond character (green dashed line) and intramolecular noncovalent attractive (gold dashed line) and repulsive (red dashed line) interactions..... 86

Figure 3.17 Dihedral angle analyses carried out on the MD simulations of the isolated molecules at vacuum, with the colors red, green, and blue representing the torsions moving from central core to the periphery of the oligomers in respective order. 88

Figure 3.18 Calculated dihedral angles along simulation time for isolated PT-TT in infinite dilution in CB and DIO solutions. The starting configurations for the simulations are shown in the bottom, with the AA, AS, and SS notation referring to the initial conformation of the innermost dihedral angles. Results are shown from 20 ns of an NPT-PR simulation. Red represents the DTS-acceptor rotation and green represents the acceptor-TT rotation. 88

Figure 3.19 Calculated dihedral angles along simulation time for isolated PT-biTh in infinite dilution in CB and DIO solutions. The starting configurations for the simulations are shown in the bottom, with the AA, AS, and SS notation referring to the initial conformation of the innermost dihedral angles. Results are shown from 20 ns of an NPT-PR simulation. Red represents the DTS-acceptor rotation and green represents the acceptor-TT rotation.and blue represents the torsion between the thiophene units of biTh. 89

Figure 3.20 Calculated dihedral angles along simulation time for isolated FBT-TT in infinite dilution in CB and DIO solutions. The starting configurations for the simulations are shown in the bottom, with the AA, AS, and SS notation referring to the initial conformation of the innermost dihedral angles. Results are shown from 20 ns of an NPT-PR simulation. Red represents the DTS-acceptor rotation and green represents the acceptor-TT rotation. 91

Figure 3.21 Calculated dihedral angles along simulation time for isolated FBT-biTh in infinite dilution in CB and DIO solutions. The starting configurations for the simulations are shown in the bottom, with the AA, AS, and SS notation referring to the initial conformation of the innermost dihedral angles. Results are shown from 20 ns of an NPT-PR simulation. Red represents the DTS-acceptor rotation and green represents the acceptor-TT rotation.and blue represents the torsion between the thiophene units of biTh. 92

Figure 3.22 Potential of mean force (PMF) profiles determined for the four oligomers in solvent and vacuum environments, where the intermolecular backbone distance (ξ) is the reaction coordinate. 94

Figure 3.23 Time averaged dihedral angles (from the last 10 ns) of the oligomers in the two solvents 2% (w/w) for the 100 solute molecules. Only the AAAA starting configurations are shown for clarity. Dotted black horizontal lines indicate the 90° angle. 96

Figure 3.24 Time-averaged dihedral angle KDE distributions of the dihedral angles for the 100 solute molecules of PT-TT in 2% (w/w) CB or DIO solutions. The starting configurations for the simulations are shown in the far-right column, with the AA, AS, and SS notation referring to the initial conformation of the inner-most dihedral angles. Results are determined from the last 10 ns of 50 ns NPT-PR simulations. 97

Figure 3.25 Time-averaged dihedral angle KDE distributions of the dihedral angles for the 100 solute molecules of PT-biTh in 2% (w/w) CB or DIO solutions. The starting configurations for the simulations are shown in the far-right column, with the AA, AS, and SS notation referring to the initial conformation of the inner-most dihedral angles. Results are determined from the last 10 ns of 50 ns NPT-PR simulations. 98

Figure 3.26 Dihedral angle KDE population analyses carried out for (2% w/w) PT-TT and PT-biTh in comparison. The figures indicate the most representative instances among the three modeled conformational variants. 99

Figure 3.27 Dihedral angle KDE population analyses carried out for (2% w/w) FBT-TT and FBT-biTh in comparison. The figures indicate the most representative instances among the three modeled conformational variants of the inner-most dihedral angles. Results are determined from the last 10 ns of 50 ns NPT-PR simulations. 100

Figure 3.28 Time-averaged dihedral angle KDE distributions of the dihedral angles for the 100 solute molecules of FBT-TT in 2% (w/w) CB or DIO solutions. The starting configurations for the simulations are shown in the far-right column, with the AA, AS, and SS notation referring to the initial conformation of the inner-most dihedral angles. Results are determined from the last 10 ns of 50 ns NPT-PR simulations. 101

Figure 3. 29 Time-averaged dihedral angle KDE distributions of the dihedral angles for the 100 solute molecules of FBT-biTh in 2% (w/w) CB or DIO solutions. The starting configurations for the simulations are shown in the far-right column, with the AA, AS, and SS notation referring to the initial conformation of the inner-most dihedral angles. Results are determined from the last 10 ns of 50 ns NPT-PR simulations. 102

Figure 3.30 Oligomers in 2% concentrated systems during the last 40 to 50 ns analysis time in terms of a). RDF of the center of mass distance of the backbones, b). the adopted conformational populations for the modeled oligomers with AA innermost dihedral starting configuration, excluding biTh end group rotation for simplicity. 105

Figure 3.31 Time-averaged (from the last 10 ns of a 50 ns simulation) conformational populations of 2% (w/w) PT-TT in terms of all dihedral positions (right column) and only considering innermost dihedrals (left column). AA, AS, and SS notation in red color refer to the initial conformation of the inner-most dihedral angles. 106

Figure 3.32 Conformational population analysis of 2% (w/w) oligomers in CB, evaluated separately for solvated vs. the aggregated members resolved through trajectory averaged RDF cut-offs (0.4 nm) for systems with inner-most dihedrals in AA, AS and SS starting conformations used at the outset of the simulations. 107

Figure 3.33 Conformational population analysis of 2% (w/w) oligomers in CB, evaluated separately for fully solvated vs. the aggregated members resolved through trajectory averaged RDF cut-offs (0.4 nm) comparing PT-TT and PT-biTh systems. AA, AS and SS indicate the starting conformations at the outset of the simulations. 108

Figure 3.34 RDF pair correlation function peaks for PT-biTh and the corresponding major aggregation types. AA, AS, and SS represent the starting conformational population in terms of the innermost dihedrals..... 109

Figure 3.35 Time-averaged (from the last 10 ns of a 50 ns simulation) conformational populations of 2% (w/w) PT-biTh in terms of all dihedral positions (right column) and only considering innermost dihedrals (left column). AA, AS, and SS notation in red color refer to the initial conformation of the inner-most dihedral angles. 110

Figure 3.36 Time-averaged (from the last 10 ns of a 50 ns simulation) conformational populations of 2% (w/w) FBT-TT in terms of all dihedral positions (right column) and only considering innermost dihedrals (left column). AA, AS, and SS notation in red color refer to the initial conformation of the inner-most dihedral angles. 111

Figure 3.37 Time-averaged (from the last 10 ns of a 50 ns simulation) conformational populations of 2% (w/w) FBT-biTh in terms of all dihedral positions (right column) and only considering innermost dihedrals (left column). AA, AS, and SS notation in red color refer to the initial conformation of the inner-most dihedral angles. 112

Figure 3.38 Conformational population analysis of 2% (w/w) oligomers in CB, evaluated separately for fully solvated vs. the aggregated members resolved through trajectory averaged RDF cut-offs (0.4 nm) comparing FBT-TT and FBT-biTh systems. AA, AS and SS indicate the starting conformations at the outset of the simulations. 114

Figure 4.1 Crystal morphology of NDT (platelet) obtained through the BFDH model[16] using Mercury Advanced tools.[17] 119

Figure 4.2 Schematic diagram of the simulation setup with harmonic restraints for NDT at the exterior of the simulation box in all three box dimensions. 122

Figure 4.3 Example simulation setups of the equilibrated NDT crystals with the bulk (hexane) solution at 0.1 NDT mole fraction for production runs. Rough positionings of force regions (left and right) that govern the supersaturation inside the control regions are shown in red dotted lines. Only the central regions of the boxes are shown for clarity. 124

Figure 4.4 Distribution of molecular long-axis vector angles with the axis shown for (110) and (011) faces. Upper and lower boundaries used to distinguish crystalline order at the growth region are shown in dotted lines. The mean values are annotated in the middle of each population peak. 126

Figure 4.5 Example cases showing the choice of upper and lower boundaries of the adsorption layer (specified in red dotted lines) next to the template crystal (100) face (shown in purple color) in hexane and toluene solutions. 127

Figure 4.6 (left) Chemical structure of NDT. (middle-to-right) Steady-state NDT crystal morphology as predicted by the BFDH model (visualized through Mercury visualization tool[17]) compared with the early stages of nucleus formation in a homogenous supersaturated hexane solution. Faster parallel growth compared to slow perpendicular growth with respect to the (100) plane is shown in both cases. 130

Figure 4.7 Snapshots of the simulation of crystal formation in either hexane (top) and toluene (bottom) homogenous solutions. Only the solute molecules are shown for clarity. The red dotted regions highlight the first apparent crystalline layer of (100) face formation from the central cluster. 131

Figure 4.8 Schematic illustration of early stages of crystallization of NDT in a homogenous hexane solution, where the growth perpendicular to the (100) plane is seen after all other faster growing surfaces are assembled to form a 2-D nucleus that is parallel to the (100) plane. 132

Figure 4.9 Controlled concentrations of the right-side control regions during the production runs that allow crystal formation at varied concentrations in hexane and toluene solutions. Different colors represent different repeat simulations. The x axis denotes the time in ns. 133

Figure 4.10. 2D critical nuclei observed at the critical concentrations in toluene and hexane on top of the (100) face. The red circle roughly highlights the participating members with short-axis molecular stacking. Solvent molecules and the template crystal surface are not shown for clarity. 134

Figure 4.11 (top) $s1$ crystallinity descriptor and (bottom) adsorbed solvent (h) descriptor for different concentrations of NDT in toluene growing on the (100) face as a function of time. The different colors in each plot correspond to the repeat simulations, each initiated with random input structures extracted from equilibrated systems. 135

Figure 4.12 Free energy profiles of crystal layer growth on the (100) face in toluene in terms of the crystallinity descriptor ($s1$) and solvent adsorption (h) for each concentration (shown in different shades of color). The most dissolved instance of the growth layer is normalized to represent the zero-point energy. NDT concentrations for each FES are provided in mole fraction units. 136

Figure 4.13 Free energy surface (FES) of NDT crystal layer growth on the (100) face in toluene in terms of the $s1$ crystallinity and h solvent adsorption descriptors. NDT concentrations for each FES are provided in mole fraction units. 136

Figure 4.14 (top) $s1$ crystallinity descriptor and (bottom) adsorbed solvent (h) descriptor for different concentrations of NDT in hexane growing on the (100) face as a function of time. The different colors in each plot correspond to the repeat simulations, each initiated with random input structures extracted from equilibrated systems. 138

Figure 4.15 Multi-layer growth of NDT crystals on the (100) face in 0.08 mole fraction NDT solutions of hexane, showing the second to third layer grown on top of the first layer after 200 ns. Colors green, purple and magenta shows hexane, the NDT crystal template, and the newly formed NDT layers respectively. Top views (cross sections) of the adlayers are shown in the second row. 139

Figure 4.16 First adlayer of NDT crystals on the (100) face for all five repeat simulations in 0.08 mole fraction hexane solution at 298 K. Only NDT molecules are shown for clarity. The empty gaps trap hexane molecules. Red circles highlight defective integrations of NDT. 139

Figure 4.17 Free energy profiles of crystal layer growth on the (100) face in hexane in terms of the crystallinity descriptor ($s1$) and solvent adsorption (h) for each concentration (shown in different shades of color). The most dissolved instance of the growth layer is normalized to represent the zero-point energy. NDT concentrations for each FES are provided in mole fraction units. 140

Figure 4.18 Free energy surface (FES) of NDT crystal layer growth on the (100) face in hexane in terms of the $s1$ crystallinity and h solvent adsorption descriptors. NDT concentrations for each FES are provided in mole fraction units. 141

Figure 4.20 Adsorbed toluene (top row) and hexane (bottom row) on the surface during crystallization at each temperature for the (100) face. Colors correspond to the repeat simulations initiated with random input structures from equilibrium solutions of corresponding temperatures. 143

Figure 4.21 Free energy profiles of crystal layer growth on the (100) face in toluene and hexane in terms of the crystallinity descriptor ($s1$) and solvent adsorption (h) for each temperature (shown in different color shades). The most dissolved instance of the growth layer is normalized to represent the zero-point energy. 144

Figure 4.22 Free energy surface (FES) of NDT crystal layer growth on the (100) face in toluene and hexane in terms of the $s1$ crystallinity and h solvent adsorption descriptors. 145

Figure 4.23 Top views of the crystal templates of (011), (110) and (100) faces that are in contact with the supersaturated solutions. The arrows pointing to the short and long axis stacking directions of the surface. The annotated numbers rank the faces in the decreasing order of exposed aromatic interactions to the surface in orthogonal direction. 146

Figure 4.24 Crystallization along (011) and (110) faces within a time of 60 ns defined by the crystallization descriptor $s2$ for the (011) and (110) faces, and $s1$ for the (100) face along with solvent adsorption descriptor (h). 147

Figure 4.25 Degree of crystal growth of NDT observed in either hexane and toluene on the (011) and (110) faces at the end of each simulation. 148

Figure 4.26 Free energy obtained from probability distribution along reaction coordinates ($s1$) and (h) for each facet growth in toluene and hexane (only accounting 60 ns of simulation time). The fully dissolved instance of the growth layer is normalized to the zero-point energy. 149

Figure 4.27 Free energy surfaces (FES) of NDT crystal layer growth on the faces (011), (110), and (100) in hexane and toluene expressed in terms of crystallinity descriptors $s1$ or $s2$ with solvent adsorption (h), sampled from 60 ns of simulation time..... 151

Figure 5.1 Schematic diagram of the chemical structures of the molecules and select experimentally reported thermal properties (sublimation T_s, melt T_m, and crystallization T_c)[12-16] of the OSC studied here. Corresponding molecular symmetries are provided in blue text. 155

Figure 5.2 Types of short- and long-axis stacking types isolated in crystallographic faces of the case of tetracene crystal structure. Vectors representing short-axis and long-axis of the molecules are shown in red and blue arrows respectively. 156

Figure 5.3 (top) Radial distribution function (RDF) plots for the bulk TET crystal (grey lines) and for specific crystal planes as depicted by the teal, gold, and red color peaks that are used to resolve the dominating intermolecular stacking types: Teal represents edge-to-face, gold represents edge-to-edge, and red represents face-to-face type intermolecular stacking of the (bottom) TET crystal lattice planes. 160

Figure 5.4 Density and CV versus temperature profiles for TET along (top) heating from the solid to the melt and (bottom) cooling from the melt to the solid. The colors correspond to the density and dominant interaction types in terms of the intermolecular distances as determined by the RDF. 161

Figure 5.5 Trajectory visualizations as tetracene (top) melts from the crystal to the liquid and (condenses) from the melt to the solid at 20 K/ns rate. The simulation times and corresponding temperatures are noted. The red circle shows the region where herringbone packing begins to form during recrystallization. 163

Figure 5.6 Density curves and collective variables (CV) corresponding to crystal planes versus temperature for tetracene for cooling simulations at either (top) 20 K/ns or (bottom) 10 K/ns rates. 164

Figure 5.7 (top) Radial distribution function (RDF) plots for the bulk ABT crystal (grey lines) and for specific crystal planes as depicted by the teal, gold, and red color peaks that are used to resolve the dominating intermolecular stacking types: Teal correspond to edge-to-face, gold represents edge-to-edge, and red represents face-to-face type intermolecular stacking (bottom) of the ABT crystal lattice planes. 166

Figure 5.8 Density and CV versus temperature profiles for ABT along (top) heating from the solid to the melt and (bottom) cooling from the melt to the solid. The colors correspond to the density and dominant interaction types in terms of the intermolecular distances as determined by the RDF. 167

Figure 5.9 Trajectory visualizations as ABT (top) melts from the crystal to the liquid and (condenses) from the melt to the solid at 20 K/ns rate. The simulation times and corresponding temperatures are noted. Red circle point to the region with herringbone packed layer formation during recrystallization. 168

Figure 5.10 Density curves and collective variables (CV) corresponding to crystal planes versus temperature for ABT for cooling simulations at either (top) 20 K/ns or (bottom) 10 K/ns rates. 169

Figure 5.11 (top) Radial distribution function (RDF) plots for the bulk NDT crystal (grey lines) and for specific crystal planes as depicted by the teal, gold, and red color peaks that are used to resolve the dominating intermolecular stacking types: Teal correspond to edge-to-face, gold represents edge-to-edge, and red represents co-facial type intermolecular stacking (bottom) of the NDT crystal lattice planes. 171

Figure 5.12 Density and CV versus temperature profiles for NDT along (top) heating from the solid to the melt and (bottom) cooling from the melt to the solid. The colors correspond to the density and dominant interaction types in terms of the intermolecular distances as determined by the RDF. 172

Figure 5.13 Trajectory visualizations as NDT (top) melts from the crystal to the liquid and (condenses) from the melt to the solid at 20 K/ns rate. The simulation times and corresponding temperatures are noted. The red circles point to the regions where the herringbone packing is lost, and the melt phase is propagated in a non-layer wise fashion during melting. 173

Figure 5.14 Density curves and collective variables (CV) corresponding to crystal planes versus temperature for NDT for cooling simulations at either (top) 20 K/ns or (bottom) 10 K/ns rates. 174

Figure 5.15 (top) Radial distribution function (RDF) plots for the bulk BTBT crystal (grey lines) and for specific crystal planes as depicted by the teal, gold, and red color peaks that are used to resolve the dominating intermolecular stacking types: Teal correspond to edge-to-face, gold represents edge-to-edge, and red represents face-to-face type intermolecular stacking (bottom) of the BTBT crystal lattice planes. 175

Figure 5.16 Density and CV versus temperature profiles for BTBT along (top) heating from the solid to the melt and (bottom) cooling from the melt to the solid. The colors correspond to the density and dominant interaction types in terms of the intermolecular distances as determined by the RDF. 176

Figure 5.17 Trajectory visualizations as BTBT (top) melts from the crystal to the liquid and (condenses) from the melt to the solid at 20 K/ns rate. The simulation times and corresponding temperatures are noted. The red circles point to the regions where the crystal starts to melt in non-layer wise fashion. For the cooling process, a second visualization is provided to clarify molecule entrapment in an amorphous solid form from 409 K and below during cooling. 177

Figure 5.18 Density curves and collective variables (CV) corresponding to crystal planes versus temperature for BTBT for cooling simulations at either (top) 20 K/ns or (bottom) 10 K/ns rates. 178

Figure 5.19 (top) Radial distribution function (RDF) plots for the bulk C8-BTBT-C8 crystal (grey lines) and for specific crystal planes as depicted by the teal and gold color peaks that are used to resolve the dominating intermolecular stacking types: Teal correspond to edge-to-face, gold represents edge-to-edge type intermolecular stacking (bottom) of the C8-BTBT-C8 crystal lattice planes. 179

Figure 5.20 Density and CV versus temperature profiles for C8-BTBT-C8 along (top) heating from the solid to the melt and (bottom) cooling from the melt to the solid. The colors correspond to the density and dominant interaction types in terms of the intermolecular distances as determined by the RDF..... 181

Figure 5.21 Trajectory visualizations as C8-BTBT-C8 (top) melts from the crystal to the liquid and (condenses) from the melt to the solid at 20 K/ns rate. The simulation times and corresponding temperatures are noted. The liquid crystalline smectic A phase is captured in the ~445K – 455 K region..... 182

Figure 5.22 Density curves and collective variables (CV) corresponding to crystal planes versus temperature for C8-BTBT-C8 for cooling simulations at either (top) 20 K/ns or (bottom) 10 K/ns rates. 183

Figure 5.23 (top) Radial distribution function (RDF) plots for the bulk C8-BTBT crystal (grey lines) and for specific crystal planes as depicted by the teal, gold, and red color peaks. The dominating intermolecular stacking types in terms of the center of mass distance are identified by using the tallest peak(s) positions; teal represents edge-to-face intermolecular stacking, gold represents edge-to-edge intermolecular stacking, and red represents face-to-face stacking (bottom) of the C8-BTBT crystal lattice planes..... 184

Figure 5.24 Density and CV versus temperature profiles for C8-BTBT along (top) heating from the solid to the melt and (bottom) cooling from the melt to the solid. The colors correspond to the density and dominant interaction types in terms of the intermolecular distances as determined by the RDF..... 186

Figure 5.25 Trajectory visualizations as C8-BTBT (top) melts from the crystal to the liquid and (condenses) from the melt to the solid at 20 K/ns rate. The simulation times and corresponding temperatures are noted. The solid-crystalline phase is captured at ~400 K – 500 K region during melting..... 187

Figure 5.26 Density curves and collective variables (CV) corresponding to crystal planes versus temperature for C8-BTBT for cooling simulations at either (top) 20 K/ns or (bottom) 10 K/ns rates. 188

CHAPTER 1. INTRODUCTION

1.1 Organic semiconductors as an emerging science

Semiconductors have revolutionized modern life, serving as the active components in consumer electronics and technologies that are deeply integrated in everyday practices. Silicon-based semiconductors remain at the heart of many of these devices.[1, 2] While these and other inorganic-based semiconductors are produced on massive scales, they use vacuum-based fabrication methods that are energy intensive and have large capital costs, and their often rigid and brittle mechanical form factors limit use in flexible devices.[1]

Organic semiconductors (OSC) offer intriguing, low-cost alternatives to these traditional inorganic semiconductors,[3] including low-temperature processability, electronic and optical tunability, and mechanical flexibility. These attributes open avenues for a broad spectrum of novel electronic and optical applications.[4] Although OSC do not currently reach the benchmark properties of state-of-the-art silicon (and other inorganic)-based semiconductors, OSC are ever evolving rapidly. OSC building blocks span from small, π-conjugated molecules to polymers, and are already finding use as active materials in a wide range of applications[5] that include organic field effect transistors (OFETs),[6, 7] organic light emitting diodes (OLEDs),[8] organic photovoltaics (OPV),[9] and many other technologies.

The chemical compositions and structures (including structural anisotropy) of the molecular or polymeric OSC building blocks impact the solid-state morphologies, in terms of both local and long-range order, and thereby the resulting OSC electronic,

optoelectronic, and mechanical properties.[10] Charge-carrier transport across the bulk, for instance, is mediated in part through conductive pathways facilitated at local levels by effective intermolecular electronic couplings (transfer integrals) among neighboring molecular or polymeric units. In general, better solid-state order (i.e., higher levels of crystallinity) yields improved pathways for uninterrupted charge-carrier transport, although some non-crystalline materials have also proven effective. For crystalline systems, charge-carrier transport pathways can be shown to follow particular crystallographic planes.[10] Important intermolecular electronic couplings along these pathways can be defined through face-to-face (including co-facial), edge-to-face, and edge-to-edge molecular packing orientations. Figure 1.1 depicts common molecular stacking types observed in crystalline OSC.

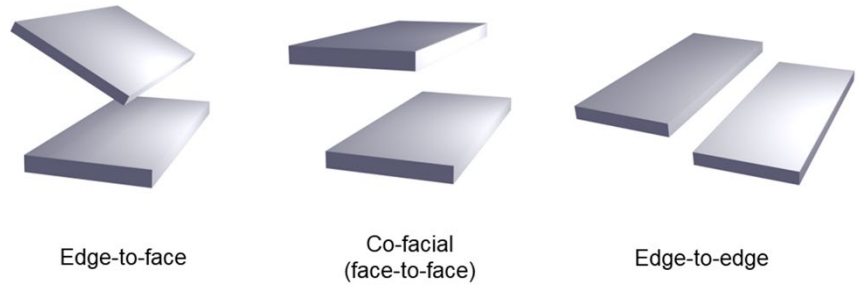

Figure 1.1. A diagrammatic illustration of common molecular stacking types observed in OSC crystal structures.

A significant challenge facing OSC development is acquiring molecular-level understanding of the complex interconnections among the building block chemistry and structure, processing, and the resulting solid-state morphology and order. Limited understanding as to how these different aspects engage makes it difficult to achieve *a priori* control or even predict OSC structure–processing–function relationships, and, especially for solution processed materials, serves as a significant roadblock to the

adoption of OSC in advanced technologies.[11-14] This challenge, however, also provides a great opportunity, as defining detailed relationships among molecular design, processing chemistry, and the solid-state structure over multiple scales can allow for first principles OSC design concepts that can be interrogated *in silico* to create OSC with specific function,[12, 15] and a move beyond the Edisonian approaches generally employed to construct and assess OSC.[12, 16-18]

Understanding the physicochemical mechanisms that regulate molecular-scale aggregation and assembly mechanisms during the transition from solution to the solid is of considerable importance.[15, 19-22] During such processes, the π-conjugated molecules (or chromophores) can adopt configurations (or topologies) that are influenced by the processing environment and the natures and strengths of the inter-chromophore interactions.[15, 23, 24] However, the function behind these mechanisms is poorly understood, in part due to limitations of experimental approaches that allow in situ probing of these transitions, and owing to the complexities in developing appropriate theoretical/computational models and methods of the appropriate temporal scales.[25] Small-angle neutron scattering (SANS) techniques can be used to identify the structure of polymers, aggregate formation in solution, and phase segregation of systems blended with multiple components.[19, 26-29] X-ray crystallography is capable of distinguishing subtle solid-state structural variations as a function of chromophore chemistry and materials processing, though this technique is limited to crystalline materials.[30-32] For more disordered, thin-film materials that do maintain some degree of local and/or long-range order, grazing incidence x-ray scattering spectroscopy (GIXS) has proven to be a go-to technique to probe morphology to establish structure–processing connections,

including the time-dependent formation of OSC morphologies.[21, 26, 33] Atomic force and transmission electron microscopies (AFM and TEM, respectively) can be used to image surface textures of fabricated films.[34 13] Solid state magic-angle spinning (MAS) nuclear magnetic resonance (NMR) spectroscopy can be used to identify topological transformations exhibited during crystallization from solution.[30] Further, UV/vis and fluorescence techniques, when combined with computational approaches, can be used to find correlations between chromophore structure and optical response. These techniques, however, often offer only a snapshot in time of structure from which assertions as to OSC formation are comprised. [20, 21, 35, 36]

1.2 Crystallization of organic semiconductors

This dissertation will focus on materials that possess crystalline order. Crystallization is a ubiquitous, natural phenomenon through which crystals are formed from solution, vapor, or melt processing. Crystals possess characteristic long-range order in terms of their constituent particle arrangement and orientation in three-dimensional (3D) space, i.e., the packing configuration/order, making them unique and distinguishable from other forms of non-crystalline solids or liquids. Crystals can be formed by "particles" made of atoms, ions, molecules, polymers, or can even extend into large biomolecules including proteins. *a priori* control over crystallization, whether one is attempting to induce or prevent crystallization, is critical across many facets of chemistry, including those in relevance to organic molecules where, controlling crystallization has tremendous impact on the development of areas including pharmaceuticals,[37-43] semiconductors,[10, 44-52], energy storage materials[53-55], and nano materials,[56] etc.

Crystalline long-range order is a characteristic feature of interest in developing OSC with excellent charge-carrier mobilities.[57] In addition to various other methods, solution processing has been widely employed to process OSC materials into thin films as they offer a variety of low-cost fabrication protocols to produce thin films with preferred crystalline order.[58, 59] In addition, external process conditions such as the solvent of choice, temperature and pressure are routinely used as tunable parameters to optimize the solid-state order for each application.[59-61] However, modulating crystallinity beyond Edisonian approaches requires first principles understanding of the interrelationships among molecular chemistry, structure and the environment under which crystallization occurs at the solution. Therefore, in this section we aim to provide fundamental first-principles insights into the process of crystallization and the associated mechanisms orchestrated at the atomic and molecular scale.

1.2.1 Understanding mechanisms of crystallization

The mechanisms behind crystallization can be highly influential towards the final packing configuration and morphology of the resulting crystal.[62] There exist several theoretical frameworks to describe the process of crystallization that include: 1) The initial phase separation of the solid phase from bulk, resembling attributes of the crystalline structure usually known as nucleation step, and 2) the continued expansion of the separated nucleus into bulk crystal phase, known as growth, that leads to the evolution of the morphology of the crystal.

There are longstanding efforts to acquire first principles understanding of such mechanisms as a function of molecular building block chemistry and the processing environment to synthetically regulate crystallization. Several in-situ and ex-situ

characterization techniques are routinely used to reveal molecular scale insights associated with crystallization,[26, 63] including small/wide angle X-ray scattering (SAXS, WAXS), transmission electron microscopy (TEM) and later-developed TEM at very low temperatures (cryo-TEM) to capture early stages of crystal nucleation, resonant soft X-ray scattering spectroscopy (RSOXS), UV-visible spectroscopy etc. for developing theoretical models. However, information revealed through such experimentation techniques are limited due to the fast timescales of the steps involved in crystallization. Therefore, computational modeling and simulations are often used to study these complex processes.

Classical nucleation theory (CNT)[64-66] provides robust, fundamental thermodynamic explanations behind crystallization. CNT postulates that the crystallization process first undergoes a first-order phase transition where stochastic density fluctuations of the crystallizing particles homogenously give rise to a "nucleus" of the new phase. The nucleus consists of a small assembly of particles initially forming the solid crystalline state, to which the capillary assumption is applied,[67] i.e., the nucleus will have the same crystallinity as the bulk crystal. For an ideal spherical nucleus (consisting of spherical particles) that is growing out of the bulk solution (or vapor), the Gibbs free energy excess (ΔG_{ex}) is proposed to be a function of two opposing components, 1) surface free energy ($4\pi r^2\gamma$ – an increasing function along growth with positive energy vs., 2) bulk free energy of the growing crystal ($4/3\,\pi r^3 \Delta G_v$– a decreasing function along growth with negative free energy (Equation 1.1. and Figure 1.2), where, r is the radius of the growing nucleus, and γ is the surface tension.[68] The critical nucleation energy (ΔG_{ex}^*) manifests as the cost of energy (or the thermodynamic

energy barrier to overcome) to form a nucleus of critical size with specific radius, known as the critical size that reflects a thermodynamically metastable state. Any infinitesimal changes to the critical radius will render either dissolution (if decreased) or infinite growth (if increased) of the crystalline phase.

$$\Delta G_{ex} = 4\pi r^2 \gamma + \frac{4}{3}\pi r^3 \Delta G_v \qquad \text{Equation 1.1}$$

where, G_v is the bulk free energy change per unit volume.

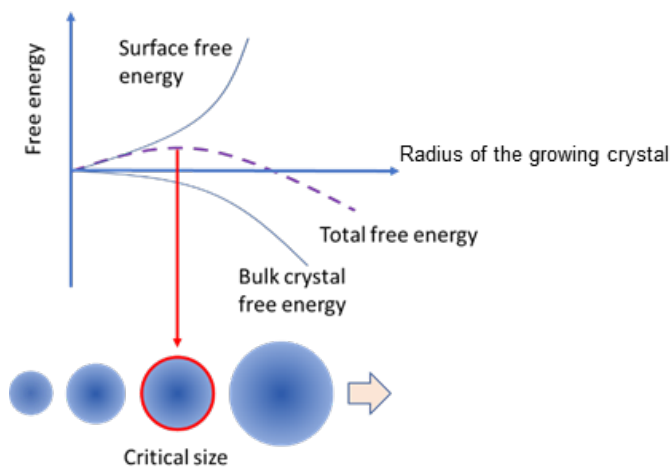

Figure 1.2. Gibbs free energy associated with a growing spherical nucleus. The surface energy and bulk crystal free energy components are shown in solid lines and the dotted line indicate the overall energy.

Although the crystallization of organic molecules is far from the ideal behavior that is assumed by CNT, it remains valid for providing fundamental descriptions for nucleation of organic materials. In general, organic molecules are non-spherical systems with prominent shape anisotropy, and thus are often grown into faceted shapes. Consequently, the overall local order and molecular packing may not always reflect the features of the lowest surface energy polymorph, i.e., the thermodynamic equilibrium

morphology.[68, 69] For such faceted growth of crystals, the energy associated with formation of a layer-wise 2D nucleus (when applicable – Figure 1.3), i.e., the 2D nucleation energy barrier associated with the $\{hkl\}$ surface ($i.e., \Delta G^{*}_{\{hkl\})}$), can be an analogous, although underestimated, representation of the ΔG^{*}_{ex} discussed in CNT, as surface stabilization provided from the previous layer to the next that grows on top of it jump-starts nucleation.

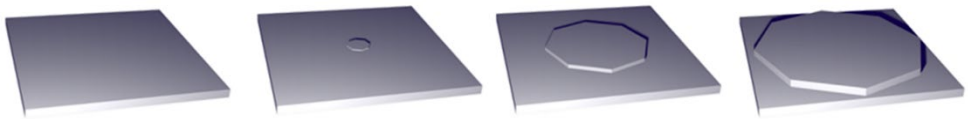

Figure 1.3. Illustration of the 2D layer growth on top of the crystal surface, that follows the birth and spread of the 2D layer.

The 2D nucleation of crystal faces can be comparable to the macroscale description of heterogeneous crystallization, where crystals nucleate on top of a surface are associated with a contact angle θ, originate from the stabilization from the surface, thereby causing critical energy for heterogeneous growth to be always lower than that of the homogenous case (Equation 1.2, and 1.3).[63, 70] However, at the molecular scale, such contact angle cannot be readily defined as the surface in general is separated by a vanishingly thin interface between the solvent and the solute, and the surface area of the growing crystal layer on top of the crystal face is established by the solvent accessible surface area, that is a function of van der Waals radii of atoms of participating molecules. This interface is in general difficult to quantify at the atomic scale due to its highly dynamic nature (Figure 1.4).

$$\Delta G^{Hetero}_{critical} = \phi \Delta G^{Homo}_{critical} \qquad \text{Equation 1.2}$$

where, ϕ is a function that depends on the contact angle θ:

$$\phi = \frac{(2+\cos\theta)(1-\cos\theta)^2}{4} \qquad \text{Equation 1.3}$$

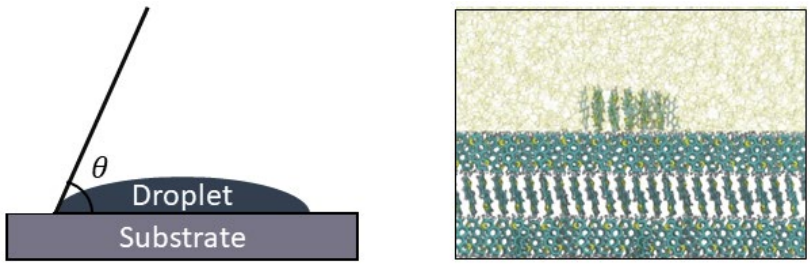

Figure 1.4. Comparison of heterogenous crystallization at the macroscale forming a droplet on top of the substrate surface (left) having contact angle θ, with the layer-wise crystal formation of on top of the substrate surface at molecular scale.

1.2.2 Impact of supersaturation on crystallization

The supersaturation level of the solution is a key parameter that governs the mechanism by which crystallization is undertaken. Solution supersaturation can be expressed by:[71]

$$s = \frac{\chi}{\chi^*} \qquad \text{Equation 1.4}$$

where, x* is the solubility expressed in mole fraction, which is the fine balance by which the crystalline solid is at dynamic equilibrium with the solution. $\chi > \chi^*$ means solution is at supersaturation, while the opposite $\chi < \chi^*$ denotes undersaturation. Solubility of a crystalline solid is a function of the chemical potential μ:

$$\frac{\Delta\mu}{k_B T} = \ln S \qquad \text{Equation 1.5}$$

where, Δμ is the chemical potential difference between solid and the liquid:[71]

$$\Delta\mu = \mu_{solid} - \mu_{liquid} \qquad \text{Equation 1.6}$$

Here, Δμ determines the driving force for phase separation based on the criteria:

1. Δμ > 0; solute is dissolved in solution, no driving force for phase separation.
2. Δμ < 0; driving force is present for phase separation, thereby crystallization can occur.
3. Δμ = 0 solution and the crystal surface are at dynamic equilibrium

therefore, it is important that the parameter Δμ to be maintained below zero to observe continued growth to prevent re-dissolving of the growing crystal, that is achieved through maintaining supersaturation above required levels.

1.2.3 Thermodynamics and kinetics of nucleation and growth

The crystallization process in a homogenous solution can be assumed to occur first through nucleation, until there is enough bulk free energy to overcome surface destabilization to ensure continuous growth. Inspired from transition state theory, the nucleation rate (J) can be approximated by Equation 1.7 [68]:

$$J = A\, exp\left(\frac{-E_A^*}{k_B T}\right) exp\left(\frac{-\Delta G_{ex}^*}{k_B T}\right) \qquad \text{Equation 1.7}$$

where, ΔG_{ex}^* represents the thermodynamic energy barrier, emerging from metastable critical nucleus that is gradually achieving bulk crystal attributes (i.e., thermal relaxation of the assembly of finite number of molecules to achieve of positional, orientational, and coordination number achieving attributes of the crystal lattice). E_A^* represent the kinetic energy barrier that is difficult to quantify but is originated from the dynamic solute-solvent interactions/collisions and diffusion of molecules on top of the crystal surface.

The pre-factor A depends on the properties of the material itself, including shape anisotropy of the building block molecules.[68]

Following nucleation, the continuous growth of the crystal bulk requires successive attachment of molecules in appropriate orientations. The growth can also be assumed to be controlled by similar functional form presented by Equation 1.7, that is an interplay between thermodynamics and kinetics on the molecular attachment (assuming Markov behavior,[72] given the availability of critical nucleation energy to overcome the formation of the nucleus of critical size). The perpendicular growth rate of the {hkl} face during steady state is expressed by Equation 1.8, assuming no kinetic interference is present.

$$\tau_{\{hkl\}}^{-1} = \xi exp\{\frac{-\Delta G_{\{hkl\}}^{*}}{k_B T}\} \qquad \text{Equation 1.8}$$

Here, the $\Delta G_{\{hkl\}}^{*}$ represents a collective energy barrier for the growing face at the steady state, combining the dependencies coming from the infinite surface itself and the solution environment.[60] We clarify that the $\Delta G_{\{hkl\}}^{*}$ often do not fully represent the actual ΔG_{ex}^{*} in homogenous case, due to the availability of substrate surface from the previous layer. The pre factor ξ is applied to an ideal growth behavior with no associated kinetic barriers being involved.

1.2.4 Mechanisms of nucleation and growth of faceted crystallization

Crystallization mechanisms of organic molecules in general are categorized into several major domains (Figure 1.5) with relevance to their solution supersaturation level: 1) Spiral growth, 2) two-dimensional (2D) nucleation and growth (i.e., the one-step 'birth and spread' mechanism), 3) direct crystallization in barrierless fashion (barrierless

growth), also referred to as rough growth.[60, 62, 73] The 2D nucleation or spiral growth type mechanisms are applicable at low supersaturation levels: A prominent nucleation step initiates the crystallization of the composition of the crystal bulk in 2D nucleation and growth mechanism, while that of spiral growth, a defect site present on the surface initiate crystallization.[73] Rough (or barrierless) growth is of relevance in the presence of low to no $\Delta G^*_{\{hkl\}}$ requirement, i.e., absence of significant 2D nucleation step under available thermal energy ($k_b T$), often seen at high supersaturation levels where nucleation step merged with growth directly. Such mechanism often introduces surface roughness to the newly forming layers due to the absence of smooth assembly where factors such as molecular crowding, lack of surface diffusion imposing complex effects.[50, 74]

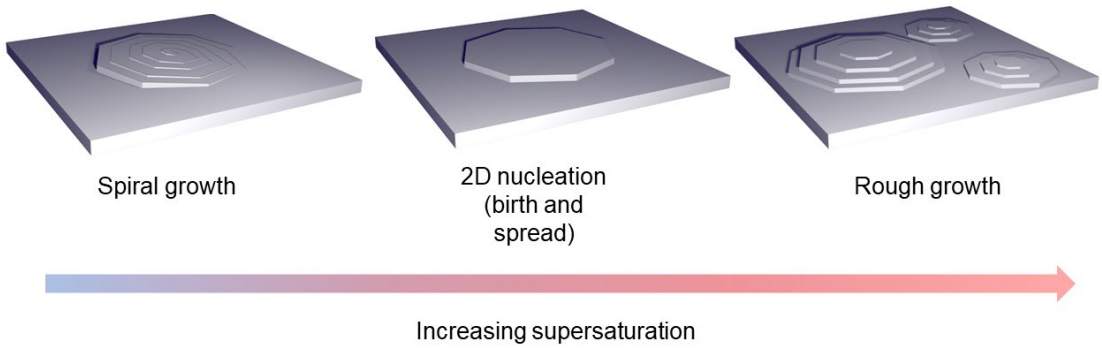

Figure 1.5 The three regimes of facet growth of crystals as a function of supersaturation.

CNT postulates that crystallization follows capillary assumption where the nucleating phase already possesses perfect crystallinity resembling the bulk phase, i.e., through one-step nucleation. However, several studies have shown occasions where multiple nucleation steps are being involved, giving rise to metastable phases with attributes that are different from the final crystalline bulk.[63]

1.2.5. Solution growth and morphology evolution of OSC crystals

The morphology evolution of crystal structure from solution is understood to be a function of both thermodynamic and kinetic aspects that are engaged during molecular assembly.[75] The overall crystal morphology is determined by steady-state crystal habits in the crystal phase-space, which are described by kinetics-driven dynamic process. Crystal habit selection is subject to several external factors including solution environment, temperature, and pressure, where variations in each aspect can alter the overall morphology of the crystal.[60, 61, 76]

During early descriptions, the Gibbs criterion proposed that the equilibrium shape of a crystal of a fixed volume emerging out of a fluid (vapor or liquid) phase to be always the one that minimize the total surface energy,[77] but notably mentioning that eventually the slow growing surfaces will dominate the resulting crystal while not necessarily maintaining lowest surface energy. Following, Wulff extended the Gibbs criterion to defining the Gibbs-Wulff shape of faceted crystals. Here, the magnitude of perpendicular distance of face i (i.e., H_i) from common origin are proportional to the surface free energy that corresponds,[78-80] i.e., controlled by thermodynamics.

Under most supersaturation conditions, OSC crystals spontaneously grow into faceted shapes, mostly with limited number of surfaces resulting in morphologies that are not the lowest in terms of surface free energy,[81, 82] therefore points out to the shortcomings of the strictly thermodynamic understanding. Later, Frank and Chernov included the contribution of kinetics on growth through steady-state dynamics where the overall crystal morphology is an outcome of relative growth rates of the individual faces at steady-steady state. Frank-Chernov condition also establishes that the faster growing

surfaces gradually disappear during growth while the slow growing faces dominate on the steady state morphology. The steady-state growth rates of the facets are proportional to the magnitude of H.

$$\frac{G_1}{H_1} = \frac{G_1}{H_1} \ldots = \frac{G_i}{H_i} \ldots = \frac{G_N}{H_N} \qquad \text{Equation 1.9}$$

where, G_i is the absolute normal growth rate of face i.

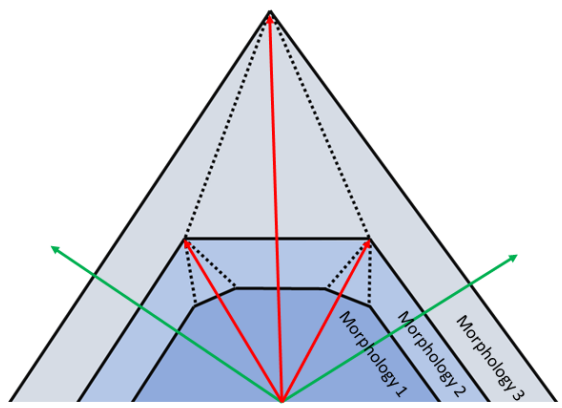

Figure 1.6 Diagrammatic illustration of how fast-growing crystallographic faces (red arrows) are taken over by slow-growing faces (green arrows) during morphology evolution from steps 1 through 3.

Early approaches for theoretical predictive models for crystal selection were strictly based on the structure, geometry, and static interactions of the crystal unit cell, and several of them are still in use for predicting the growth/dissolution rate of surfaces. The Bravais-Friedel-Donnay-Harker, or BFDH, model[83] is one of the earlier approaches that is exclusively based on the structure and interactions of the crystal where perpendicular growth rate is inversely proportional to the interplanar spacing.

$$G_{\{hkl\}} \propto \frac{1}{d_{\{hkl\}}} \qquad \text{Equation 1.10}$$

Based on periodic bond chain (PBC) theory, Hartman and Perdock theorem[19,84] predicts growth rate by accounting for the attachment energy per surface. Growth rate is assumed to be slow when fewer chains of strong bonds are involved. [84, 85]HP theorem accounts for the energies of bonding in terms of crystal interactions on different surfaces in addition to the geometry:

$$G_{\{hkl\}} \propto E^{att}_{\{hkl\}} \qquad \text{Equation 1.11}$$

In other words, the perpendicular growth rate here is analogous to the attachment energy, that is expected to be anticorrelated with the time (t) it takes for the crystal face to grow. Here kinetics is assumed to play a major role over thermodynamic aspects, where the resulting steady-state morphology may not necessarily satisfy the conditions required by the equilibrium crystal structure. However, lack of dynamic perspective in both these predictive models at the molecular and/or atomic levels, i.e., the dynamic interactions among the lattice surface and the solution environment leads to limited levels of predictability.[86]

1.3 Objectives and outline of the dissertation

OSC can be designed with fine-tuned redox, electronic, and optical properties that result in promising high-performance metrics for new generations of electronics applications.[20] However, hard-and-fast design rules that connect chromophore construction and processing strategy to afford fine control over required OSC solid-state morphology are critical. The overarching hypothesis of this dissertation is that by

determining thermodynamic and kinetic parameters of structure-processing-function relationships at the atomistic/molecular scale, the in-depth understanding required to assist in the rational design of OSC, via both chromophore design and solvent optimization strategies, can be obtained, to assist in the rational design of OSC, including via both chromophore design and process parameter optimization strategies.

The required first-principles understanding to establish structure-processing-morphology relationships of OSC are investigated here through multiscale modeling and simulations that combine quantum mechanics and classical mechanics descriptions with data science approaches. Chapter 2 provides an overview of the methods that were employed throughout this dissertation, combining both quantum mechanical and classical dynamics approaches. An outline of the electronic structure theory is provided along with appropriate descriptions of the quantum mechanical details. The rationalization behind the use of all classical mechanical approaches, and clarifications as to under what assumptions each technique/method is operated, are also provided in detail.

Chapter 3 discusses the results of the impact of π-conjugated chromophore chemistry and the processing environment on the structure of OSC oligomers in solution. The structures investigated are comprised of electron-rich donor and electron-deficient acceptor moieties. Here, both quantum-chemical calculations and MD simulations are carried out to systematically investigate how variations in molecular design and processing chemistry influence the structural configurations, dynamics, and pre-aggregation tendencies. Notably, questions are brought forward concerning the current emphasis on the roles of noncovalent intramolecular interactions in the design of OSC building blocks. The study reveals that the level of balance between the rigidity

(thermodynamic equilibrium over kinetics) versus the flexibility (kinetics over thermodynamics) of the structural confirmations can alter the extent of aggregation versus solution processability of molecules in solution that are used to build OSC, which serve as important tunable parameters for controlling morphology.

The deceivingly simple yet complex mechanisms behind crystal nucleation and growth of OSC are investigated in Chapter 4. First-principles understanding required to synthetically regulate OSC nucleation and growth through tunable process parameters to regulate morphology and packing is revealed. Throughout this study, classical MD simulations are employed to simulate the growth of a molecular system that crystalizes in a herringbone packing arrangement from solution. The discussions necessary for extending the current crystallization models which are based on spherical/atomistic systems, into the space of highly shape anisotropic OSC molecules are portrayed. Ultimately, a descriptive atomic-scale rationale behind different crystallization mechanisms in different solution environments and supersaturation levels is provided to fine-tune surface roughness and crystal domain size through controlling thermodynamic vs. kinetic aspects, that can in turn be used to develop process protocols for regulating morphology.

The insights acquired through Chapter 4 in relevance to solution crystallization are extended in Chapter 5 into crystallization of OSC from the melt. Here, a series of rigid small molecule OSC are systematically investigated to uncover chemical structure to morphology relationships to reveal how different atomic compositions and symmetry etc. contribute to the order/disorder of crystal strictures and their associated capacity to self-assemble or disassemble. Simultaneously, we develop semi-to-fully automated high-

throughput schemes to automate the complex and labor-intensive simulation procedures to generate large scale data based on crystal structures with varied building block chemistry. In return, important molecular-scale dynamic insights are provided with relevance to the phase behavior shown by the OSC molecules under fast anneal conditions (that tend to encourage kinetic effects). Insights are revealed as to how varied molecular chemistry and thereby the varied interaction dynamics can lead to regaining thermodynamic equilibrium crystalline structure of the melts.

Chapter 6 provides a synopsis covering the aspects discussed throughout the dissertation. The perspectives of broader implications, how well the hypothesis is supported, and future directions based on the work done in this dissertation is discussed to bridge the knowledge gap between the molecular-scale features and the corresponding macroscale properties.

CHAPTER 2. COMPUTATIONAL METHODS

Macroscopic materials properties are deeply interconnected to their constituent atomic- and molecular-scale features and investigating structure–property relationships across many length scales has been a longstanding goal to aid the design of high-performing organic materials. The application of computational approaches has proven to be effective in the pursuit of these multiscale investigations, especially in connection with experimental characterization.[1, 2] In this chapter, we briefly outline the theoretical concepts behind the theoretical and computational methods used in this thesis, with a focus on classical dynamics and electronic structure methods. This chapter presents an overview of well-established computational approaches, and the information presented was derived from several sources.[1, 3-7] Specific references for approaches are provided as needed

2.1 Overview of Concepts: Classical Mechanics and Molecular Dynamics

Classical mechanics approaches describe the motion of macroscopic objects through Newtonian physics (also known as classical physics), governed by Newton's laws of motion. The core idea is centralized around Newton's second law of motion, which can be applied for a moving object with mass m and acceleration a, to obtain the Force (F) acting on the particle:

$$F = ma \qquad \text{Equation 2.1}$$

2.1.1 Molecular mechanics

Molecular mechanics (MM) treats molecular systems through classical mechanics descriptions; the atoms in molecules are considered classical objects that are purely

particle-like in nature. Macroscopic properties that originate from atomic-scale behavior can be obtained efficiently through simulation of the system through MM approaches. Although quantum mechanical descriptions are a more accurate alternative to describe small particles like atoms and molecules, classical descriptions provide reasonable approximations to overcome the prohibitively high computational cost associated with investigating complex systems that involve thousands to millions of atoms, and those necessitate dynamic calculations over the static picture. At the heart of molecular mechanics, Newton is second law governs calculation of the force acting on particle i with mass m_i and acceleration a_i:

$$F_i = m_i a_i \qquad \text{Equation 2.2}$$

2.1.2 Molecular dynamics

Molecular dynamics (MD), a statistical-mechanics-driven computational technique, which falls under the umbrella of molecular mechanics, calculates the time-dependent trajectory of particles (consisting of atoms, atomic groups, or molecules) through Newton's laws of motion. In atomistic simulations, atoms are modeled as finite point masses, with fixed charges/partial charges, to which all related bonding and non-bonding attributes are defined through harmonic oscillator functions.[4, 5] This is only an approximation to the true quantum mechanical description, in which only the dynamics of the nuclear motion is considered. The motion of electrons is not explicitly accounted for, instead, the electronic contribution on the nuclei is included though implicit empirical potential, based on the Born-Oppenheimer approximation, which allows the decoupling of electron-nuclear interactions.[7] The time evolution of atoms in molecules of the system is determined through repeated integration of equations of motion.

A general workflow of a MD simulation requires: 1) Input of definitions of atoms in terms of their masses and charges, along with their initial positions and velocities; 2) Input of parameters for interaction potential function (U), that is defined through the force field (FF), that estimates the forces exerting on atoms in their interacting environment; 3) Repeated calculation of time evolution in small time step ($t + \Delta t$) intervals through equations of motion using a specific integration algorithm; and 4. Updating the calculated new positions and velocities to generate the simulation trajectory.[5] MD calculates the net force acting upon ith atom, F_i, through the negative spatial derivative of the potential energy function $U(R)$:

$$F_i(R) = m_i \frac{d^2\vec{r_i}}{dt^2} = -\nabla_i U(R) = -\left(\frac{\partial U}{\partial x_i}, \frac{\partial U}{\partial y_i}, \frac{\partial U}{\partial z_i}\right) \qquad \text{Equation 2.3}$$

where, R denotes the coordinates $(r_1, \dots, r_N)$ of the N atoms of the system, each consisting of x_i, y_i, and z_i spatial coordinates.

The potential function U aims to provide reasonable descriptions through approximations to mimic true potential energy (E_{pot}) surface. The atomic force fields of MD take the general functional form to give out the E_{pot}:

$$E_{pot} = E_{bond} + E_{angle} + E_{torsion} + E_{n.b.} \qquad \text{Equation 2.4}$$

where, the E_{pot} sums over the bonding, i.e., bond stretching, angle, torsion, and non-bonding (atom pair interactions such as van der Waals and coulombic) potentials, defined by the structure of the molecular system.

2.1.2.1 Nonbonded interactions through Lennard-Jones potential

The level of accuracy of non-bonded descriptions adds to the simulation accuracy of many macroscopic phenomena especially such as crystal simulations and phase transitions, where nonbonding interactions play a critical role. The non-bonding interaction term of the $U(R)$ represents the interactions between atoms pairs separated by the distances r_{ij}=$|(r_i - r_j)|$ that are not bonded chemically. Throughout investigations carried out in this text, we employ the Lennard-Jones (LJ) type interaction potential[5] V_{ij} of which the potential between two atoms i and j equals:

$$V_{ij} = 4\epsilon\left[\left(\frac{\sigma}{r_{ij}}\right)^{12} - \left(\frac{\sigma}{r_{ij}}\right)^{6}\right] \qquad \text{Equation 2.5}$$

where, a reasonable approximation of two major forces between non-bonded atoms are applied: a strong repulsive term at shorter r_{ij}, (the $(\sigma/r)^{12}$ term), and the attractive term at intermediate r_{ij} (the $(\sigma/r)^{6}$ term), representing van der Waals interaction through mutual polarization of the two atoms.

Note that the V_{ij} overall describes interactions in the short-range whereas to account for long range interactions such as coulombic interactions, other descriptions are necessary. LJ potential has been widely used, due to fast computation and applicability in varied scenarios. Computational cost can be further reduced through application of cut-off protocols:

$$V_{ij}^{cutoff} = \begin{cases} V_{\alpha\beta}(r_{ij}) - V_{\alpha\beta}(r_{\alpha\beta}^{cut}) & r_{ij} < r_{\alpha\beta}^{cut} \\ 0 & (otherwise) \end{cases} \qquad \text{Equation 2.6}$$

where, the potential is truncated and shifted at the cutoff limit:

$$r_{ij} = r_{\alpha\beta}^{cut} = 2.5\sigma_{\alpha\beta} \qquad \text{Equation 2.7}$$

2.1.2.2 Forcefields for representing organic molecular systems

The Optimized Potential for Liquid Simulations (OPLS) forcefield, developed by Jorgensen et al.,[8] uses optimized parameters derived from the experimental properties of liquids including density, heat of vaporization and gas phase dihedral energy profiles. Therefore, OPLS serves as a complete FF that provides reasonable estimations for a wide range of liquid and solid-state simulations, making it a popular choice. In this thesis, we use the all-atomistic OPLS (OPLS-AA) forcefield to simulate solutions of organic solute-solvent systems in Chapter 3 and to perform simulations of crystal formation from solution in Chapter 4. The potential energy through OPLS force field acting on particle i and j pair is defined as:

$$E_{pair} = \sum_{bonds} \frac{1}{2} k_b (r - r_0)^2 + \sum_{angles} k_\theta (\theta - \theta_0)^2 + \sum_{torsions} \left\{ \frac{V_1}{2} [1 + \cos(\phi)] + \frac{V_2}{2} [1 - \cos(2\phi)] + \frac{V_3}{2} [1 + \cos(3\phi)] + \frac{V_4}{2} [1 - \cos(4\phi)] \right\} + \sum_{i=1}^{N-1} \sum_{j=i+1}^{N} \left\{ 4\epsilon_{ij} \left[\left(\frac{\sigma_{ij}}{r_{ij}} \right)^{12} - \left(\frac{\sigma_{ij}}{r_{ij}} \right)^{6} \right] + \frac{q_i q_j e^2}{r_{ij}} \right\} f_{ij}$$

Equation 2.8

where, the potential energy combines bonds, angles, torsions, along with the nonbonded interactions which include Lennard-Jones and Coulombic interactions. The r_{eq} and θ_{eq} are equilibrium parameters of interatomic distance and angles. The bonding energies represent the covalently bonded atoms with bond stretching and bending described as simple harmonic oscillators with force constant k_b and k_θ, in the bonded interaction

terms. The torsions are described fundamentally in a similar fashion where, ϕ is the dihedral angle and V_1, V_2, V_3 and V_4 are Fourier coefficients. The nonbonded parameters combine short-range van der Waals interactions and long-range coulombic interactions. The van der Waals type interactions are described through Lennard-Jones function where the term ϵ_{ij} represents the depth of the potential well, and σ_{ij} is the distance at which the particles i and j interaction potential is considered to be zero. The coulombic term includes charges q_i, q_j and interatomic distance r_{ij} between atoms i and j.

The General Amber Force Field (GAFF) is another force field used for systems involving organic molecules and biomolecules.[9] GAFF provides a complete force field that can provide reasonable approximations to describe systems with molecules containing C, N, O, H, S, P, F, Cl. Br, and I, where parameters are derived from a large data set of experimental properties of organic and bio molecules. The potential energy through GAFF can be expressed as:

$$E_{pair} = \sum_{bonds} K_r (r - r_0)^2 + \sum_{angles} K_\theta (\theta - \theta_0)^2 + \sum_{dihedrals} \frac{V_n}{2} [1 + \cos(n\phi - \gamma)] + \sum_{i<j} \left[\frac{A_{ij}}{r_{ij}^{12}} - \frac{B_{ij}}{r_{ij}^{6}} + \frac{q_i q_j}{\varepsilon r_{ij}} \right] \quad \text{Equation 2.9}$$

where, γ is the phase angle of torsional angle parameters, A, and B are relevant constraints for nonbonding (LJ) terms.

2.1.2.3 Force field parameterization of molecules

For an accurate representation of organic molecular systems, the parameterization step of the forcefield is critical. The level of resolution that can be provided by the forcefield with the level of details to account for atoms in various chemical environments

has a profound impact on the calculated macroscopic properties. Therefore, for improved accuracy, we further optimize parameters associated with OPLS and GAFF forcefield by incorporating explicit partial charges and dihedral potentials, derived from ab initio calculations.

We perform geometric optimizations for molecules to derive partial charges associated with atoms through the Charge Model 5 method[10] via density functional theory (DFT) at the ωB97XD/6-31G(d,p) level. To explicitly parameterize dihedral potentials, we first obtain the potential energy surfaces associated with dihedral rotations through PES scans via DFT, and then calculate the change in potential energy at each optimized geometry along torsion. Next, we calculate potential energies of each optimized geometry at the MD level, but with dihedral potential parameters set to zero. Lastly, we subtract the calculated energies of MD level from those derived by DFT to obtain the PES and fit through the Equation 2.10 to obtain the improved parameters.[11]

$$V(\{\phi\}) = \left\{\frac{V_1}{2}[1+\cos(\phi)] + \frac{V_2}{2}[1-\cos(2\phi)] + \frac{V_3}{2}[1+\cos(3\phi)] + \frac{V_4}{2}[1-\cos(4\phi)]\right\} \qquad \text{Equation 2.10}$$

where, V_n are the dihedral parameters of interest, and ϕ is the torsion angle. The PES obtained with the new parameters applied are then compared with the PES at the ab initio level to validate the accuracy.

2.1.2.4 Initial velocity generation and numerical integration of the equations of motion

Determining the time evolution of the system entails calculation of the positions and velocities of the atom i at time $t + \Delta t$ in terms of the already known positions and velocities at time t. This is computed through numerical integration of Newtons equations

of motion using varied algorithms. Initial velocities are assigned to atoms by assuming Maxwell-Boltzmann velocity distribution along the 3-dimensional space.[4] The Maxwell-Boltzmann distribution function can be expressed in terms of the fraction of the particles within an infinitesimal portion of the d-dimensional velocity space (d^3v), with velocity vector with magnitude v is:

$$f(v)d^3v = \left(\frac{m}{2\pi k_b T}\right)^{\frac{3}{2}} e^{\frac{-mv^2}{2kT}} d^3v \qquad \text{Equation 2.11}$$

where, m is the mass of particle, k_b is the Boltzmann constant, and T is the absolute temperature. The velocity (along spatial coordinates (x, y and, z) of the ith particle is generated ensure that it follows Maxwell-Boltzmann type population is by multiplying random gaussian numbers with a mean square velocity $\sqrt{2k_bT/m}$, to ensure total momentum of the system to be zero.

$$v_{i,\alpha} = \sqrt{\frac{k_bT}{m_i}}\, N(0,1) \qquad \text{Equation 2.12}$$

$$\alpha = \epsilon\, \{x, y, z\} \qquad \text{Equation 2.13}$$

where, $N(0,1)$ is a gaussian random number that is of variance 1 and mean 0.

Once initial velocities are generated, they are used as input for the calculation of the trajectory along with the positional coordinates. Numerical integration algorithms are used to efficiently compute the trajectories and calculate energy. Basic formulation of the commonly used Varlet integrator algorithm[6] can be obtained through Taylor expansion of the positional coordinates and the velocities, that update the new velocities and positions:

$$r_i(t+\Delta t) = r_i(t) + v_i(t)\Delta t + \frac{1}{2}a_i(t)(\Delta t)^2 \qquad \text{Equation 2.14}$$

$$v_i(t+\Delta t) = v_i(t) + \frac{1}{2}[a_i(t) + a_i(t+\Delta t)]\Delta t \qquad \text{Equation 2.15}$$

where, $v_i(t+\Delta t)$ denotes the infinitesimal updates of velocity along time step intervals, and $a_i(t)$ is the acceleration at time t.

2.1.2.5 Calculation of energy and average temperature

Energy calculations are carried out by simply combining the potential energy (PE) and kinetic energy (KE) to obtain total energy E_{tot}:

$$E_{tot} = PE + KE \qquad \text{Equation 2.16\}$$

where, PE is obtained through the potential function $U(r)$, that is defined through the force field. KE is obtained through:

$$KE = \langle \sum_{i=1}^{N} \frac{|p_i|^2}{m_i} \rangle \qquad \text{Equation 2.17}$$

where, p_i is the momentum of the particle and m_i is the mass of the particle. The average temperature T is calculated from the KE as follows using equation 2.18:

$$T = \frac{1}{3Nk_b} \langle \sum_{i=1}^{N} \frac{|p_i|^2}{m_i} \rangle = \frac{1}{3Nk_b} KE \qquad \text{Equation 2.18}$$

2.1.2.6 Periodic boundary conditions and minimum image convention

Periodic boundary conditions (PBC)[12] allow simulations of infinite systems by using a periodic unit cell (also referred to as periodic box) representation to reasonably approximate the bulk properties. Here, only the particles interacting within the unit cell

are treated, saving computational cost. The movement of particles between the unit cells are accounted for by using the minimum image convention where the interactions between particles within the unit cell as well as between unit cells are also considered. PBC conditions for a cubic type of unit cell can allow periodic boundaries in two (x, y laboratory axes) or in all three (x, y, and, z) directions. Other types of periodic unit cell types include triclinic and octahedron etc. that are often used in simulation of biomolecules.

2.1.2.7 Statistical ensemble

As MD is based on statistical mechanics, the macroscopic properties of physical observables are simulated using statistical ensembles (SEs).[4] The Gibbs ensemble, for instance establishes that properties of large macroscopic systems can be reasonably approximated through many small individual samples of it, mitigating the requirement of knowing the precise details of all particles in the system. Statistical ensembles consider ensemble averages of physical observables sampled through large number of identical systems, varied by different microstates or configurations. SE used in MD are typically characterized by fixed entities such as number of particles N, volume V, pressure P, temperature T, chemical potential μ, and energy E etc. The micro-canonical ensemble is one of the most fundamental examples of SEs used that is characterized by NVE conditions, i.e., constant N, V and E. Other SEs used in the MD equilibration procedures are the NVT (canonical ensemble - constant N, V and T) and NPT ensemble (isothermal-isobaric ensemble – constant N, P and T), through control algorithms of each aspect. The application of these ensembles represents the control parameters used in real world experiments. A classical MD simulation assumes that given infinite simulation time, the

entire energetic landscape associated with the microstates of the system will be visited, and this is known as the ergodic hypothesis. Under the ergodic hypothesis, averaging over the statistical ensemble equals to the averaging over the trajectory of the system.

2.1.2.8 Temperature control

Temperature scaling algorithms are used to force the system temperature to be exactly the desired T during each time step by controlling the velocities of the atoms in the system. Direct scaling algorithms such as Berendsen scaling method[3], velocities are scaled at each time step by factor λ that is defined by:

$$\lambda = \sqrt{1 + \frac{\Delta t}{\tau_T}\left(\frac{T_0}{T} - 1\right)} \qquad \text{Equation 2.19}$$

where, τ_T is the time constant of temperature control. Berendsen criteria requires that $\tau_T > 100$ to ensure the system has natural fluctuations about the average.

2.1.2.9 Pressure control

Simulations that need to be conducted at constant pressure ensemble utilize constant pressure bath algorithms. The pressure tensor P is calculated using the Clausius virial theorem:

$$P = \frac{2}{v}(E_{kin} - \Xi) \qquad \text{Equation 2.20}$$

where, E_{kin} is the kinetic energy and v is the simulation box volume. Ξ is the inner virial tensor that is defined as:

$$\Xi = -\frac{1}{2}\sum_{i<j} r_{ij} \cdot F_{ij} \qquad \text{Equation 2.21}$$

the isotropic pressure of the simulation box is then calculated from the trace of the pressure tensor:

$$P = Tr\ \frac{(P)}{3} \qquad \text{Equation 2.22}$$

The pressure baths applied in the investigations carried out throughout the chapters includes the Berendsen[3] and Parrinello-Rahman[13] pressure coupling algorithms.

2.1.2.10 General simulation protocol

We follow a specific simulation protocol to represent the simulated systems: Once the initial input structures are modeled and parametrized, equilibration of the configurations at the chosen MD level are necessary prior to the production runs of simulations that are used in the trajectory analyses. We make use of a combination of steps carried out in the NVT and NPT ensembles to achieve equilibration of the system of which the Gibbs free energy convergences to a minimum. Achieving equilibration can be listed through the fivefold procedure where input of each following step is the output of the previous ensemble:

1. Steepest descent energy minimization (EM) – a fast initial equilibration of the atoms in molecules minimizing energy
2. Equilibration under NVT ensemble – Temperature coupling is introduced for the first time with the initial velocities assigned to atoms/particles according to the Maxwell Boltzmann distribution
3. Equilibration under the NPT ensemble 1 – Pressure coupling is introduced for the first time through the Berendsen barostat algorithm[3] to achieve equilibrium density

4. Equilibrium under the NPT ensemble 2 – The more accurate Parrinello-Rahman barostat algorithm[13] is applied to further equilibrate the system
5. Production runs under NPT ensemble 2 – The final simulation runs to which all the trajectory analyses are carried out

2.1.3 Collective variables

Collective variables (CVs) are functions of atomic coordinates that are formulated to characterize interested properties of the system along the reaction coordinates. The CVs serve to reduce the high dimensional state space of the system to human-interpretable lower-dimensional terms. CVs can therefore be used to effectively characterize the slowest degrees of freedom associated with the physicochemical processes that are captured through the simulation trajectories. Mathematically, CV can be expressed using atomic coordinates R:

$$s(R) = \left(s_1(R), \dots, s_d(R)\right) \qquad \text{Equation 2.23}$$

where, the CV, s, is a set of coordinates combining characteristics relevant for describing a property. The expectation of an ideal CV is to characterize all relevant configurations/microstates of a process of interest including all metastable states.

2.1.4 Constant chemical potential molecular dynamics algorithm

The constant chemical potential molecular dynamics (CμMD) algorithm developed by Perego et. al.,[14] provides an effective simulation ensemble to overcome finite size effects associated with classical MD simulations of solutions through active control of solution supersaturation level. The constant chemical potential (μ) ensemble provides a reasonable approximation of the grand canonical ensemble, allowing one to

investigate processes of which the particles are in equilibrium with a large reservoir.[15] Such approximation allows to overcome strong finite effects associated with classical MD simulations that prevent direct comparisons with experimental data for physical observables. Throughout Chapter 4, we use CμMD algorithm to simulate crystal formation of organic molecules from solution where we gain control and maintain solution supersaturation consistently at desired levels throughout the crystallization process. The original CμMD code allocate the simulation box Z axis direction into five regions (Figure 2.1), moving outwards from the center: (1). A central crystal slab, (2). Two growth regions on either side, (3). Two gradient regions of concentration to account for concentration drop during crystal growth, (4) Two control regions (CR) where the supersaturation level is maintained at the desired value and finally (5). a continuous reservoir (R) region that allow transfer of solute molecules in and out to the CR.

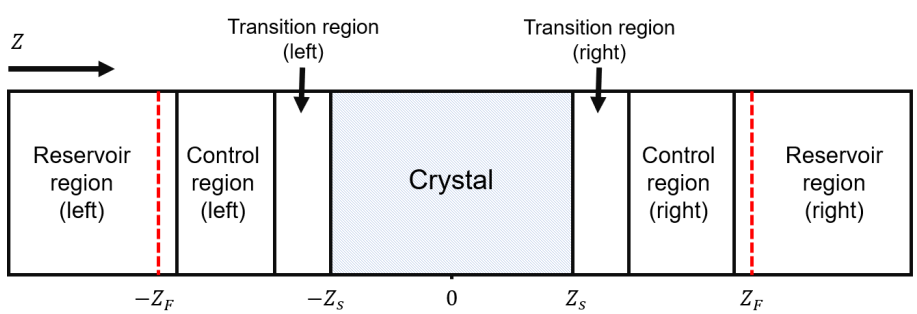

Figure 2.1 Schematic diagram of the layout of the simulation box for implementation of CμMD procedure. The box is oriented horizontally along with the laboratory axis z

Here, a simple harmonic force at constant chemical potential F^{μ} is exerted on to the solute molecules of the reservoir region to accelerate between CR and the R regions depending on the concentration of the CR at time t, as described by the Equation 2.21.

$$F^{\mu}_{(t,z)} = k(C_{CR}(t) - C_0)\, G_{\omega}(z - z_F) \qquad \text{Equation 2.24}$$

where, t is the time, C_{CR} and C_0 are the instantaneous concentration at time t and the pre-defined set concentration of CR, respectively. z_F is the z axis distance from the crystal surface to the force region. The k serves as the simple harmonic force constant for the concentration control and, $G_{\omega}(z - z_F)$ defines to the bell-shaped function of which the height and width are set by the parameter ω:

$$G_{\omega}(z, z_p) = \frac{1}{4\omega}\left[1 + \cos\left(\frac{z - z_p}{\omega}\right)\right]^{-1} \qquad \text{Equation 2.25}$$

To introduce small modifications to the original CμMD algorithm for systems discussed in Chapter 4 to account for the relatively larger molecule size (compared with its usage for smaller molecules to date). We limit our simulation layout to accommodate only one growth region per simulation, so that only one crystal layer is allowed to form per simulation (see Figure 2.2). The growth region on the other side is turned into an inhibitor region where growth is restricted through bias force to facilitate full extent of the layer growth on the other side. We have also removed the regions where two concentration gradients were applied from the crystal surface to the control region, from the original layout, to address more appropriately for larger molecule used. Besides we also acknowledge that such macroscopic effects like concentration gradients would be more appropriate for much larger systems.

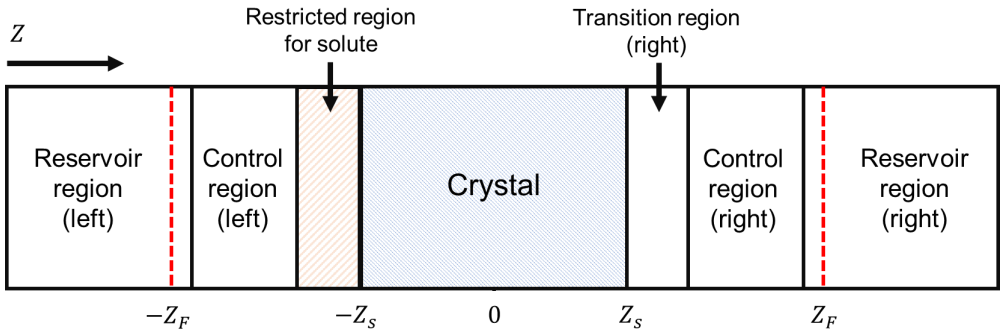

Figure 2.2 Modified layout of the simulation box adapt CμMD for NDT simulations allowing for only one growth region per simulation.

2.1.5 Enhanced sampling through umbrella simulations

To effectively simulate non-ergodically behaving systems that are associated with large energy barriers along reaction coordinates, enhanced sampling techniques are relevant. Umbrella simulation developed by Torrie and Valleau[16] provides means to overcome insufficient sampling associated with classical MD simulations by modifying the potential function $\gamma'(r^N)$, that can be expressed in terms of a perturbation function:

$$\gamma'(r^N) = \gamma(r^N) + W(r^N) \qquad \text{Equation 2.26}$$

where, $W(r^N)$ is the adaptive weighting function, which takes the quadratic form:

$$W(r^N) = k_w(r^N - r_0^N)^2 \qquad \text{Equation 2.27}$$

Here, r_0 is the equilibrium state and r^N is the current state. The potential function is modified in such a way that weighting function adapts according to the extent deviation of the system away from the equilibrium to provide biasing to overcome non-ergodicity. The function yields a non-Boltzmann distribution that can be reweighted to extract Boltzmann averages:

$$\langle A \rangle = \frac{\langle A(r^N) \exp[+W(r^N)/k_B T] \rangle W}{\langle \exp[+W(r^N)/k_B T] \rangle W} \qquad \text{Equation 2.28}$$

where, subscript w signifies that the average distribution that is obtained through probability that is determined through the modified potential function $\gamma'(r^N)$. The usual practice is to separate out the entire simulation trajectory into small overlapping windows to apply the modified potential function, thereby effectively sampling the reaction coordinates. Properties such as potential of the mean force (PMF) can be calculated by combining the sample windows through appropriate techniques such as weighted histogram averages (WHAM) technique.[16]

2.1.6 MD trajectory analysis techniques

2.1.6.1 Heat capacity

Under constant pressure, the isobaric heat capacity C_p can be defined thermodynamically as follows:

$$\Delta C_p = \frac{\Delta H}{\Delta T} \qquad \text{Equation 2.29}$$

where, ΔH is the enthalpy change and ΔT is the temperature change. We perform calculations of heat capacities for the heating and cooling simulations discussed in chapter 4, using GROMACS *energy* function. To calculate isobaric heat capacity, the NPT ensemble is necessary, and the temperature and enthalpy change is computed to apply to the equation 2.29 in specific time intervals of data collection. The obtained heat capacity values are then smoothened out using moving averages technique.

2.1.6.2 Mean square displacement

The mean square displacement (MSD) calculates the random motion/diffusion of particles through space with time by providing a measure of the deviation of position with respect to its original position along time. The MDS can be defined:[4]

$$MSD = \langle (r - r_0)^2 \rangle = \frac{1}{N} \sum_{n=1}^{N} \left(r_i(t) - r_i(0) \right)^2 \quad \text{Equation 2.30}$$

where, $r_i(t)$ is the location in terms of center of mass of molecule i at time t, for a system with N number of particles.

2.1.6.3 Radial distribution function

The radial distribution function (RDF) provides a measure of how the density of particles vary radially outwards form a central position.[17] A pair correlation function can be formulated between particle i and j:

$$\rho(\bar{r}, \vec{r}') = \left\langle \sum_{i=1}^{N} \delta(\bar{r} - \bar{r}_i) \sum_{j=1}^{N} \delta\left(\vec{r}' - \bar{r}_j\right) \right\rangle \quad \text{Equation 2.31}$$

where the two-particle distribution function is:

$$g(r) = \rho^{(2)}\left(\bar{r}, \bar{r}'\right) / \rho^2 \quad \text{Equation 2.32}$$

therefore, we can generalize the g(r) between particle a and b:

$$g_{ab}(r) = \frac{\rho_{ab}(r)}{N_b / V} \quad \text{Equation 2.33}$$

$$N_b = \int_V dr 4\pi r^2 \, \rho_{ab}(r) \quad \text{Equation 2.34}$$

and the potential of mean force, the free energy associated with the particle interaction along reaction coordinate r can be expressed in terms of radial distribution function.

$$W(r) = -k_B T \ln g\,(r) \qquad \text{Equation 2.35}$$

where, $W(r)$ is the potential of mean force.

2.1.6.4 Potential of mean force

Potential mean force (PMF) calculates the free energy change as a function of the reaction coordinate. The PMF of a system is constructed through the average interaction potential force over all configurations along the reaction coordinate. For a system with two moving particles, the mean force can be calculated using the potential function $U(r^N)$:[16]

$$\langle F \rangle = -\left\langle \frac{d}{dr} U(r^N) \right\rangle_{r_1, r_2} = \frac{-\int dr_3 \ldots dr_N \frac{dU}{dr_1} e^{-\beta U}}{\int dr_3 \ldots dr_N e^{-\beta U}} \qquad \text{Equation 2.36}$$

The reversible work associated with the two-particle movement can be found by integration, which equals to the Helmholtz free energy A change for transition between two states (1 to 2).

$$W_{1\to 2} = \int_{r_1}^{r_2} \langle F_1 \rangle dr_1 = \Delta A_{1\to 2} \qquad \text{Equation 2.37}$$

and the free energy can be also expressed in terms of radial distribution function g(r):

$$A(r) = -k_B T \ln g\,(r) + constant \qquad \text{Equation 2.38}$$

where, k_b is the Boltzmann constant and T is the temperature. The constant is applied to set the zero-point energy to correspond to the most probable configuration.

2.1.6.5 Weighted histogram analysis

The weighted histogram analysis (WHAM) technique provides an efficient scheme for obtaining unbiased probability distribution (true Boltzmann distribution) from the biased probability distributions where bias potential $V_i(\xi)$, is applied.[18] The biased potential enables efficient sampling of regions where conformations are rarely visited by confining the configurational space into a narrow region. Often when enhanced sampling is used, configurational space is separated into overlapping segments, (i.e., sampling windows in umbrella simulations). WHAM combines each individual biased window, "stitching" together statistically into a single unbiased probability distribution. For one-dimensional reaction coordinate, the combined probability distribution is:

$$\rho(\xi) = \frac{\sum_{i=1}^{N_w} n_i \rho_i^{(b)}(\xi)}{\sum_{j=1}^{N_w} n_j e^{-\beta\left(V_j(\xi) - F_j\right)}} \qquad \text{Equation 2.39}$$

$$e^{-\beta F_i} = \int e^{-\beta V_i(\xi)} \beta(\xi) d\xi \qquad \text{Equation 2.40}$$

where, β is $1/k_b T$.

2.1.7 MD software packages

In the work carried out through Chapters 3, 4, and 5, we use GROMACS[19, 20] 2019 and 2020 software packages with OPLS-AA and GAFF-AA forcefields. GROMACS is a widely used software suite for simulating organic molecules, due to its high compatibility with parallelized simulations in high performance computing CPU and GPU environments, and because GROMACS is an open access software. To carry out biased simulations and post-processing and analyses, we employed the PLUMED plugin,[21] patched with GROMACS. PLUMED is a community developed tool that

enhances the capabilities of MD codes including GROMACS simulations to investigate physicochemical phenomena based on theoretical models.

2.2 Overview of Quantum Mechanics and Electronic-Structure Theory

We now briefly discuss the electronic-structure descriptions derived from quantum mechanical (QM) approaches. As discussed in the previous section, classical mechanics approaches rely on the pure particle-like behavior of objects (i.e., classical objects), and therefore, are more appropriate for describing particles of macroscopic scale. However, classical mechanics often fails to describe small systems such as electrons, atoms, and molecules, as it does not acknowledge the uncertainty associated with small particles of such scale (i.e., described by the wave-particle duality highlighted in the Heisenberg's uncertainty principle), and all energetic exchanges through Newtonian physics are considered continuous. Therefore, more appropriate treatments for small objects rely on QM descriptions to predict the motion of atoms and electrons involved in molecules. The fundamental definitions of QM consider all energy exchanges involved in a quantum system to be quantized, hence the name 'quantum' mechanics. The following texts are referred to outline the principles mentioned below: Levine,[22] Cohen-Tannoudji,[23] Szabo and Ostlund,[24] Jensen[25], Cramer,[26] and Koch and Holstein.[27]

2.2.1 The time-independent Schrödinger Equation

The time-independent Schrödinger equation predicts the probabilistic behavior of a quantum system in terms of the eigenfunction:

$$\hat{H}\psi = E\psi \qquad \text{Equation 2.41}$$

where, the Hamiltonian operator $\hat{H}$ operates on the wavefunction ψ to obtain E – the energy eigenvalue that combines kinetic and potential energy of the quantum system. The wavefunction ψ represents the quantum state of a particular quantum system in terms of a probability amplitude. Likewise, the electronic structure of a stationary molecular system with N electrons and nuclei can be described by extending the Schrödinger equation in the form:

$$\hat{H}\left|\psi\left(\{\vec{R}_I\},\{\vec{r}_i\}\right)\right\rangle = E_n\left|\psi\left(\{\vec{R}_I\},\{\vec{r}_i\}\right)\right\rangle \qquad \text{Equation 2.42}$$

where, $\vec{r}_i$ and $\vec{R}_i$ are position vectors of electrons and nuclei respectively, E_n is the energy of nth eigenstate. The ψ is the many body wavefunction that pertaining to the quantum system.

The Hamiltonian operator $\hat{H}$ of the many-body system is:

$$\hat{H} = \hat{T}_n + \hat{T}_e + \hat{V}_{nn} + \hat{V}_{ee} + \hat{V}_{ne} \qquad \text{Equation 2.43}$$

where, Hamiltonian $\hat{H}$ combines Kinetic terms of nuclei ($\hat{T}_n$) and electrons ($\hat{T}_e$) with the potential terms coming from interactions among nuclei and electrons ($\hat{V}_{nn}$, $\hat{V}_{ee}$, and $\hat{V}_{ne}$). Kinetic energy terms can be expressed as:

$$\hat{T}_n + \hat{T}_e = \sum_{i=I}^{M} \frac{P_I^2}{2M_I} + \sum_{i=1}^{M} \frac{P_i^2}{2} \qquad \text{Equation 2.44}$$

where, P_I and P_i are the momentum operators belonging to the Ith nucleus of mass M_I and i^{th} electron respectively. Consecutively, the potential energy terms are expressed as:

$$\hat{V}_{nn} + \hat{V}_{ee} + \hat{V}_{ne} = \sum_{I\neq J} \frac{Z_I Z_J}{2|\vec{R}_I - \vec{R}_J|} + \sum_{i\neq j} \frac{1}{2|\vec{r}_i - \vec{r}_j|} + \sum_{i,I} \frac{Z_I}{2|\vec{r}_i - \vec{R}_I|} \qquad \text{Equation 2.45}$$

where, charges of the Ith nucleus are Z_I and Z_J, and the $\hat{V}_{nn}$, $\hat{V}_{ee}$, and $\hat{V}_{ne}$ terms denote the nucleus-nucleus, electron-electron, and nucleus-electron interactions. Overall, the total Hamiltonian can be of the form of:

$$\hat{H} = \sum_{i=I}^{M} \frac{P_I^2}{2M_I} + \sum_{i=1}^{M} \frac{P_i^2}{2} + \sum_{I \neq J} \frac{Z_I Z_J}{2|\vec{R}_I - \vec{R}_J|} + \sum_{i \neq j} \frac{1}{2|\vec{r}_i - \vec{r}_j|} + \sum_{i,I} \frac{Z_I}{2|\vec{r}_i - \vec{R}_I|} \qquad \text{Equation 2.46}$$

2.2.2 Born-Oppenheimer approximation

The exact solution to the Schrödinger equation provides a complete description of the quantum system. However, achieving this becomes prohibitively complicated when many body systems are considered, i.e., such as molecules with many nuclei and electrons interacting with each other. Therefore, alternative means of solving Schrödinger equation necessitates introduction of approximations to simplify the associated degrees of freedom. The Born-Oppenheimer (BO) approximation assumes the motion of atomic nuclei to be negligible in relative terms of the electronic motion, due to the large mass ratio between proton to electron (~1840:1), therefore electronic motion is assumed to occur under stationary nucleic fields of nuclear forces. Thus, the simplified Hamiltonian allows separation of nuclear and electronic energy terms in the quantum system such that:

$$\hat{H}(\{\vec{R}_I\}, \{\vec{r}_i\}) = \hat{H}_n(\{\vec{R}_I\}), + \hat{H}_e(\{\vec{R}_I\}, \{\vec{r}_i\}) \qquad \text{Equation 2.47}$$

where, $\hat{H}_e$ and the $\hat{H}_n$ are the separated electronic and nuclear Hamiltonians. According to the BO approximation, the motion of the electrons can be considered independent of the nuclear motion, allowing the definition of $\hat{H}_e$ in the absence of nuclear terms as follows:

$$\hat{H}_e = \hat{T}_e + \hat{V}_{ee} + \hat{V}_{ne} \qquad \text{Equation 2.48}$$

The total wavefunction $\hat{H}$ can be reduced to obtain the electronic wavefunction, often identified as the Born-Oppenheimer wave function, that explicitly depend on the electronic coordinates whereas nuclear coordinates depend only parametrically. The $\hat{H}_e$ operating on ψ_e therefore yields the electronic Schrödinger equation:

$$\hat{H}_e\left|\psi_e\left(\{\vec{R}_I\},\{\vec{r}_i\}\right)\right\rangle = E_e(\{\vec{R}_I\})\left|\psi_e\left(\{\vec{R}_I\},\{\vec{r}_i\}\right)\right\rangle \qquad \text{Equation 2.49}$$

where, the ψ_e represents the probability to find electron i within a defined volume. Note it is however a non-observable term.

The nuclear Hamiltonian $\hat{H}_n$ for the nuclear motion within an average filed of fast-moving electrons can be expressed as follows:

$$\hat{H}_n = \hat{T}_n + \hat{V}_{nn} + \hat{V}_{ne} \qquad \text{Equation 2.50}$$

that can also be expressed as:

$$\hat{H}_n = -\frac{1}{2}\sum_{I=1}^{N}\frac{1}{M_I}\nabla_I^2 + E_{total}(\{\vec{R}_I\} \qquad \text{Equation 2.51}$$

Therefore, the corresponding Schrödinger equation obtained for the nuclear motion:

$$\hat{H}_n\left|\psi_n\left(\{\vec{R}_I\}\right)\right\rangle = E_n\left|\psi_n\left(\{\vec{R}_I\}\right)\right\rangle \qquad \text{Equation 2.52}$$

This equation can be used to describe nuclear motion including vibrational, translational, and rotational motion of the molecular system.

2.2.3 Density functional theory (DFT)

Although Born-Oppenheimer (BO) approximation simplifies the Schrödinger equation, obtaining the exact solution can still be complicated. The density functional theory (DFT) approach provides further simplifications to solving the Schrödinger

equation, based on the assumption that the ground state electronic energy of a quantum system can be completely determined by its electron density, as proven by Hohenberg and Kohn theorem.[28] Using functionals of electron density allows to reduce down the many body electronic wavefunction that is of $3N$ degrees of freedom (where N is the number of atoms with the 3 representing the (x, y, z) positional coordinates in space), into only a function of spatial coordinates, which is only 3 degrees of freedom. Unlike wavefunction, the electron density is an observable quantity and a function of space and time.

The Hohenberg and Kohn theorem (HK) establishes that the electron density uniquely determines the Hamiltonian operator, therefore all associated properties of the quantum system can be also determined, where the average value of any observable can be written in a functional form of the electron density (ρ). Kohn and Sham (KS) contributed with further developments; HK theorem states that F_{HK} [ρ] *delivers the lowest energy, if and only if that input density is the true ground state density*. KS equation express the total energy in terms of electron density:

$$E[\rho] = T_s[\rho] + \int dr v_{ext}(r)\rho(r) + E_H[\rho] + E_{xc}[\rho] \qquad \text{Equation 2.53}$$

where, v_{ext} is external potential acting on the interacting system, $E_H[\rho]$ is Hartree(coulombic) energy, and the $E_{xc}[\rho]$ is exchange-correlation energy. The KS kinetic energy term is represented by the T_s[p], that is expressed through Kohn Sham orbitals $\phi_i(r)$:

$$T_s[\rho] = \sum_{i=1}^{N} \int dr \phi_i^*(r) \left(-\frac{h^2}{2m}\nabla^2\right) \phi_i(r) \qquad \text{Equation 2.54}$$

Improving accuracy of the DFT level electronic-structure calculations is achieved through basis set expansions of the KS orbitals and/or the choice of applied exchange-correlation functionals that provide reasonable approximations.

2.2.3.1 Approximate exchange-correlation functionals

Although guidelines are lacking for the search of the most appropriate functional form of the exchange-correlation energy, three most commonly reached-out forms are the localized density approximation (LDA), generalized gradient approximation (GGA) and the use of hybrid functional in which part of the exact Hartree-Fock exchange term is incorporated in the DFT functional. Virtually, all exchange-correlation functional forms are based on the approximation of homogenous electron gas with a density of $\rho(\boldsymbol{r})$.

2.2.3.1.1 Local density approximation *(LDA)*

The local density approximation (LDA) provides a basic approximation to the exchange correlation functional based on the uniform electron gas of density $\rho(\vec{r})$ where electrons move through a positive background of charge distribution, and the total ensemble is electrically neutral. The electron density is finite; however, the number of electrons and the volume of the gas is allowed to be infinite. The exchange correlation energy E_{ex} can be expressed as follows:

$$E_{XC}^{LDA}[\rho] = \int \rho\,(\vec{r})\varepsilon_{XC}\rho(\vec{r})d\bar{r} \qquad \text{Equation 2.55}$$

here, the ε_{XC} is exchange-correlation energy per particle within the uniform electron gas. The LDA model assumes that the exchange correlation terms are linearly composed.

The local spin density approximation (LSDA) further modifies the LDA, taking the electronic spin into account, where the ε_{XC} combines the separate exchange and correlation contributions

$$\varepsilon_{XC}\big(\rho(\vec{r})\big) = \varepsilon_X\big(\rho(\vec{r})\big) + \varepsilon_C \qquad \text{Equation 2.56}$$

The exchange component $\varepsilon_X\big(\rho(\vec{r})\big)$ can be expressed generally in the form of:

$$\varepsilon_X\big(\rho(\vec{r})\big) = -\frac{3}{4}\sqrt[3]{\frac{\rho(\vec{r})}{\pi}} \qquad \text{Equation 2.57}$$

For the correlation component, no explicit expression is available, and is derived from homogenous electron gas simulations with high accuracy. LDA approximation overall provides a reasonable model for electronic structure calculations using the DFT level.

2.2.3.1.2 Generalized gradient approximation (GGA)

The generalized gradient approximation (GGA) further improves the LDA model, where limitations associated with LDA due to assumption of uniform electron gas is overcome by supplementing gradient of the charge density into the electron density at a particular point r (also known as gradient corrected approximation – GCA). The original LDA/LSDA exchange correlation term $\varepsilon_{X/C}\big(\rho(\vec{r})\big)$ is therefore modified with the GGA functionals:

$$\varepsilon_{X/C}^{GGA}[\rho(\vec{r})] = \varepsilon_{X/C}^{LDA/LSDA}[\rho(\vec{r})] + \Delta\varepsilon\left[\frac{\nabla\rho(\vec{r})}{\rho^{4/3}(\vec{r})}\right] \qquad \text{Equation 2.58}$$

with the x/c signifying the same functional form holds true for both (separate) exchange or correlation terms. The exchange correlation energy can be expressed in combined terms as follows:

$$E_{XC}^{GGA} = E_X^{GGA} + E_C^{GGA} \qquad \text{Equation 2.59}$$

GGA provides reasonable approximation to DFT level calculations. A few commonly used GGA functionals include B or B88 – developed by Becke[29, 30], that accurately treats long range behavior, P86 – developed by Perdew[31], PW91 – by Burke, Perdew, and Wang[32], LYP – by Lee, Yang, and Parr[33], and AM05 by Armiento-Mattsson.[34]

2.2.3.1.3 Hybrid functionals

Hybrid functionals combine exact Hartree-Fock level with the DFT to perform electronic-structure calculations. The exchange contribution term is replaced with exact HF exchange expression and only the electron correlation term is expressed in DFT approximate terms. This is an adequate approach as in general, as the exchange contributions is more prominent than the correlation effects. The exchange-correlation energy therefore can be expressed as:

$$E_{XC} = E_X^{exact} + E_C^{KS} \qquad \text{Equation 2.60}$$

Although hybrid functionals can be very accurate for atomic orbitals, the separated exchange and correlation terms of hybrid functionals often fails to describe molecular systems accurately, as the two terms are not completely independent of one another. A more reasonable expression can be obtained through weighted terms:

$$E_{XC} = aE_X^{HF} + (1 - a)E_{XC}^{KS} \qquad \text{Equation 2.61}$$

where, a is a constant value for the fractional weight.

A commonly used hybrid exchange-correlation function is the three-parameter B3LYP functional:[30, 33, 35-37]

$$E_{XC}^{B3LYP} = (1-a)E_X^{LSDA} + aE_X^{HF} + b\Delta E_X^B + (1-c)E_C^{LSDA} + cE_C^{LYP} \quad \textit{Equation 2.62}$$

where, the energy is expressed in combination of the exchange energies derived from both HF and LSDA, and the Becke exchange and LYP correlation terms, with the optimized values obtained for a, b and c are 0.20, 0.72, and 0.81 respectively.[30]

2.2.3.1.4 Range-separated functionals

Although hybrid functionals are widely used, they do not offer reliable descriptions through explicit considerations for the long-range interactions. Note that hybrid functionals still rely on the approximations of LDA model, wherein the electron density at a particular point is given focus, that can only describe short-range interactions accurately. Range separated (RS) functionals[38] address this issue by explicit considerations: The coulombic term ($1/r_{12}$) is split into two parts to account for the short- and long-range interactions. The short-range (SR) term is approximated by the GGA model, whereas the long-range term (LR) is expressed in terms of Hartree-Fock method. The two terms are smoothly scaled between each other by:

$$\frac{1}{r_{12}} = \frac{1-g(r)}{r_{12}} + \frac{g(r)}{r_{12}} \qquad \text{Equation 2.63}$$

Here, the r_{12} represent the coordinate vectors: $|r_1\text{-}r_2|$, and $g(r)$ is the scaling function that can be defined as:

$$g(r) = \alpha + \beta\, erf(\omega r) \qquad \text{Equation 2.64}$$

where, alpha and beta are functional dependent mixing parameters. The erf is the error function that bridge the SR and LR smoothly, under range separation parameter ω, that needs to be determined empirically[38-41]. Optimal ω can vary on the target system.[40, 41]

In the investigations throughout the text, we make use of the range-corrected ωB97X-D functional, developed by Chai and Gordon et al.,[42] to carry out all electronic structure calculations. Through range separated approach, a long-range correction (LRC) is applied to provide an improved description. Here, the exact HF exchange contribution increases analogously with the distance, that leads to a more reliable description of the exchange energy.

2.2.4 Basis sets

Basis sets combine a set of functions known as basis functions to model the electronic wave function. This allows the conversion of complex partial differential equations involved in solving the SE into algebraic equations that can be efficiently solved computationally. Molecular orbitals used in the SE are expressed in terms of combination of different basis functions. One such common combination rule is the linear combination of atomic orbitals (LCAO). The choice of basis functions impact the quality of the calculation, in the context of resolution of the orbital that they represent. In a general sense, incorporation of more basis functions allows better resolution of the orbital, however fewer may be used if the orbital can be represented adequately.

2.2.4.1 Slater and Gaussian type orbitals

There are many varieties of types of orbitals available for representation of the molecular orbitals, among which the Slater type and the Gaussian type are commonly used and are proven effective. Slater type orbitals (STOs) can be expressed in terms of spherical polar coordinates as:

$$\chi_{\zeta,n,l,m}(r,\theta,\varphi) = NY_{l,m}(\theta,\varphi)r^{n-1}e^{-\zeta \mathrm{r}} \qquad \text{Equation 2.65}$$

where, the n, l, and m are the relevant quantum numbers, the N and $Y_{l,m}$ are normalization constant and spherical harmonic functions respectively. ζ controls the width of the orbital. STOs can be useful for calculating more accurate results however they suffer from longer computational time on attempting the integrals.

Alternatively, Gaussian type orbitals (GTOs) are used, with the following form:

$$\chi_{\zeta,n,l,m}(r,\theta,\varphi) = NY_{l,m}(\theta,\varphi)r^{(2n-2-l)}e^{-\zeta r^2} \qquad \text{Equation 2.66}$$

This can also be expressed in terms of cartesian coordinates:

$$g_v(r) = \chi_{\zeta,l_x,l_y,l_z}(x,y,z) = Nx^{l_x}y^{l_y}z^{l_z}e^{-\zeta r^2} \qquad \text{Equation 2.67}$$

The sum of the angular momentum quantum numbers l_x, l_y, and l_z defines the type of the orbital. GTOs can be a better alternative for faster and efficient computation of integrals. GTOs can be used in linearly combined fashion represent STOs, often referred to as "STO-nG". Such basis sets are identified as contracted gaussian type orbitals (CGTOs), that can be expressed as:

$$G_a(r) = \sum_{v=1}^{N_\alpha} c_v g_v(r) \qquad \text{Equation 2.68}$$

and functions that combine the full set of basis functions are called primitive GTOs (PGTOs).

2.2.4.2 Basis set nomenclature

By convention, a basis set that combines different types of orbitals are denoted in a specific way. When each atomic orbital (AO) uses one basis function, it is called a

minimal basis set. When multiple basis function per AO is used, it is denoted by the Greek letter zeta (ζ), giving rise to double zeta (DZ) and triple zeta (TZ), quadruple zeta (QZ) etc. basis sets.

Split valence basis sets

Additionally, split valence basis sets can be used to separately treat core atomic orbitals (CO) and valence atomic orbitals (VO), based on the realization that core orbitals and valence orbitals do not play equal roles in chemical reactions and energetics etc. One routinely used basis set is the split-valence double-zeta basis set, that use one basis function per CO and two basis functions per VO. Commonly used split valence basis sets are:

3-21G – CO are a contraction of 3 PGTOs. The VO represented by 3 PGTOs, out of which 2 and 1 assigned for inner and outer parts of the VO respectively.

6-31G – CO are a contraction of 6 PGTOs. The VO represented by 4 PGTOs, out of which 3 and 1 are assigned for inner and outer parts of the VO respectively.

6-311 – A triple zeta split valence basis that is similar to 6-31G except for VOs that is now split into 3, 1 and 1 PGTOs respectively.

Polarization and diffuse functions can be incorporated to further improve resolution of the orbital representation. Polarization functions are denoted by '*', that adds higher angular momentum terms to account for polarization on heavy atoms, or "**" to apply those for both heavy atoms and hydrogens. Note for instance, the 6-31* is identical with 6-31(d), and 6-31** is identical with 6-31(d,p) where d and p denote the p type or d type polarization.

Diffuse functions are incorporated to capture different attributes involved further away from the nucleus, such as describing loosely bound electrons in radical anions. Diffuse functional denoted by "+" indicates one set of diffuse s and p functions on heavy atoms. "++" denotes the addition of s- function for hydrogens on top of the diffuse s and p functions added to heavy atoms.

2.2.5 Polarizable continuum model for simulating solvent environment

The polarizable continuum model (PCM) was used to simulate solvent effects in the absence of explicit solvent-solute interaction calculations.[43] Ideally, for an accurate calculation of solvation effects, simulating all participating components of the solution environment is necessary, which entails explicit consideration of interactions among solute and the solvent molecules of the solvation spheres, as well as the interactions amongst such spheres themselves. However, due to prohibitively high computational expense associated with such model through ab initio calculations, PCM models the solvent as a polarizable continuum with a dielectric constant, filling the space outside the quantum system of interest. The boundary between the quantum system (with a dielectric constant of unity) and the high-dielectric exterior is identified as the surface.[44] The charge (or partial charge) distribution associated with the quantum system is allowed to polarize the continuum, which in turn acts back on the quantum system itself, altering the distribution of charges, creating a reaction field. This is iteratively calculated through solving Poisson or Poisson-Boltzmann equations[45] to achieve self-consistency between the charge distribution and the charge distribution of the quantum system, a method identified as SCRF (self-consistent reaction field).[43] A cavity is created to occupy the quantum system within the polarizable continuum using integral equation formalism

variant (IEFPCM)[43]. Solvation Gibbs free energy (G_{solv}) is then computed as the sum of electrostatic (G_{es}), dispersion-repulsion (G_{d-r}) and cavitation (G_{cav}) Gibbs free energies (Equation 2.56).

$$G_{solv} = G_{es} + G_{d-r} + G_{cav} \qquad \text{Equation 2.69}$$

2.2.6 Quantum theory of atoms in molecules

The quantum theory of atoms in molecules (QTAIM) developed by Bader and et. al.,[46] identifies atoms and bonds existing in molecules in terms of electron density $\rho(r)$ and energy density. The electron density is expressed as an electron density distribution in which the probability distribution of electrons of molecular systems is distributed throughout the real space, under the nuclear attractive field. QTAIM provides explanations as to how bonding interactions can be defined unambiguously, and how the properties attributed to atoms and groups of atoms (i.e., functional groups) can be transferable from molecule to molecule, in terms of the electron density and its topology.

2.2.6.1 Critical points of electron density

Molecular topology is dominated by the attractive forces between nuclei and electrons. Such topology mark boundaries that maintain fine-balance between electron-nuclei attractions, electron-electron repulsions and the attractions occurring from the neighboring nuclei, resulting in characteristic local maxima of electron density distribution. Critical points of electron density (CP)s are defined as points in space of which the first derivatives of the electron density is zero across the topological arrangement of atoms in space[47], i.e.:

$$\nabla\rho = i\frac{d\rho}{dx} + j\frac{d\rho}{dy} + k\frac{d\rho}{dz} \rightarrow \begin{cases} = \vec{0} & (At\ critical\ points\ and\ at\ \infty) \\ Generally \neq \vec{0} (At\ all\ other\ points) \end{cases} \qquad \text{Equation 2.70}$$

where, each individual gradient term is zero (signified by the zero vector 0). Nuclear critical points (NCPs) are identified as critical points existing on atomic positions. Local minima, local maxima and saddle points can be distinguished by considering the second derivative, generating the Hessian matrix of the electron density. At a CP located at r_c, the Hessian matrix will be:

$$A(r_c) = \begin{pmatrix} \frac{\partial^2\rho}{\partial x^2} & \frac{\partial^2\rho}{\partial x\partial y} & \frac{\partial^2\rho}{\partial x\partial z} \\ \frac{\partial^2\rho}{\partial y\partial x} & \frac{\partial^2\rho}{\partial y^2} & \frac{\partial^2\rho}{\partial y\partial z} \\ \frac{\partial^2\rho}{\partial z\partial x} & \frac{\partial^2\rho}{\partial z\partial y} & \frac{\partial^2\rho}{\partial z^2} \end{pmatrix}_{r=r_c} \qquad \text{Equation 2.71}$$

where, when diagonalized can be written explicitly as:

$$\Lambda = \begin{pmatrix} \frac{\partial^2\rho}{\partial x'^2} & 0 & 0 \\ 0 & \frac{\partial^2\rho}{\partial y'^2} & 0 \\ 0 & 0 & \frac{\partial^2\rho}{\partial z'^2} \end{pmatrix}_{r'=r_c} = \begin{pmatrix} \lambda_1 & 0 & 0 \\ 0 & \lambda_2 & 0 \\ 0 & 0 & \lambda_3 \end{pmatrix} \qquad \text{Equation 2.72}$$

where, $U^{-1}AU = \Lambda$, and U is a unitary matrix, generated from eigenvalue equations $Au_i = \lambda_i u_i$;(i = 1,2,3) where u_i is ith column vector in U. The λ_i are the curvatures of the density in terms of principle axes x', y' and z'.

The rotation invariant trace of Hessian of density, addressed as the Laplacian of the density is given by:

$$\nabla^2\rho(r) = \nabla.\nabla\rho(r) = \underbrace{\frac{\partial^2\rho(r)}{\partial x^2}}_{\lambda 1} + \underbrace{\frac{\partial^2\rho(r)}{\partial y^2}}_{\lambda 2} + \underbrace{\frac{\partial^2\rho(r)}{\partial z^2}}_{\lambda 3} \qquad \text{Equation 2.73}$$

that is when $x = x'$, $y = y'$, $and\ z = z'$.

CP are classified in terms of rank and signature (ω and σ respectively), The rank signifies the number of non-zero curvatures of electron density at the CP. In equilibrium, only ω = 3 are stable and are present. The signature represents the algebraic sum of the signs of curvatures, with positive of negative curvatures indicated by ±1. Four types of CP with ω = 3 can be defined that are stable and have three non-zero eigenvalues.

1. (3, -3) – nuclear critical point (NCP – three negative curvatures: $\boldsymbol{\rho}$ is a local maximum)
2. (3,-1) – bond critical point (BCP – two negative curvatures: $\boldsymbol{\rho}$ is a maximum along the plane defined by the corresponding eigenvalues, but minimum along third axis that is perpendicular to the plane)
3. (3, +1) – Ring critical point (RCP – two positive curvatures: $\boldsymbol{\rho}$ is minimum along the plane defined by the corresponding eigenvalues, and maximum along the third axis that is perpendicular to the plane)
4. (3,+3) – Cage critical point (CGP – three positive curvatures: $\boldsymbol{\rho}$ is a local minimum)

For isolated finite systems such as molecules, Poincare-Hopf relationship establishes that:

$$n_{NCP} - n_{BCP} + n_{RCP} - n_{CCP} = \begin{cases} 1 & (Isolated\ molecules) \\ 0 & (Infinite\ crystals\ ) \end{cases} \quad \text{Equation 2.74}$$

where, n is the number of CP of the specified type. This is considered as proof for validity of equation 2.74. Bond critical points specify the existence of inter-atomic bonding whereas ring critical points signifies the enclosure of a ring of chemically bonded atoms.

2.2.6.2 Reduced density gradient of electron density

The reduced density gradient of the electron density (RDG) is a dimensionless form of electron density gradient norm, expressed as:[48]

$$RDG(r) = \frac{1}{2(3\pi^2)^{1/3}} \frac{|\nabla\rho(r)|}{[\rho(r)]^{4/3}} \qquad \text{Equation 2.75}$$

RDG against sign $(\lambda_2)\rho$ is used to reveal weak interaction regions of molecular systems.[48] The sign $(\lambda_2)\rho$ denotes the sign belonging to the second largest eigenvalue of the Hessian matrix of electron density, allowing to distinguish between attractive and repulsive interactions.

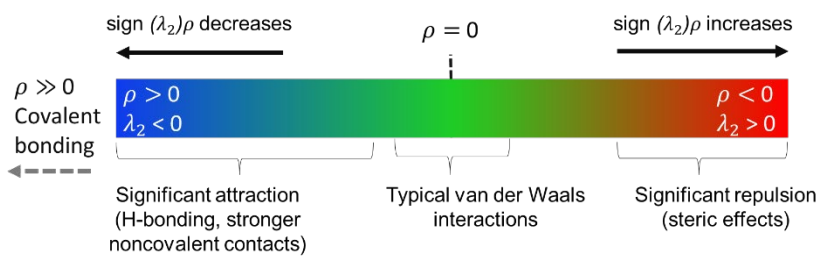

Figure 2.3 Schematic illustration of the colors used to indicate interaction types of the isosurface obtained by RDG analysis.

Relatively strong interactions are shown in the region with high ρ and thus large sign $(\lambda_2)\rho$ magnitude and vice versa indicated for the weak to no interactions (including weak vdW interactions). Isosurface map of RDG at low ρ can be used to visually represent regions involved in different kinds of noncovalent interactions and notable steric effects.[49]

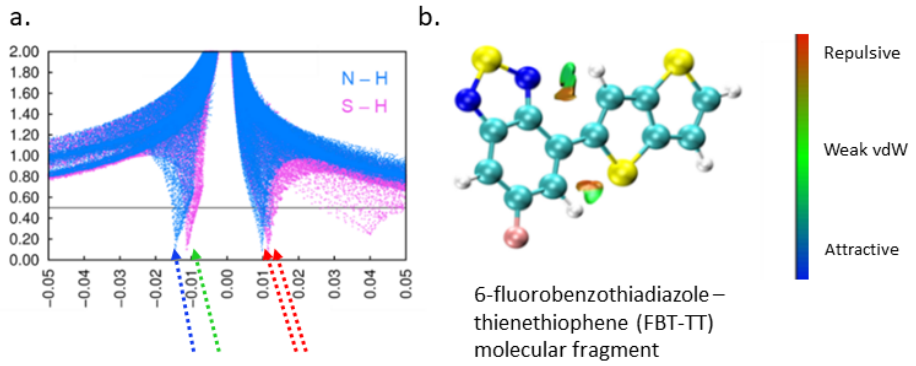

Figure 2.4 An example RDG against sign $(\lambda_2)\rho$ plot of FBT-TT molecular fragment (a), investigated in chapter 3 that reveals stronger attractive (blue), weak van der Waals (green), and repulsive (red) like forces found along the 0.5 isosurface (b) pointed out through colored dotted arrows.

2.2.7 QM software packages

In the work carried out through Chapters 3, 4, and 5, we use GAUSSIAN software suite 16[50] for calculating DFT level calculations. For AIM analyses carried out in the Chapter 3, we use the MULTIWFN[51] software in combination with the visualization software Visual Molecular Dynamics.

CHAPTER 3. ROLES OF INTRAMOLECULAR NONCOVALENT INTERACTIONS IN π -CONJUGATED MOLECULES ON STRUCTURE AND AGGREGATION

3.1 Introduction

Organic, π-conjugated chromophores, ranging from small molecules to oligomers through polymers, used as OSC building blocks are often comprised of alternating patterns of electron-rich donor (*D*) and electron-deficient acceptor (*A*) moieties. OSC containing such building blocks can be made with fine-tuned redox, electronic, and optical properties that result in high performance metrics for several applications,[1] though hard-and-fast design rules that connect chromophore construction, processing strategy, and OSC properties remain limited. Chromophore-specific variables that need to be considered include the chemical composition and architecture of the π-conjugated backbone, backbone rigidity, and chemistry of (generally) alkyl side chains that influence both solubility and solid-state molecular packing.[1-10] From the perspective of (solution-based) OSC fabrication, solvent composition, deposition techniques (*e.g.*, spin coating, drop casting, blade coating) and parameters, and post-processing routines (*e.g.*, solvent-vapor or thermal annealing) can impose varying kinetic and thermodynamic limitations towards the development of the OSC morphology that, in turn, impact the material characteristics extrinsically.[10-17]

In this chapter, we examine how chromophore chemistry and solvent environment impacts rotational isomer populations of *D*-*A* oligomers. In particular, we focus on a series of oligomers (Figure 3.1) reported by McDowell and coworkers[9] that are nearly isostructural yet show significant differences in their solid-state morphology according to

GIWAXS characterization for both single crystals and fabricated thin films. All of the four oligomers share an electron-rich dithienosilol (DTS) core that is flanked by either pyridyl-[2,1,3]thiadiazol (PT) or fluorinated benzo[c][1,2,5]thiadiazol (FBT) acceptor units; the acceptors are then connected to either electron-rich bithiophene (biTh) or thieno[3,2-b]thiophene (TT) end groups, giving the oligomers an overall *D'-A-D-A-D'* structure. The observed morphology variations were attributed to different conformational populations of the oligomers, based on gas-phase Boltzmann population analyses of density functional theory (DFT)-minimized energies of isolated, rotational isomers (rotamers). The conformations of FBT-containing oligomers were hypothesized to be influenced by through-space, noncovalent intramolecular F•••H interactions, while those with the PT acceptor were stabilized through S•••N through-space intramolecular interactions.[9] Both types of through-space noncovalent interactions have been suggested to control molecular and polymer conformations, and their inclusion has become a common strategy in molecular and polymer design for OSC.[2, 18, 19] We note, however, as Kharandiuk and coworkers point out, such noncovalent interactions can be quite dependent on the chemical environment, and mostly weak in strength to impart changes to the conformational diversity, and that noncovalent repulsive interactions can be more dominant over the weak attractive forces among rotatable groups.[20] Therefore, we further explore both the nature of these static interactions and the essential dynamics associated with the solution environment to systematically demonstrate how the oligomer chemistry and solution environment, including the choice of solvent and oligomer concentration may impact on the oligomer structure, conformational preferences, dynamics, and thereby the assembly tendencies.

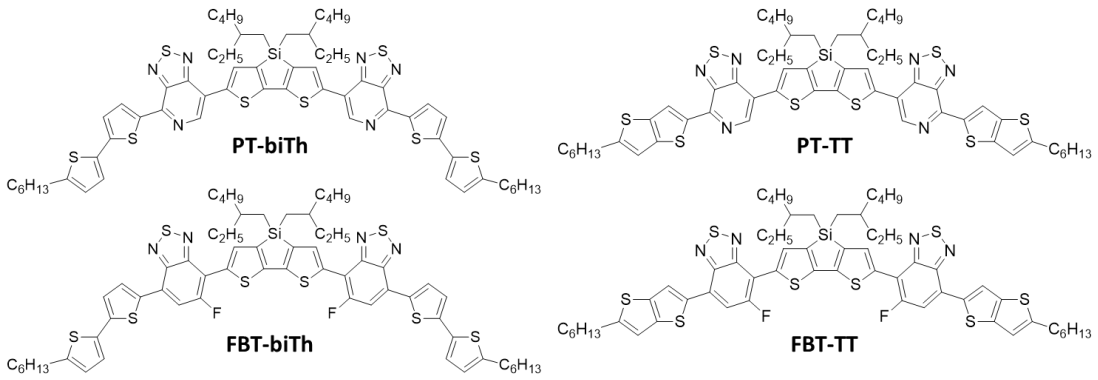

Figure 3.1 Chemical structures of oligomers of interest. PT ≡ pyridyl-[2,1,3]thiadiazole; FBT ≡ fluorinated benzo[*c*][1,2,5]thiadiazole; biTh ≡ bithiophene; TT ≡ thieno[3,2-*b*]thiophene.

We start our investigation by exploring the intramolecular noncovalent interactions through DFT and atoms-in-molecules (AIM)-based analyses. We then turn to molecular dynamics (MD) simulations to compare oligomer structure and dynamics in infinitely dilute solutions in chlorobenzene (CB) and 1,8-diiodooctane (DIO). For more concentrated solutions, we examine how inter-oligomer interactions impact oligomer conformational preferences. We follow the kernel density estimated (KDE) statistical approach to treat the massive amount of dihedral angle information obtained in these simulations to generate population densities. We compare our multi-scale information obtained through the MD level solution dynamics with the previous speculations made from purely gas-phase Boltzmann population analyses and show the importance of including system dynamics. Finally, we examine the structure, dynamics, and assemblies formed as a function of oligomer concentration and conformer populations, thereby connecting oligomer conformer populations to the aggregation.

A note related to nomenclature: We adopted the notation *anti* (or A) and *syn* (or S) to describe the relative orientations of neighboring moieties in the oligomers: "A" refers to the conformation of any two moieties where the sulfur atoms in the respective units are oriented in opposite directions (≈180°), while "S" refers to the scenario where these atoms lie on the same side of the backbone (≈0°), see Figure 3.2. This nomenclature is used for both the DFT-based dihedral scans of single torsional units, and as identifiers of the rotational conformations found for the full oligomers in the different MD simulations (as represented by the four-letter nomenclature on the left-side of the chemical structures in Figure 3.2).

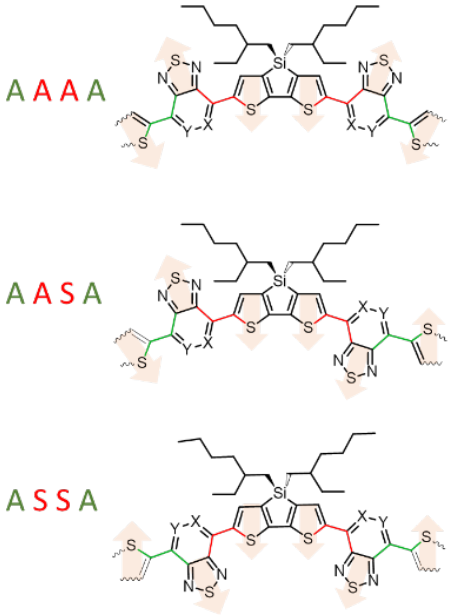

Figure 3.2 Three conformations for the central segments of the *D-A* oligomers considered in this work, with the corresponding notation scheme adopted to identify conformations. Each of these conformations is used as a starting point for different MD simulations. The green bonds represent the dihedral of the TT or biTh group with respect to the acceptor (either PT or FBT), whereas the red bonds represent the dihedral of the acceptor with respect to DTS. The arrows follow the direction of the sulfur atoms in the different aromatic groups and show the *anti*- (A) or *syn*- (S) orientations among these groups.

3.2 Computational Methods

All density functional theory (DFT) calculations were carried out at the ωB97XD/6-31G(d,p) level of theory using the Gaussian 09 Rev. E.01 suite.[21] The polarizable continuum model (PCM) with the integral equation formalism variant[22] (IEFPCM) was used to simulate chlorobenzene solvent reaction field to perform calculations. The multi-wfn[23, 24] package was used for the atoms-in-molecules (AIM) analysis of DFT-optimized (at the ωB97XD/6-31G(d,p) level of theory) fragments. The natures and strengths of select noncovalent intramolecular interactions were analyzed using scatter plots of reduced density gradients (RDG) and the sign of (λ_2) ρ functions.[25] A grid spacing value of ~0.11 Bohr was chosen for the scatter plots to maintain sufficient resolution. All iso-surface representations were generated using the VMD visualization package.

All MD simulations were carried out using the GROMACS 2019 package.[26, 27] Molecular topologies and bonding and nonbonding parameters were parametrized using OPLS-AA forcefield.[28] The charges and dihedral angle torsion parameters were explicitly determined for each system via DFT calculations at the ωB97XD/6-31G(d,p) level of theory. Inter-moiety dihedral scans were performed at the same DFT level, with rotations from 0° to 180°, with 10° increments.

For isolated oligomer MD simulations, 10 nm x 10 nm x 10 nm simulation boxes were used to generate input structures. For the concentration solution simulations with 100 oligomers, the box dimensions were chosen so that the final concentrations were 2% by weight (w/w) (approximately 22 mg/mL), to closely resemble 20 mg/mL as cast solutions used by the experimental study carried out by McDowell and coworkers.[9] The

oligomers were then (i) randomly inserted into the empty simulation boxes by invoking GROMACS_*insert-molecule* function, and (ii) solvated with pre-equilibrated solvents (either chlorobenzene – CB – or 1,8-diiodooctane – DIO) by invoking GROMACS_*solvate* function. The systems were allowed to reach solution equilibrium at 298 K and 1 bar through an initial steepest decent energy minimization followed by one NVT (constant number of molecules N, volume V, and temperature T) ensemble with the initial velocities assigned via Maxwell distribution, and two NPT (constant number of molecules N, pressure P, and temperature T) ensembles steps using the leap-frog integrator algorithm with 2 fs time steps. Hydrogen bonds were constrained using the LINear Constraint Solver (LINCS) to their equilibrium values. The first NPT was run under the Berendsen barostat algorithm[29] for the pre-equilibrium step. For the production runs, the Parrinello-Rahman[30] barostat algorithm was followed. Both barostats used a coupling frequency of 1.0 ps and a compressibility of 4.5 x 10^5 bar^{-1}. The velocity rescaling thermostat was used to couple temperature of the simulation boxes at 298 K, with coupling frequency of 1.0 ps. Three-dimensional periodic boundary conditions (PBC) were applied for the simulation boxes. Both short-range van-der Waals (vdW) interactions, and long-range electrostatic interactions were calculated using a spherical cut-off of 1.4 nm, using particle-mesh Ewald (PME) method. The NVT and first NPT steps were run for 2 ns, and the second NPT step under the Parrinello-Rahman barostat were allowed to equilibrate for longer times: 20 ns for single oligomer systems and 50 ns for multi-oligomer systems. For simulations carried out *in vacuo*, only the NVT step was followed. Dihedral angle analyses among select moieties were carried out using the GROMACS_*gangle* function.

Inter-oligomer interactions between two adjacent moieties were simulated using the umbrella simulation procedure of GROMACS.[31] Potential-of-mean-force (PMF) profiles were calculated in all three environments: *in vacuo*, and in CB and DIO solvents for comparison. For each PMF simulation, pairs of the four oligomer types were placed in 8 x 8 x 8 nm^3 cubic boxes, starting with a 3 nm COM separation. A production MD run was then carried out followed by the equilibration scheme: Initial steepest-decent energy minimization, one NVT run, one NPT run under the Berendsen barostat, and one NPT run with the Parrinello-Rahman barostat. Umbrella sampling was conducted under a biased potential, allowing one molecule to move closer to the other molecule that was anchored in a fixed position through position restraints. The moving rate was kept at 0.005 nm/ps along the laboratory Z direction to maintain smooth movement. Each PMF simulation were carried out to maintain sufficient sampling overlap between each window for statistical strength (~140 configuration). Each window was then individually equilibrated for 5 ns at time steps of 2 fs for the PMF that contained CB or DIO. For the *in vacuo* PMF simulations, a similar process was undertaken but with only a 2 ns equilibration time for each sampling window. PMF profiles were then calculated by using weighted histogram analysis (WHAM) method.[32, 33]

To examine rotational conformational disorder, dihedral angles associated with rotatable bridging bonds in chromophores were calculated using GROMACS through *gangle* function. The torsional angle was defined in terms of two vectors, each defined by a pair of reference atoms. Outputs were calculated for each angle per frame along the simulation trajectory.

For the large-scale data obtained for simulation trajectories with the dihedral angle calculations covering multiple molecules under varied environments, each system containing several dihedral rotational points per molecule, population distributions were generated using the kernel density estimation (KDE). For this task, Python Pandas application programming interface (API) was implemented.[34, 35] The built-in smoothing settings, including the bandwidth (h) were used. A Gaussian-type kernel function was used to non-parametrically estimate the probability density function of a random variable. For a univariate independent and identically distributed sample (x_1, x_2,..,x_n) with an unknown density $\hat{f}_h$, the kernel density estimator is expressed as follows;

$$\hat{f}_h(x) = \frac{1}{n}\sum_{i=1}^{n} K_h\,(x - x_i) = \frac{1}{nh}\sum_{i=1}^{n} K\left(\frac{x-x_i}{h}\right) \qquad \text{Equation 3.1}$$

where, K is the kernel function, and h is the bandwidth of smoothing. The kernel estimators smooth out the contributions of data points over their local neighborhoods.[36] Rotamer conformational population analysis was performed by using 90 angle as the cut-off criteria for separating angle distributions into *syn* and *anti*-conformational orientations. Python Pandas API[37] Data Frame function was used to handle large data with ~12 million datapoints to pass through the cut-off criterion to categorize into conformational rotamers to reveal the rotational behavior shown by each solution environment, and express in terms of conformational variants.

Molecular aggregation in solution was estimated by using the GROMACS pair correlation function (radial distribution function – RDF), with respect to the center-of-mass of the oligomer backbones. Molecular aggregation was identified by calculating the average center of mass distance distribution of the backbones belonging to oligomers.

The cut-off distance that separates fully solvated to aggregated molecules were chosen by referring to the RDF and the PMF profiles. Populations analyses were carried out for the time averaged dihedral data by using in-house Python scripts. The MD simulations were checked to confirm they reached equilibrium by monitoring the energy and the root-mean-square displacement vs. time, prior to the analyses described above.

3.3 Results and Discussion

3.3.1 Determining existence of intramolecular noncovalent interactions

We calculate the potential energy surface (PES) associated with rotation about each bridging bond that connect the donor (*D*) and acceptor (*A*) moieties of the four oligomers through DFT calculations. We then evaluate the nature and strength of the noncovalent intramolecular interactions to identify interactions that may be important to maintaining oligomer rotational configurations. Next, we turn to the results of the MD simulations, starting with how the solvent environment impacts oligomer dynamics and conformational preferences. Multi-oligomer simulations are used to explore both the conformational preferences and aggregation tendencies of the four oligomers. Figure 3.3 provides clarification on structural fragments and the abbreviated names used in the analysis.

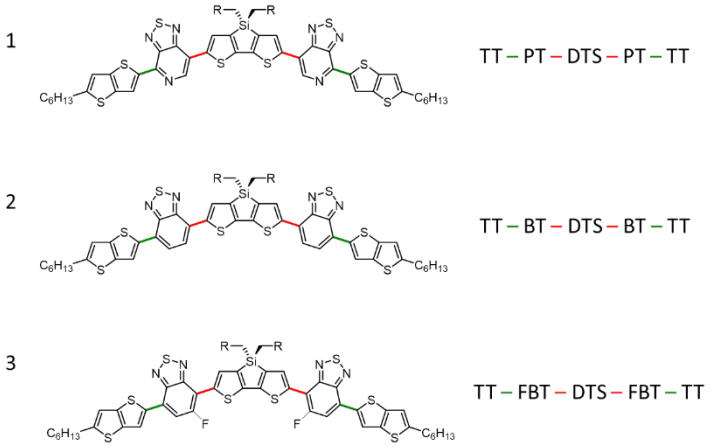

Figure 3.3 Oligomer structures and fragment abbreviations. The colored bonds (red and green) correspond to the rotatable bonds among the fragments. Following established convention, we note that molecules 1, 2 and 3 are identified as PT-TT, BT-TT and FBT-TT for simplicity.

Figure 3.4 shows the torsional potential energy surfaces (PES) for select *A* and *D* groups that comprise the four oligomers as determined at the ωB97XD/6-31G(d,p) level of theory. We focus on two main features of the PES, (i) the barrier height and (ii) the curvature of the minima, to derive relationships with the intramolecular noncovalent interactions among the moieties. In addition, we also explore the PES for benzothiadiazole (BT) with the *D* groups, which serves as a chemical intermediary between PT and FBT acceptor groups. Note that the available thermal energy (*kT*) at 298 K, approximately 0.6 kcal/mol, is provided as a reference (dashed line) in Figure 3.4.

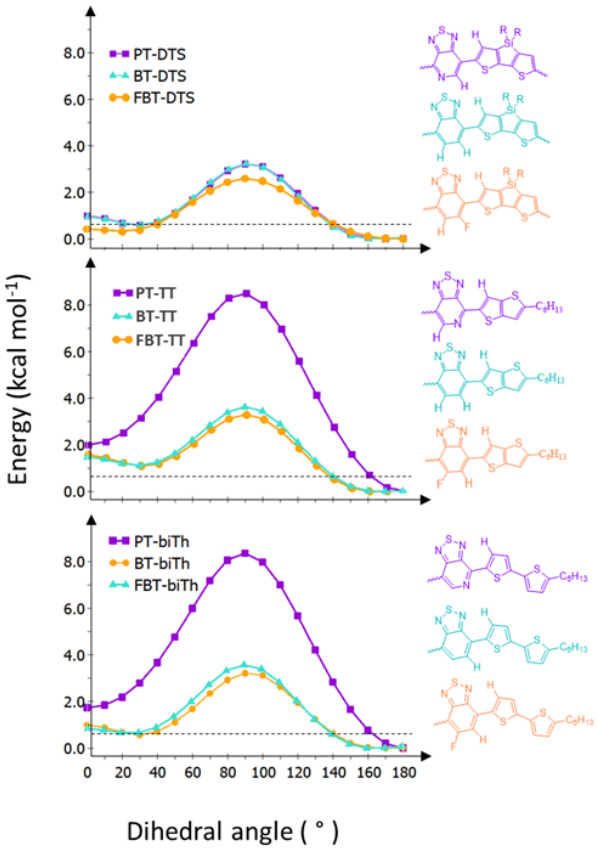

Figure 3.4 Torsional (dihedral) potential energy surfaces (PES) derived at the ωB97XD/6-31G(d,p) level of theory among select donor and acceptor moieties.

Comparing the obtained PES, we see similar energy profiles for all three innermost rotational groups. However, significant differences are shown for that of outermost rotational groups, especially with respect to the central PES barriers at 90 ° angle. To provide rationalization as to how the intramolecular noncovalent interactions contribute to the observed PES, it is worth realizing that at either end (i.e., 0° and 180°) of the PES is where these interactions (*e.g.*, S•••N, S•••F, F•••H, *etc.*) are expected to be the strongest due to preferred positioning at nearby vicinity. Therefore, small PES barriers or wells may very well be introduced by the interacting atoms into the PES minima regions at near-planar angles.

Traversing the PES towards 90°, although we see the potential energies maximize, the noncovalent intramolecular interactions become considerably weaker, due to the through-space nature of the interactions as the interacting atoms separate out around rotation. Therefore, one can rationalize that the observed central energy barrier does not correspond to the noncovalent contacts.

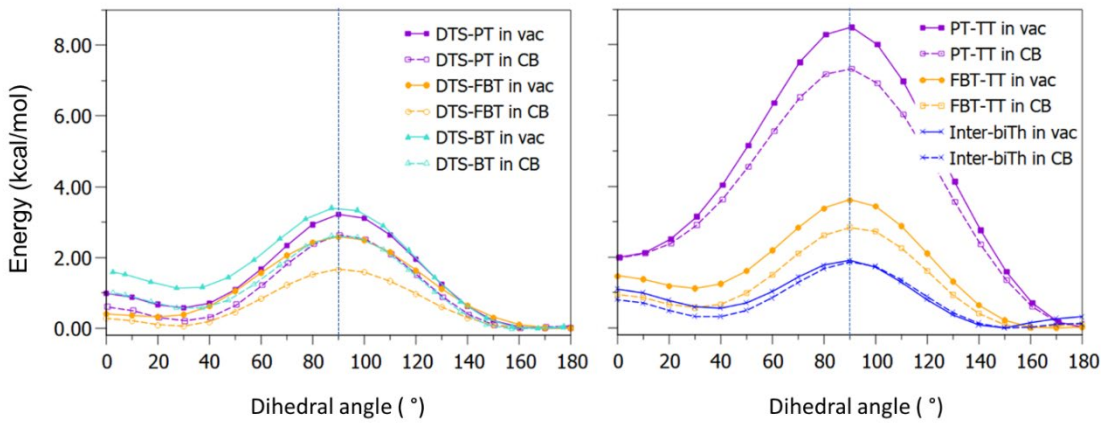

Figure 3.5 Potential energy surfaces (PES) for rotation among the noted fragments in gas phase as determined at the ωB97XD/6-31G(d,p) level of theory. The dotted lines with open symbols represent PES determined with the polarizable continuum model with the integral equation formalism variant (IEFPCM) simulating chlorobenzene solvent reaction field. The vertical dotted line references 90°.

Comparing the PES obtained for the calculations carried out under polarizable continuum model simulating CB solvent and vacuum (Figure 3.5), we highlight that overall, all barrier heights show a decrease of ~1 kcal/mol (except for the biTh rotation). Interestingly, almost all the minima near 0° and 180° also show a decrease. We clarify that this potential energy decrease is due screening of the seperation in terms of opposite dipoles by the high dielectric constant, under the CB solvent (as compared to vacuum). This therefore weakens the interaction strengths between participating atoms. Therefore, the drop in PES minima in CB signals the pre-existence of noncovalent contacts.

Interestingly however, no such decrease shown by PT-TT rotation and we provide rationale behind this observation in the next section. The central barrier drop can also be explained using the same rationale, where at orthogonal angles, the π-delocalozation across rotatable groups is distupted, and the CB solvent dielectric can weaken this disruption energy by the charge screening.

We now turn to atoms-in-molecules (AIM) theory to investigate the existence of the noncovalent intramolecular interactions in terms of electron density distribution. AIM provides several descriptors that can be used to characterize these interactions, in particular:

(i) The bond critical points (BCP; Figures 3.6, 3.11 and 3.12) through minimum between the electron densities between nuclei, indicating bonding between two atoms.

(ii) The reduced density gradient (RDG) profiles, which reveal the presence of noncovalent contacts, as well as their nature, shown as spikes where the electron density ρ(r) and reduced density gradients (s) are small (Figures 3.7 – 3.10).

(iii) The ring critical points (RCP), which indicate five or six membered ring stabilization (Figure 3.13);[38] that may also describe the completion of the aromatic circuit through noncovalent contact.

Figure 3.6 depicts all the existing critical points (CPs) for all of the rotatable groups at their optimized dihedral angle of rotation, calculated at the DFT ωB97XD/6-31G(d,p) level of theory. Note that in addition to BCPs, ring critical points (RCPs) are also shown. RCPs are present where through-space interactions are present, resulting here

in five membered rings (mostly shown by the cases where S•••N and N•••H noncovalent contacts are present and assist in completing the through-space ring aromaticity).

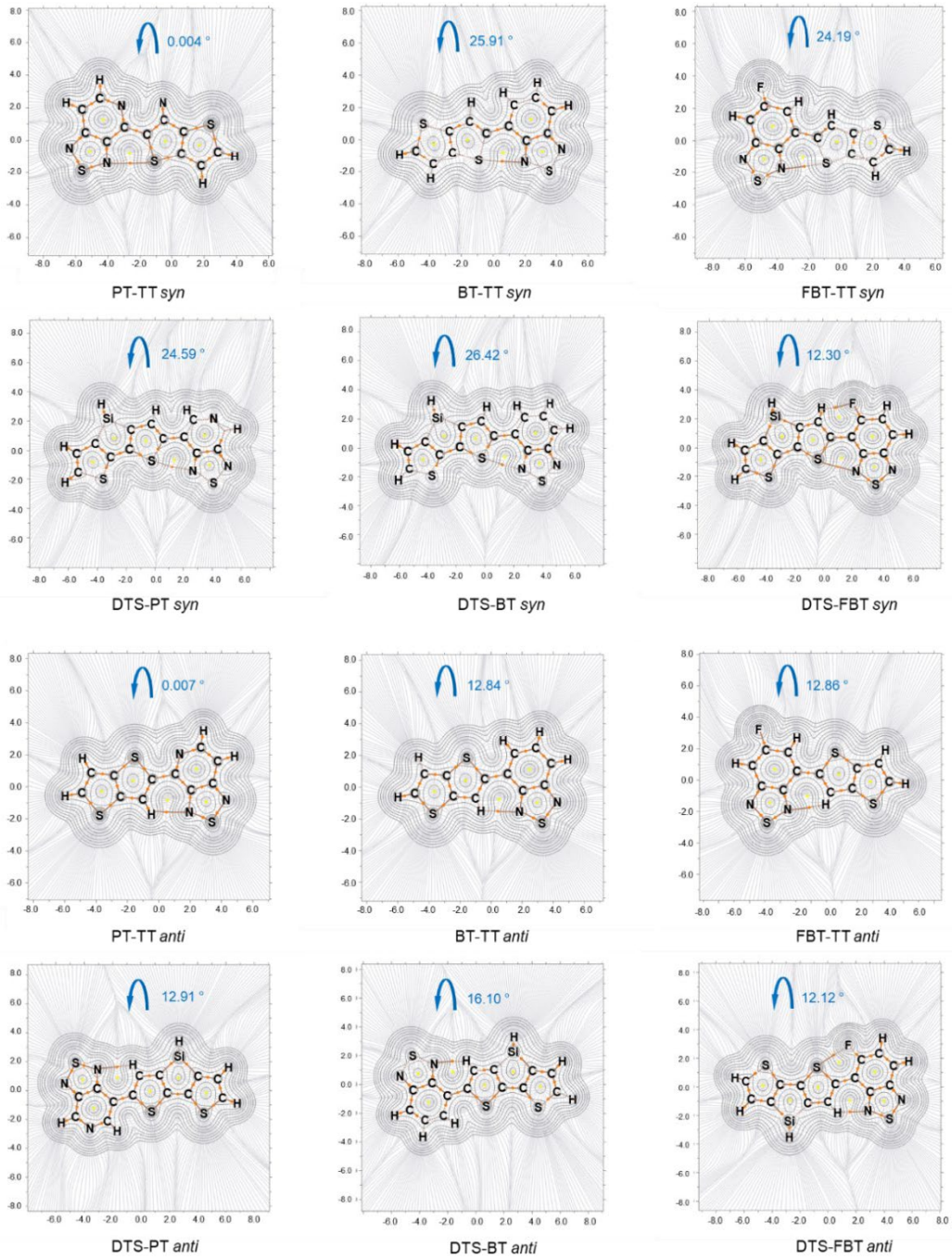

Figure 3.6 Contour plots of the electron density for ωB97XD/6-31G(d,p)-optimized molecular fragments in the syn (top two rows) and anti (bottom two rows) configurations. Length units of X and Y axes are shown in Angstroms. The +3, -1 type (bond) critical points shown as orange dots (with paths shown by the brown straight lines) and +3, +1 (ring) type critical points are shown as yellow dots. Bonds that lie out of the plane are shown in dotted lines. The twist angle between D-A groups is annotated in blue.

3.3.2 Determining nature and strength of intramolecular noncovalent interactions

To reveal the nature and strengths of the interactions among the noncovalently interacting atoms of rotatable groups (revealed by the CPs), we turn to reduced density gradient vs. sign(λ_2)ρ scatter plots. The characteristic spike like features indicate the through space interactions, and the spike positioning along the x axis (i.e., the sign(λ_2)ρ value) correspond to the attracting or repulsive natures in the interactions. Attractive interactions are shown by negative sign(λ_2)ρ, with the high negative values corresponding to the existence of higher attractive components. Conversely, repulsive interactions are indicated by spikes pointing to high positive sign(λ_2)ρ, Overall nature of the interaction can be a function of the interplay between attracting and repulsive components (Figures 3.7 through 3.10).

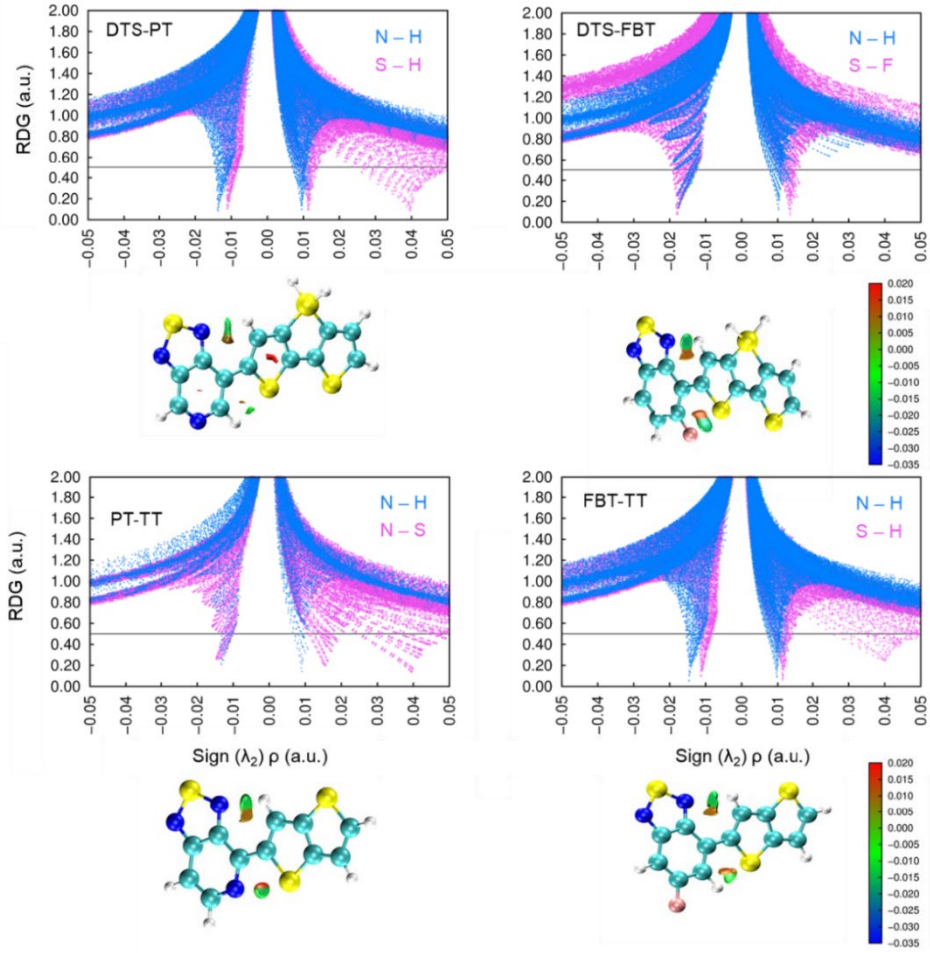

Figure 3.7 RDG vs. sign(λ_2)ρ scatter plots for PT and FBT with either DTS (top) or TT (bottom) for the ωB97XD/6-31G(d,p) optimized *anti* orientations, highlighting the 0.5 isosurfaces of the sign(λ_2)ρ value

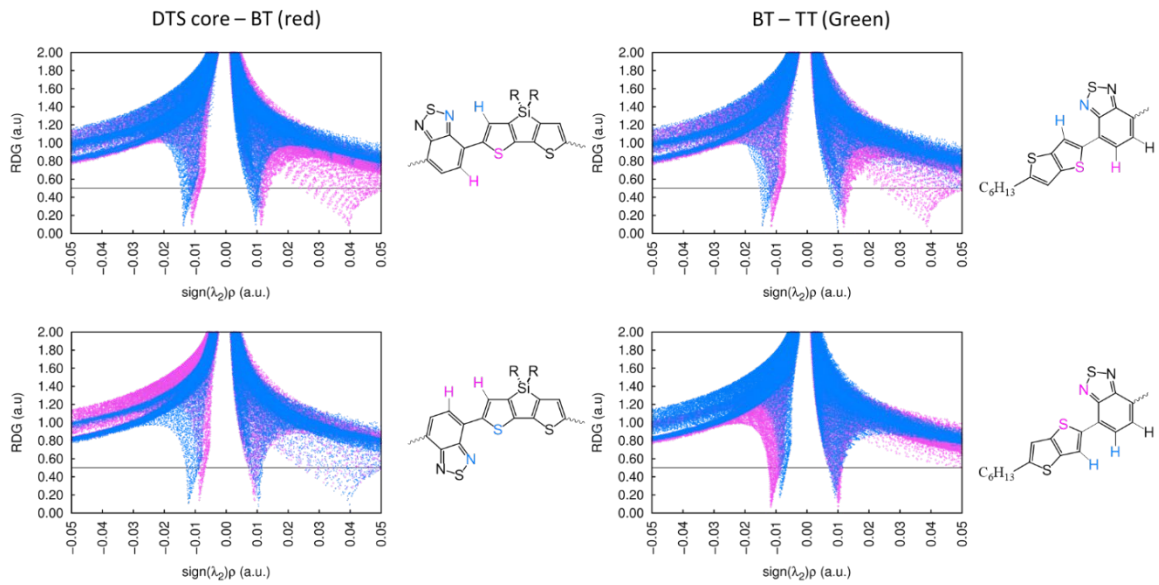

Figure 3.8 RDG vs. sign(λ_2) scatter plots for BT - DTS and BT – TT in the *anti* (top row) and *syn* (bottom row) orientations optimized at the ωB97XD/6-31G(d,p) level of theory

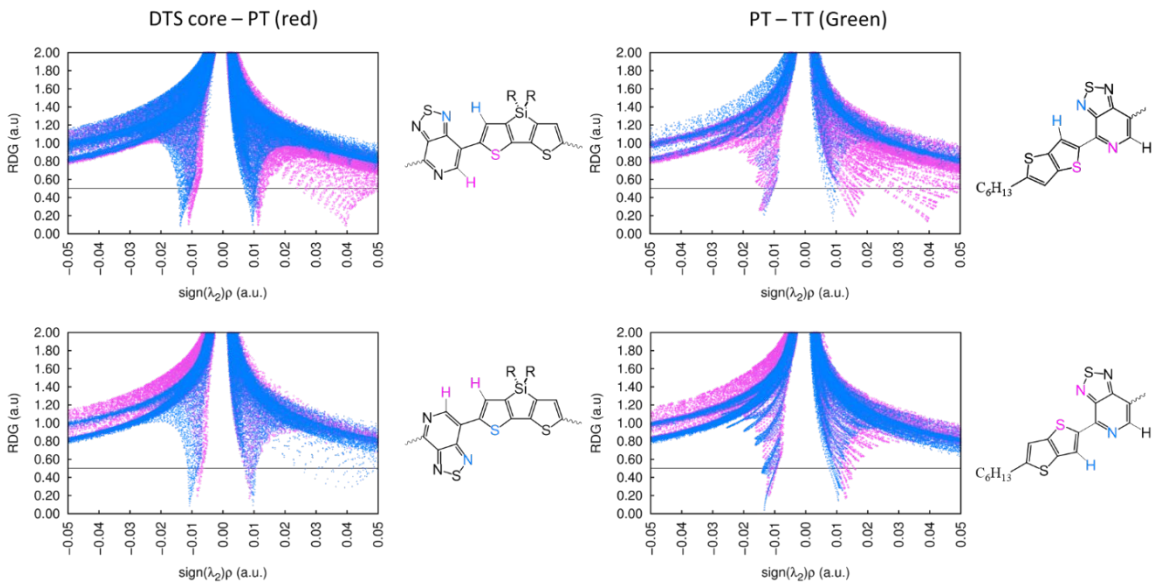

Figure 3.9 RDG vs. sign(λ_2) scatter plots for PT - DTS and PT – TT in the *anti* (top row) and *syn* (bottom row) orientations optimized at the ωB97XD/6-31G(d,p) level of theory

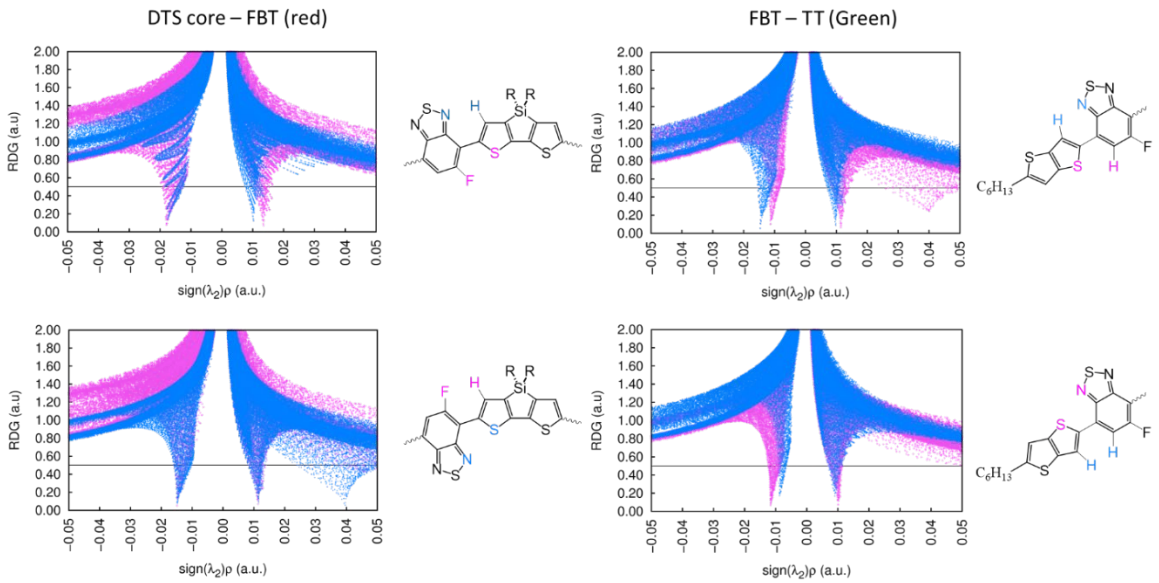

Figure 3.10 RDG vs. sign(λ_2) scatter plots for FBT - DTS and FBT – TT in the *anti* (top row) and *syn* (bottom row) orientations optimized at the ωB97XD/6-31G(d,p) level of theory

Combining the information revealed through AIM theory for the DFT optimized structures, we describe the observed PES, accounting for the contribution from intramolecular noncovalent contacts. Starting with the PES of the acceptors bound to DTS (the *A-D* interaction), one observes that, overall, the PES shapes and energies are each quite similar, though there are distinct differences for the S conformation (approaching 0°): For BT-DTS and PT-DTS, H•••H repulsion (Figure 3.4 and 3.11) leads to the presence of a small secondary barrier that is not present in FBT-DTS that contains the attractive F•••H interaction (as revealed by BCP and RCP); note, however, that this secondary barrier is ~*kT* at 298 K. BCP and RCP showcase the presence of N•••S noncovalent interactions for each system in the S conformation. Note that the coexistence

of the N•••S and F•••H interactions in FBT-DTS lead to a somewhat smaller optimized torsional angle of the S conformation when compared to the other systems.

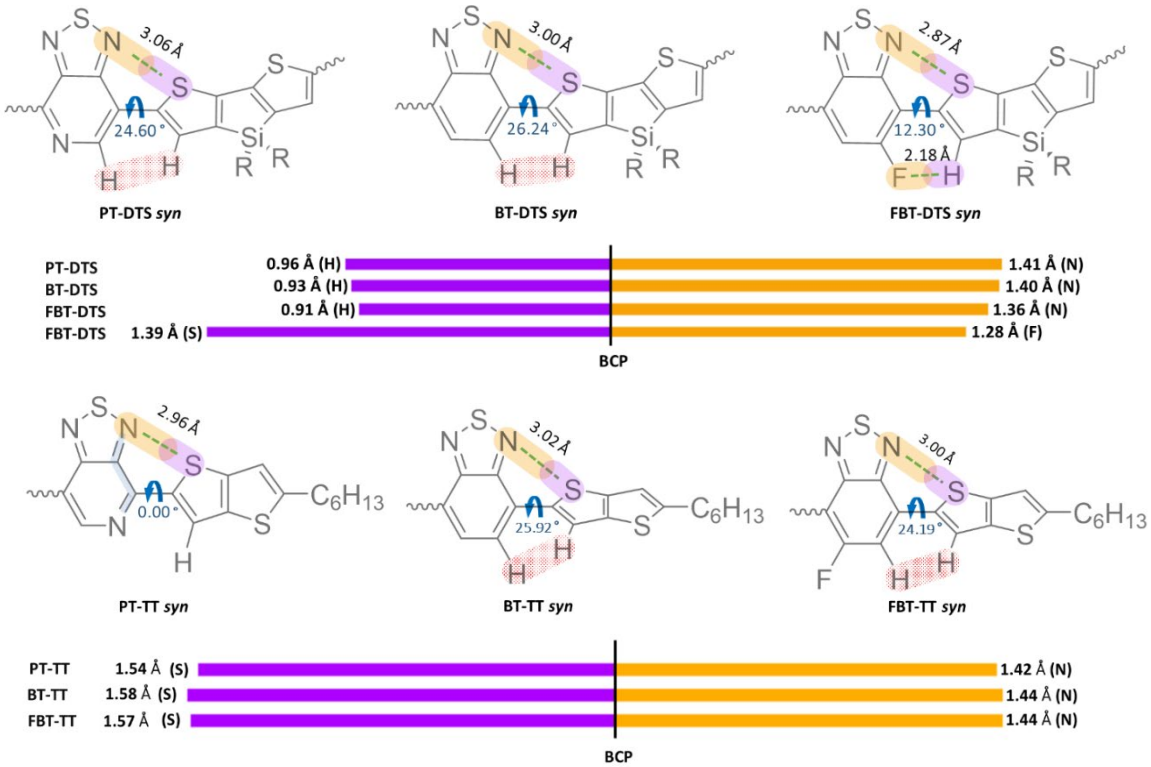

Figure 3.11 Diagramatic representation of intramolecular noncovalent interactions between rotatable fragments optimized in the *syn* (S) orientation, determined at ωB97XD/6-31G(d,p) level of theory. The noncovalent bonding interactions are identified through +3,-1 type bond critical points (BCP) of the electron density (shown by the green dashed lines). The repulsive interactions are shown in red shaded regions (identified thorugh RDG vs. sign(λ_2)ρ scatter plots). The annotated bar charts show the relative intramolecular noncovalent bonding interaction distances with respect to their BCP center, with orange and violet colors showing the overall electronegative and electropositive sides of the interactions.

For the optimized A conformations, the BCP and RCP reveal N•••H attractive interactions in all three systems, S•••F attractive contacts in FBT-DTS, and repulsive H•••S interactions in BT-DTS and PT-DTS (Figure 3.11). Again, it is the coexistence of these noncovalent interactions on either side of the bridging single bond that define the

minimized/optimum geometries of the systems. The repulsive H•••S interactions in BT-DTS and PT-DTS do minimize the strength and enlarge the noncovalent bond length of the N•••H contact when compared to that of FBT-DTS. However, though FBT-DTS has the H•••F (S conformation) and S•••F (A conformation) attractive interactions present, these are not enough to alter the energetic profile considerably when compared to the other species, suggesting that the fluorine atom does not act as a noncovalent "lock", as has often been described;[2] this result is in agreement with other studies in the literature.[20]

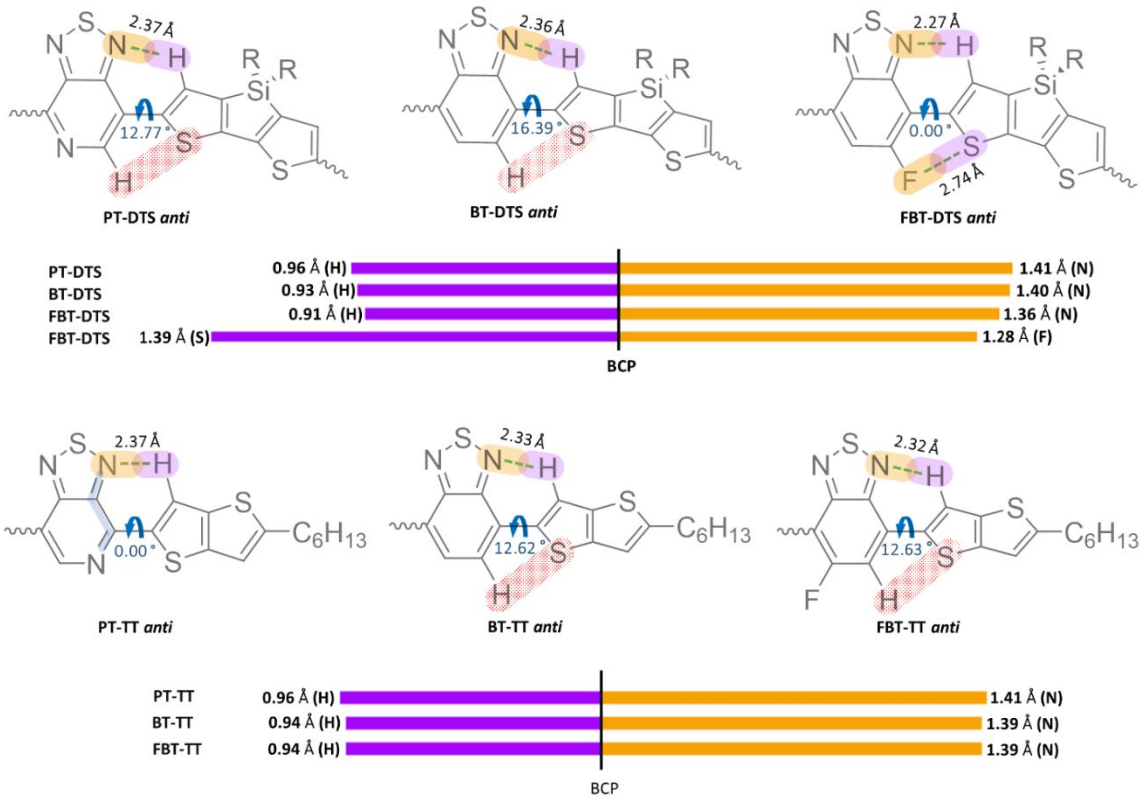

Figure 3.12 Diagramatic representation of intramolecular noncovalent interactions between rotatable fragments optimized in the *anti* (A) orientation, determined at ωB97XD/6-31G(d,p) level of theory. The noncovalent bonding interactions are identified through +3,-1 type bond critical points (BCP) of the electron density (shown by the green dashed lines). The repulsive interactions are shown in red shaded regions (identified thorugh RDG vs. sign(λ_2)ρ scatter plots). The annotated bar charts show the relative intramolecular noncovalent bonding interaction distances with respect to their BCP center, with orange and violet colors showing the overall electronegative and electropositive sides of the interactions.

We now turn to the PES for the acceptor moieties bound to the TT groups (the *D'-A* interaction). We note that the PES for the acceptor moieties bound to the biTh groups follow very similar trends, and so we will solely focus on the description of the PES containing the TT groups. The PES for FBT-TT and BT-TT are quite similar, showing almost no variation due to the substitution of the fluorine atom. Considering the inter-moiety noncovalent interactions, this observation is intuitive as the noncovalent

interactions surrounding the torsion are identical – N•••H (attractive) and S•••H (repulsive) interactions for the A conformation, and H•••H (repulsive) and N•••S (attractive) for the S conformation (Figures 3.12). The electron-withdrawing fluorine atom on the opposite side of the acceptor plays only a minor role in altering the distribution of the electron density when compared to the electron-donating hydrogen atom in the same position. For PT-TT, however, the PES is drastically different: (i) The curvatures of the A and S minima are considerably tighter, (ii) the minima of the A and S configurations are closer to 180° and 0°, respectively, (*i.e.*, the optimized PT-containing structures are more planar), and (iii) the barrier height is significantly larger (by ~5 kcal/mol). The BCP distance for the N•••H interaction of the PT-TT A conformation is quite similar, if not slightly longer (*i.e.*, weaker), than that for FBT-TT and BT-TT; this weaker interaction is due in part to the smaller electron density in the pyridyl ring of PT compared to the phenyl rings in FBT and BT that reduces the electron density on the thiadiazol nitrogen atom that partakes in the N•••H interaction. All three species do have RCP arising from the N•••H contacts. Further, for the optimized A conformation of PT-TT, the RDG analyses reveal that the pyridyl N•••S interaction is repulsive overall (Figure 3.8) – the dominant peak existing at ≈ (+)0.015 sign(λ_2) ρ value, for which the contribution is visible to the 0.5 RDG isosurface appearing more superimposed, suggestive of dominating crowded interactions in the four membered ring system. Therefore, considering the weaker N•••H attraction and the existence of a relatively strong N•••S (overall) repulsion in PT-TT, it becomes clear that the intramolecular noncovalent interactions do not play a considerable role in the overall shape and energetics of the PES. Similar observations are made for the S conformations.

3.3.3 π-electron delocalization across rotatable bridging bonds

With a better understanding of the impact of the noncovalent interactions near the PES minima, one can move to examine the barriers that are observed when the *D* and *A* moieties approach orthogonal conformations; the barriers are important when considering if certain conformations are preferred / locked as a large barrier would suggest it to be more difficult to change the inter-moiety conformation (while a smaller barrier would allow for more ready transition among minima). In these geometries, the distances among the atoms that could act as noncovalent locks are too large for such intramolecular interactions to hold the structures in given conformations. Therefore, one needs to consider the distribution of the electron density as the torsion angle of the bridging bond changes. An ideal single (σ) bond with no π-bonding contribution would hypothetically result in no or small barrier to rotation, given that no gauche or eclipsed noncovalent interactions are present during rotation. On the other hand, for π-electrons delocalized across two planar aromatic structures, where some double bond character is expected in the bridging bond, it would be expected that preventing the loss of π-electron delocalization may lead to a steep barrier. To validate this assertion, the bond lengths, bond ellipticities (BE)[39] (Figure 3.13 and 3.14) and Mayer bond orders (MBO; Figure 3.15) of the bridge and adjoining bonds are evaluated.

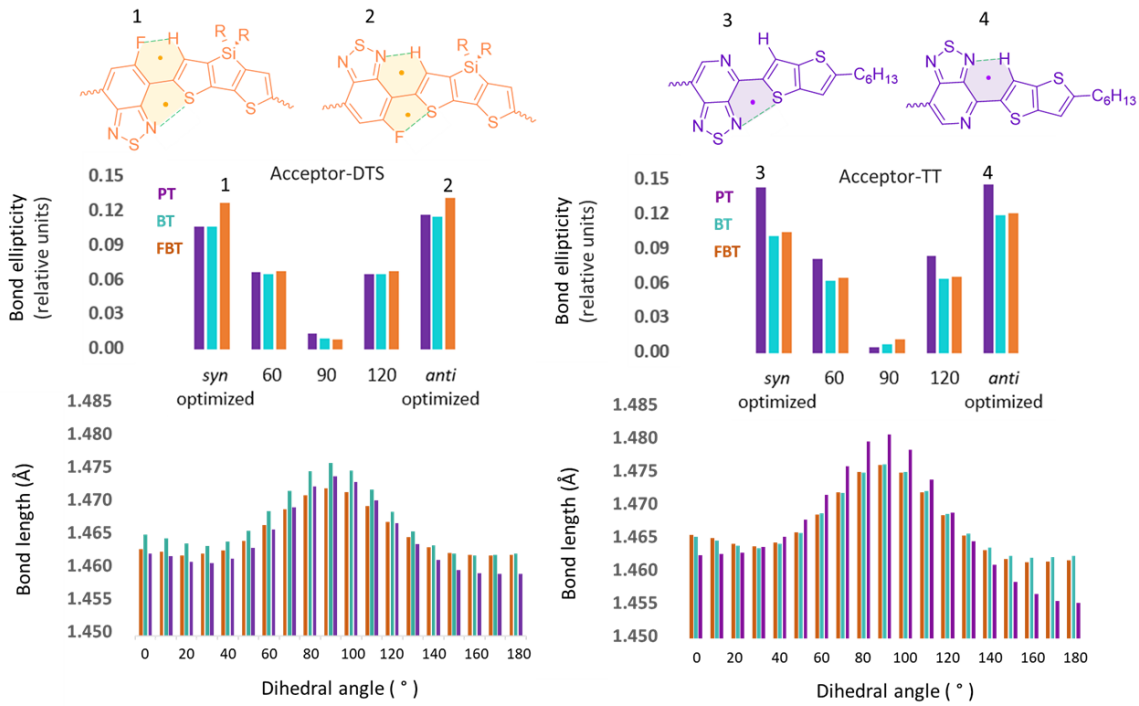

Figure 3.13 The ellipticity of electron density and bond length and variation of the bridging bond between acceptor and donor groups during dihedral rotation. The labeled structures that are colored to correspond to the conformations that give rise to higher bond ellipticities for the bridging bonds. The bond critical point paths

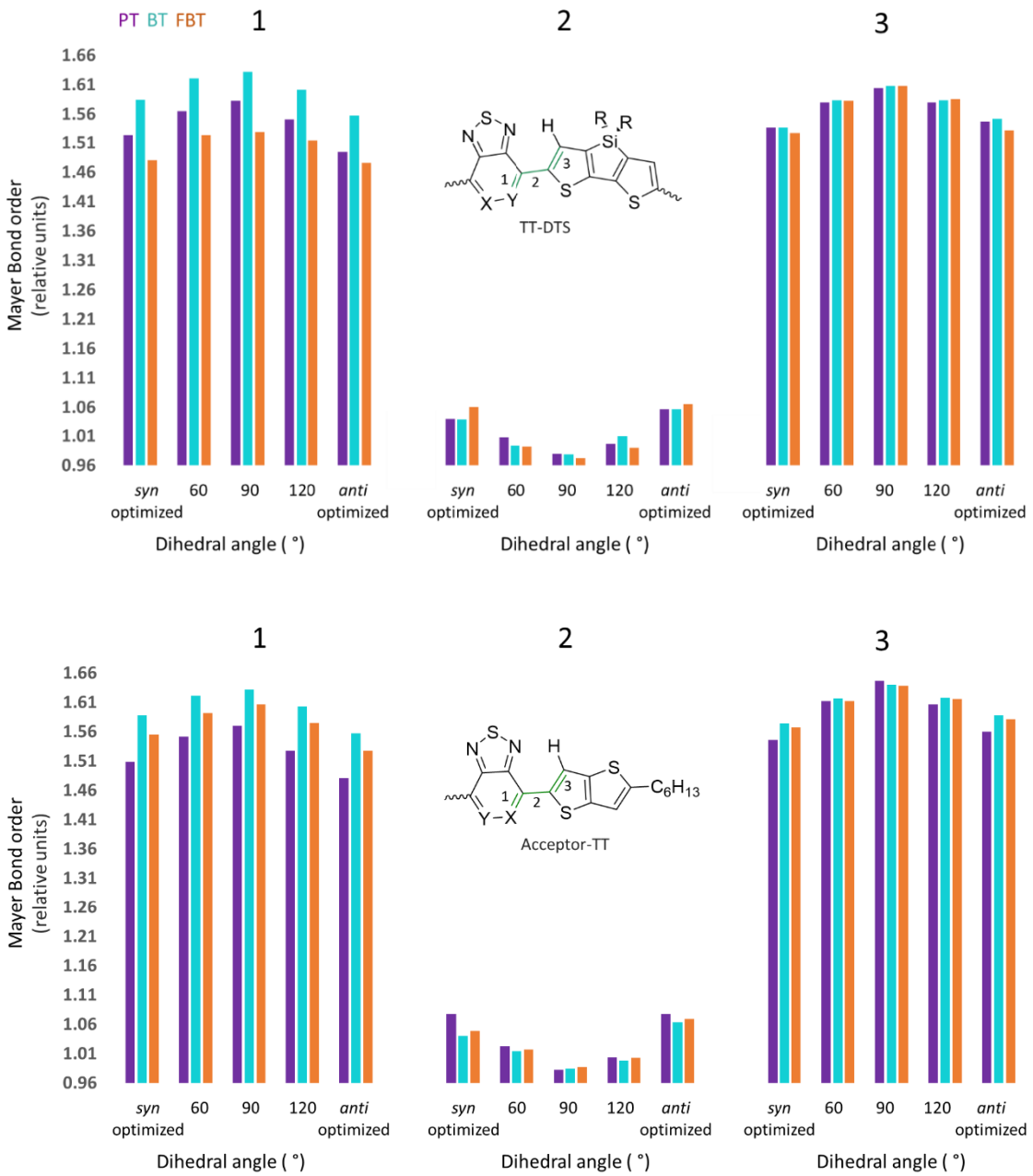

Figure 3.14 Electron density ellipticities of bonds labeled 1, 2, and 3 as the bond is rotated from *syn* optimized through 60°, 90°, 120°, to the *anti*-optimized angles for the acceptor-DTS (top) and TT-acceptor (bottom) fragments and ring critical points shown in dotted green lines and shaded regions, respectively

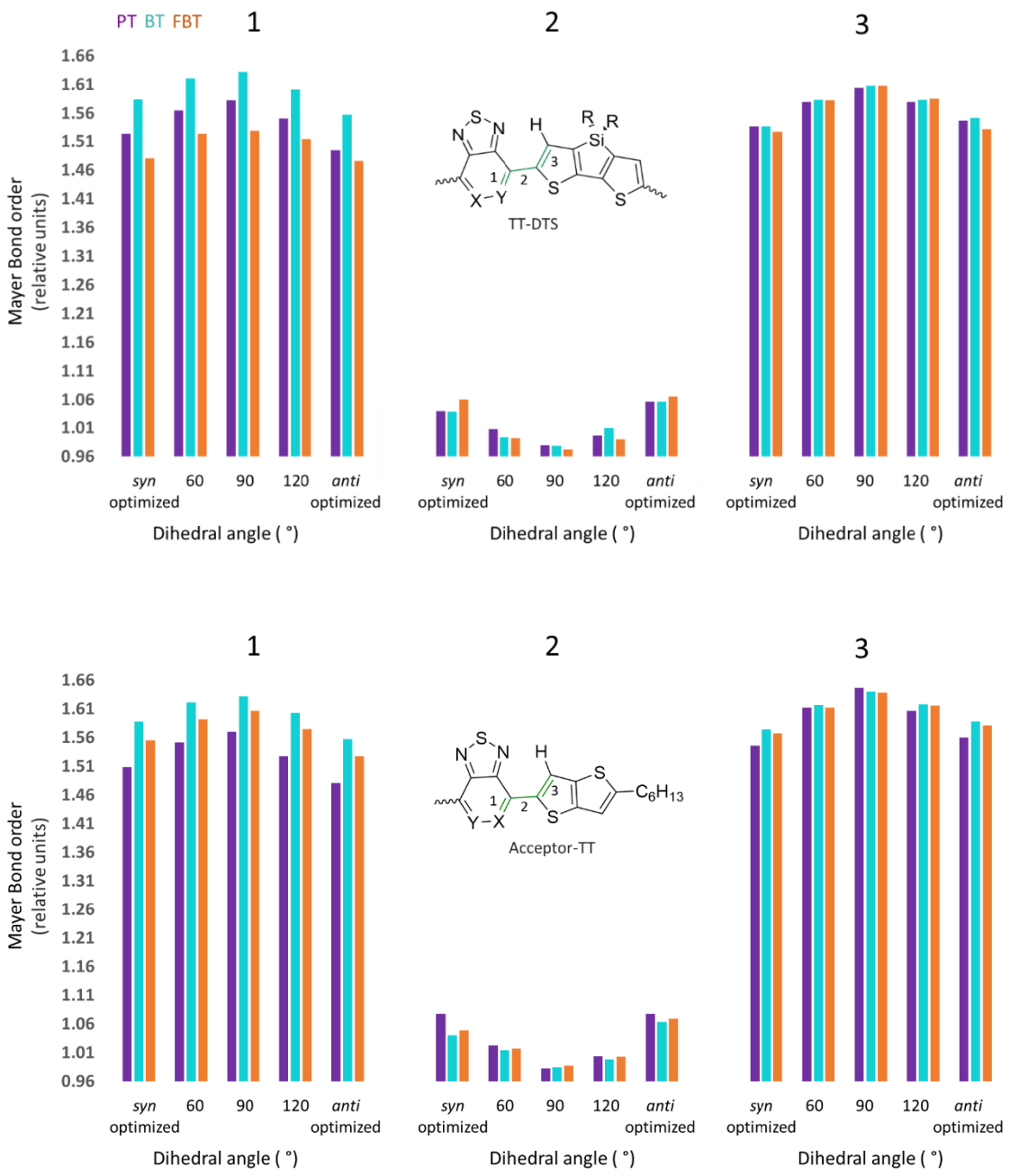

Figure 3.15 Mayer bond orders of bonds labeled 1, 2, and 3 as the bond is rotated from *syn* optimized through 60°, 90°, 120°, to the *anti*-optimized angles for the acceptor-DTS (top) and TT-acceptor (bottom) fragments

We start with the *A*-DTS systems. Recall the PES were quite similar for the three systems, with the fluorine containing FBT having a slightly lower barrier (by ~1 kcal/mol) and larger curvature in the minima. For all three systems, the bond length and MBO descriptors for the bridging bond are quite similar – the bond has some double bond character that diminishes as the torsion approaches 90°. The BE and MBO descriptors do reveal additional double-bond character for FBT-DTS at the optimized A and S conformations, due to the influence of the electron-withdrawing fluorine atom being in direct alignment and a conformation that is more planar. Hence, the fluorine atom, in addition to providing some attractive noncovalent intramolecular interactions, also affects the double bond character of the bridging bond in these conformations. However, at 60°, where there is still considerable π-electron delocalization, the degree of double bond character in all three systems is nearly identical. Likewise, the bond character is similar for all three systems at 90°. So, while the fluorine atom does influence the π-electron delocalization near the PES minima, and also provides some attractive noncovalent interaction, the PES for the *A*-DTS systems are all quite similar. The changes in these bond descriptors are very small, and of similar magnitude as recently reported bond length and MBO parameters by Che and Perepichka.[40] We note, however, that care should be taken to not over-emphasize the observed changes, *i.e.*, the bonds maintain considerable single-bond character even in the geometry optimized conformations. In addition, the changes in the PES barrier heights when comparing fluorinated vs. non-fluorinated *A* (in line with previous studies[18]) are quite small and will not impose restrictions upon the interconversion from A to S conformations.

Turning to the systems with the TT donor, the bond descriptors for the FBT- and BT-containing structures are alike; this is not surprising given that the chemistry of the *D* and *A* groups surrounding the bridging bond is identical. The situation for PT-TT, where the pyridine nitrogen atom is in direct proximity to the torsion, is demonstrably different. As in the case of FBT-DTS, the double-bond character of the bridge bond is larger than in the other donor-acceptor systems at both optimized geometries (A and S conformations). Now, however, the double bond character, via the BE descriptor, also remains larger at the 60° (and 120°) torsion. It is not until the torsion reaches 90°, focusing on the BE, that the bridge bond in PT-TT has the same BE character as TT with the other two acceptors. Hence, with the electron deficient pyridine replacing the benzene ring, there is a stronger resistance to torsion that then appears to snap near the 90° conformation.

3.3.4 Summary: Impact of noncovalent intramolecular interactions on structure

We highlight that the PES barrier height is associated with the energy required to disrupt the π-electron delocalization; the energetic cost, as can be seen in PES (Figure 3.4), can be quite large. This seems to be a realization that is commonly overlooked in literature[2, 41] in favor of the idea of noncovalent interactions "locking in" conformations. The PES minima curvatures are also a function of the distribution of the π-electron density, with small alterations being introduced by the presence of intramolecular noncovalent interactions: Repulsive interactions will result in potential hills near the minima, while attractive interactions can introduce potential wells, broadening the curvature (Figure 3.16). The dielectric constants associated with the solvent environment can further impact on the interaction strengths of the noncovalent contacts, where at high

dielectric, the dipole interactions between participating atoms are screened, thereby weakening the interaction strengths.

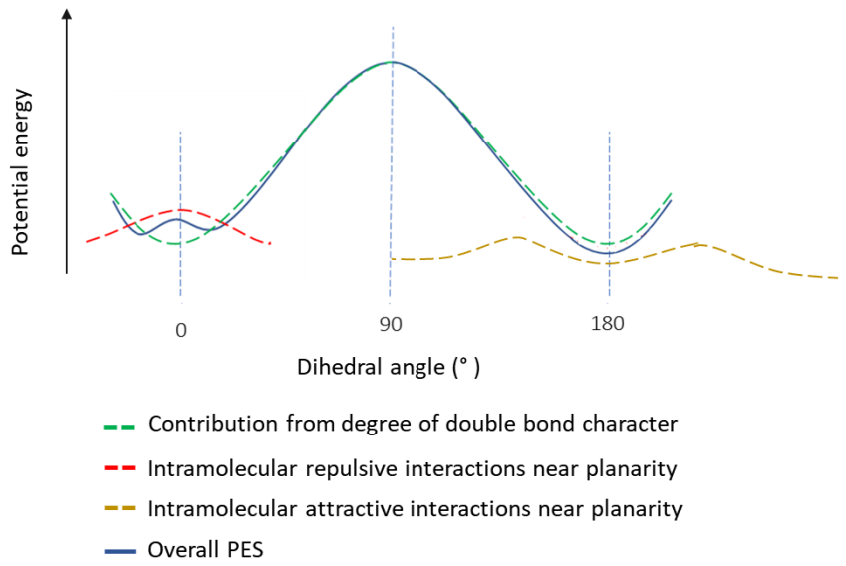

Figure 3.16 Model depicting the potential energy surface for rotation among π-conjugated moieties with contributions from the degree of double bond character (green dashed line) and intramolecular noncovalent attractive (gold dashed line) and repulsive (red dashed line) interactions.

Hence, while there is an important interplay among the degree of π delocalization and, here, attractive intramolecular noncovalent contacts in determining the preferred (enthalpic) configurations of moieties in the oligomers, the distribution of the π-electron density across rotatable donor acceptor groups plays the significant role.[41, 42]

3.3.5 The explicit role of solvent on the conformations of isolated oligomers in solution

At this stage, we have developed a static view of the torsional profiles and preferred conformations of oligomer fragments using DFT level ab-initio approaches. We now turn to MD simulations at room temperature, starting with simulations of the (full) isolated oligomers in explicit vacuum and two solvents – chlorobenzene (CB) and 1,8-diiodooctane (DIO) environments; these two solvents were chosen as they have been

used as co-solvents in the deposition of OSC active materials, including FBT-biTh, in solar cell applications.[43, 44] We note that the MD simulations were initiated from different conformations so as to not bias the results towards a particular conformation; these starting conformations are denoted by the orientations of the two inner-most torsions, and we label the three possible combinations as AA, AS, and SS (the other torsional positions in the oligomers are initially set to A). In general, there is much more dynamic variability in the torsions on the periphery of the oligomers than in the proximal regions across all systems investigated, though, the *A* chemistries do play important roles in the observed structural and dynamic characteristics.

We start with PT-TT oligomers in vacuum, CB, and DIO environments. In all environments, the conformations quickly adopt all-A configurations regardless of the starting conformation (Figures 3.17 through 3.21). The results are consistent with the PES, especially the rotation between PT and TT groups (green), where there is a larger energetic barrier to resist reorientation and a stronger energetic driving force to the all-A configuration. However, this is not to say that these torsions are not dynamic: For instance, the DTS-PT dihedral (red) can undergo reorientation when in CB, though the structure maintains a strong preference for the A conformation in DIO (Figure 3.18); these differences are an indication of the explicit nature of the interactions with the solvent and kinetic factors, which will be discussed in the next section. The flexibility to change from A or S conformations is also to be noted: Shallower PES minima correlate to more widespread scatter near 0° and 180° (red) whereas a tighter curvature of the minima reveals a narrower spread (green).

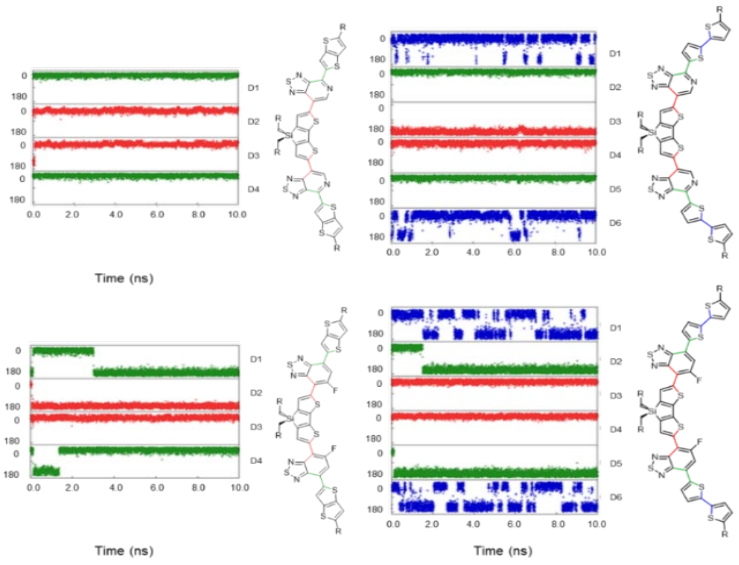

Figure 3.17 Dihedral angle analyses carried out on the MD simulations of the isolated molecules at vacuum, with the colors red, green, and blue representing the torsions moving from central core to the periphery of the oligomers in respective order.

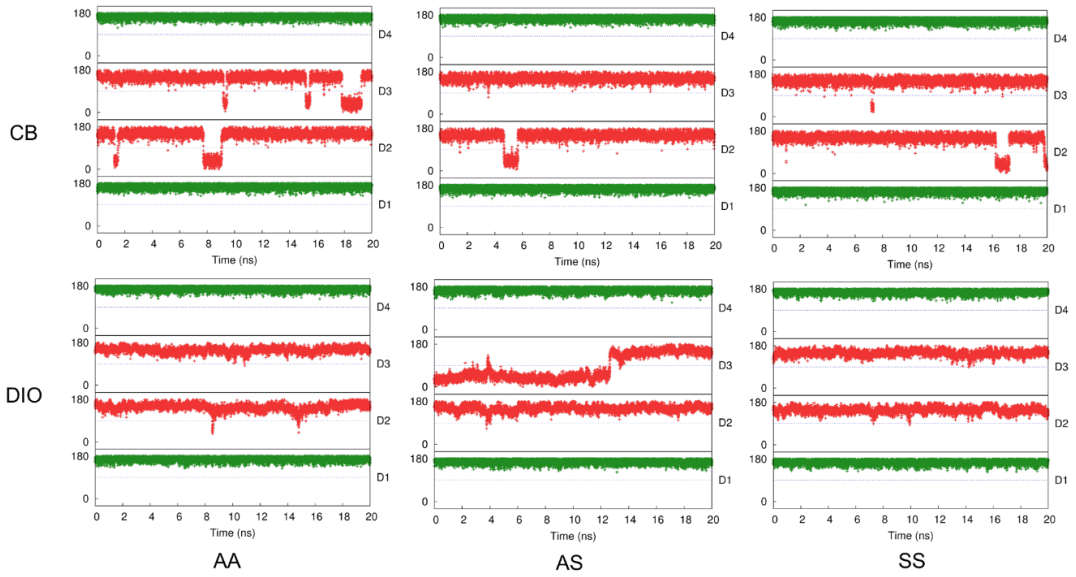

Figure 3.18 Calculated dihedral angles along simulation time for isolated PT-TT in infinite dilution in CB and DIO solutions. The starting configurations for the simulations are shown in the bottom, with the AA, AS, and SS notation referring to the initial conformation of the innermost dihedral angles. Results are shown from 20 ns of an NPT-PR simulation. Red represents the DTS-acceptor rotation and green represents the acceptor-TT rotation.

For PT-biTh in CB, the dynamics of the inner-most dihedral angles are quite similar (Figure 3.19) to those of PT-TT, though they do show a larger tendency to spend longer times in the S conformation. The outermost torsion of the biTh group (blue) showcases a large propensity for reorientation; the PES for biTh showed the lowest barrier height and widest curvature of the minima of all structures considered here. A similar, but muted, trend is observed for DIO, where again the solvent appears to prevent molecular rearrangement.

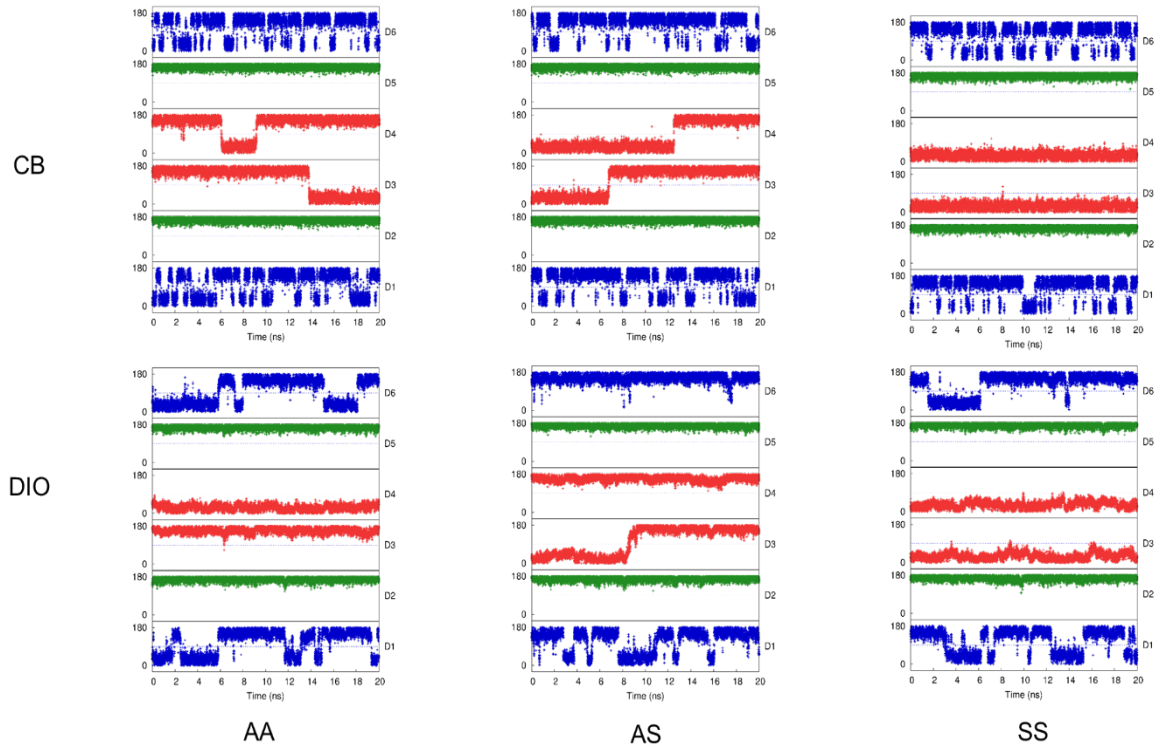

Figure 3.19 Calculated dihedral angles along simulation time for isolated PT-biTh in infinite dilution in CB and DIO solutions. The starting configurations for the simulations are shown in the bottom, with the AA, AS, and SS notation referring to the initial conformation of the innermost dihedral angles. Results are shown from 20 ns of an NPT-PR simulation. Red represents the DTS-acceptor rotation and green represents the acceptor-TT rotation.and blue represents the torsion between the thiophene units of biTh.

Moving on to the FBT-containing systems, we observe an increase of the dynamic behavior, especially in CB (Figures 3.20 and 3.21), as might be predicted by the shallower PES with smaller barrier heights and wider minima curvatures for fragments with this acceptor. We also note that shallower energetic and dipole moment landscapes were previously reported for FBT linked oligomers, consistent with the wider dispersion of rotational conformations in solution.[9] As with the PT-containing structures, DIO stabilizes the initial conformations used at the onset of the simulation, and generally limits the ability of the oligomers to change conformation. We hypothesize that the DIO preferentially interacts with the alkyl chains on the DTS and peripheral donor moieties, preventing the moieties from changing their orientation.

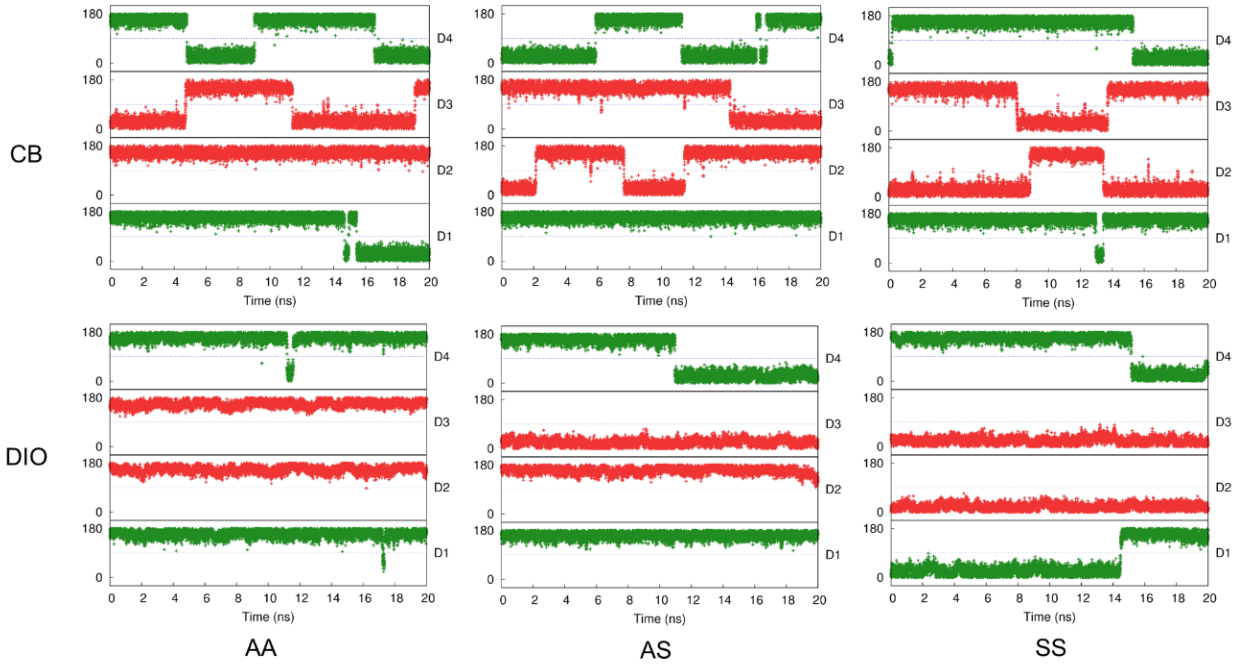

Figure 3.20 Calculated dihedral angles along simulation time for isolated FBT-TT in infinite dilution in CB and DIO solutions. The starting configurations for the simulations are shown in the bottom, with the AA, AS, and SS notation referring to the initial conformation of the innermost dihedral angles. Results are shown from 20 ns of an NPT-PR simulation. Red represents the DTS-acceptor rotation and green represents the acceptor-TT rotation.

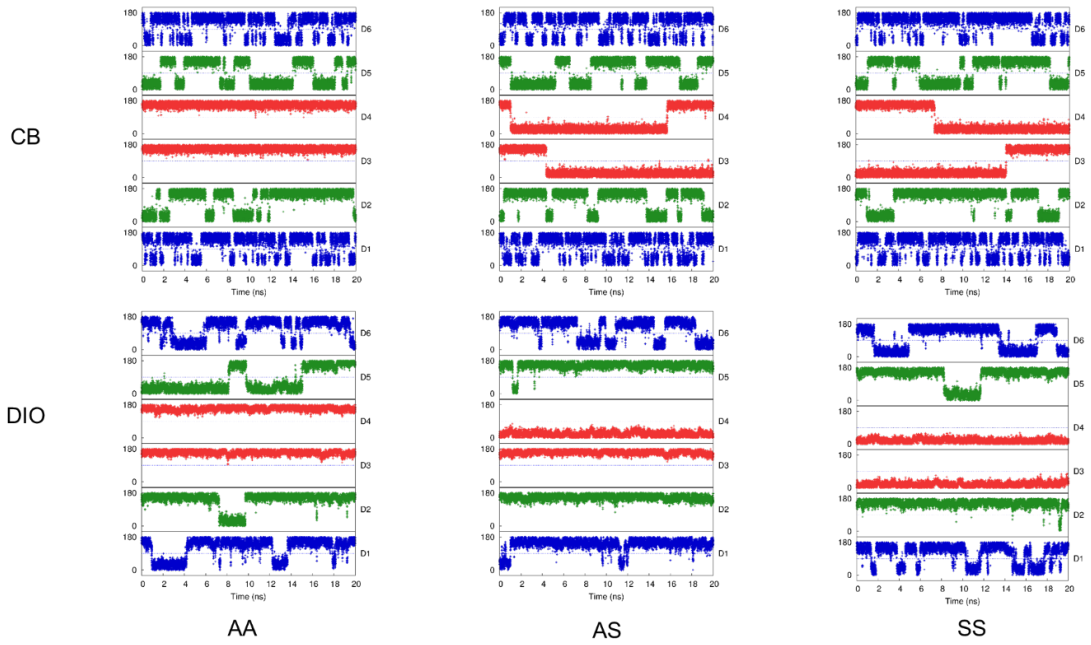

Figure 3.21 Calculated dihedral angles along simulation time for isolated FBT-biTh in infinite dilution in CB and DIO solutions. The starting configurations for the simulations are shown in the bottom, with the AA, AS, and SS notation referring to the initial conformation of the innermost dihedral angles. Results are shown from 20 ns of an NPT-PR simulation. Red represents the DTS-acceptor rotation and green represents the acceptor-TT rotation.and blue represents the torsion between the thiophene units of biTh.

In summary, the overall rotational dynamics of the four oligomers in solution are mainly associated with the dihedral barrier heights determined from the PES. The noncovalent close contacts may possibly contribute towards minimizing the rotational flexibility about the vicinity of A or S orientations but are clearly insignificant in strength to “lock” particular conformations in solution. Interestingly, in DIO, the overall propensity for conformational interchange is significantly quenched. Therefore, the work of DIO as a processing additive can be envisioned partly as a rotational conformational

stabilizer for the oligomers during solvent drying, that could in turn minimize the conformational disorder.

3.3.6 Accounting for the inter-oligomer interactions: Effects on conformational preferences in concentrated solutions

We now turn to solutions where oligomers can interact with each other to further explore how a more concentrated solution environment will impact oligomer conformational preferences and the tendencies of the oligomers to aggregate. Before delving into concentrated systems, we first establish how the solvent impacts inter-oligomer interactions via potential-of-mean-force (PMF) simulations in vacuum, CB, and DIO.

For the vacuum simulations, all four oligomers show a large intermolecular interaction energy of about 20 kcal mol^{-1} at ~0.4 nm intermolecular center-of-mass (COM) distance. However, when the molecules are solvated in CB and DIO, the interaction profiles change substantially (Figure 3.22). In CB, the four oligomers still present an attractive interaction well at ~0.4 nm, suggesting a likelihood to aggregate in solution. In DIO, however, the interaction profile is either non-interacting or repulsive, suggesting that aggregation will not be favored. We speculate that this may be related to the mostly alkyl-like nature of DIO that, again, preferentially solvate the pendant alkyl chains of the oligomers.

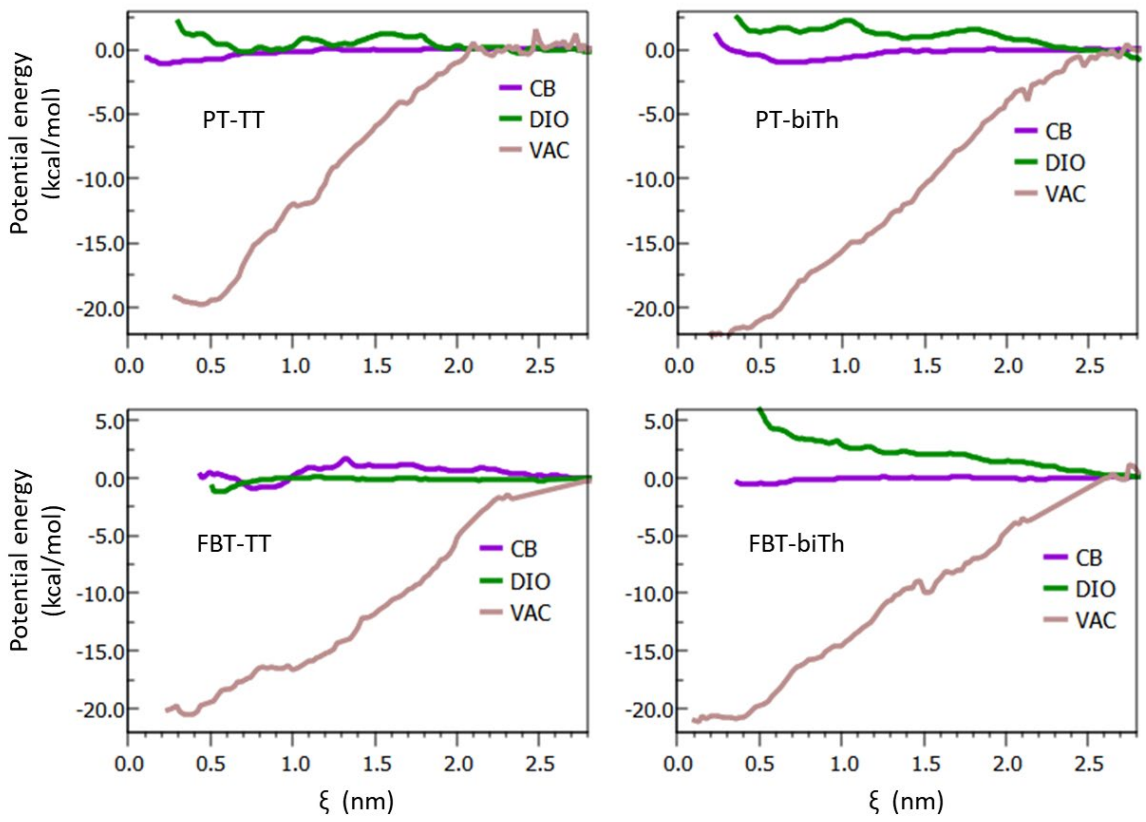

Figure 3.22 Potential of mean force (PMF) profiles determined for the four oligomers in solvent and vacuum environments, where the intermolecular backbone distance (ξ) is the reaction coordinate.

We now focus on simulations of solutions that are 2% by weight [2% w/w] or ~22 mg/mL oligomer. These are quite concentrated solutions, chosen as such not only to represent experimental supersaturation conditions,[9] but also to ensure aggregation on the timescale of the MD simulations. We calculate averaged dihedral angle per solute molecule in the solution for all oligomer systems. To reveal the time-averaged dihedral angle profiles for the oligomer backbones, kernel density estimated (KDE) distribution analyses are used (Figure 3.23 through 3.29).

For PT-TT, as seen for the isolated oligomer, the KDE distributions imply strong preference for each torsion taking the A conformation (Figure 3.23 and 3.24). The narrow widths around this conformation indicate limited oligomer rotation (especially for the dihedrals shown in green). These results suggest that PT-TT maintains a rigid structure in both CB and DIO solutions, regardless of the presence of other oligomers in solution or the solvent molecules themselves. On the other hand, PT-biTh in CB does reveal more breadth of the inner-most torsions about the A and S conformations (Figure 3.23 and 3.25), consistent with the variations observed for the isolated oligomer simulations. In DIO, however, the A conformations are more favorable. As expected, there is a broad dispersion of the torsion among the thiophene rings of the biTh group.

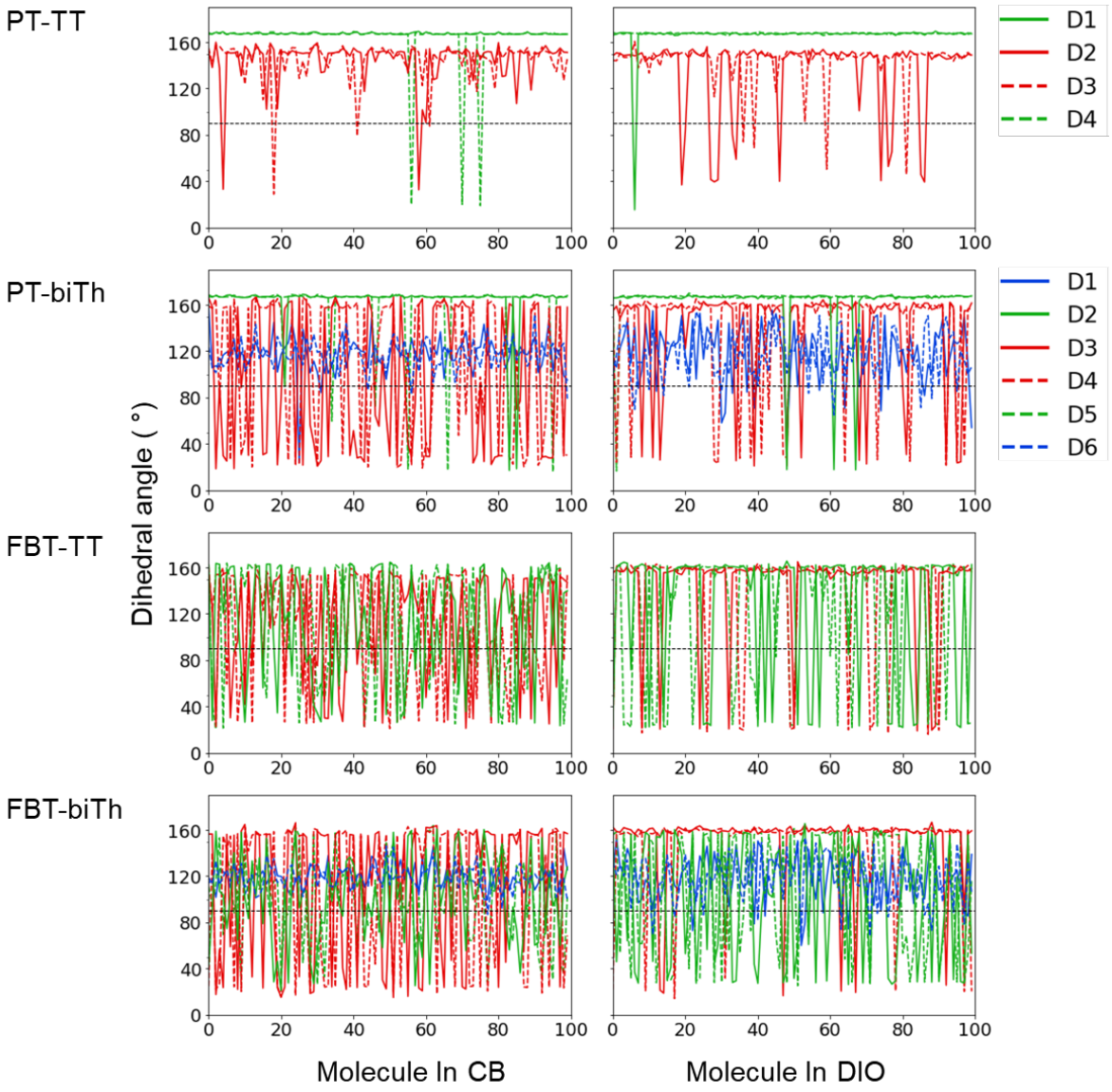

Figure 3.23 Time averaged dihedral angles (from the last 10 ns) of the oligomers in the two solvents 2% (w/w) for the 100 solute molecules. Only the AAAA starting configurations are shown for clarity. Dotted black horizontal lines indicate the 90° angle.

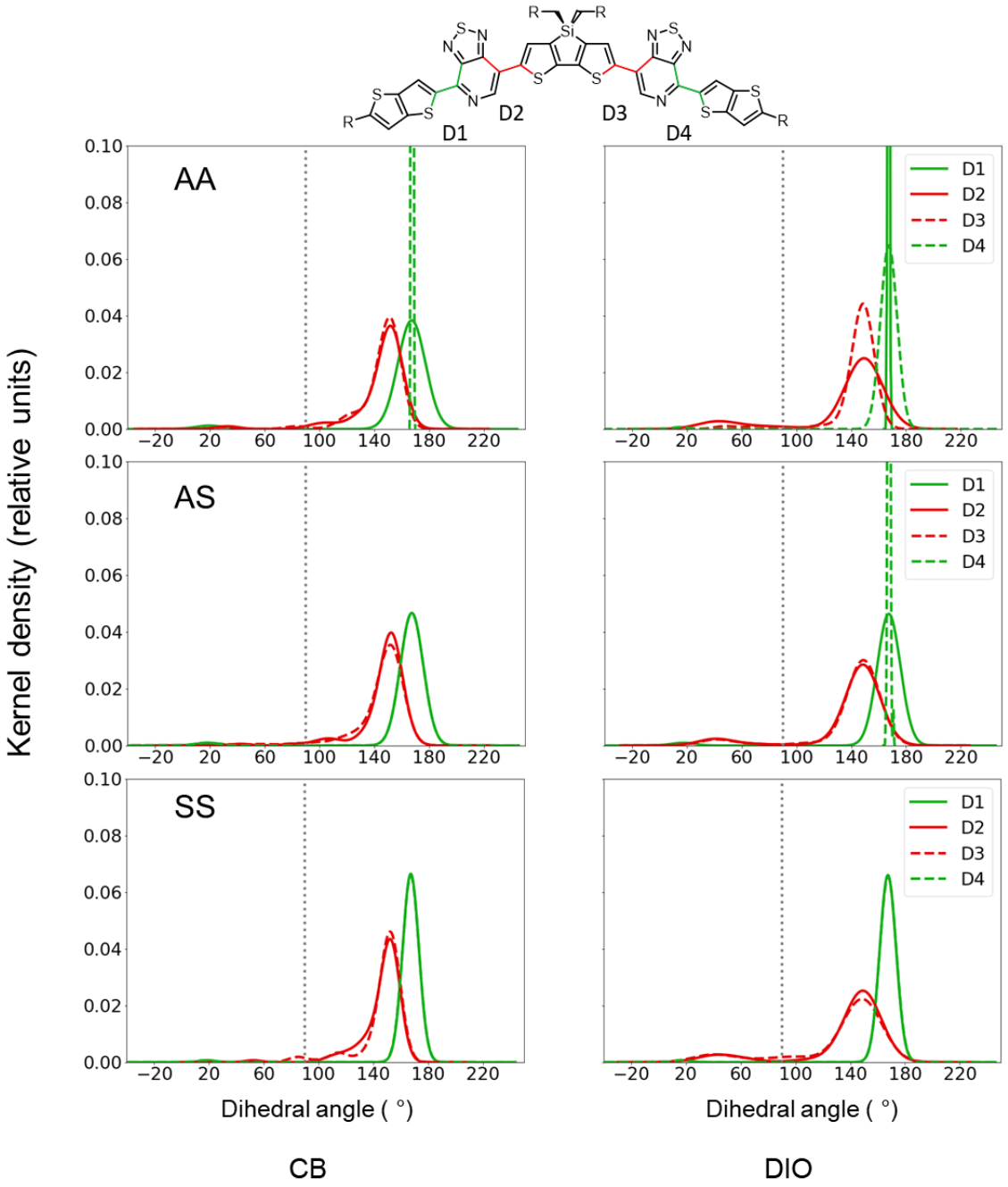

Figure 3.24 Time-averaged dihedral angle KDE distributions of the dihedral angles for the 100 solute molecules of PT-TT in 2% (w/w) CB or DIO solutions. The starting configurations for the simulations are shown in the far-right column, with the AA, AS, and SS notation referring to the initial conformation of the inner-most dihedral angles. Results are determined from the last 10 ns of 50 ns NPT-PR simulations.

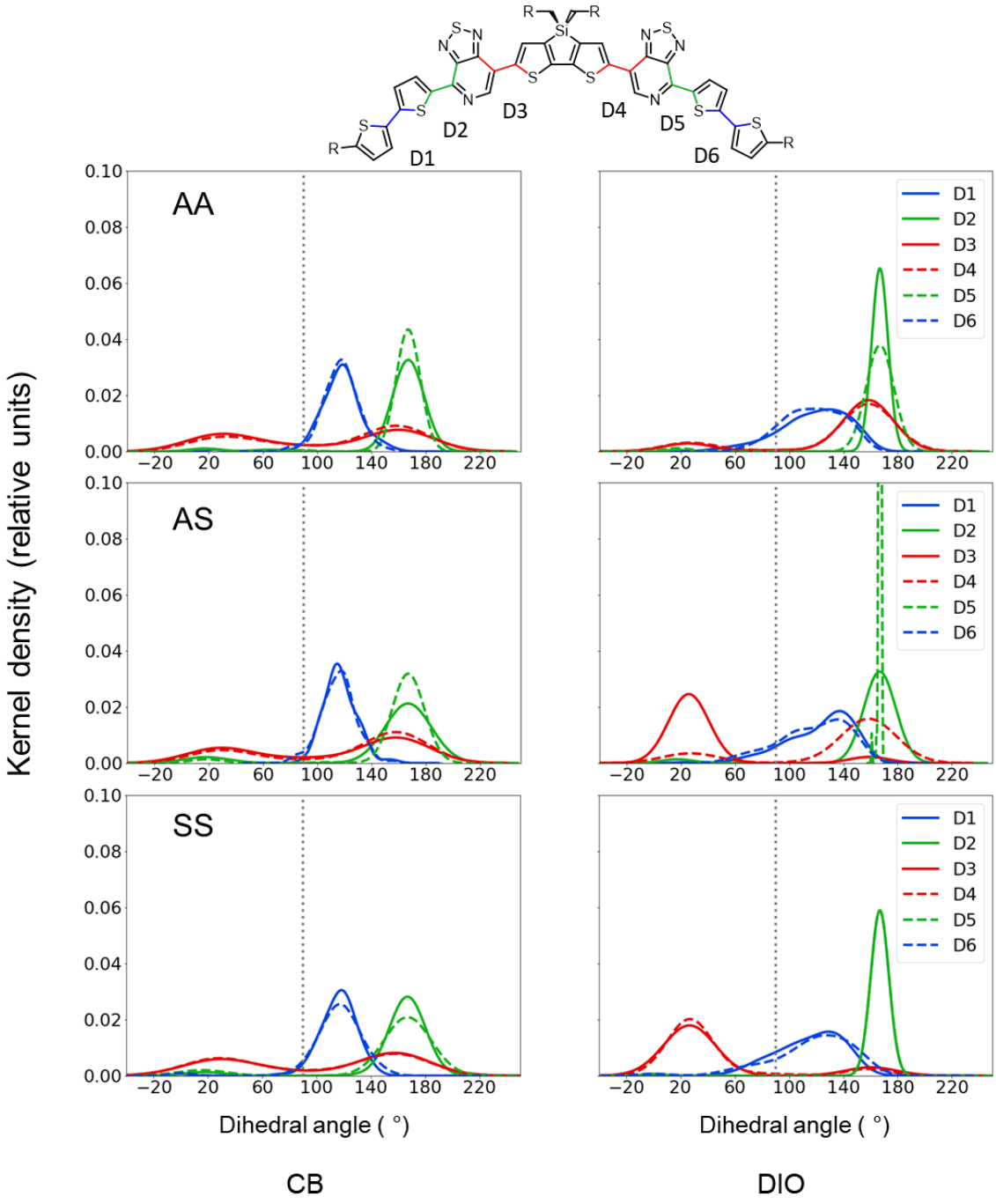

Figure 3.25 Time-averaged dihedral angle KDE distributions of the dihedral angles for the 100 solute molecules of PT-biTh in 2% (w/w) CB or DIO solutions. The starting configurations for the simulations are shown in the far-right column, with the AA, AS, and SS notation referring to the initial conformation of the inner-most dihedral angles. Results are determined from the last 10 ns of 50 ns NPT-PR simulations.

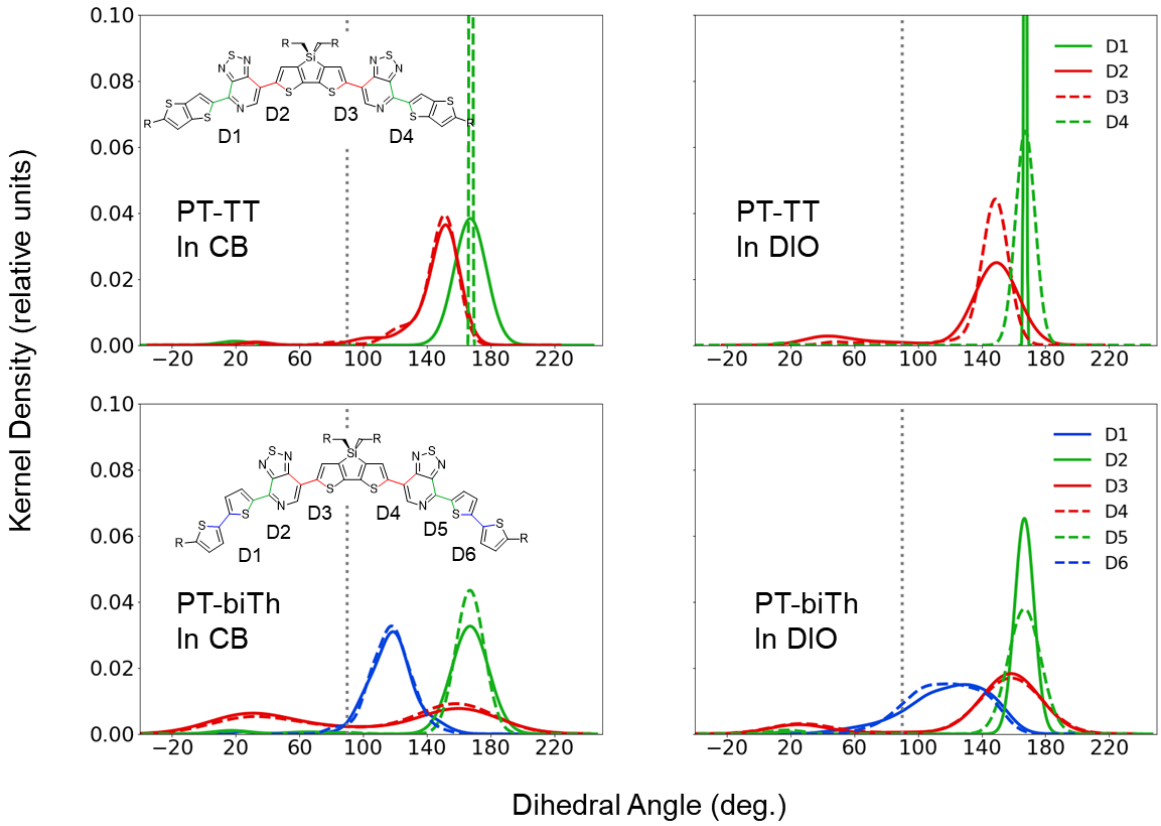

Figure 3.26 Dihedral angle KDE population analyses carried out for (2% w/w) PT-TT and PT-biTh in comparison. The figures indicate the most representative instances among the three modeled conformational variants.

In comparison Figure 3.26 shows the decreased rotational flexibility and tendency for conformational reorientations between A and S shown by DTS-PT rotation in both CB and DIO environments. Moving from the center to the periphery, the rotational activity is increased.

Turning to the FBT-containing oligomers, the KDE profiles are distinctly different when compared to their PT analogs. In CB, both FBT-TT and FBT-biTh torsion distributions are highly dispersed, with no dependence of the configuration based on the initially solvated conformations (Figures 3.27 through and 3.29). The nearly identical,

disperse KDE profiles that are observed for the different starting oligomer conformations again reveal limited-to-no influence of the noncovalent intermolecular interactions in CB. In DIO, there is some preserved dependence on the initial conformation used in the simulations, but this again is more a factor of solvent–oligomer interactions as opposed to the chemical nature of the oligomer providing a means to lock in a particular structure.

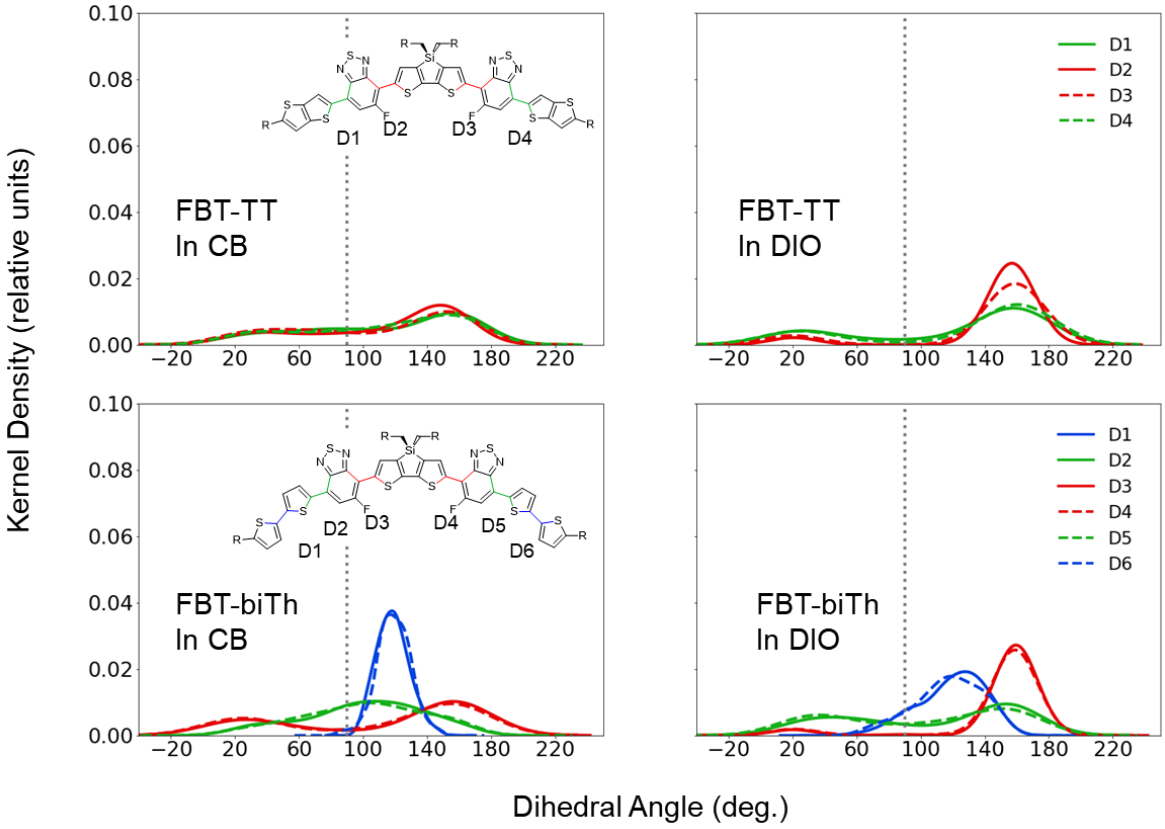

Figure 3.27 Dihedral angle KDE population analyses carried out for (2% w/w) FBT-TT and FBT-biTh in comparison. The figures indicate the most representative instances among the three modeled conformational variants of the inner-most dihedral angles. Results are determined from the last 10 ns of 50 ns NPT-PR simulations.

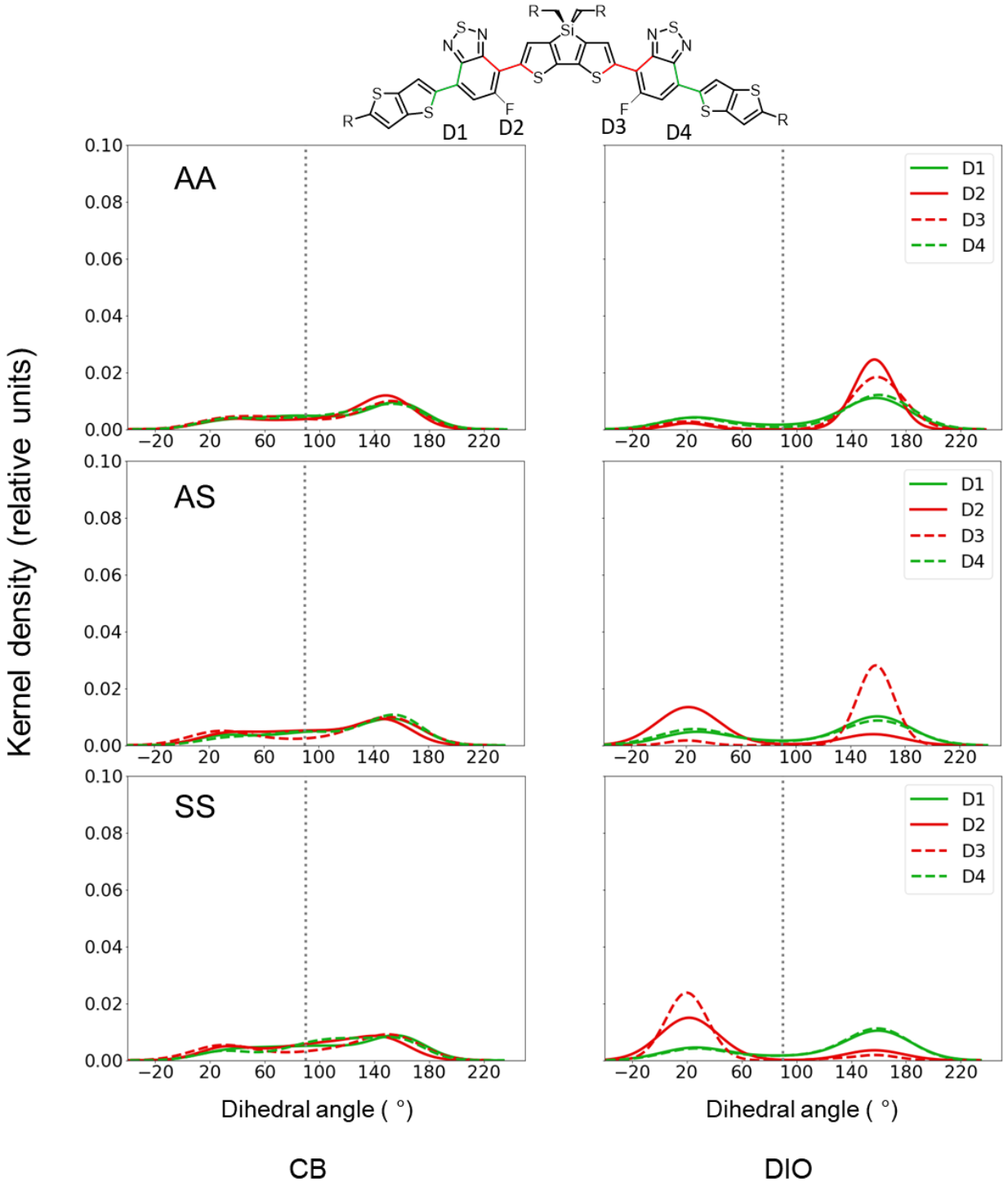

Figure 3.28 Time-averaged dihedral angle KDE distributions of the dihedral angles for the 100 solute molecules of FBT-TT in 2% (w/w) CB or DIO solutions. The starting configurations for the simulations are shown in the far-right column, with the AA, AS, and SS notation referring to the initial conformation of the inner-most dihedral angles. Results are determined from the last 10 ns of 50 ns NPT-PR simulations.

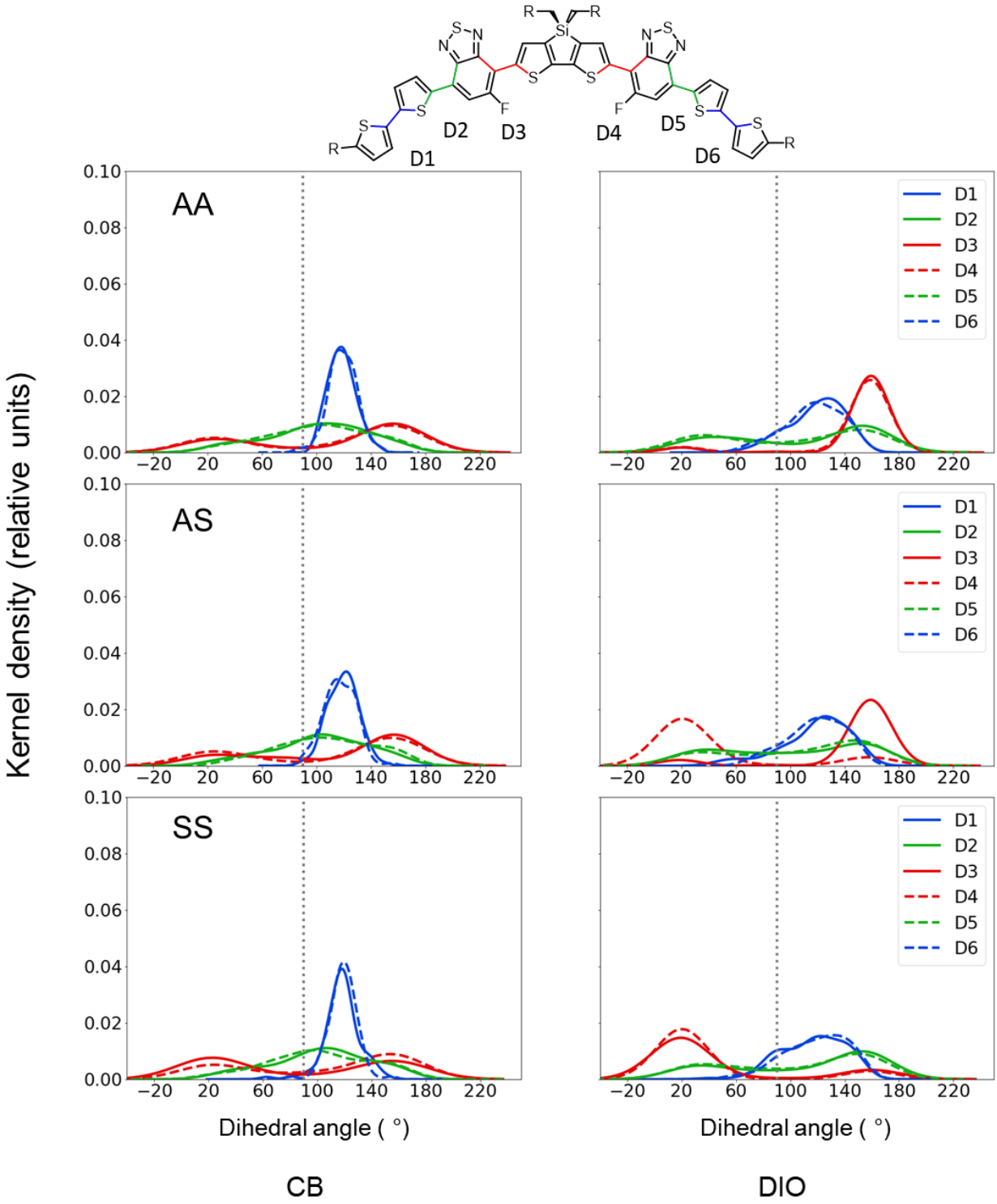

Figure 3. 29 Time-averaged dihedral angle KDE distributions of the dihedral angles for the 100 solute molecules of FBT-biTh in 2% (w/w) CB or DIO solutions. The starting configurations for the simulations are shown in the far-right column, with the AA, AS, and SS notation referring to the initial conformation of the inner-most dihedral angles. Results are determined from the last 10 ns of 50 ns NPT-PR simulations.

3.3.7 From conformational preferences to aggregation

In addition to revealing the degree of conformational diversity to be expected for the four oligomers in the two solvents, these simulations also provide information as to the formation of aggregates, and the oligomer conformations within those aggregates. We recall that the simulations each have 100 oligomers in the solvent at 2% w/w. Given the relatively short timescale of the simulations, it should not be expected that the full suite of events related to crystal nucleation and growth will be observed. Rather, we use these results to demonstrate how aggregates / nucleates that form in solution are impacted by the conformational diversity of the oligomers.

In CB, the four oligomers each show a tendency to form small aggregates (of up to four oligomers per aggregate). The situation in DIO is dramatically different, where almost no aggregate formation is observed. Recall that the PMF simulations revealed that the oligomers would have no or repulsive interactions in DIO, and hence it is not surprising that aggregates did not form in the timeframe of the simulations. Further, the observation that the oligomers do not form aggregates in DIO is consistent with experimental results that FBT-biTH:PCBM films deposited from a CB:DIO co-solvent are less dense than those derived from CB alone.[45] Given that no aggregates are observed to form in DIO, we focus solely on the CB simulations.

Before turning to the remaining computational analyses, we review the relative degree of order as determined by GIWAXS for thin films of these oligomers deposited from CB.[9] Recall that each oligomer has a *D'-A-D-A-D'* architecture, where the *D'* are either biTh or TT and the *A* are PT or FBT. As one might expect, removing the extra torsion (potential for conformational [entropic] disorder) on going from biTh to TT led to

an overall increase of the thin-film order. Changing from PT to FBT also led to an increase in thin-film order. The latter, given the results presented so far, *i.e.,* the PT-containing oligomers have overall lower conformational disorder in the solution simulations compared to those with FBT, may seem counter-intuitive. As we will see, however, too large conformational restriction can lead to an overall smaller packing order.

Radial distribution function (RDF, also referred to as pair correlation function) and conformer population analyses are combined to determine the relationships among the oligomer conformations and aggregation. Note that the RDF analyses (Figure 3.30) were carried out explicitly for the center of mass of oligomer backbones. Overall, large RDF peaks exist at ~0.30 - 0.45 nm for the oligomer aggregates in CB, while no structural features are found for the oligomers in DIO. These distances are consistent with the PMF simulations. Following the intensity of the first peak, the RDF follows FBT-TT > PT-TT > PT-biTh > FBT-biTh. FBT-TT and PT-TT each have a single, large RDF peak near ~0.35 nm, PT-biTh has a distinct two peak profile, while FBT-biTh has a broader, low-intensity RDF.

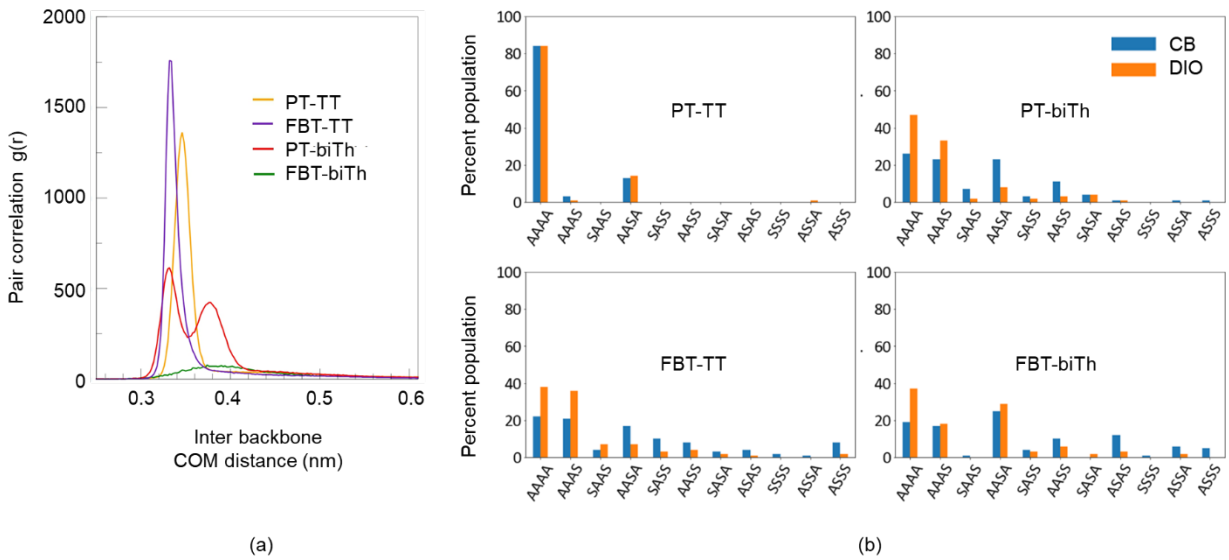

Figure 3.30 Oligomers in 2% concentrated systems during the last 40 to 50 ns analysis time in terms of a). RDF of the center of mass distance of the backbones, b). the adopted conformational populations for the modeled oligomers with AA innermost dihedral starting configuration, excluding biTh end group rotation for simplicity.

For PT-TT, the sharp and relatively tall RDF is indicative of only one type of aggregate packing being present; that only one packing configuration is preferred is consistent with differential scanning calorimetry (DSC) measurements that show a single thermal transition, and considerable thin-film packing order in semi-crystalline thin films observed with GIWAXS.[9] Time-averaged conformational population analyses confirm that PT-TT largely favors the all-A orientation (AAAA), with trace amounts of AAAS also present (Figures 3.30 and 3.31), regardless of the initial conformation induced for the MD simulation run; these results are consistent with the narrow peaks derived from the KDE analyses. Further, similar aggregation profiles are observed for the three starting conformations of the MD systems, with all three systems leading to quite similar ratios of solvated:aggregated oligomers at 70:30 (that of FBT-TT is roughly 80:10 in comparison,

but with significant changes corresponding to the initial configuration, see Figure 3.32). We also observe that the same conformations are populated similarly by both aggregated and solvated members (Figure 3.33), suggesting the limited rotation of oligomer backbones.

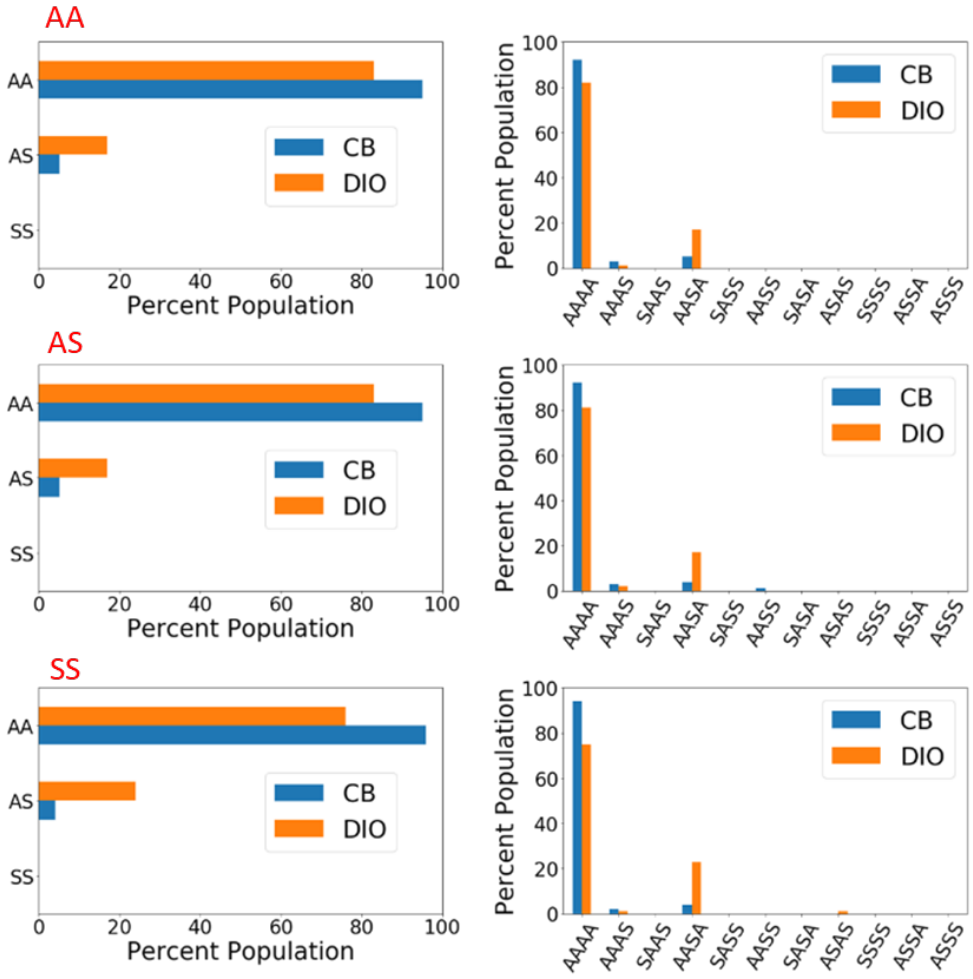

Figure 3.31 Time-averaged (from the last 10 ns of a 50 ns simulation) conformational populations of 2% (w/w) PT-TT in terms of all dihedral positions (right column) and only considering innermost dihedrals (left column). AA, AS, and SS notation in red color refer to the initial conformation of the inner-most dihedral angles.

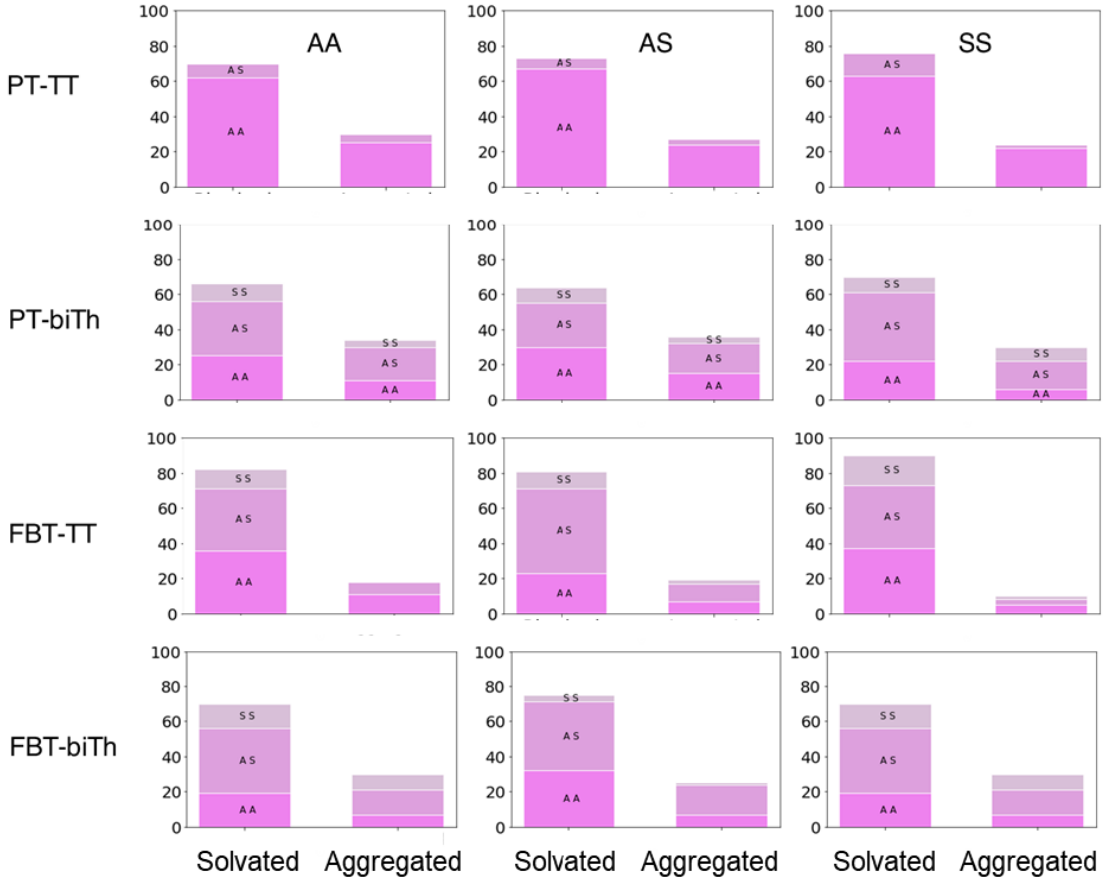

Figure 3.32 Conformational population analysis of 2% (w/w) oligomers in CB, evaluated separately for solvated vs. the aggregated members resolved through trajectory averaged RDF cut-offs (0.4 nm) for systems with inner-most dihedrals in AA, AS and SS starting conformations used at the outset of the simulations.

Figure 3.33 Conformational population analysis of 2% (w/w) oligomers in CB, evaluated separately for fully solvated vs. the aggregated members resolved through trajectory averaged RDF cut-offs (0.4 nm) comparing PT-TT and PT-biTh systems. AA, AS and SS indicate the starting conformations at the outset of the simulations.

For PT-biTh, two RDF peaks are observed (Figures 3.30). This suggests the presence of two different aggregation types. Again, this is consistent with DSC results that show multiple transition temperatures, indicative of polycrystallinity, and decreased thin-film order compared to PT-TT as determined by GIWAXS.[9]

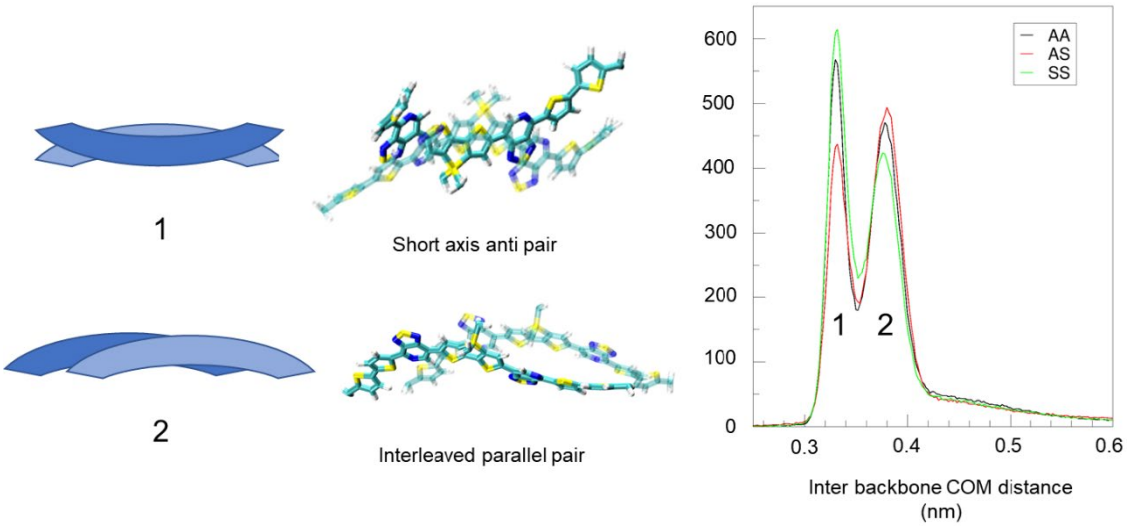

Figure 3.34 RDF pair correlation function peaks for PT-biTh and the corresponding major aggregation types. AA, AS, and SS represent the starting conformational population in terms of the innermost dihedrals.

Visualization of the trajectories reveals two types of interactions: Short-axis anti-pairs and parallel-interleaved pairs (Figure 3.34) that correspond with peak one and two, respectively. Population analyses for PT-biTh reveal similar populations adopted in the CB solution, with AA and AS innermost conformations dominating, and some SS (Figure 3.35). We recall that SS conformations are high energy and represent the least populated conformations in the previous DFT/Boltzmann theory analyses.[9]

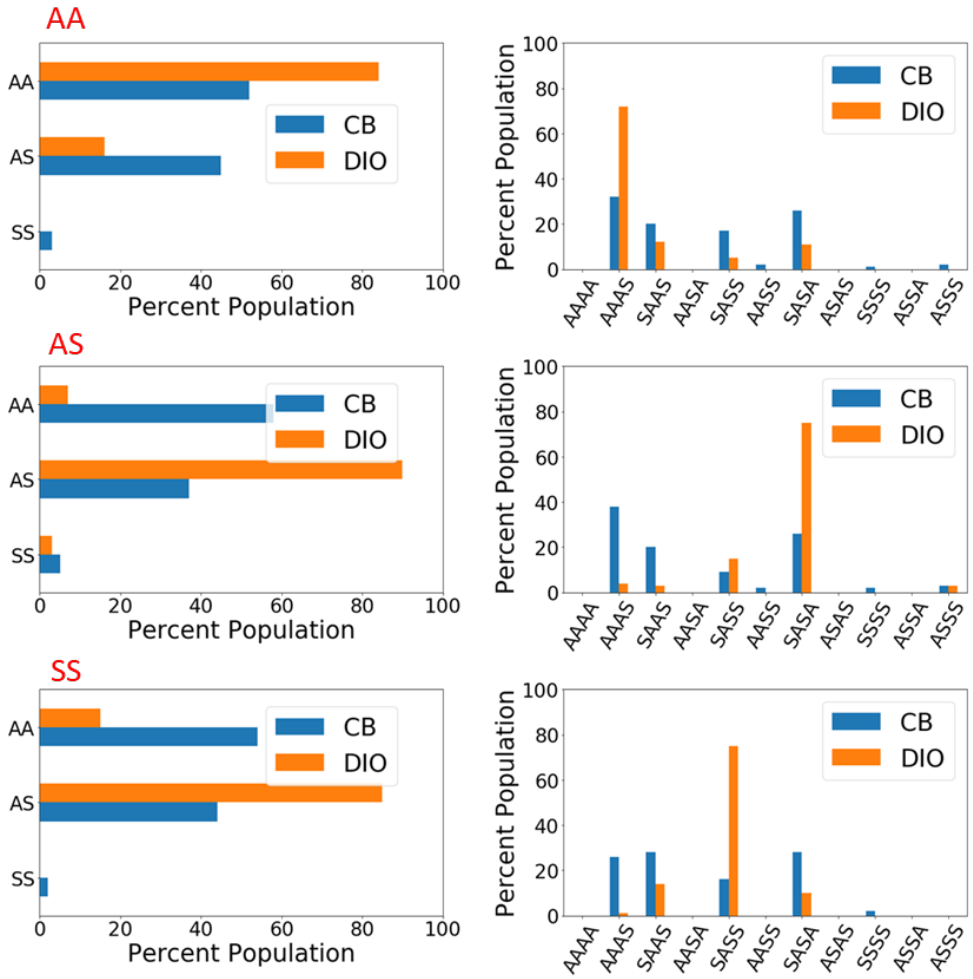

Figure 3.35 Time-averaged (from the last 10 ns of a 50 ns simulation) conformational populations of 2% (w/w) PT-biTh in terms of all dihedral positions (right column) and only considering innermost dihedrals (left column). AA, AS, and SS notation in red color refer to the initial conformation of the inner-most dihedral angles.

The population analyses of the FBT oligomers in CB (Figures 3.36 through 3.37) show clear indication of almost all the conformations being populated during the analysis time (40 to 50 ns). This high population of different conformers is consistent with the low

barrier heights in the PES for FBT linked oligomers, and also agrees with the previous DFT/Boltzmann analyses.[9]

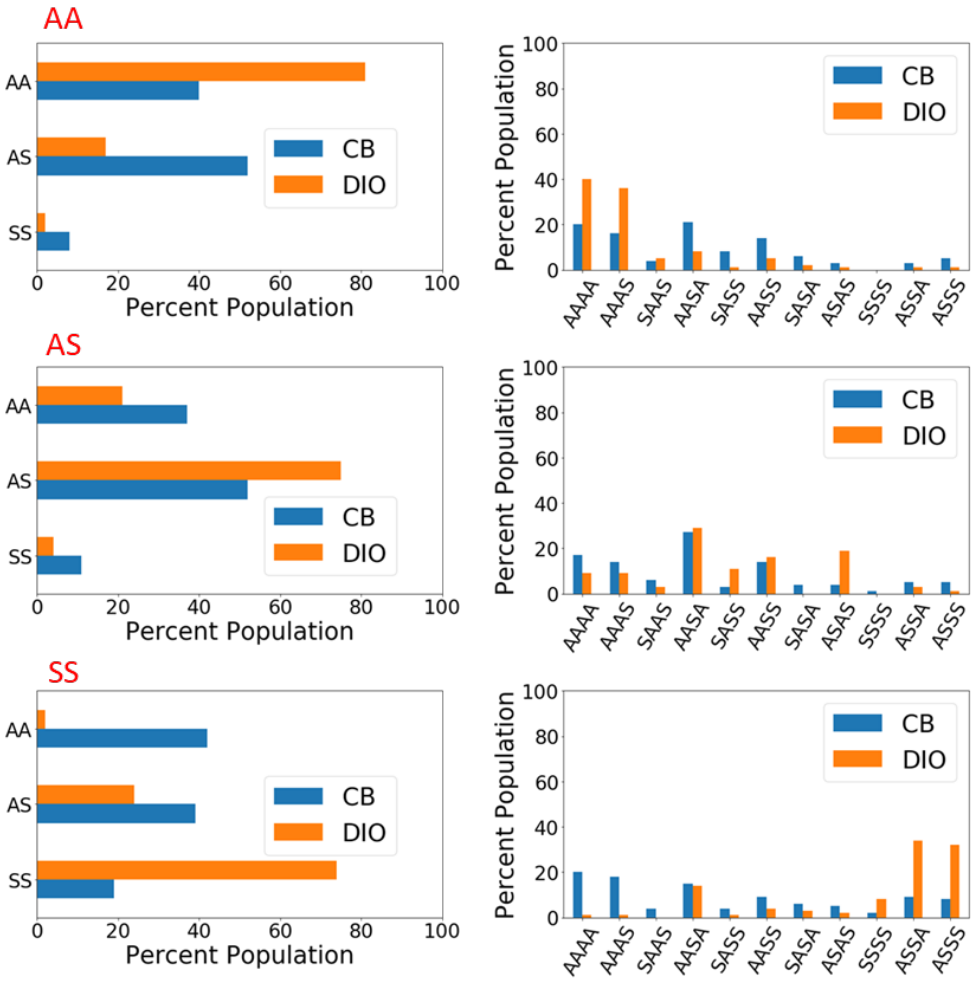

Figure 3.36 Time-averaged (from the last 10 ns of a 50 ns simulation) conformational populations of 2% (w/w) FBT-TT in terms of all dihedral positions (right column) and only considering innermost dihedrals (left column). AA, AS, and SS notation in red color refer to the initial conformation of the inner-most dihedral angles.

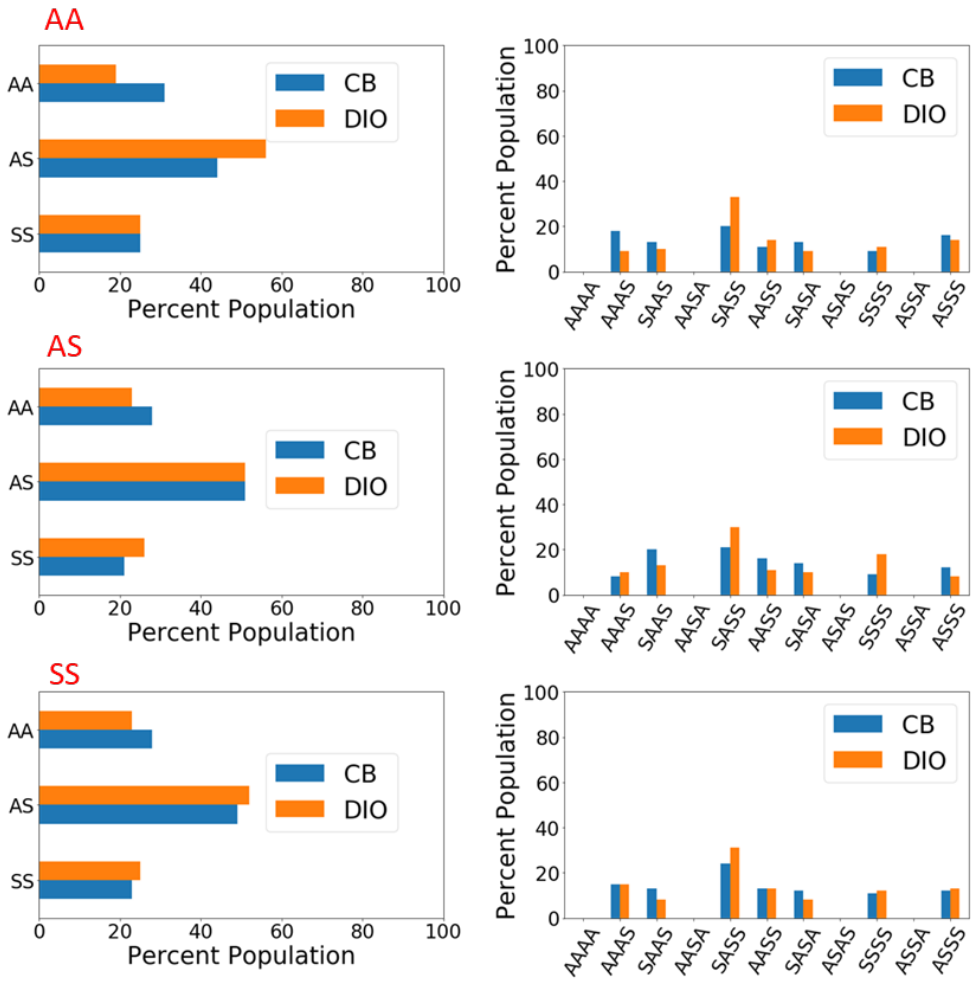

Figure 3.37 Time-averaged (from the last 10 ns of a 50 ns simulation) conformational populations of 2% (w/w) FBT-biTh in terms of all dihedral positions (right column) and only considering innermost dihedrals (left column). AA, AS, and SS notation in red color refer to the initial conformation of the inner-most dihedral angles.

Note that this effect can be more prominent in the higher dielectric constant of CB (see PES for torsions in comparison – Figure 3.4). For FBT-TT specifically, we see a relatively tall, single, and narrow RDF correlation peak at ~0.35 nm backbone separation, suggesting only a single type of backbone interaction (Figure 3.30), a result in line with DSC and temperature dependent XRD. FBT-TT shows the highest morphological order and crystallinity among the four oligomers, in terms of both as-cast and blend films.[9]

Visualization of the FBT-TT trajectories reveals short-axis anti pairs (and triples) of oligomers; notably, the crystal structure of FBT-TT reports the same type of interactions, but only with antisymmetric (AASA) conformations present.[9] However, in solution we observe both AA and AS with some of SS contributing to the aggregates (Figure 3.36). Considering these two scenarios, we hypothesize that unfavorable conformations that may be kinetically trapped in early stages of aggregation can disengage from the aggregate and reorient to accommodate more favorable interactions. Hence, the low energy barriers described in the PES aid in providing the capacity to form well-ordered packing configurations, a proposal similarly made in like MD studies of related molecules.[46] We also note that, compared to the other oligomers, FBT-TT demonstrates higher solvation characteristics, with as high as 80% of the oligomers not being aggregated (or 20% being aggregated) at the end of the current simulations (Figure 3.32).

For FBT-biTh in CB, we observe solvation up to about ~70% on average, but again with the highest value (75%) for the more linear (innermost) AS starting conformation. RDF analyses show a broad correlation peak for FBT-biTh. Visualizations of the trajectories reveal several types of interacting pairs present, leading towards more disordered aggregates as well as frequent switching of the oligomers among aggregated to solvated forms. FBT-biTh aggregates are comprised of either two or three oligomers, displaying different packing configurations: anti-pairs, interleaved pairs, and pairs associated with each other through slipped backbone interactions. We again observe that biTh end group in place of TT can impart more rotational character on the innermost dihedral positions as discussed in the case of PT-biTh. Averaged conformational populations of aggregated members in CB show dependency on the starting

conformations that is suggestive of the wide conformational stability shown by FBT-biTh (3.37 and 3.38).

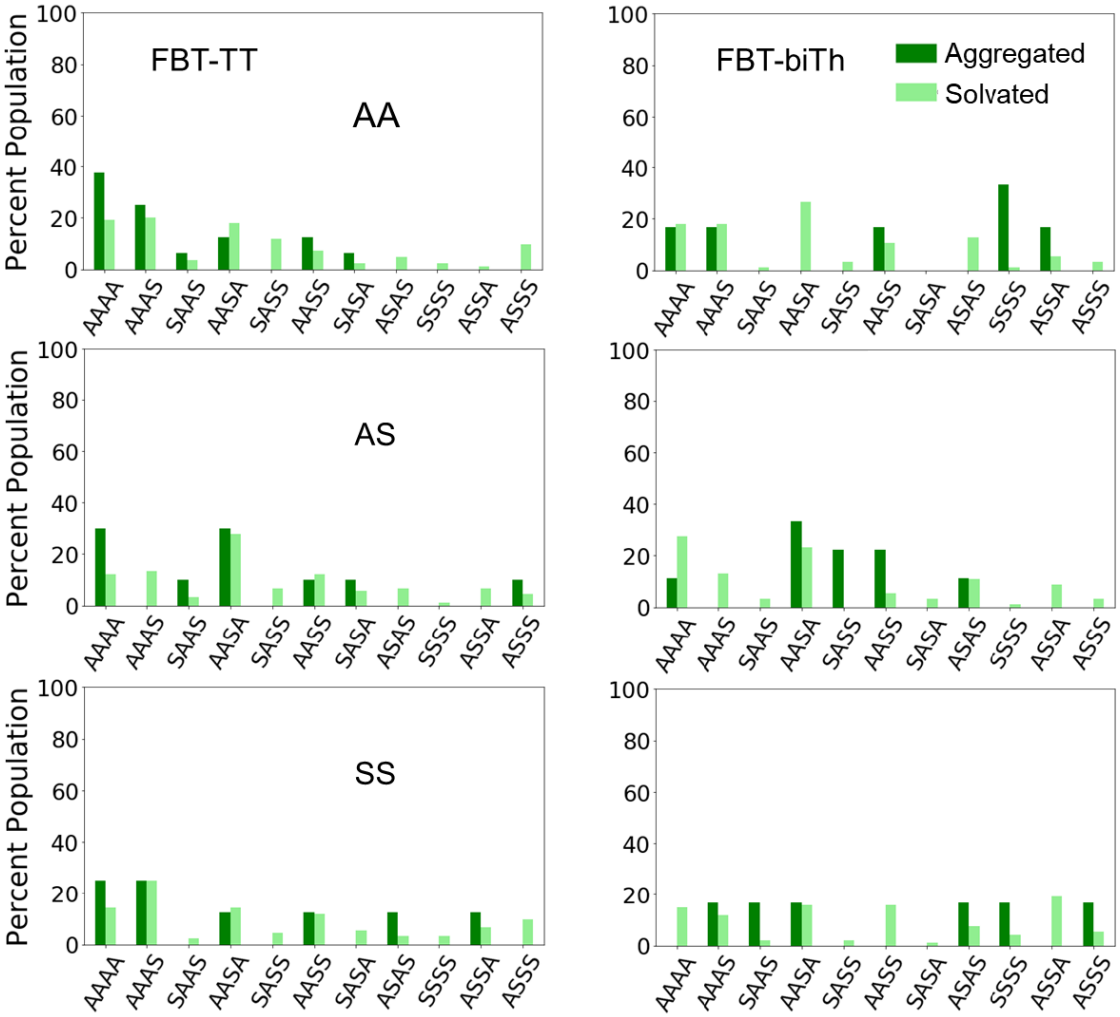

Figure 3.38 Conformational population analysis of 2% (w/w) oligomers in CB, evaluated separately for fully solvated vs. the aggregated members resolved through trajectory averaged RDF cut-offs (0.4 nm) comparing FBT-TT and FBT-biTh systems. AA, AS and SS indicate the starting conformations at the outset of the simulations.

3.4 Conclusions

In this investigation, we make use of quantum-chemical calculations and MD simulations to explore the impacts of intramolecular noncovalent interactions in *D-A* oligomers on the conformational structures and dynamics. A key finding is that the relatively weak noncovalent interactions, *e.g.*, N•••H, F•••H, S•••F, S•••N, often considered to act as conformational locks, do not offer such capacity. Rather, it is the degree of delocalization of the π electron density across the bridging single bonds among the *D* and *A* moieties that serves as a more important proxy to determine structure, at least from a static perspective. Though, we do note that caution should be considered when evaluating differences as to the degree of single-bond or double-bond character of this bridging bond as the differences can be quite small.[40]

MD simulations in different solvent environments reveal critical features related to oligomer dynamics and aggregation. Notably, the choice of solvent – here CB and DIO – can lead to distinctive tendencies for the oligomers to adopt particular conformations and, in the case of DIO, prevent aggregation. The solvent can influence both intramolecular and intermolecular interactions and should be considered as a crucial design parameter (beyond molecular structure) in thin-film development. Careful solvent optimization may also enable controlled polymorphic growth.[47] The MD results also reveal that oligomers that favor a particular conformation may actually lead to unfavorable aggregation – if the torsions among the moieties are too stiff and one conformation is favored, solvation will decrease and the capacity of the oligomers to adopt conformations that favor ordered growth over long distances will diminish (*e.g.*, consider the difficult solubility of rigid molecules such as pentacene and efforts to

enhance solubility and processing through the addition of flexibly alkyl chains). There is, of course, a fine balance to be had, as too much solvation or disorder / entropy (*e.g.*, amongst the thiophene moieties of biTh) will prevent the capacity to form aggregates and consistent thin film structures.

Overall, the results from this study provide an in-depth molecular-scale foundation that will assist in the design of pathways for kinetic and thermodynamic control of OSC morphology development through chromophore design and solvent optimization.

CHAPTER 4. CRYSTALLIZATION OF HERRINGBONE PACKED MOLECULAR CRYSTALS FROM SOLUTION

4.1 Introduction

Crystallization is a natural phenomenon that is of fundamental importance and practical relevance across chemistry as a science. In the pursuit of decoding the crystallization mechanisms of organic molecules, features of interest include the molecular chemistry and contributions from molecular shape anisotropy, which originate from non-unity aspect ratios between the molecular short and the long axes. Such anisotropy can impose profound impacts on molecular assembly pathways, producing an array of crystal packing configurations including herringbone, brickwork, slip-stack, and many other variants, both named and unnamed.[1-5] Moreover, organic crystals grow in faceted shapes, resulting from different growth rates along varied crystal faces, which serve to define the overall crystal morphology, i.e., the geometric shape.[4, 6, 7] Notably, these processes are not solely defined by the packing order, resulting from the noncovalent interactions exposed by a particular face of the crystal lattice, but they are often dynamically modulated by external processing conditions such as solution environment, temperature, and pressure etc., which can serve as important handles to tune process protocols for crystal design and growth.[8-11]

Here, our interest is to provide atomistic insights into the crystal growth of anisotropic organic molecules that contain no strong chemical directors (e.g., hydrogen bonds) in solution. We are particularly interested in understanding how crystals with the herringbone packing feature grow, especially given the wide-spread nature of this packing motif across organic crystals. In particular, we explore the growth of naptho[1,2-

b:5,6-b']dithiophene (NDT)[12] from supersaturated solutions via atomistic molecular dynamics (MD) simulations, choosing hexane and toluene-based solutions to simulate homoepitaxial (layered) growth on different crystal faces, namely the (100), (001), and (110) faces. The two solvent choices present distinctively different molecular environments for comparison: Toluene can be expected to be a more effective (good) solvent with favorable noncovalent interactions with that aromatic NDT, while the noncovalent interactions between hexane and the aromatic NDT are non-favorable for solvation, increasing the driving force for phase separation.[11] We make use of the constant chemical potential molecular dynamics (CμMD) algorithm by Perego et. al.[13] to simulate bulk solutions at constant supersaturation while mitigating finite size effects, which affect more traditional MD approaches[9]. We set as a baseline for our study to observe how crystallization is directed at the critical concentration (CC), i.e., the minimum supersaturation concentration at which the development of the growth-limiting surface(s) (i.e., the surfaces with high relative surface area; see Table 4.1) can prevail following the required critical nucleation event, i.e., stable 2D-nucleus formation on such a surface. This scenario allows us to observe crystallization mechanisms in the absence of interfering extrinsic effects, including molecular crowding, limitations associated with diffusion and the availability of molecules/mass transport, and surface rearrangement at the nucleating/growing region, all of which may introduce complications to the investigation. We then compare crystal growth under varied processing conditions, including solution supersaturation and temperature, to reveal useful insights to govern crystal nucleation and growth via tunable degrees of freedom.

Table 4.1 Steady state morphology of NDT crystal and relative surface areas predicted by the BFDH model

planes	{100}	{011}	{110}	{002}	{111}	{102}
Relative surface area	0.292	0.051	0.037	0.01	0.007	0.004

We provide reasoning behind the choice of NDT for our study is as follows,

1. NDT is a simple π-conjugated system with no strong crystallization directors, such as H-bonding, yet an extension from the previously studied smaller molecules including urea[10], isoniazid[14] and naphthalene.[15]
2. NDT exhibits a platelet like crystal morphology with $P2_1/C$ symmetry[12] therefore inversed planes are the same in terms of molecular faces, thereby simplifying the study in terms of the different major planes to be analyzed (Figure 4.1).

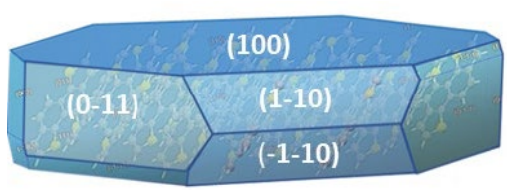

Figure 4.1 Crystal morphology of NDT (platelet) obtained through the BFDH model[16] using Mercury Advanced tools.[17]

4.2 Methods

All MD simulations were performed with the GROMACS 2019[18, 19] software suite interfaced with PLUMED 2.6.3 plugin[20-22] and using the OPLS-AA forcefield.[23]

Atom-centered partial charges were explicitly calculated using density functional theory (DFT) at the ωB97XD/6-31G(d,p) level[24-26] using the Charge Model 5 (CM5)[27] framework through the Gaussian 16 software suite.[28] The validity of the forcefield was confirmed (Table 4.2) by simulating an NDT crystal supercell structure and comparing the resulting crystal structure parameters with experiment.

Table 4.2 Lattice parameters extracted from the crystallographic information file (CIF) at cell measurement temperature of 293 K, and the parameters obtained from molecular dynamics (MD) simulations at the same temperature.

	a	b	c	α	β	γ
CIF	1.7973	0.74851	0.8244	90	93.482	1.7973
MD	1.7984	0.74899	0.8249	90	93.480	1.7984
Percentage difference	0.14%	0.06%	0.03%	0.00%	0.00%	0.14%

The leap-frog integrator was used as the time integrator with 2 fs time step value at 298 K. One NVT (constant number, N, volume, V, and temperature, T) and two NPT (constant number, N, pressure, V, and temperature, T) ensembles were used to obtain initial equilibrium of both crystal structures and concentrated solutions of NDT in hexane or toluene to simulate the bulk solution. Following the same procedure, initial systems with input structures containing desired bulk concentration in contact with the crystal were modeled and equilibrated using the GROMACS_solvate function. For NVT simulations, a velocity rescaling thermostat with a temperature coupling time of 0.1 ps

was used. For the two NPT simulations, firstly the Berendesen[29] and secondly the Parrinello–Rahman[30] barostat algorithms were used with 2.0 ps pressure coupling constant. The velocity rescaling thermostat was used for temperature coupling with coupling constant of 0.1 magnitude. Anisotropic compressibility of 4.5×10^{-5} bar was applied. Periodic boundary conditions were applied in all directions (X, Y, and Z) to all simulations with a spherical cutoff of 1.4 nm for both short-range van der Waals (vdW) interactions and for long-range electrostatic interactions, treated via particle-mesh Ewald (PME) method for improved accuracy. The LINCS (LINear Constraint Solver) algorithm[31] was used to constrain hydrogen bonds. Initial equilibration before production runs were run for 50 ns at the NPT ensemble with Parrinello-Rahman barostat before applying the chemical potential control procedure discussed in the next section. The second equilibration step using the CμMD procedure[13] was run under periodic boundary conditions in all laboratory X, Y, and Z directions, but with crystallization restricted using a solute density restraint at the interface (explained further in the SI) for 10 ns to achieve desired supersaturation levels at the control region before performing the production runs. We allowed the simulations to run for a maximum time of 200 ns during the production runs in the NVT ensemble with the density restraints turned off to allow for crystallization.

For simulating homogenous solution, simulation boxes of NDT in both hexane and toluene were equilibrated for 20 ns using the same NVT and NPT ensembles. Harmonic restraints were imposed for the number density of the NDT at the exterior of the simulation box using the PLUMED[32] DENSITY and UPPER_WALLS functions to gradually increase supersaturation (Figure 4.2). Production runs were run for 100 ns for

both solutions. The simulation parameters with harmonic restraints are listed in the Table 4.3.

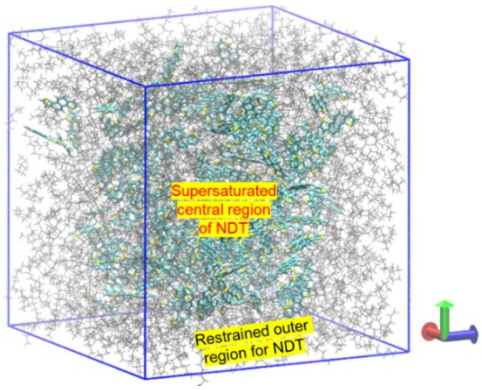

Figure 4.2 Schematic diagram of the simulation setup with harmonic restraints for NDT at the exterior of the simulation box in all three box dimensions.

Table 4.3 Density restraint parameters used for crystallization simulations of homogenous solutions.

Axis	Box length	Virtual atom position (Z)	Upper boundary	Lower boundary	Kappa
Hexane					
X upper	7.138	6.424	0.7	-0.7	0.08
X lower		0.714	-0.7	0.7	0.08
Y upper	7.138	6.424	0.7	-0.7	0.08
Y lower		0.714	-0.7	0.7	0.08
Z upper	7.138	6.424	0.7	-0.7	0.08
Z lower		0.714	-0.7	0.7	0.08
Toluene					
X upper	9.227	8.304	0.91	-2.0	0.01
X lower		0.910	-0.91	2.0	0.01
Y upper	9.227	8.304	0.91	2.0	0.01
Y lower		0.910	-0.91	2.0	0.01
Z upper	9.227	8.304	0.91	2.0	0.01
Z lower		0.910	-0.91	2.0	0.01

To simulate the bulk molecular environment during crystal growth while maintaining the chemical potential fixed and to mitigate finite size effects, we implemented CμMD.[13] Through the all-atomistic CμMD approach, we are able to control and maintain solution supersaturation at desired levels throughout the crystallization process, akin to the demonstrated case for crystal structure prediction of naphthalene[15] and urea[10] in solution. The CμMD code is run at the NVT ensemble for adequately equilibrated input structures, obtained from different crystallographic templates in contact with the solution (Figure 4.3) in the NPT ensemble.

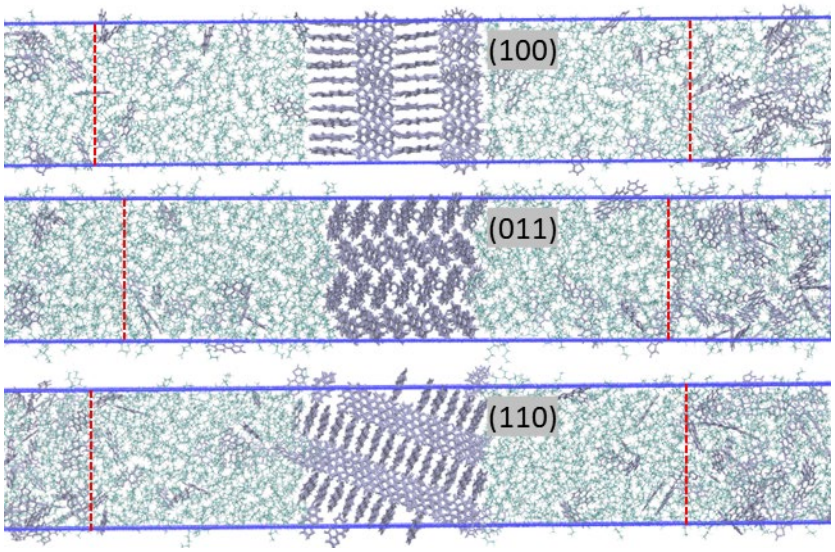

Figure 4.3 Example simulation setups of the equilibrated NDT crystals with the bulk (hexane) solution at 0.1 NDT mole fraction for production runs. Rough positionings of force regions (left and right) that govern the supersaturation inside the control regions are shown in red dotted lines. Only the central regions of the boxes are shown for clarity.

We determine the growth limiting surface during faceted crystal growth by investigating homogenous crystallization from solution. We promote homogenous growth in the simulation box by gradually supersaturating NDT solutions in hexane and toluene using density restraints to force solute molecules to concentrate on the interior, applied through PLUMED plugin for the GROMACS MD code. Along with insights from BDFH model, we establish the contribution of the slowest growing crystal face to stabilize the formation of critical nucleus that allows for the continued growth of the rest of the faster growing crystallographic faces.

With the growth limiting surface identified, we determined the critical concentration required to observe formation of the critical nucleus through production runs of templated growth simulations of NDT per different solvent environments. We define CC as the concentration at which ~50% of the repeats show nucleation events,

stochastically resulting in successful (continued) growth during the time of the analysis. We bear in mind that CC will be well above solubility limits as we observe nucleation, and therefore the solution is assumed to be at supersaturation conditions. The CC 2D nucleation and growth can be used as a fair standard concentration to demonstrate the comparative behavior between two solution environments with relevance to their intrinsic dynamics during crystallization, i.e., when all other extrinsic effects such as molecular crowding, diffusion limitations, and mass transport to the surface are minimal.

The reaction coordinates for crystallization of NDT on different faces are identified using slow degrees of freedom associated with the transformation of solvated molecules to the solid crystalline phase. Here, two descriptors were used to represent the crystallinity of new molecules to the crystal lattice surface depending on the growth mechanism. For the nucleation and growth mechanisms (i.e., 2D nucleation with the birth and spread mechanism) that follows a prominent nucleation step, we define crystallinity using the crystallinity descriptor (s_1) in the growth region, akin to the case of naphthalene reported by Bjelobrk et. al.[15] s_1 defines the crystallinity of the growth layer in combined terms of the local density, local orientation, and coordination number of a molecule on the crystal surface. [15] The definition of s_1 allows one to characterize the thermodynamic metastability associated with the critical nucleus For the surfaces that show growth in the absence of a prominent nucleation step (i.e., direct crystallization in barrier-less fashion), we define the second crystallinity descriptor (s_2) for the growth region entirely based on the local orientations (in terms of the torsional angle of the long axis molecular vector against the unit cell a vector) of the molecules in this region (Figure 4.4).

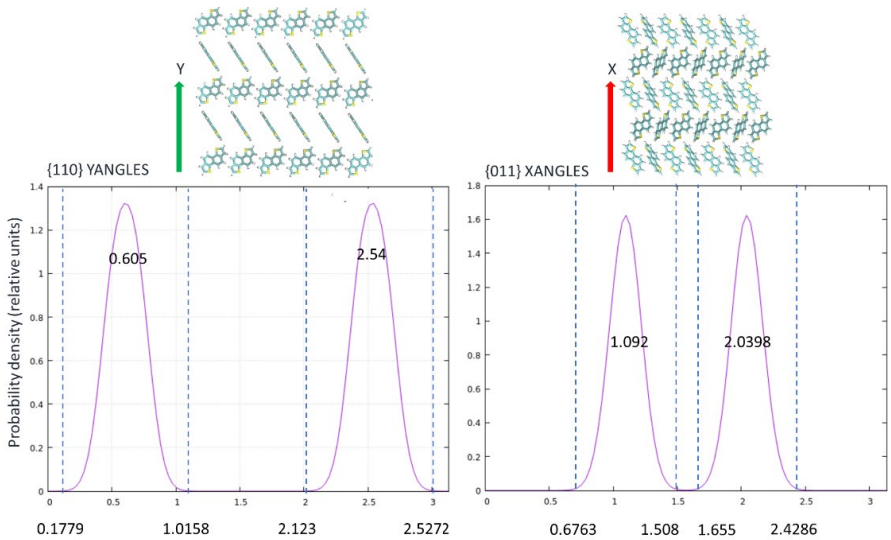

Figure 4.4 Distribution of molecular long-axis vector angles with the axis shown for (110) and (011) faces. Upper and lower boundaries used to distinguish crystalline order at the growth region are shown in dotted lines. The mean values are annotated in the middle of each population peak.

Here, s_2 accounts for the barrierless growth observed by faster growing surfaces. Both s_1 and s_2 describe crystallinity by mostly accounting for the thermodynamics associated with achieving attributes of crystallinity.[33] To account for kinetic components involved in crystallization, we determine the number density of the solvent molecules adsorbed onto the surface (h). Here the solute adsorption and solvent desorption are mutually inclusive events and can be assumed to be controlled by the same energetics. By assuming the thermodynamic work function for adsorption of the relevant solvents on the crystal surface can be easily overcome by the available thermal energy at the respective temperatures used, we consider the solute adsorption (or desorption) to be primarily due to kinetics. Finally, we generate free energy surfaces (FES) associated with the crystallization process within the phase space of the s and h descriptors, where thermodynamic and kinetic contributions can be contrasted effectively (see SI for more

details). We note that since the CμMD code is operated under the NVT ensemble, the obtained free energies from the calculations resemble Helmholtz free energy terms. However, the well-equilibrated input structures that were pre-relaxed under the NPT ensemble provide close approximations to the Gibbs free energy terms for the representation of FES. Nevertheless, to circumvent the confusion between energies, the term 'free energy' (F) has been used throughout the results and discussion section.

Solvent adsorption onto the crystal surface is accounted for by calculating the number density of solvent molecules on the surface. The upper and lower boundaries of surface adsorption region is selected separately for toluene and hexane through visualizations that only account for the adsorbed molecules (Figure 4.5 shows an example depiction of how the region is selected based on visualizations). The center-of-mass of either toluene or hexane is considered to determine molecular location with respect to the top of the crystal surface.

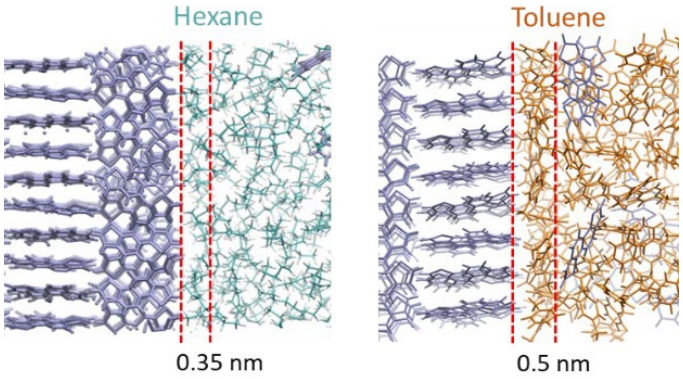

Figure 4.5 Example cases showing the choice of upper and lower boundaries of the adsorption layer (specified in red dotted lines) next to the template crystal (100) face (shown in purple color) in hexane and toluene solutions.

Collective variables for the crystallinity (s) and solvent adsorption (h) were calculated from the production simulation runs of 200 ns. From all the multiple repetitions that were performed, all collective variables were combined to generate an overall histogram of probability densities (python kernel density estimated probability densities), which were then transformed into free energy surface (FES) using the Equation 4.1.

$$F = -k_b T ln(P_i) \qquad \text{Equation (4.1)}$$

During the growth of a crystalline layer on top of the crystal template, we expect s to increase, while h decreases, as solvent molecules desorb from the surface while the solute molecules adsorb and crystallize. This often results in an anticorrelated relationship between s and h. Paying close attention to the anticorrelation between s and h along the reaction coordinate can reveal useful information about the dynamics at play: A perfect linearity might suggest and 'ideal' crystallization behavior where kinetic interferences coming from solvent desorption or solute diffusion is minimal. In other words, all the solute molecules make their way into to the growth region can quickly achieve crystallinity while expelling the adsorbed solvent molecules away from the surface. The presence of an energy barrier between low and high s and h reflects 2D nucleation where the energy barrier is associated with the formation of a critical nucleus. On the other hand, any indication of a non-linearity might imply limitations imposed by either s or h, along growth indicated by either the thermodynamic metastability associated with formation of 2D critical nucleus or kinetic effects associated with molecular diffusion, adsorption/desorption, and reorganization.

4.3 Results and Discussion

To determine the rate limiting surface(s) associated with NDT crystal growth, we begin by exploring NDT crystallization in hexane and toluene solutions. Figure 4.6 shows the predicted crystal structure through the BFDH model, wherein the molecular short axes stack parallel to the (100) plane through face-to-edge packing, whereas the molecular long axes lie mostly orthogonal to the plane normal. Growth along the molecular long axes (i.e., orthogonal to the (100) plane) is predicted to be slower, therefore providing the surface with the larger surface area. This result is hypothesized to be due to decreased intermolecular interactions among molecules as they stack. From CNT, we can also assume this to be partly contributed by the surface energy, where stacking along directions with high surface energy destabilize growth, while those of low surface energy grow faster. Conversely, all fast-growing surfaces grow mostly parallel to the (100) plane normal, which has lower surface energy associated with assembly, and more exposed substrate surface from the adjacent neighbors to establish favorable interactions for the newly attaching molecules to thermally equilibrate in correct orientations and dissipate extra energy to the bulk crystal phase.

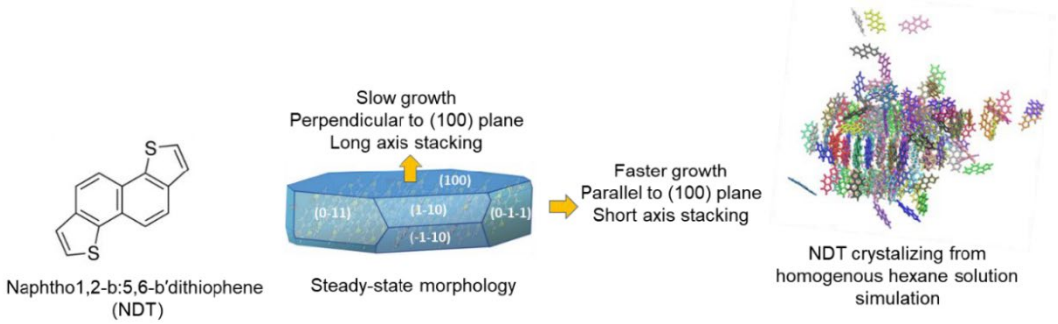

Figure 4.6 (left) Chemical structure of NDT. (middle-to-right) Steady-state NDT crystal morphology as predicted by the BFDH model (visualized through Mercury visualization tool[17]) compared with the early stages of nucleus formation in a homogenous supersaturated hexane solution. Faster parallel growth compared to slow perpendicular growth with respect to the (100) plane is shown in both cases.

Turing to the homogenous crystallization simulations in hexane, we observe ready formation of crystalline order within the first 20 ns of the 100 ns long simulation (under conditions of high solution supersaturation – Figure 4.7). During the early stages of phase separation and crystallization, a crystalline molecular layer resembling the (100) face is assembled through short-axis stacking from the completely random population of NDT. This initial assembly appears to be a cluster containing multiple critical nuclei (i.e., the first, first-order phase separations from solution to the crystalline solid), which rapidly merge into one 2D layer that then allows formation of additional layers on top and bottom. In toluene, although no crystallization was observed during the early stages (up to ~40 ns) of the simulation, we observed gradual formation of NDT assemblies oriented by the same short-axis stacking seen in the case of hexane, generating (100) face that ultimately produced crystalline order in a layered fashion at the end of the 100 ns simulation. We thereby postulate that the assembly of (100) face in both hexane and toluene serve as the limiting step to initiate crystallization along all other surfaces.

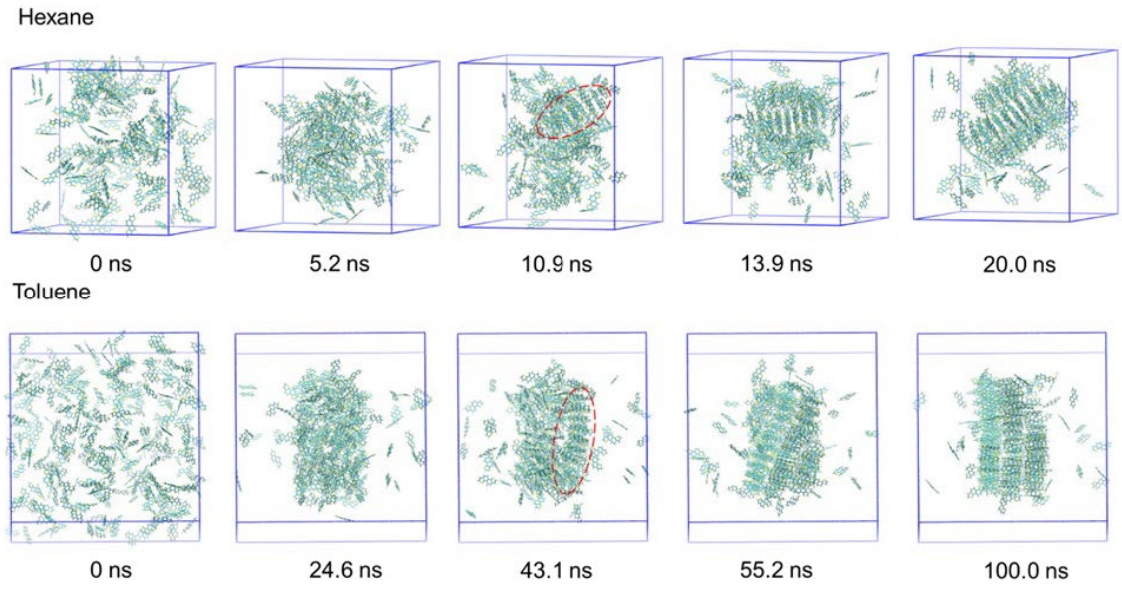

Figure 4.7 Snapshots of the simulation of crystal formation in either hexane (top) and toluene (bottom) homogenous solutions. Only the solute molecules are shown for clarity. The red dotted regions highlight the first apparent crystalline layer of (100) face formation from the central cluster.

We observed that NDT crystallizes in hexane at the center of the simulation box after 20 ns, initiated through short-axis stacking. In toluene, no crystallization is observed at first, though aggregates are noted, until short-axis stacking begins to appear after ~40 ns and then quickly produces crystal formation from about 50 ns and on. Both simulations reveal that the (100) face serve as the growth limiting surface where formation of all other faces are contingent upon the initial assembly of (100) face (Figure 4.8).

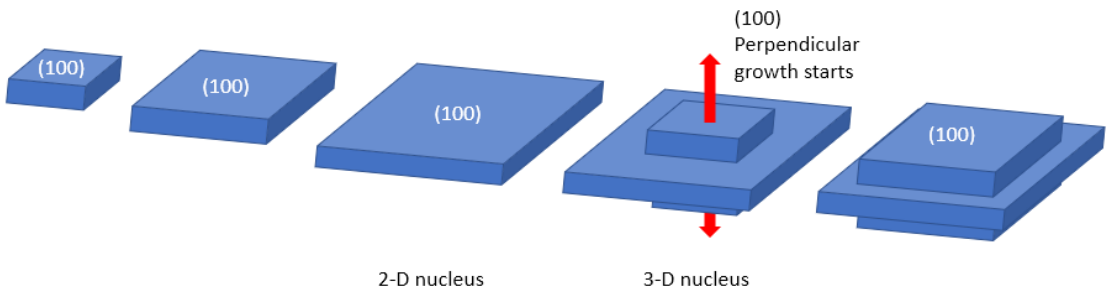

Figure 4.8 Schematic illustration of early stages of crystallization of NDT in a homogenous hexane solution, where the growth perpendicular to the (100) plane is seen after all other faster growing surfaces are assembled to form a 2-D nucleus that is parallel to the (100) plane.

We now turn to facet growth simulations to monitor events associated with the early stages of NDT crystallization. From the BFDH model, we select the three crystal faces with highest relative surface areas (From Table 4.1) that provide major contributions to the steady-state crystal morphology – the crystal faces of (100), (011), and (110) planes – to explore the crystallization mechanisms under varied process conditions. These faces are the three slowest growing in a perpendicular direction to the plane (based on BFDH model), therefore associated with high surface area, that impose most contributions to the overall steady state morphology. Moreover, if infinite growth is considered, faster growing faces will be engulfed by the slow growing faces during morphology evolution as only the slow growing surfaces dominate.[6] We start by carrying out simulations of varied NDT concentrations in toluene to estimate the NDT critical concentration (CC) for crystallization. Each simulation is repeated five times to establish reproducibility and improve sampling for the generation of free energy surface of crystallization. We start by looking at the (100) face, as it was found to be the growth

limiting surface. The concentration control maintained by the CμMD procedure is provided in Figure 4.9.

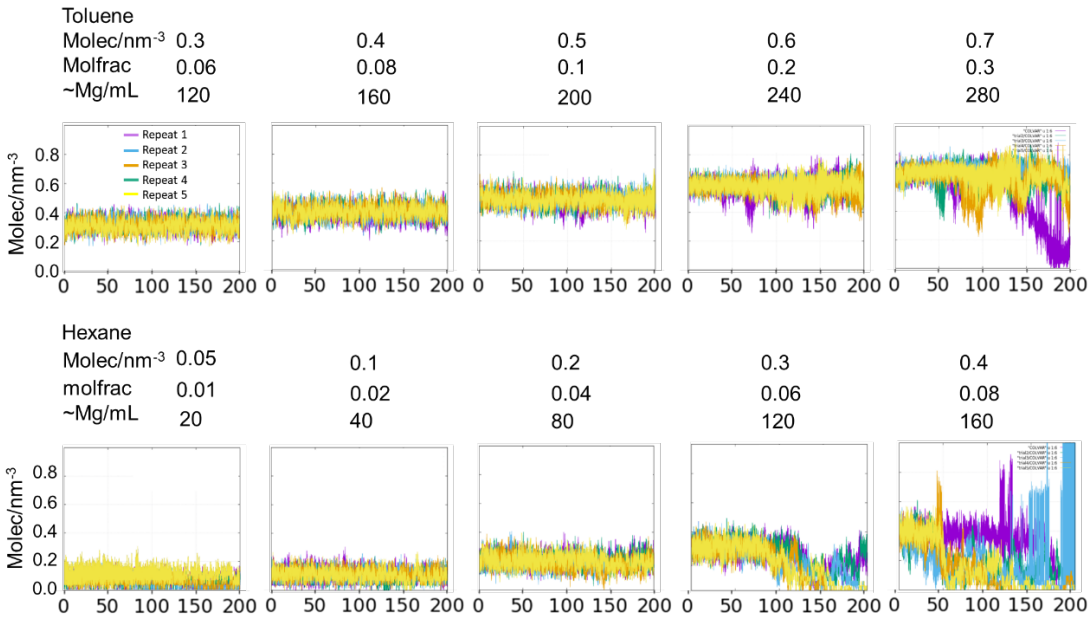

Figure 4.9 Controlled concentrations of the right-side control regions during the production runs that allow crystal formation at varied concentrations in hexane and toluene solutions. Different colors represent different repeat simulations. The x axis denotes the time in ns.

For simulations with higher concentrations, the drop in concentration in the control region is due to fast removal of NDT molecules away from the solution, as a result of fast growth or the growth of multiple layers, occupying the control region. However, with the completion of the first layer we assume no redissolving occurred, and thereby ignored the concentration drop due to the presence of second layer and so on, on top of the first adlayer.

We determined the critical concentration (CC) for NDT nucleation in toluene to be an NDT mole fraction of approximately 0.1, corresponding to ~50% growth observed under the 200 ns simulation time. As the crystallinity increases, the number density of

toluene adsorbed to the crystal template surface drops correspondingly to accommodate space for more crystallization. At the CC, we observe that an assembly of at least eight (8) molecules is required on the surface to form a critical nucleus, which is then transformed through a significant surface rearrangement to achieve crystalline order (Figure 4.10).

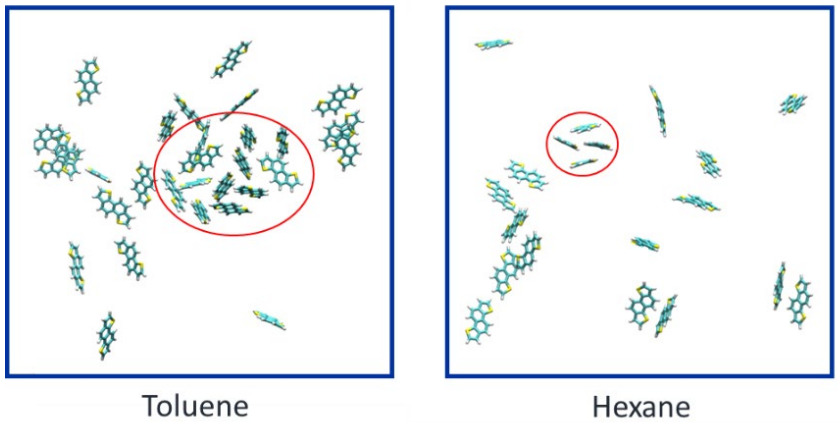

Figure 4.10. 2D critical nuclei observed at the critical concentrations in toluene and hexane on top of the (100) face. The red circle roughly highlights the participating members with short-axis molecular stacking. Solvent molecules and the template crystal surface are not shown for clarity.

At larger NDT concentrations, a higher propensity for nucleation is observed, facilitated by faster surface rearrangement. However, after the nucleation step, the growth rate appears to not be well correlated with concentration, as different apparent growth rates are observed for the five repeat simulations (Figure 4.11). Therefore, it is assumed that the surface rearrangement step for the formation of the critical nucleus serves to limit overall growth, and therefore, the growth rate is not very dependent on the considered supersaturation levels.

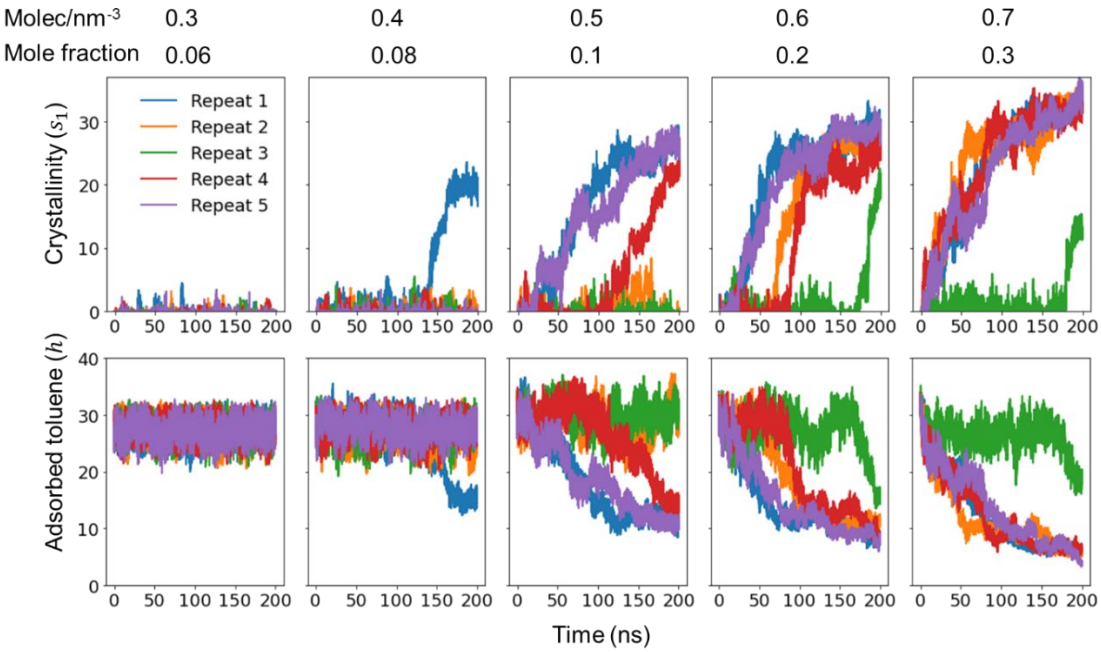

Figure 4.11 (top) s_1 crystallinity descriptor and (bottom) adsorbed solvent (h) descriptor for different concentrations of NDT in toluene growing on the (100) face as a function of time. The different colors in each plot correspond to the repeat simulations, each initiated with random input structures extracted from equilibrated systems.

Traversing all FES from fully dissolved NDT-toluene solutions (large h and small s) towards the near completion of crystalline monolayer (small h and large s), we observe the presence of a clear nucleation energy barrier (i.e., the critical free energy barrier for nucleation on the (100) face or $\Delta F^*_{\{100\}}$). At CC, the $\Delta F^*_{\{100\}}$ takes the highest affordable magnitude that can still allow continued growth (note that this is analogous to critical nucleation energy in homogenous conditions – ΔG^*_{homo} – from CNT). With increasing concentration, we observe a decrease in $\Delta F^*_{\{100\}}$ (Figures 4.12 and 4.13), which can be attributed to increased favorable inter-solute interactions due to higher availability of NDT molecules in the growth region, promoting crystal nucleation and phase

separation (as shown for the 0.2 and 0.3 NDT mole fractions, where crystallization starts early in the simulation).

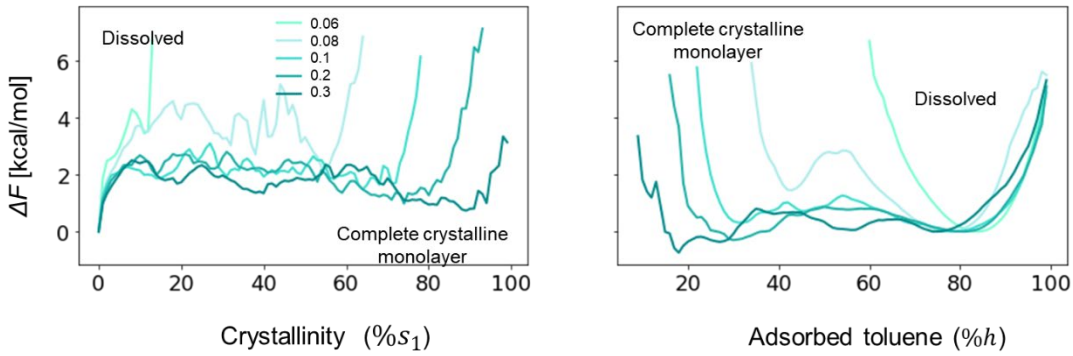

Figure 4.12 Free energy profiles of crystal layer growth on the (100) face in toluene in terms of the crystallinity descriptor (s_1) and solvent adsorption (h) for each concentration (shown in different shades of color). The most dissolved instance of the growth layer is normalized to represent the zero-point energy. NDT concentrations for each FES are provided in mole fraction units.

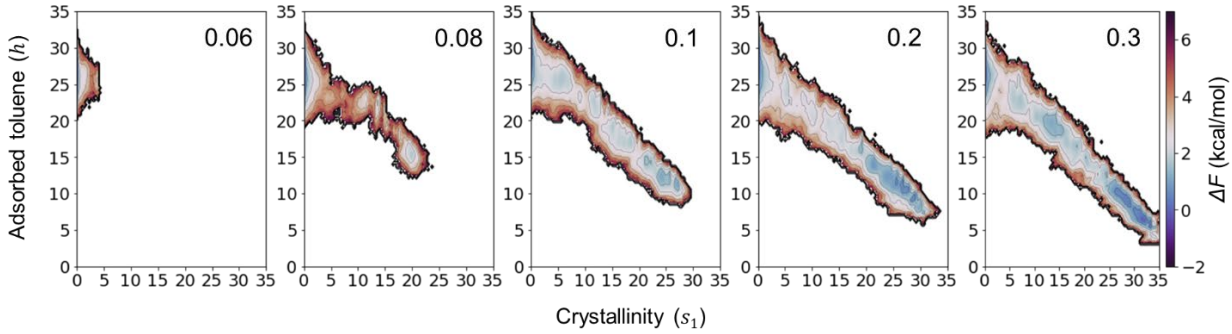

Figure 4.13 Free energy surface (FES) of NDT crystal layer growth on the (100) face in toluene in terms of the s_1 crystallinity and h solvent adsorption descriptors. NDT concentrations for each FES are provided in mole fraction units.

Additionally, entropic contributions may also assist in nucleation of the phase separated NDT through increased probability of achieving favorable microstates at the surface. We note that the growth observed at all concentrations follows smooth FES profiles, as the growth rate appears somewhat similar in all supersaturation levels

examined, especially in terms of s_1. We also observe that the variations along h are small (i.e., minimized kinetic involvement) when significant crystallinity is achieved. However, at lower concentrations, kinetic barriers (i.e., the energy barriers of energy profile of h, Figure 4.12), become more prominent, to the extent that growth is prevented, whereas at concentrations above CC, such barriers substantially reduce.

We now turn to the crystallization of NDT on the (100) face in hexane, where weaker interactions among the alkane solvent molecules the aromatic NDT lead to poor solvation; here, stronger solute–solute interactions (compared to solute–solvent) exert an additional driving force for the two non-ideally mixing molecule types to phase separate faster. We again compare crystallization at several concentrations to determine CC (Figure 4.14). Here, CC is found to be 0.04 NDT mole fraction units, a value nearly one-half as large as in toluene. The critical nucleus size is also one-half of that observed in toluene, being only four (4) NDT molecules (Figure 4.10). At concentrations large than CC, we again observe a larger propensity for nucleation, but now with growth rates being affected more significantly as higher concentrations lead to a clear increase in growth rate.

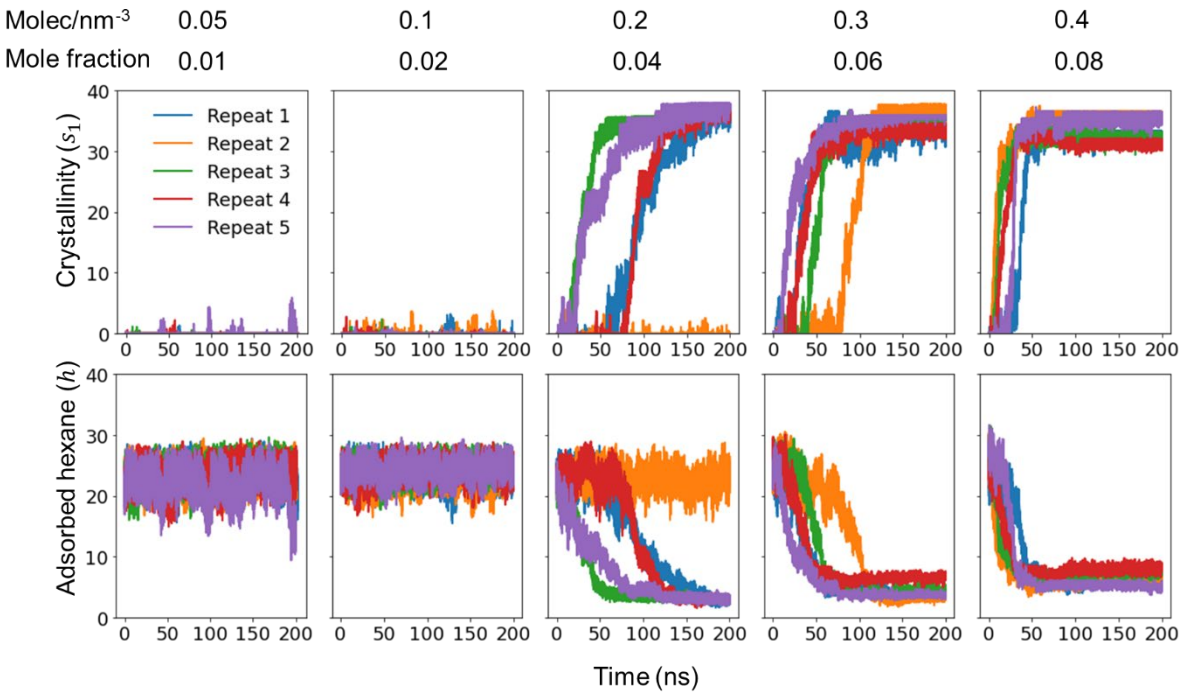

Figure 4.14 (top) s_1 crystallinity descriptor and (bottom) adsorbed solvent (h) descriptor for different concentrations of NDT in hexane growing on the (100) face as a function of time. The different colors in each plot correspond to the repeat simulations, each initiated with random input structures extracted from equilibrated systems.

Through trajectory visualizations, we confirm that the surface rearrangement is fast, giving rise to easy nucleation that thereby promotes fast growth. Consequently, at all concentrations that show crystallization, we observe multilayer growth on the (100) surface (Figure 4.15) at the end of the 200 ns of simulation time. Approaching large NDT concentrations in hexane (around ~0.08), we observe that the growth rates become more uniform in addition to being fast, with less discontinuities along growth due to fast surface integration. However, through trajectory visualizations, we observe that more defects and imperfections are associated with the first adlayer at such large concentrations (Figure 4.15), where other layers continue to grow on top, resembling characteristics of a rough growth mechanism.

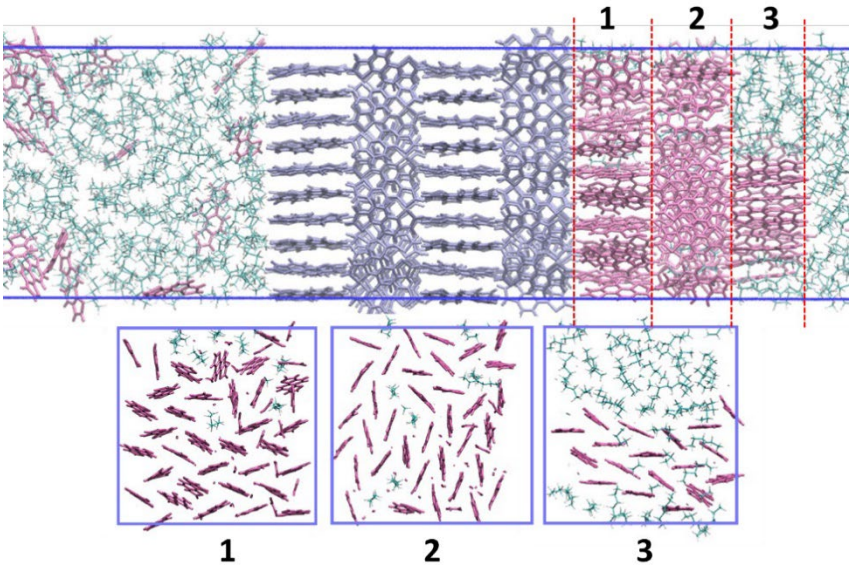

Figure 4.15 Multi-layer growth of NDT crystals on the (100) face in 0.08 mole fraction NDT solutions of hexane, showing the second to third layer grown on top of the first layer after 200 ns. Colors green, purple and magenta shows hexane, the NDT crystal template, and the newly formed NDT layers respectively. Top views (cross sections) of the adlayers are shown in the second row.

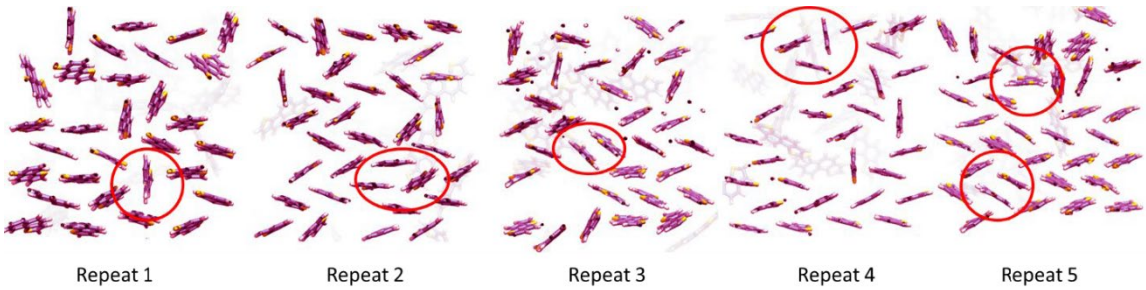

Figure 4.16 First adlayer of NDT crystals on the (100) face for all five repeat simulations in 0.08 mole fraction hexane solution at 298 K. Only NDT molecules are shown for clarity. The empty gaps trap hexane molecules. Red circles highlight defective integrations of NDT.

The FES for NDT in hexane (Figure 4.17) appear to be rougher and show more breadth along the reaction coordinate h when compared to those for NDT in toluene. Free energy profiles of s_1 at all concentrations that show crystallization exhibit very similar energetics, with relatively small nucleation barriers (~2 kcal/mol, Figure 4.17), revealing similar thermodynamics.

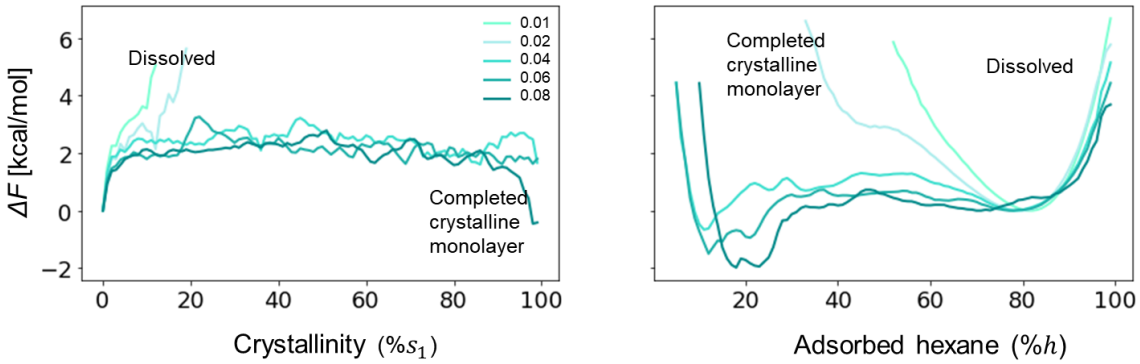

Figure 4.17 Free energy profiles of crystal layer growth on the (100) face in hexane in terms of the crystallinity descriptor (s_1) and solvent adsorption (h) for each concentration (shown in different shades of color). The most dissolved instance of the growth layer is normalized to represent the zero-point energy. NDT concentrations for each FES are provided in mole fraction units.

However, the solvent desorption shows prominent differences in the free energy corresponding to changes in concentration. This reveals the importance of kinetic features from the solute desorption from the template surface, that contribute to the roughness of overall FES, especially at lower NDT concentrations. At increased NDT concentrations, however, the FES show smoother characteristics, where kinetic barriers (i.e., the free energy barriers of h, Figure 4.18) become almost absent, highlighting fast desorption of hexane from the surface as the thermodynamics dominate when inter-solute interactions become more abundant.

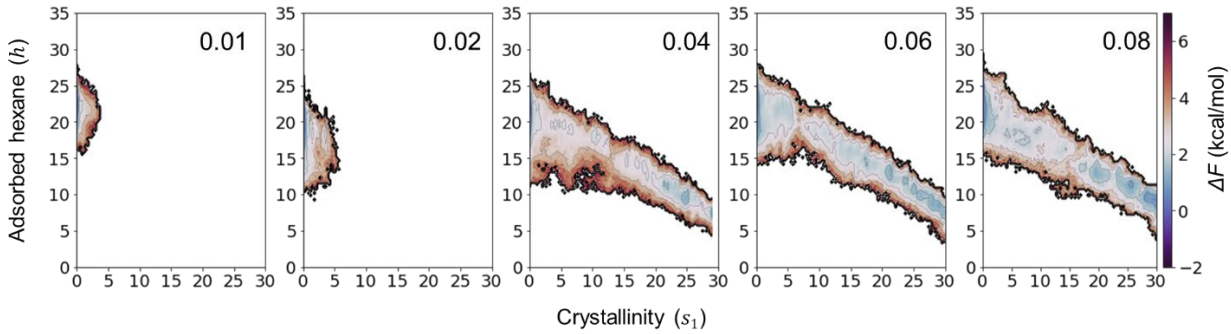

Figure 4.18 Free energy surface (FES) of NDT crystal layer growth on the (100) face in hexane in terms of the s_1 crystallinity and h solvent adsorption descriptors. NDT concentrations for each FES are provided in mole fraction units.

We now explore the effect of temperature on the nucleation and growth of NDT in toluene and hexane at their CC (0.1 and 0.04 in NDT mole fractions, respectively). Temperature can serve to impose changes in both thermodynamics and kinetics, thereby affecting both the nucleation and growth mechanisms involved. In toluene (Figures 4.19 and 4.20 top rows) above room temperature (298 K), crystallization is not observed (possibly as increased solubility becomes a considerable factor) whereas below the room temperature, crystal nucleation is promoted as the clusters start to nucleate from early in the simulations (e.g., all five repeat simulations show successful critical nucleation below 298 K). However, at the same low temperatures, the growth is slowed significantly, as it takes longer times to achieve high crystallinities (s_1). Conversely in hexane (Figures 4.19 and 4.20 bottom rows), we observe major differences in the crystallization mechanism. The largest apparent growth rates are achieved at 318 K, though with a significantly delayed critical nucleation. However, increasing the temperature above 318 K is detrimental for crystallization: note that at 338 K, we see evidence for the transient formation of (sub)critical nuclei, that quickly dissolve. On the other hand, when temperatures are below 298 K, we again observe a higher propensity for nucleation, with

more of the repeat simulations showing nucleation and successful growth from early on as seen for the case of toluene.

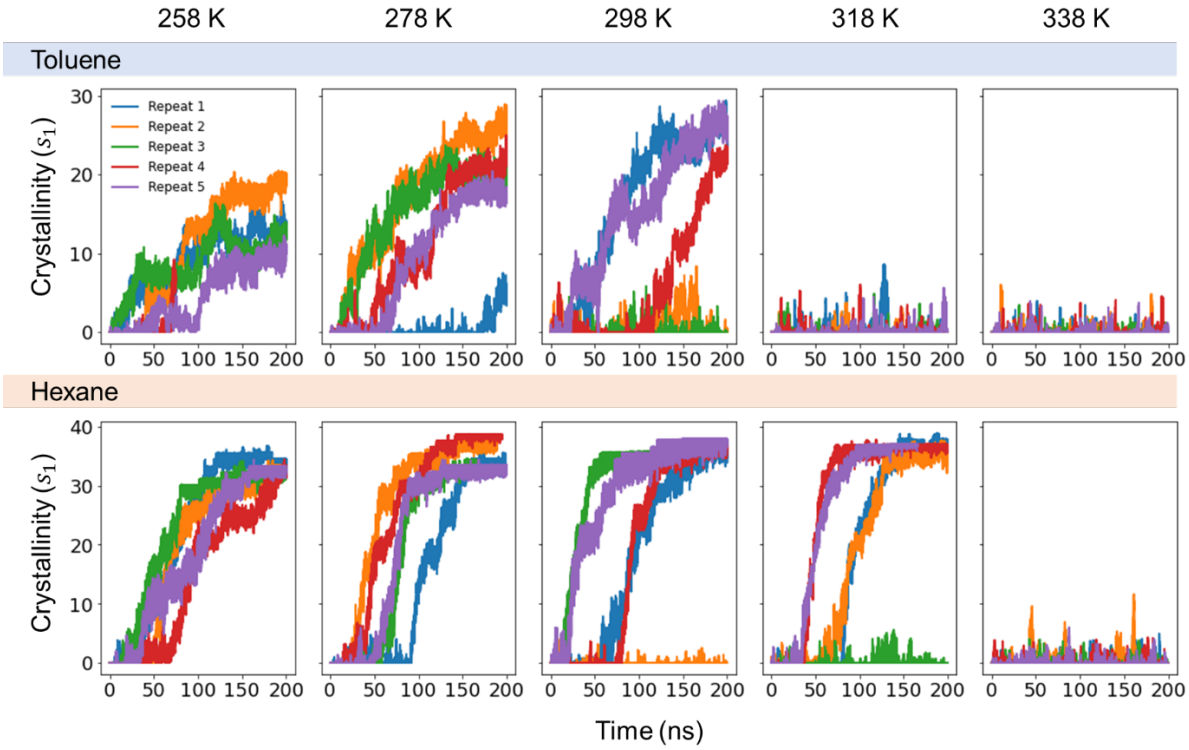

Figure 4.19 Crystallinity descriptor s_1 as a function of temperature in (top) toluene and (bottom) hexane for NDT growth on the (100) face. The different colors in each plot correspond to the repeat simulations, each initiated with random input structures extracted from equilibrated systems.

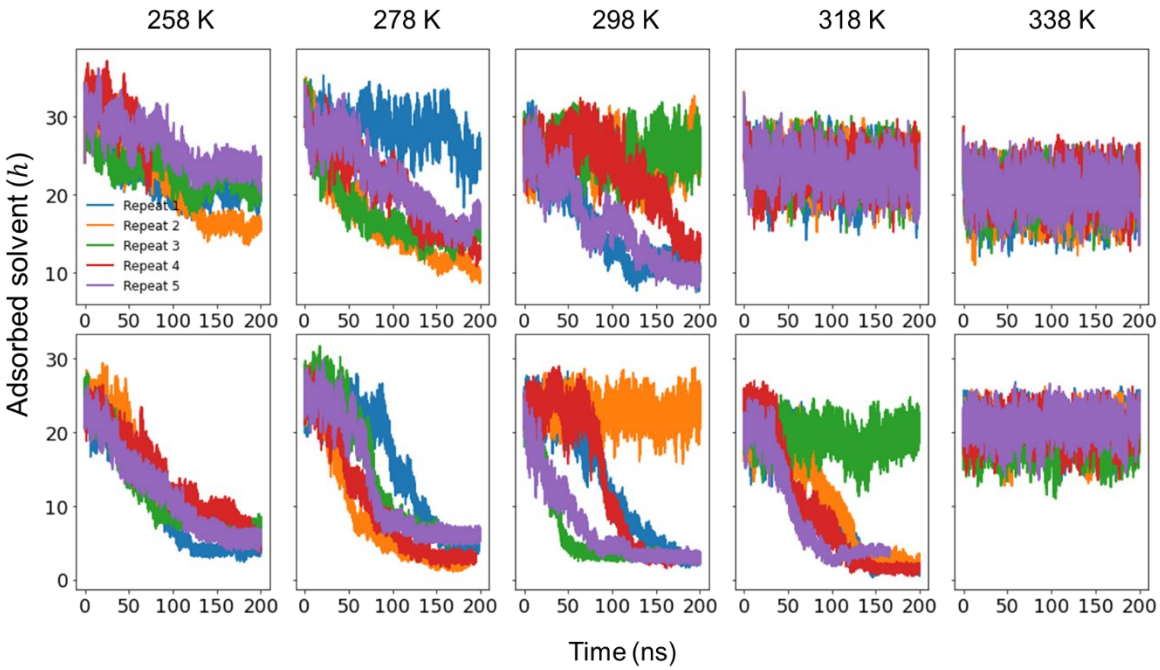

Figure 4.20 Adsorbed toluene (top row) and hexane (bottom row) on the surface during crystallization at each temperature for the (100) face. Colors correspond to the repeat simulations initiated with random input structures from equilibrium solutions of corresponding temperatures.

From the FES that show crystal layer growth as a function of temperature (Figure 4.21 and 4.22), we see that in general, the $\Delta F^*_{\{100\}}$ becomes larger for temperatures above room temperature with respect to the available thermal energy at the respective temperatures: At 318 K and 338 K, almost no growth is observed (with the exception of NDT in hexane at 318 K). On the other hand, moving towards colder temperatures (i.e., 278 K and 258 K), the nucleation barriers decrease, enabling faster/easier nucleation but however with slower and diminished growth.

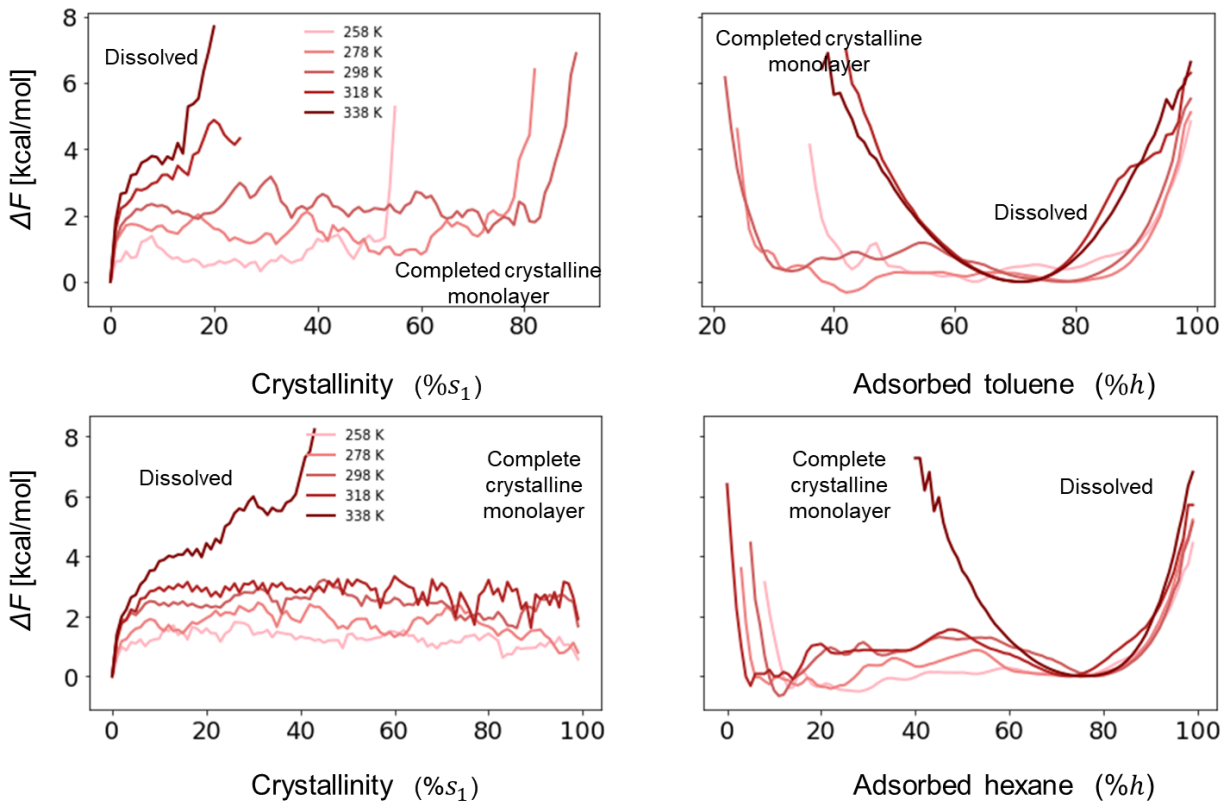

Figure 4.21 Free energy profiles of crystal layer growth on the (100) face in toluene and hexane in terms of the crystallinity descriptor (s_1) and solvent adsorption (h) for each temperature (shown in different color shades). The most dissolved instance of the growth layer is normalized to represent the zero-point energy.

For NDT crystallization in toluene, this generalization appears more valid at low temperatures, as when temperature is decreased below 298 K the nucleation rate and the propensity show a clear increase, however with limited and slower growth as the largest s_1 being explored is also decreased. In other words, the decreased temperature seems favorable for the thermodynamics associated with nucleation step, though, detrimental to the kinetics associated with growth. For the case of NDT crystallization in hexane, we still observe improved nucleation but however with the decrease in growth rate being

moderate enough to allow for continued growth (Figure 4.21 and 4.22). Consequently, we observe that the rougher FES shown by NDT crystallization in hexane at 298 K and above have become significantly smoother at temperatures 278 K and 258 K. Therefore, NDT crystallization in hexane demonstrates an 'optimum' balance between the opposing thermodynamic and kinetic factors at sub-room temperatures (278 K and 258 K), where the overall crystallization no longer appears to resemble rough growth mechanism.

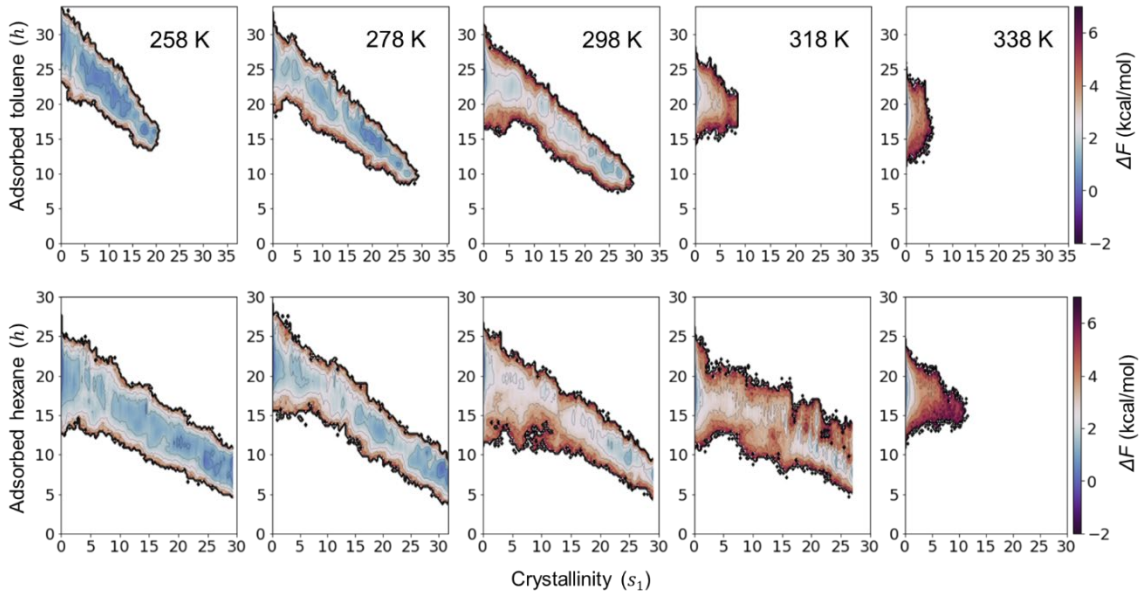

Figure 4.22 Free energy surface (FES) of NDT crystal layer growth on the (100) face in toluene and hexane in terms of the s_1 crystallinity and h solvent adsorption descriptors.

We now turn to the (011) and (110) faces. Note that now, unlike in the case of (100) face, a combination of both molecular long- and short-axis stacking takes place across the surface area, whereas for the (100) face this anisotropy in shape is absent with only short-axis stacking being present (Figure 4.23).

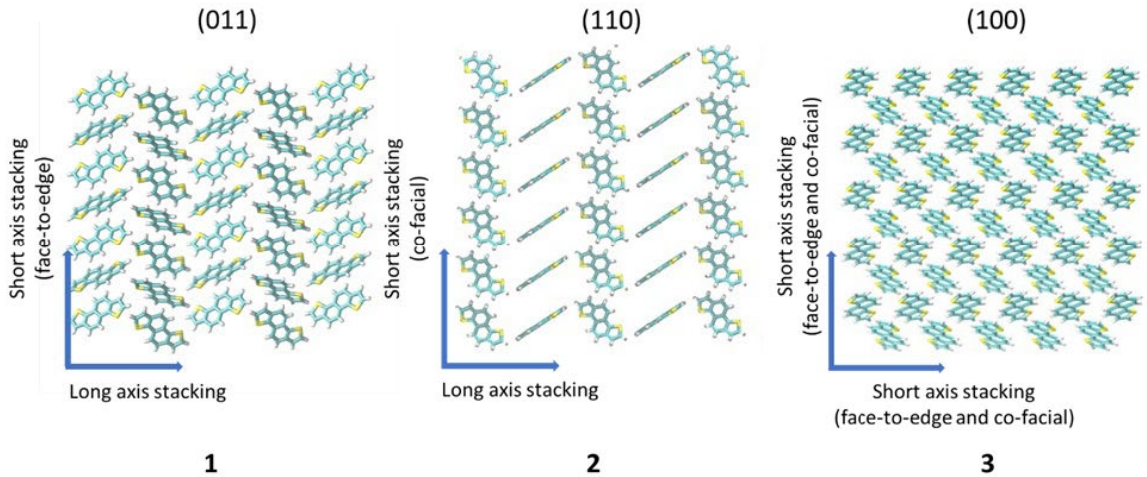

Figure 4.23 Top views of the crystal templates of (011), (110) and (100) faces that are in contact with the supersaturated solutions. The arrows pointing to the short and long axis stacking directions of the surface. The annotated numbers rank the faces in the decreasing order of exposed aromatic interactions to the surface in orthogonal direction.

We also note that the molecular orientations on the surface allow for increased interactions amongst the aromatic planes at the solution interface upon adsorption. Note that we use the CC of NDT determined in toluene and hexane, respectively, for the (100) face, as this is the CC for the slowest growing face. For the (011) and (110) faces, crystallization no longer involves a distinguishable nucleation step prior to growth. The growth is significantly less stochastic and faster for these two faces in hexane when compared to that of the (100) face (Figures 4.24).

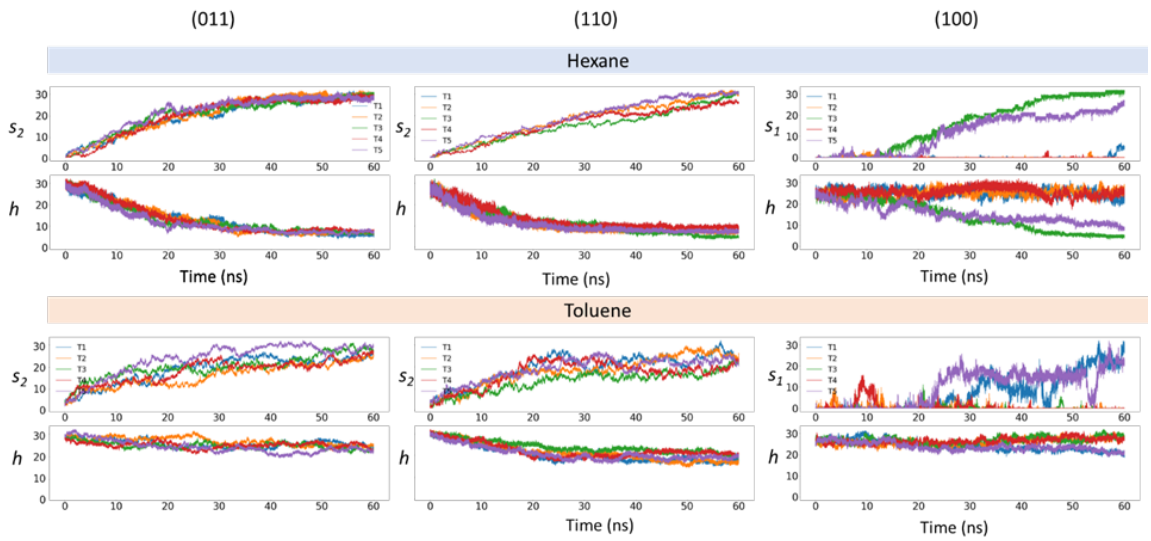

Figure 4.24 Crystallization along (011) and (110) faces within a time of 60 ns defined by the crystallization descriptor s_2 for the (011) and (110) faces, and s_1 for the (100) face along with solvent adsorption descriptor (h).

However, when comparing growth in toluene and hexane, growth of (011) and (110) faces in toluene is slower and more stochastic in nature than in hexane. The nucleation appears very similar: Fast and ready assembly from very early stages in each solvent; visualizations of the simulations show a multilayer growth for these faces after 60 ns and on. (Figure 4.25).

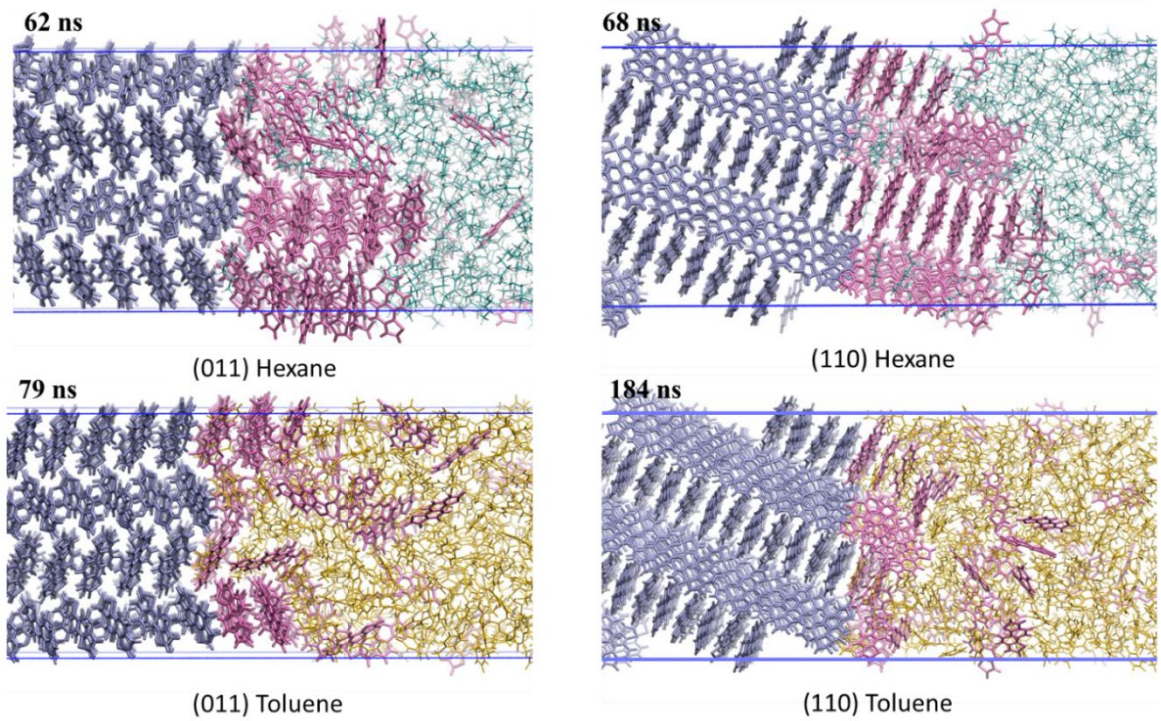

Figure 4.25 Degree of crystal growth of NDT observed in either hexane and toluene on the (011) and (110) faces at the end of each simulation.

Comparing the FES, we observe clear differences in the facet growth mechanisms of the three faces (Figures 4.24 and 4.26). Recall that the crystallinity descriptor s_2 is used to define crystallinity for the faces (011) and (110), chosen to reflect the absence of a nucleation step, as opposed to the case of face (100) that show a prominent critical nucleation barrier, and the descriptor s_1 is necessary.

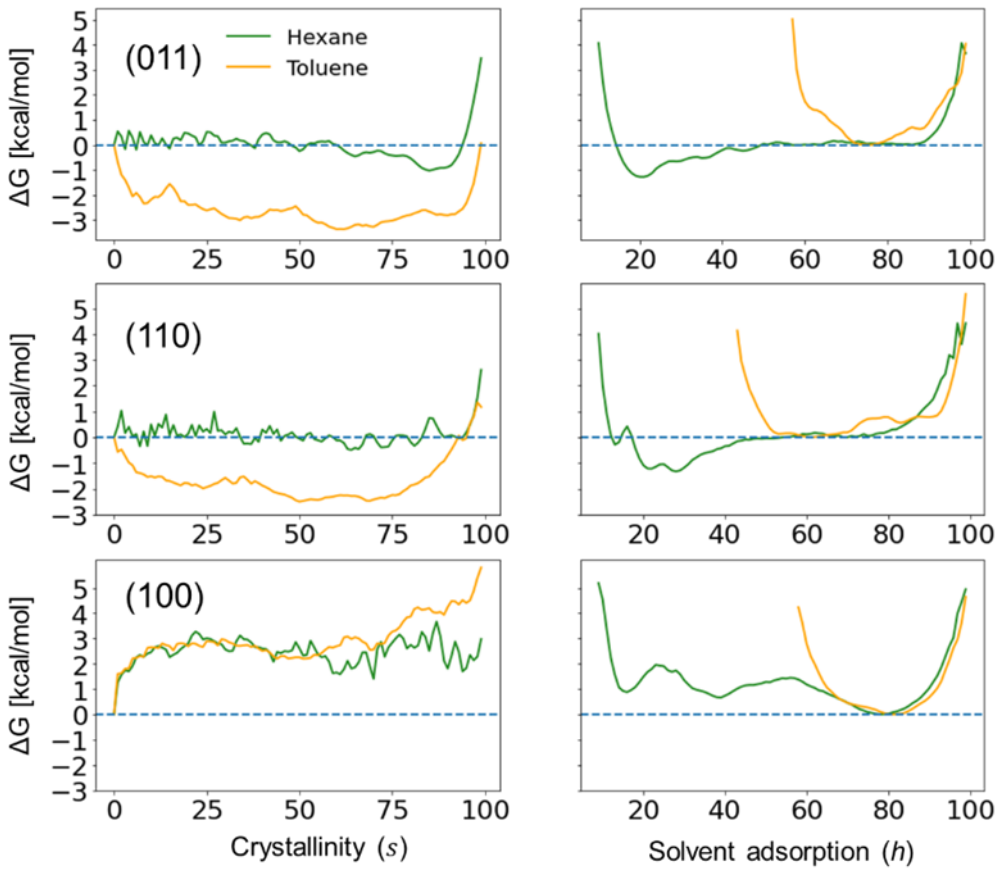

Figure 4.26 Free energy obtained from probability distribution along reaction coordinates (s_1) and (h) for each facet growth in toluene and hexane (only accounting 60 ns of simulation time). The fully dissolved instance of the growth layer is normalized to the zero-point energy.

Via visualization of the trajectories, the absence of the nucleation step is observed in both the (011) and (110) FES (Figure 4.25), and the attachment of NDT onto

the surfaces appear faster due to negative or zero free energy associated with increasing s_2. We note that the same solvent adsorption descriptor h is used for all three crystal faces, providing an even comparison of kinetic effects. In toluene, there is a significant negative free energy associated with achieving crystallinity (Figure 4.26). The FES overall indicate smoother assembly (Figure 4.27), reflecting an ideal crystallization behavior where thermodynamic metastability is minimal, and interference from kinetics is minimal, (as shown by the relatively narrow breadth along the reaction coordinate h), allowing for more thermodynamically feasible molecular integration on to the first adlayer on top of the templated surface. However, we note that although this is true for the growth of the first layer, the smoothness of the layers that are grown seem to greatly suffer from kinetic barriers associated with the surface integration (thereby introducing surface 'roughness'), where uneven affinity to newly adsorbing NDT render stacking non-uniformly across the surface area (Figure 4.25). Furthermore, we observe no molecular rearrangement involved at the surface. Therefore, we clarify that the inability of the molecules to detach and reorient through surface diffusion may serve to impede uniform layer growth.

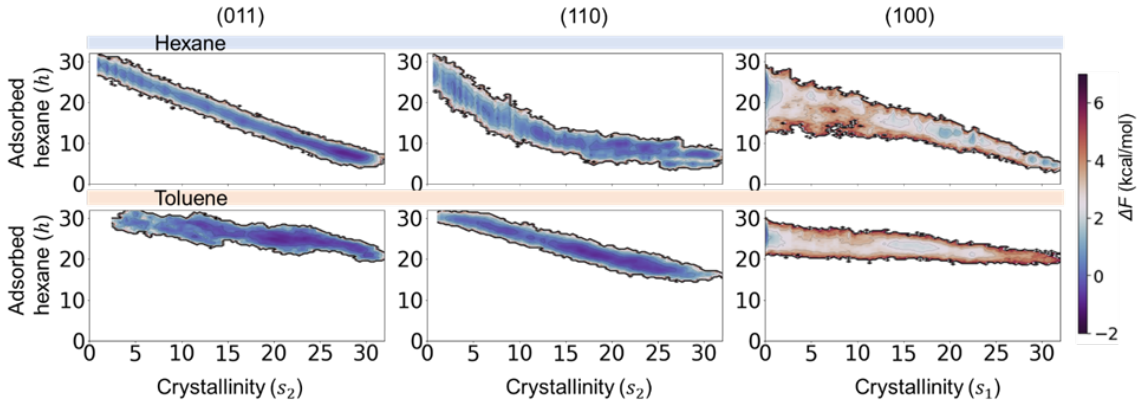

Figure 4.27 Free energy surfaces (FES) of NDT crystal layer growth on the faces (011), (110), and (100) in hexane and toluene expressed in terms of crystallinity descriptors s_1 or s_2 with solvent adsorption (h), sampled from 60 ns of simulation time.

From trajectory visualizations, the growth normal to the (011) and (110) planes does not appear to be uniform across the plane, as the anisotropy associated with molecular short- and long-axes impact growth directionality; faster growth is observed along the molecular short axis (co-facial) stacking direction of the molecules (which in fact belongs to the (100) plane when orthogonal direction is considered), whereas slower growth is seen along the molecular long axis direction. We also highlight that the growth orthogonal to both the planes can be quite fast as again it comes to molecular short axis stacking direction (Figure 4.25), belonging to the (100) plane (when considered orthogonally to the plane), as predicted by the BFDH model.

4.4 Conclusions

The results of the atomistic simulations of NDT crystal growth described here uncover molecular-scale insights pertaining to varied crystallization mechanisms as a function of the solvent environment, concentration, and temperature. Comparing crystallization under distinctively different solution environments, we reveal that the varied non-ideal behaviors of the solution, in terms of solute-solvent interactions plays a dominant role on the overall crystallization mechanism adopted by the organic molecules. We confirm that weaker solute–solvent interactions promote phase separation that can speed up the crystallization process. However, overly high driving forces for phase separation can serve to negatively impact assembly, as the molecules often can find themselves in unfavorable, kinetically trapped conformations.

The homogenous crystallization of NDT is shape anisotropic and is contingent on the formation of a thermodynamically metastable critical nucleus, formed through molecular short-axis stacking. The uniformity of short axis edge-to-face interactions among neighboring molecules enabled through herringbone packing pattern stabilizes 2D layer growth reinforced by a 2D network of favorable interactions. On the contrary, the slow growth rates associated with the molecular long-axis stacking directions (despite the long-axis herringbone packing assist faster growth to some extent) is due to the non-uniformity associated with the interactions across the surface. We reveal that this not only determines the overall crystal shape, but also the roughness evolution of the crystal surfaces, directed through 3D island formation (i.e., Stranski-Krastanov or Volmer-Weber Islands[34-36]) over smooth layer-by-layer growth (Frank-vander-Merwe growth[37]) on top of the substrate surfaces, which is an important parameter to control during thin

film growth. We also clarify that the surface integration of new molecules onto the crystal surfaces with more exposed (near) in-plane π-interactions are less affected by the solvent interaction dynamics, however such increased interaction strengths can often introduce kinetic barriers against smooth layered assembly. We further uncover details of the thermodynamic and kinetic factors associated with the surface nucleation and growth of the crystal as a function of temperature.

The descriptive, atomic-scale details of the crystallization mechanisms as a function of different solution environments, supersaturation levels, and temperatures reveal how one can vary process conditions to regulate crystallization of herringbone-based molecular crystals. Notably, the molecular material considered here has no strong crystallinity director, a common feature of molecular systems used found in organic semiconductors and other applications. Control of these variables allow one to fine tune surface roughness, crystal domain size, and crystal shape, allowing for the development of precise process protocols to optimize crystallization.

CHAPTER 5. THERMAL TRANSITIONS OF HERRINGBONE-PACKED ORGANIC SEMICONDUCTORS: INFLUENCE OF CHEMICAL MODIFICATIONS ON MELTING AND SOLIDIFICATION

5.1 Introduction

OSC are of interest as the active layer across a wide range of electronic and optical applications.[1] In addition to the capability to fine tune OSC electronic, redox, optical, and mechanical response through organic synthesis, OSC have demonstrated capacity to be readily developed via high-throughput, robust, and low-cost processing.[2-4] The ability to govern the solid-state morphology, from local molecular-scales through the bulk material, is critically important to OSC response. While there exist strategies to design the static properties of the OSC molecular building blocks, reliable control OSC morphologies through chemical or process design requires understanding the dynamic interactions of the molecules in different phases.[4-6]

The exploration of OSC thermal transitions and the associated phase behavior can reveal important structure–function insights relevant to morphology, thereby associated properties including charge-carrier transport, mechanical properties, and operational durability under varied environmental conditions.[7-11]. Here, we use classical molecular dynamics (MD) simulations to simulate phase transitions for a series of crystalline OSC wherein the rigid molecules that serve as the OSC building blocks vary in terms of their molecular structure (topology), chemistry, and symmetry to reveal how these characteristics impact dynamics associated with molecular (dis)assembly and order as a function of temperature. The molecules are each four-ringed chromophores, with their

chemical compositions and key experimentally derived thermal transitions shown in Figure 5.1. We compare phase transformations between solid OSC crystals to the melt to provide comparative descriptions as to how the differences in chemical composition e.g., the presence of thiophene or phenyl groups in the four membered chromophore structure, translate into variations in molecular (dis)assembly and (dis)order.

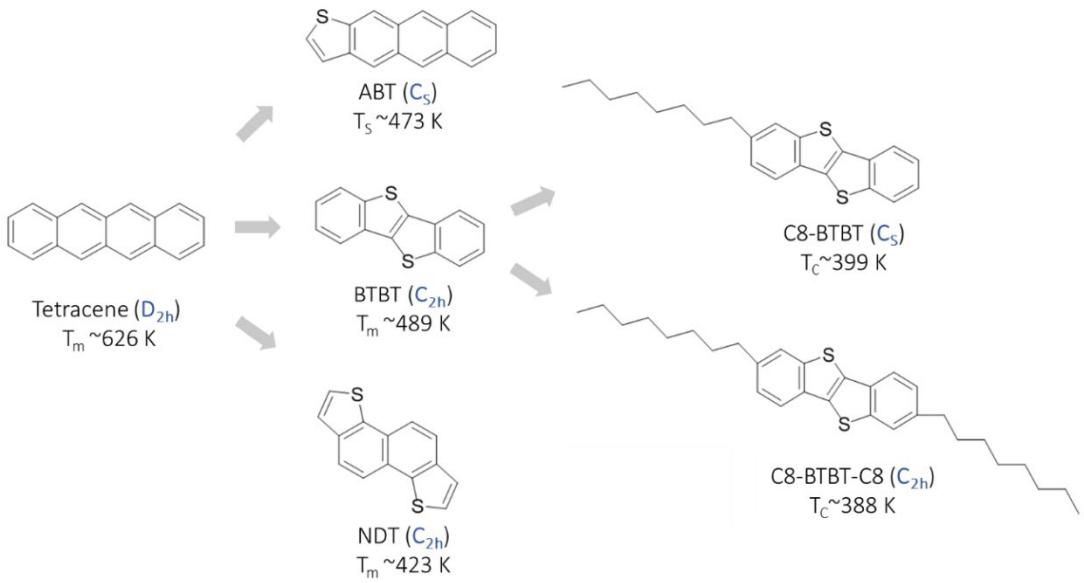

Figure 5.1 Schematic diagram of the chemical structures of the molecules and select experimentally reported thermal properties (sublimation T_s, melt T_m, and crystallization T_c)[12-16] of the OSC studied here. Corresponding molecular symmetries are provided in blue text.

We identify phase changes exhibited by the molecules by observing density profiles upon heating and cooling, where drastic changes in gradient signify the possible existence of phase transitions. We also express different intermolecular interactions dominant in each crystallographic face through collective variables (CV) with respect to molecular short-axis or long-axis stacking directions, defined in terms of intermolecular center of mass distances obtained by radial distribution functions (Figure 5.2).

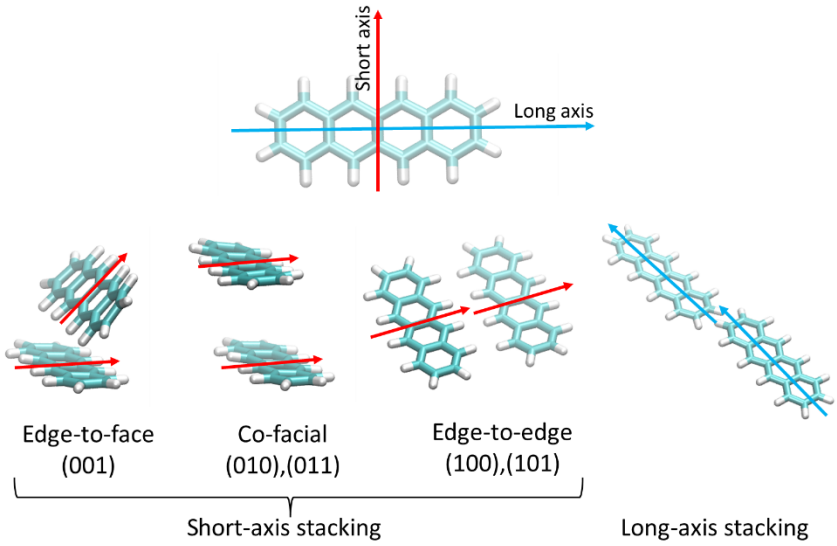

Figure 5.2 Types of short- and long-axis stacking types isolated in crystallographic faces of the case of tetracene crystal structure. Vectors representing short-axis and long-axis of the molecules are shown in red and blue arrows respectively.

We uncover types of molecular stacking/packing that are involved in different phase transitions in terms of both melting and cooling processes in combination with density variations: In other words, a CV that is relevant to a particular face reveals how well the equilibrium structural integrity of that particular crystallographic face is maintained as a function of temperature. Thereby we monitor molecular assembly/disassembly into order/disorder during phase transformation, contributing to the overall melting or solidification/crystallization. We make relationships as to how similarities/dissimilarities between melting and cooling can be made through the information revealed by different molecular packing types. In return we uncover first-principles understanding necessary to overcome limitations associated with the development of advanced OSC technologies.

5.2 Methods

All molecular dynamics (MD) simulations and quantum calculations were carried out through a fully automated simulation scheme developed in Python 3.8. The MD simulations were carried out using GROMACS software version 2020.3[17, 18] patched with the GMXAPI python interface[19] for staging and running simulations from Python 3.8 and PLUMED plugin version 2.7[20, 21] for post-processing calculations. Molecular topologies were automatically generated by incorporating the Antechamber Python parser interface (ACPYPE)[22] with the all-atom general Amber forcefield (GAFF)[23] used for obtaining bonding and non-bonding parameters. Density functional theory (DFT) calculations were automated at the ωB97XD/6-31G(d,p) level of theory[24, 25] to obtain partial charges in terms of the Charge Model 5 approach[26] using the Gaussian 16 software suite.[27] The automated algorithm takes a crystallographic information file (CIF) as an input and performs partial charge calculations on extracted, isolated molecules via DFT using the OCELOT Python interface.[28] Then, the procedure uses ACPYPE interface to automatically create the MD level topology files by incorporating DFT level charges with the GAFF forcefield. Crystal structures are then generated based on the experimental crystallographic cell parameters. The generated crystal structures are input into GROMACS energy minimization/relaxation protocol, then are subjected to thermal annealing (melting and cooling) procedure through GROMACS simulated annealing algorithm.

The validity of the automated topology generation and the GAFF forcefield was confirmed (Table 4.2) by comparing the simulated crystal supercell structures at their corresponding cell measurement temperatures and comparing the MD generated crystal

structure parameters with experimental values. Crystal supercell dimensions in terms of the repeat units were maintained to be roughly cubic in shape (while allowing their natural unit cell types – whether monoclinic or triclinic box type) and have approximately 2000 molecular units in size using the automated algorithm to improve accuracy of simulations. For each system, the equilibration procedure entails one initial steepest-decent energy minimization (2 ns), followed by one NVT (constant number of molecules N, volume V, and temperature T) ensemble (2 ns) with the initial velocities assigned through Maxwell-Boltzmann distribution, and two NPT (constant number of molecules N, pressure P, and temperature T) ensembles. The NPT ensembles operate under: Firstly, the Berendsen barostat algorithm[29] for the pre-equilibrium step (for 10ns), and, secondly, the Parrinello−Rahman barostat algorithm[30] for a more accurate equilibration (for 50 ns). Both barostats incorporated a coupling time of 1.0 ps and a compressibility of 4.5×10^{5} bar^{-1}. The velocity rescaling thermostat was used to couple the temperature of the simulation boxes corresponding to their experimental cell measurement temperatures. Periodic boundary conditions (PBC) were applied in all (X, Y and Z) directions of the simulation box. Van der Waals and coulombic interactions were calculated using particle mesh Ewald (PME) method with spherical cutoff values of 1.4 nm. Hydrogen bonds were constrained using the LINearConstraint Solver (LINCS)[31] to their equilibrium values. Temperature annealing simulations were carried out using GROMACS with heating rate of 20 K/ns and two comparative cooling rates: 20 K/ns and 10 K/ns.

The BFDH steady state crystal morphology was generated using CCDC Mercury advanced tools.[32] All surfaces with highest relative surface areas were selected and slabs of one-layer thickness of each crystallographic face was saved as *.pdb format.

GROMACS editconf function was used to convert the slabs into *.gro format which were then passed into the *rdf* (radial distribution) function (RDF) with the flags *-seltype* and *-selrpos* were chosen to have *whole_res_com* selection. The RDF of the entire supercell structure was also calculated using the same procedure and the RDF peaks were compared to develop collective variables using PLUMED plugin with SMAC CV to highlight specific aromatic stacking between molecules of the crystal slabs, both in terms of molecular short axis and long axis, that in turn used describe the crystallinity of each crystallographic face. The tallest RDF peak(s), appearing first along center of mass distance was used with slab visualizations to isolate molecular stacking in terms of the short-axis alignment; for the long-axis stacking, intermolecular distances were first measured using VMD visualization software[33, 34] to compare with the RDF peaks the corresponding RDF distances to avoid overtone peaks. More details and the parameters of the developed CVs corresponding to each crystallographic face are provided in supplementary information and additional files.

5.3 Results and discussion

We begin our investigation with TET as the base molecule, owing to its four fused benzene rings and D_{2h} molecular symmetry. Radial distribution function (RDF) profiles that compare the bulk crystal and the crystallographic faces obtained from the BFDH model are shown in **Figure 3**. From the RDF profiles, each crystallographic face can be characterized as a function of the dominant intermolecular short-axis stacking types: Edge-to-face at a center-of-mass (COM) distance of ~0.5 nm (see the teal RDF profile corresponding to the (001) face), edge-to-edge stacking at a COM distance of ~0.6 nm (see the gold RDF profile corresponding to the (010) and (011) faces), and face-to-

face stacking at a COM distance of ~0.78 nm (see the red RDF profile corresponding to the (100) and (101) faces). The intermolecular long-axis stacking interaction occurs at a COM distance of ~1.23 nm (extracted from the grey RDF profile with the aid of measured distances from visualization tools).

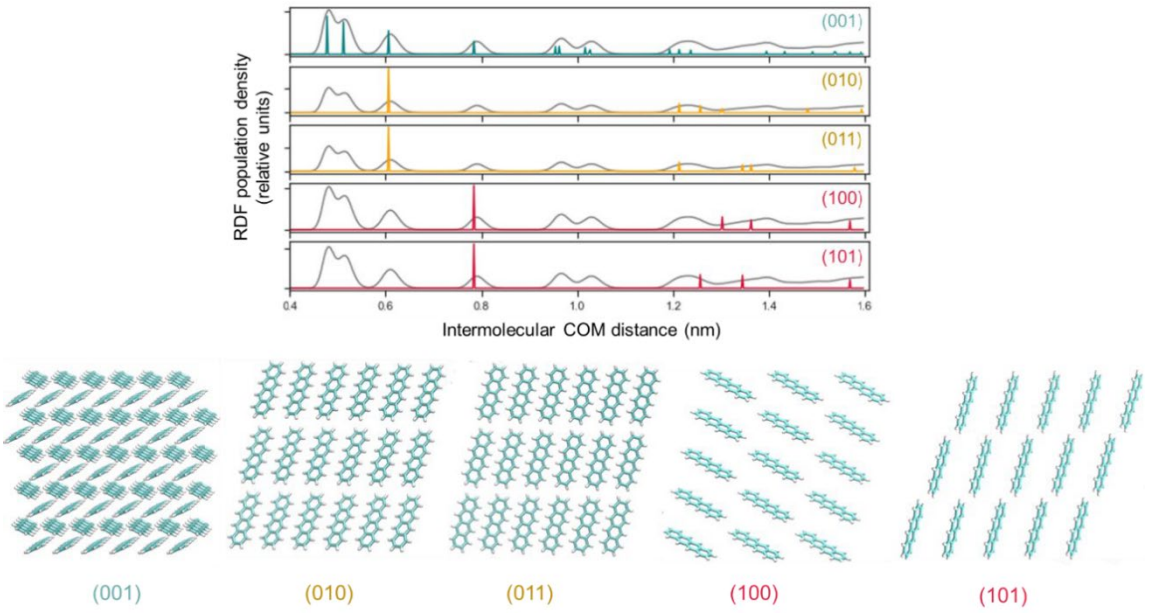

Figure 5.3 (top) Radial distribution function (RDF) plots for the bulk TET crystal (grey lines) and for specific crystal planes as depicted by the teal, gold, and red color peaks that are used to resolve the dominating intermolecular stacking types: Teal represents edge-to-face, gold represents edge-to-edge, and red represents face-to-face type intermolecular stacking of the (bottom) TET crystal lattice planes.

During melting and cooling, TET shows quite similar and reversible characteristics in terms of the CV and density versus temperature curves (Figure 5.4). The CV correspond to molecular short-axis order are shown in respective colors of their RDF profiles, and that of the molecular long-axis order is shown in blue color. The density profile is shown in purple. As expected, during melting and cooling, the density

profiles reveal clear phase changes between the solid and melt phases, indicated by the large density changes.

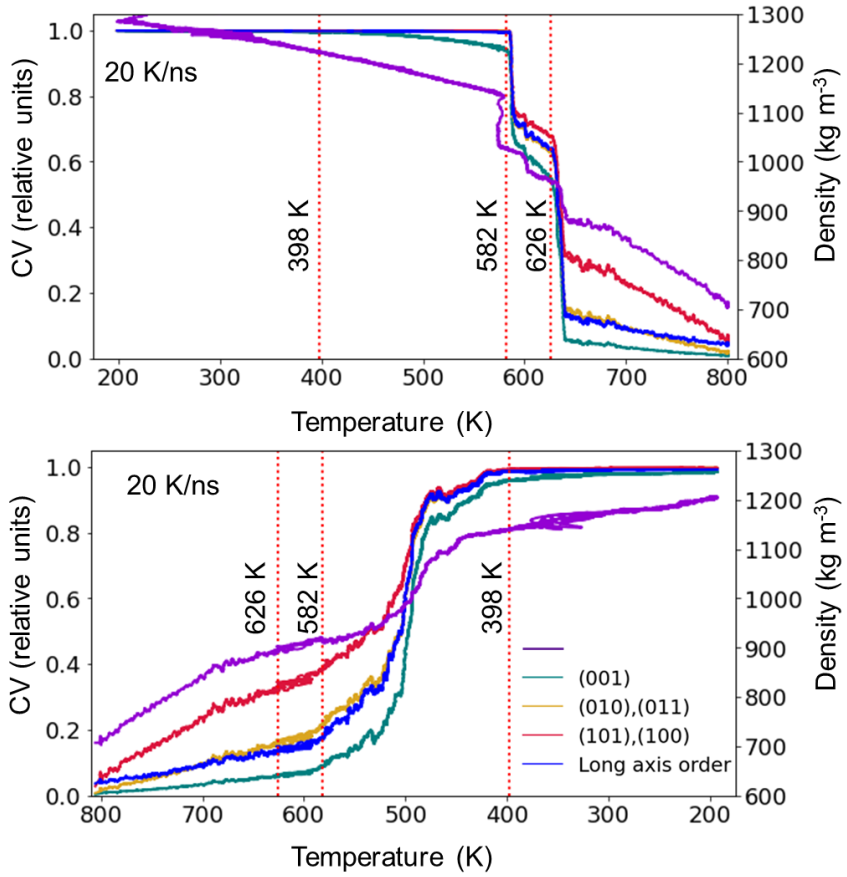

Figure 5.4 Density and CV versus temperature profiles for TET along (top) heating from the solid to the melt and (bottom) cooling from the melt to the solid. The colors correspond to the density and dominant interaction types in terms of the intermolecular distances as determined by the RDF.

As the solid TET is heated, but prior to melting (before ~ 550 K), the crystallinity of the (001) face (teal line) is the first to decrease / change, signifying the loss of edge-to-face short-axis stacking order that causes the density to decrease. The integrity of the other CV with relevance to edge-to-edge and face-to-face stacking, along with the long-axis stacking order, however, are maintained until melting begins (i.e., the drastic drop in

density and all CV). The phase transition is signified by the regions where density and CV values drop dramatically. Once melted, the (001) crystallinity is almost absent. The major stacking order type seen along (101), (100) faces, i.e., face-to-face stacking at ~0.78 nm COM distance, are somewhat present on average in the immediate melt; however, they slowly disappear with further temperature increase.

Visualizations confirm that the crystal starts to melt in a layer-wise fashion, losing the crystallinity of the (001) face (Figure 5.5), as exhibited by the CV profiles. Experimental data suggest two solid-solid transitions (~398 K and ~582 K) and melting at ~626 K, based in calorimetric measurements (with heating rate 0.5 K/min – a very slow rate compared to the rate of the anneal simulation).[12] Notably, T_m from the simulation is ~580 – 650 K, which is quite close to the experimental value mentioned above. However, during cooling, the obtained T_m is ~500 K. Such difference in T_m with the melting and cooling curves are typically caused by superheating/supercooling effects,[7, 8] which are associated with the periodic boundary conditions used to approximately represent infinite bulk of crystal in the simulations. Such approximation generally leads to overestimation of phase transitions due to the near-perfect integrity of the bulk crystal, in combination of the limitations arising from short time scales used to traverse large temperature ranges in the simulated annealing procedure. Also, we do not observe clear solid-solid crystalline phase transitions during either heating or melting, as reported in the experimental data,[12] though some discrepancies of the density and CV curves are observed at ~350 K, which may be indicative of these subtle transitions.

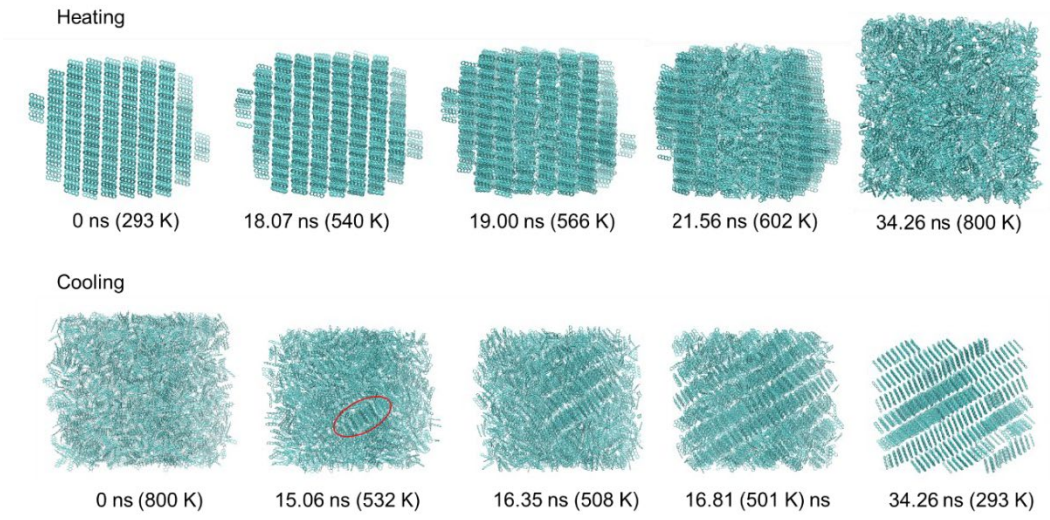

Figure 5.5 Trajectory visualizations as tetracene (top) melts from the crystal to the liquid and (condenses) from the melt to the solid at 20 K/ns rate. The simulation times and corresponding temperatures are noted. The red circle shows the region where herringbone packing begins to form during recrystallization.

Solidification from the melt has quite similar (but reversed) features to the melting curves: Upon cooling, the (101) and (100) order is increased first, i.e., the face-to-face stacking at ~0.78 nm is first developed, while the (001) order of the edge-to-face stacking increases next which is then accompanied by an increase in the orders for all other faces along with the long-axis order slowly (recall this order of CVs is reversed in the case of melting). The final crystal structures obtained for the recrystallization at two rates, 20K/ns and 10 K/ns (Figure 5.6), are both similar to the original crystal structure, though voids are present, these voids result in a somewhat smaller solid-state density than that of the experimental bulk density. The simulated solid recrystallized from the slower cooling rate results in a slightly larger density, due to decreased kinetic effects, pointing to more-feasible thermodynamic equilibration at slower cooling.

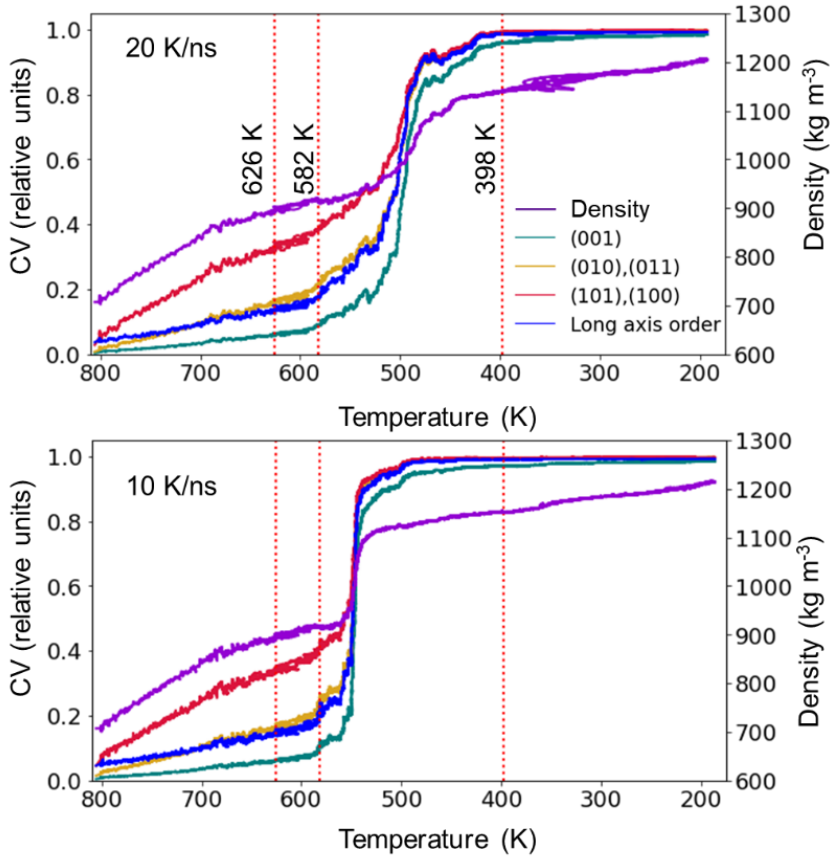

Figure 5.6 Density curves and collective variables (CV) corresponding to crystal planes versus temperature for tetracene for cooling simulations at either (top) 20 K/ns or (bottom) 10 K/ns rates.

Visualizations along the cooling trajectories confirm that upon recrystallization, the molecules assemble together with face-to-face and edge-to-edge stacking ((101) and (100) faces), that is then followed by layers of edge-to-face stacking order ((001) face) appearing before the achievement of overall crystalline bulk attributes (i.e., crystal nucleation – Figure 5.5).

We now turn to anthra(2,3-b)thiophene (ABT) and its associated phase transitions. Note that ABT contains one terminal thiophene group, replacing one benzo group in the TET backbone structure. This substitution introduces asymmetry, changing

the symmetry from D_{2h} in TET to C_s in ABT. Both TET and ABT have platelet crystal morphologies. We note that no experimentally reported melting temperatures were found for ABT, though reports indicate that crystalline ABT is vacuum deposited by sublimation (~463 – 473 K) during fabrication.[13]

The crystallographic faces from the BFDH model, and their RDF peaks in comparison to the RDF peaks obtained for the bulk crystal, are shown in **Figure 5.** From the RDF profiles, each crystallographic face is characterized as a function of the dominant intermolecular short-axis stacking types: edge-to-face at a COM distance of ~0.5 nm (see the teal RDF profile corresponding to (002) and (110) faces), shifted edge-to-edge stacking at COM distance of ~0.6 nm (see the gold RDF profile corresponding to (011) face), and face-to-face stacking at a COM distance of ~0.77 nm (see the red RDF profile corresponding to (101) face). The intermolecular long-axis stacking resides at a COM distance of ~1.2 nm (extracted from the grey RDF profile and though visualization measurement tools).

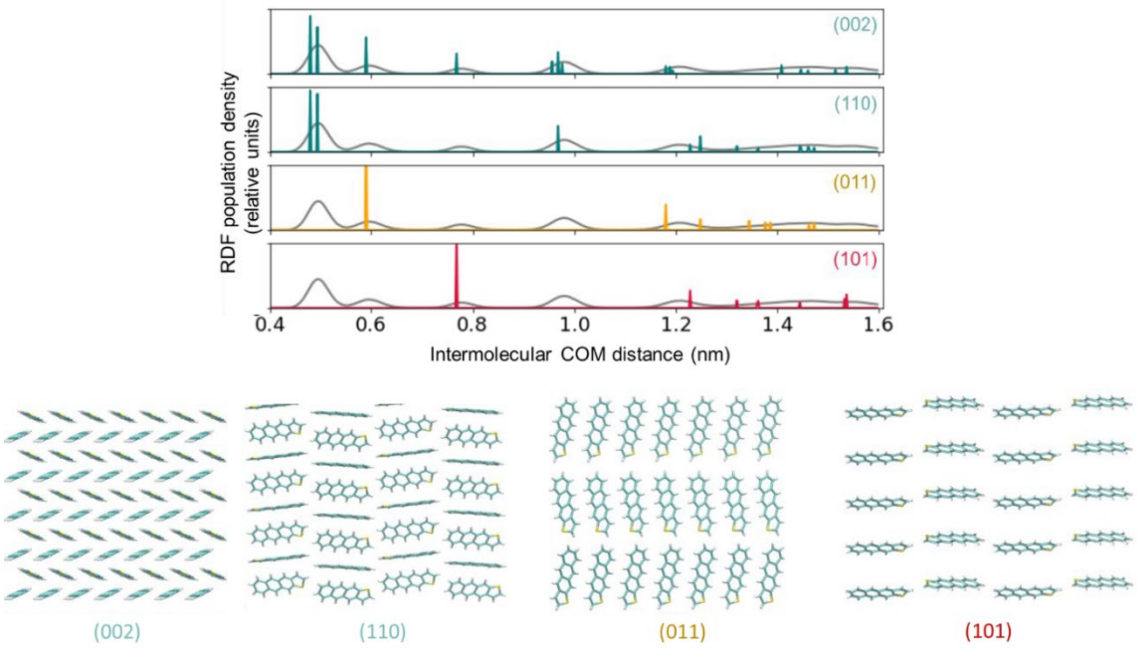

Figure 5.7 (top) Radial distribution function (RDF) plots for the bulk ABT crystal (grey lines) and for specific crystal planes as depicted by the teal, gold, and red color peaks that are used to resolve the dominating intermolecular stacking types: Teal correspond to edge-to-face, gold represents edge-to-edge, and red represents face-to-face type intermolecular stacking (bottom) of the ABT crystal lattice planes.

The density versus temperature curve upon heating reveals a clear phase transformation between solid and liquid within the range of temperatures investigated, along with the CV curves following clear trends highlighting solid-melt transition (Figure 5.8). A prominent superheating is observed for ABT during melting with the phase transformation identified near 790 K, however, during cooling, the melt phase crystallizes around 510 K, as shown by the density and CV curves. Before melting, we observe as in TET the edge-to-face short-axis stacking ((002) face) for ABT being the first to disassemble and causing the density to decrease (confirmed with visualizations – Figure 5.9), while the CV of other faces and long axis order remain quite unchanged.

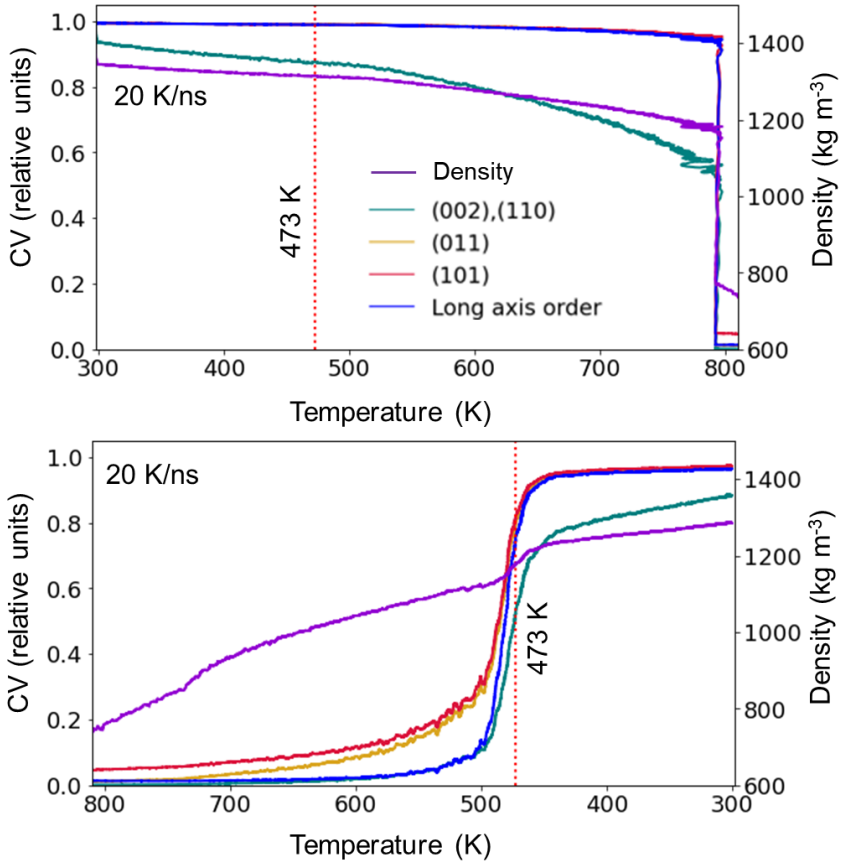

Figure 5.8 Density and CV versus temperature profiles for ABT along (top) heating from the solid to the melt and (bottom) cooling from the melt to the solid. The colors correspond to the density and dominant interaction types in terms of the intermolecular distances as determined by the RDF.

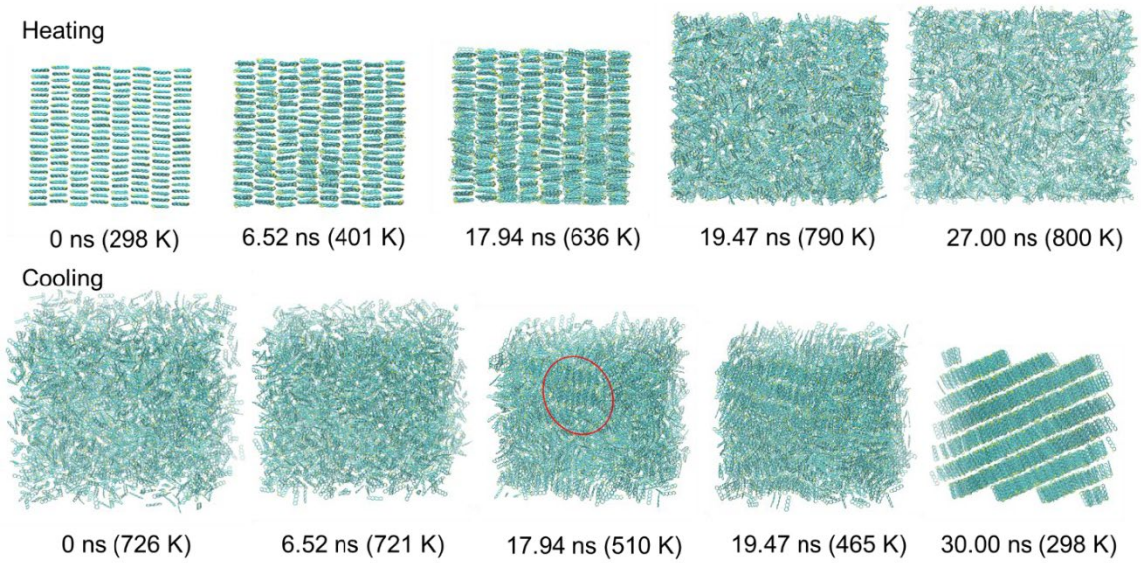

Figure 5.9 Trajectory visualizations as ABT (top) melts from the crystal to the liquid and (condenses) from the melt to the solid at 20 K/ns rate. The simulation times and corresponding temperatures are noted. Red circle point to the region with herringbone packed layer formation during recrystallization.

For the phase transition from solid to melt upon heating, all CV and densities drop drastically, except for the CV of the (101) face that retains some level of co-facial stacking at ~0.77nm stacking distance during melt, an observation that was seen in the case of TET. Cooling (recrystallization) at both cooling rates (20 K/ns and 10 K/ns, Figure 5.10) generates crystal structures with almost the exact density of the original crystal, with no voids/defects being present. The CV curves confirm that the recrystallized bulk structure is very similar in composition to the original crystal used to melt.

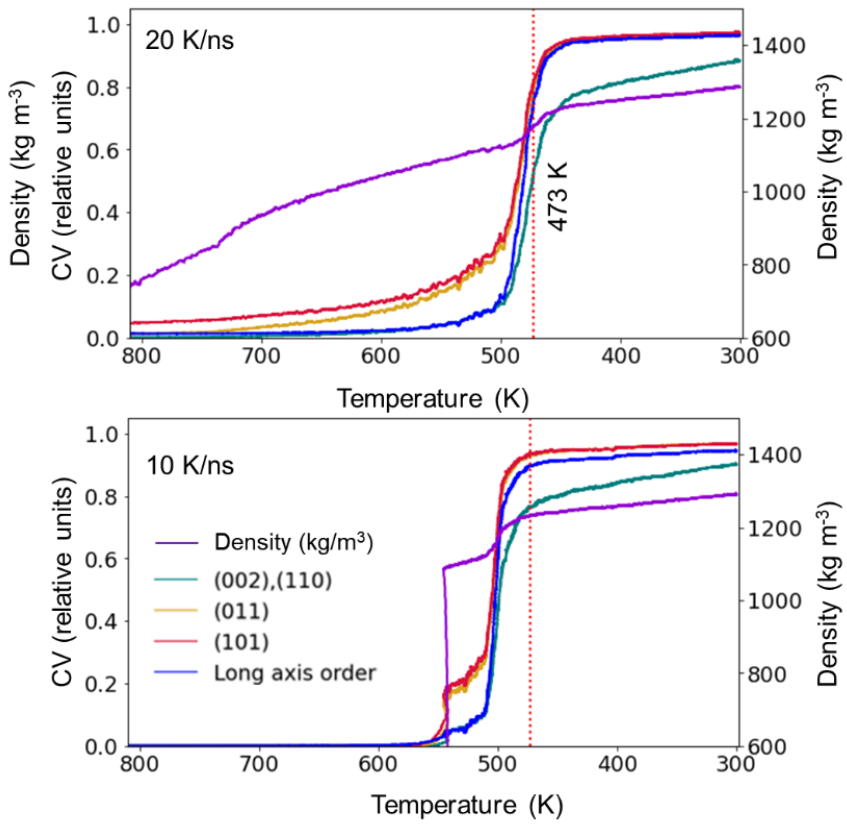

Figure 5.10 Density curves and collective variables (CV) corresponding to crystal planes versus temperature for ABT for cooling simulations at either (top) 20 K/ns or (bottom) 10 K/ns rates.

During cooling, the CV corresponding to co-facial and edge-to-edge stacking order ((101) and (011) faces) increase first (an observation similar to the case of TET cooling), which then accommodate an increase of edge-to-face short-axis order of the (002) face and the molecular long-axis order (Figure 5.9 and 5.10). Trajectory visualizations again confirm that, just like in the case of TET, the crystals start to nucleate in layer-wise fashion, here through the (002) face with short-axis edge-to-face stacking (Figure 5.9). Notably, the slow cooled simulation at 10K/ns rate starts in the gas

phase at 800 K (as superheating is minimized at slower anneal rates – recall that according to experimental data, ABT should be a gas at 800 K), and after 650 K, the CV curves become quite similar to that of the case of faster cooled simulation at 20K/ns; both cooling rates the achieve the bulk crystal in similar fashion (Figure 5.10).

Next, we move to naphtho[1,2-b:5,6-b']dithiophene (NDT) transitions. NDT had two terminal thiophene group, replacing the end benzo groups of TET, resulting in C_{2h} molecular symmetry. RDF peaks for the BFDH crystallographic faces and bulk crystal structure are shown in Figure 5.11**.** The bulk crystal structure of NDT is more complicated when compared to the previous examples, with the edge-to-face motif being present for both the short-axis and long-axis stacking directions; this is dissimilar to the cases of TET or ABT where edge-to-face packing is only present in terms of molecular short axis. From the RDF profiles, each crystallographic face is characterized as a function of the dominant intermolecular short-axis stacking types: edge-to-face at a COM distance of ~0.58 nm (see the teal RDF profile corresponding to (100), (111), and (011) faces), edge-to-edge stacking at COM distance of ~0.75 nm (see the gold RDF profile corresponding to (002) and (102) faces), and co-facial stacking at a COM distance of ~0.82 nm (see the red RDF profile corresponding to (110) face). The intermolecular long-axis stacking resides at a COM distance of ~0.97 nm (from grey RDF profile and though visualization measurement tools).

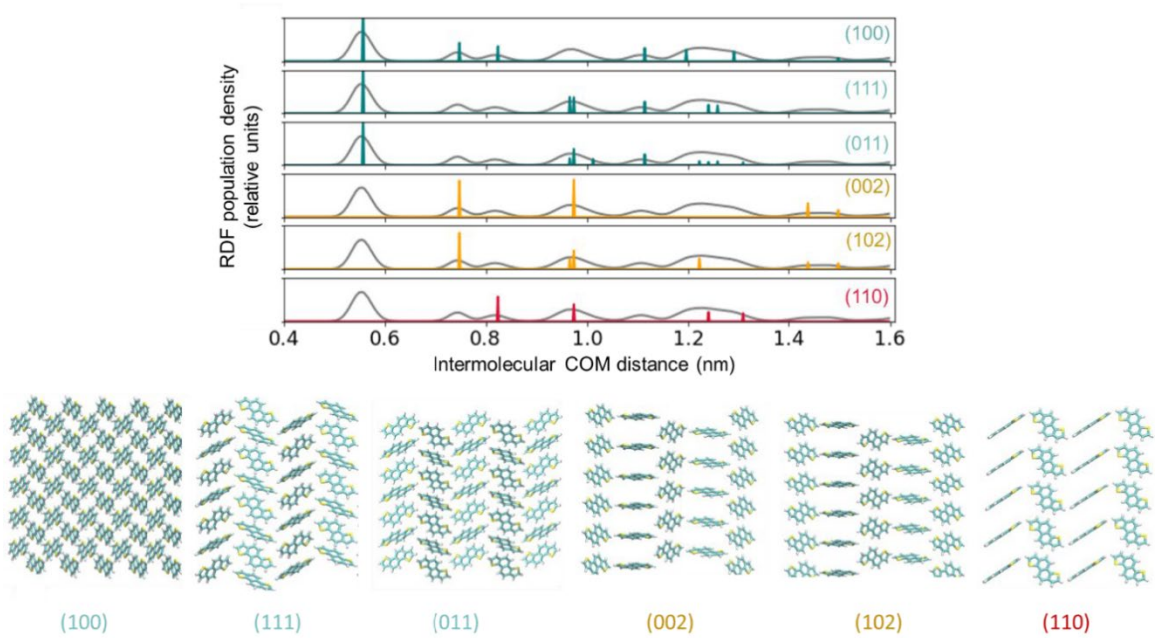

Figure 5.11 (top) Radial distribution function (RDF) plots for the bulk NDT crystal (grey lines) and for specific crystal planes as depicted by the teal, gold, and red color peaks that are used to resolve the dominating intermolecular stacking types: Teal correspond to edge-to-face, gold represents edge-to-edge, and red represents co-facial type intermolecular stacking (bottom) of the NDT crystal lattice planes.

For NDT, only the melting curves clearly indicate the presence of phase transformations, here from the solid to the melt at ~640 K (Figure 5.12); the experimentally determined T_m is ~423 K[14] (the disagreement between experiment and simulation again points to superheating). At temperatures prior to melting, the density and CV corresponding to short-axis stacking decrease gradually; both edge-to-face ((100), (011), (111) faces) interactions and co-facial stacking (faces (110), (102), and (002) faces) interactions start to lose structure upon heating, contributing to the decrease in density. The long-axis order however, is maintained before melting. During melting, all CV and density curves drop significantly. Note that for the earlier cases of TET and ABT, only the short-axis edge-to-face stacked structure was lost during the initial

heating, whereas the co-facial and long-axis orders were almost unchanged before melting occurred. Visualizations confirm that for NDT that the melting propagates in a non-layer-wise fashion with more than one type of crystallographic faces / stacking types being involved (Figure 5.13).

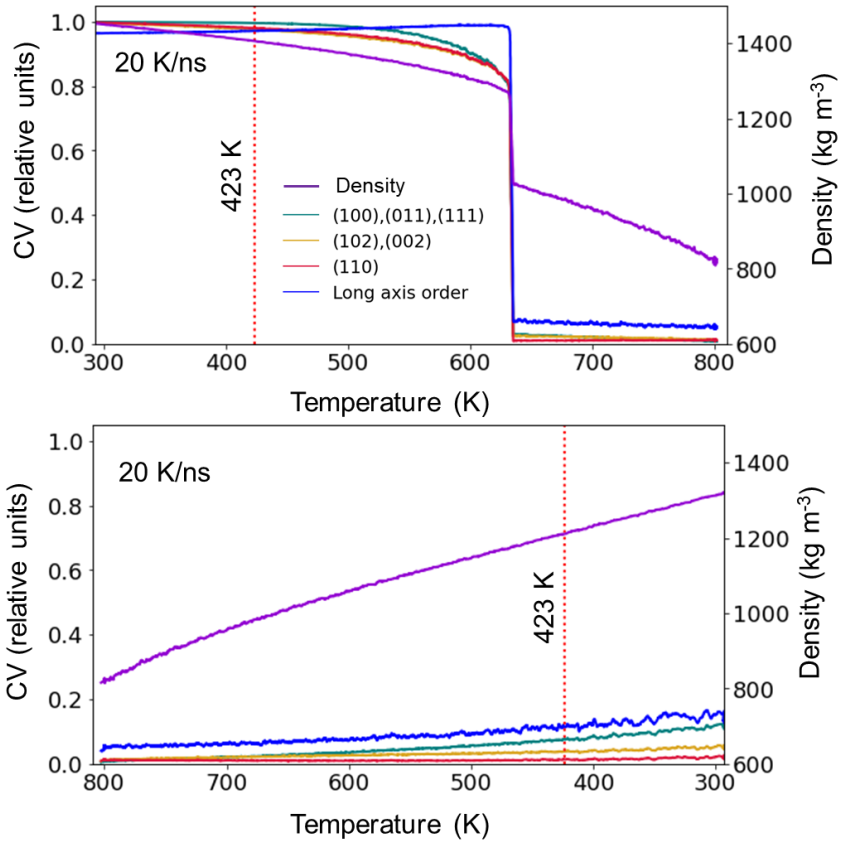

Figure 5.12 Density and CV versus temperature profiles for NDT along (top) heating from the solid to the melt and (bottom) cooling from the melt to the solid. The colors correspond to the density and dominant interaction types in terms of the intermolecular distances as determined by the RDF.

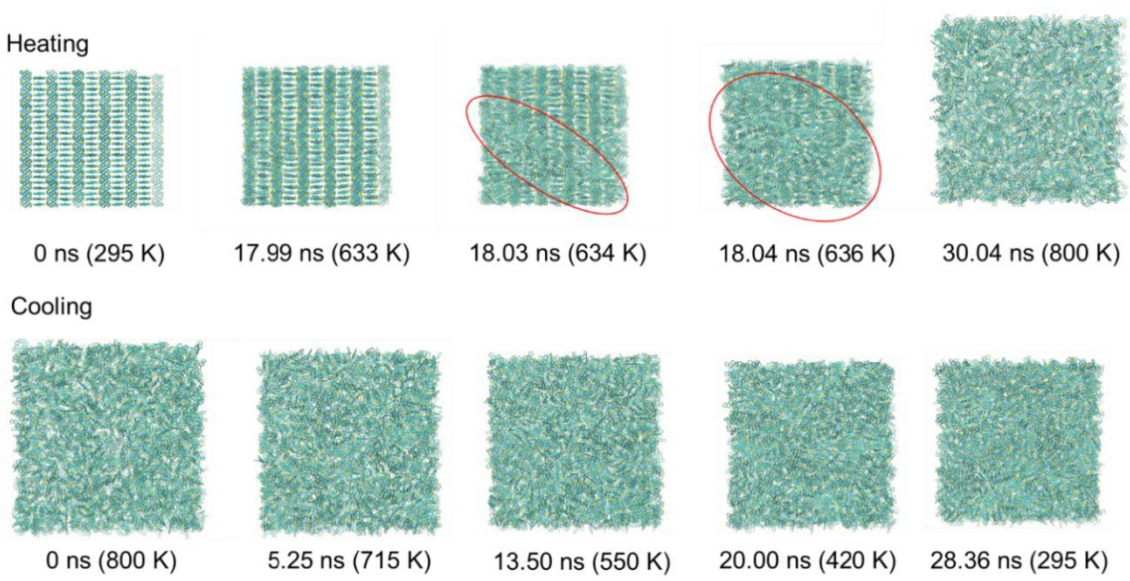

Figure 5.13 Trajectory visualizations as NDT (top) melts from the crystal to the liquid and (condenses) from the melt to the solid at 20 K/ns rate. The simulation times and corresponding temperatures are noted. The red circles point to the regions where the herringbone packing is lost, and the melt phase is propagated in a non-layer wise fashion during melting.

The density curves and CV profiles for NDT for cooling from the melt show a gradual density increase without a characteristic phase transition. Notably, the final solid does not achieve original crystal bulk structure in the time frame of the simulations, instead resulting in an amorphous-like solid phase for both cooling rates studied (20 K/ns and 10 K/ns, Figure 5.14). Visualization of the trajectories confirm that the final solid-state structure is non-crystalline and more amorphous when compared to the original bulk crystal (Figure 5.13).

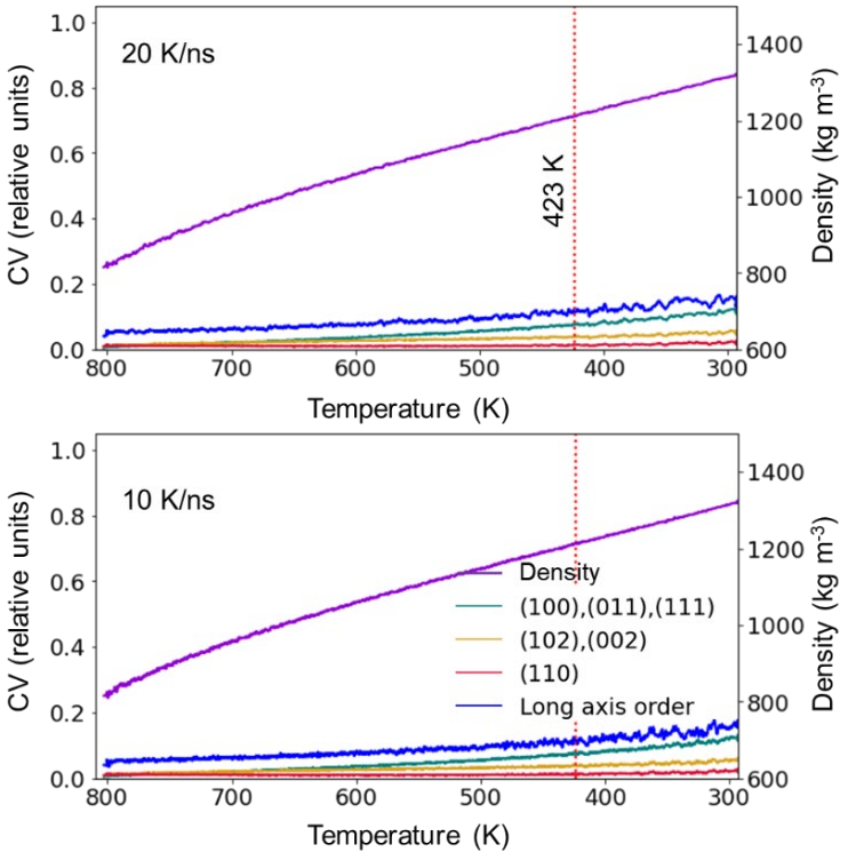

Figure 5.14 Density curves and collective variables (CV) corresponding to crystal planes versus temperature for NDT for cooling simulations at either (top) 20 K/ns or (bottom) 10 K/ns rates.

Moving to benzo[b]benzo[4,5]thieno[2,3-d]thiophene (BTBT), the ring system contains a fused thienothiophene group in the center, enclosed by benzo groups at either end; here, the symmetry is again C2h, as for the case of NDT. The BTBT crystal shows the edge-to-face packing motif. RDF peaks for the BFDH crystallographic faces and bulk crystal structure are shown in Figure 9. From the RDF profiles, each crystallographic face is characterized as a function of the dominant intermolecular short-axis stacking types: edge-to-face at a COM distance of ~0.5 nm (see the teal RDF profile corresponding to

(100), (111), and (011) faces), edge-to-edge stacking at COM distance of ~0.6 nm (see the gold RDF profile corresponding to (002) and (102) faces), and co-facial stacking at a COM distance of ~0.8 nm (see the red RDF profile corresponding to (110) face). The intermolecular long-axis stacking resides at a COM distance of ~1.17 nm (extracted from the grey RDF profile and though visualization measurement tools).

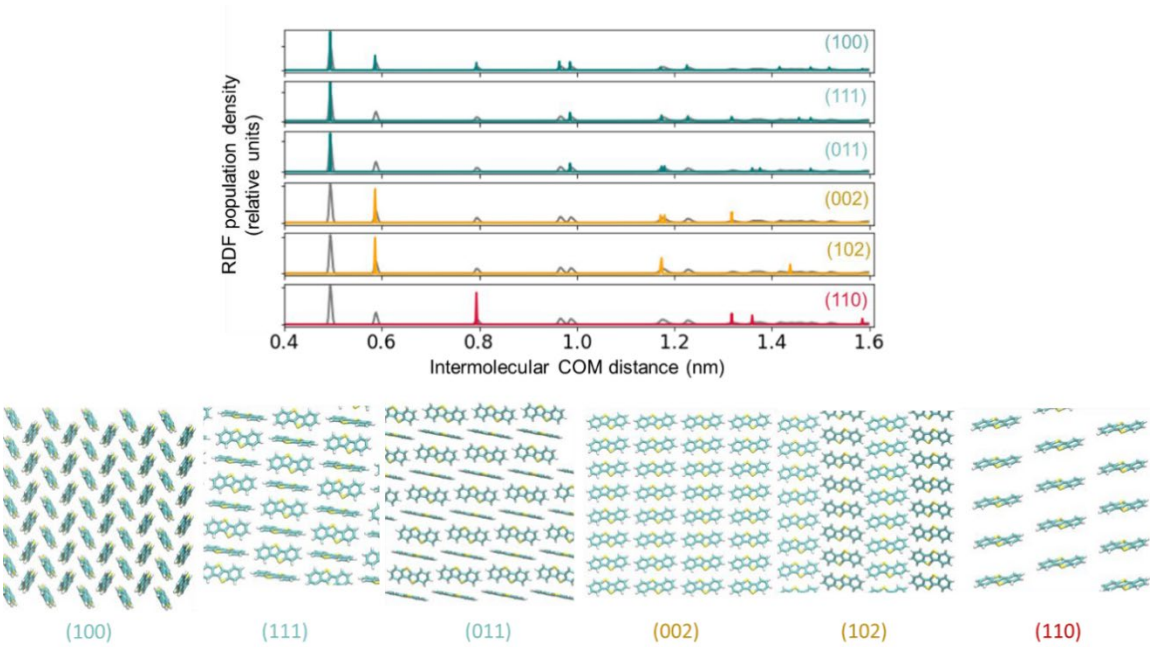

Figure 5.15 (top) Radial distribution function (RDF) plots for the bulk BTBT crystal (grey lines) and for specific crystal planes as depicted by the teal, gold, and red color peaks that are used to resolve the dominating intermolecular stacking types: Teal correspond to edge-to-face, gold represents edge-to-edge, and red represents face-to-face type intermolecular stacking (bottom) of the BTBT crystal lattice planes.

Upon melting, BTBT exhibits a clear phase transition at ~550 K; the experimental melting point is reported to be ~489 K.[15] Notably, before melting, the short-axis edge-to-face packing, as revealed by of the (100), (111), and (011) faces, show a clear and prominent decrease (teal line in Figure 5.16) starting at ~250 K that contributes to the drop in density. We note that the curve also shows some oscillatory behavior as a

function of the temperature, possibly originating from temperature coupling algorithm during faster heating. Here, we observe that the rate at which the edge-to-face packed short-axis stacking (teal) CV decreases with a clear change, starting from 250 K, which may be indicative of the presence of another solid-state crystalline phase transformation; no experimental data were available to confirm this observation. Before melting, all other CV maintain their structure until the phase transition occurs at ~550 K. Once melted, all CV drop drastically. Trajectory visualizations reveal no clear solid-solid transition before melting (Figure 5.17).

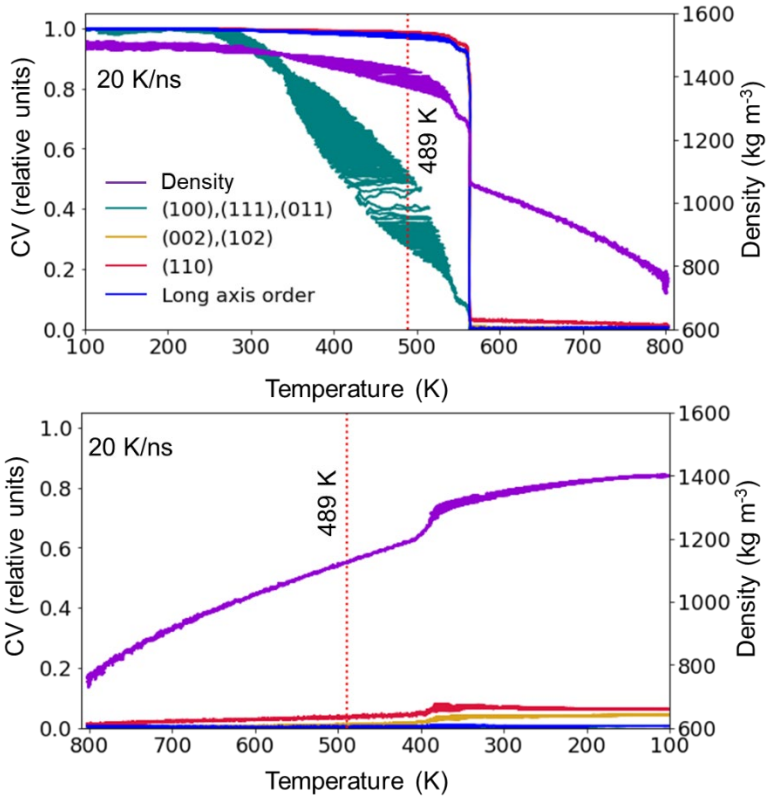

Figure 5.16 Density and CV versus temperature profiles for BTBT along (top) heating from the solid to the melt and (bottom) cooling from the melt to the solid. The colors correspond to the density and dominant interaction types in terms of the intermolecular distances as determined by the RDF.

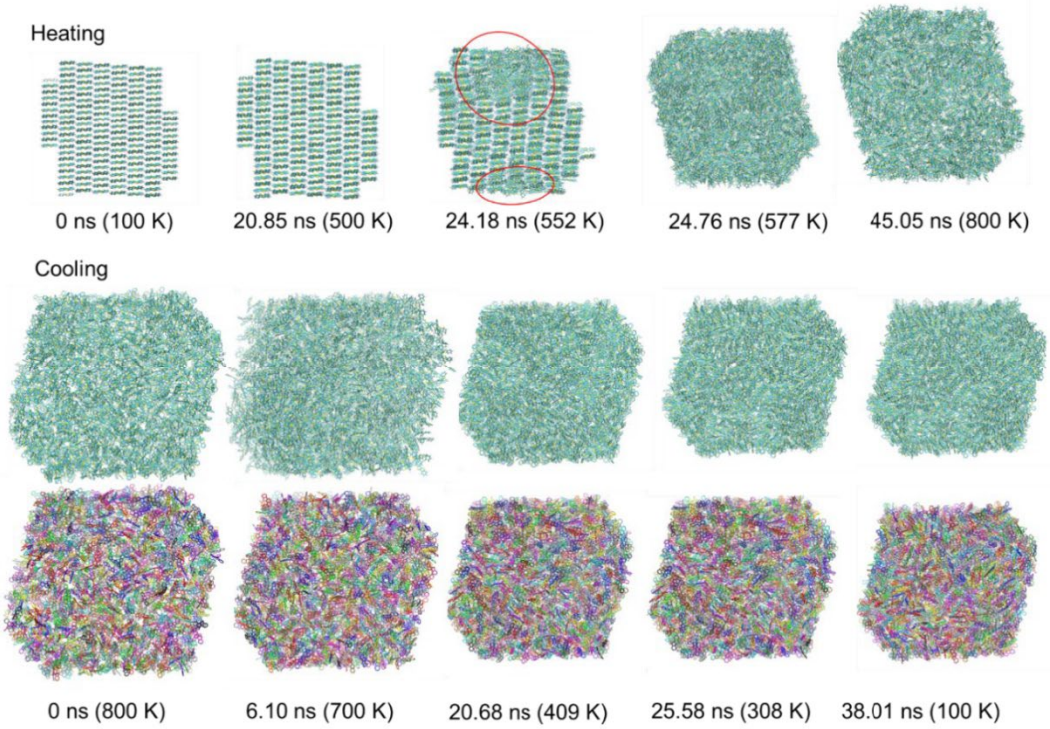

Figure 5.17 Trajectory visualizations as BTBT (top) melts from the crystal to the liquid and (condenses) from the melt to the solid at 20 K/ns rate. The simulation times and corresponding temperatures are noted. The red circles point to the regions where the crystal starts to melt in non-layer wise fashion. For the cooling process, a second visualization is provided to clarify molecule entrapment in an amorphous solid form from 409 K and below during cooling.

After cooling from the melt to the solid, the original crystalline bulk structure is again not observed, instead there is a generally amorphous solid state with some noted order obtained. A relatively weak phase transition (in terms of density) is marked at ~409 K for both cooling rates of 20 K/ns and 10 K/ns (Figures 5.18). The CV corresponding to the face-to-face and edge-to-edge stacking types ((110), (002), and (102) faces) show a noticeable increase, contributing to the increase in crystalline order, corresponding to the increase in density. However, we observe that this is not sufficient to regain the original crystalline order of the bulk (as this observation ranks in between the two extremes: NDT

with no crystallinity in the cooled solid, and TET/ABT that clearly indicate the formation of the original bulk crystal). Evidently, incorporating two S atoms in the molecular topology leads to delayed crystallization (as shown for both NDT and BTBT), where increased kinetic disorder is detrimental for achieving crystalline order.

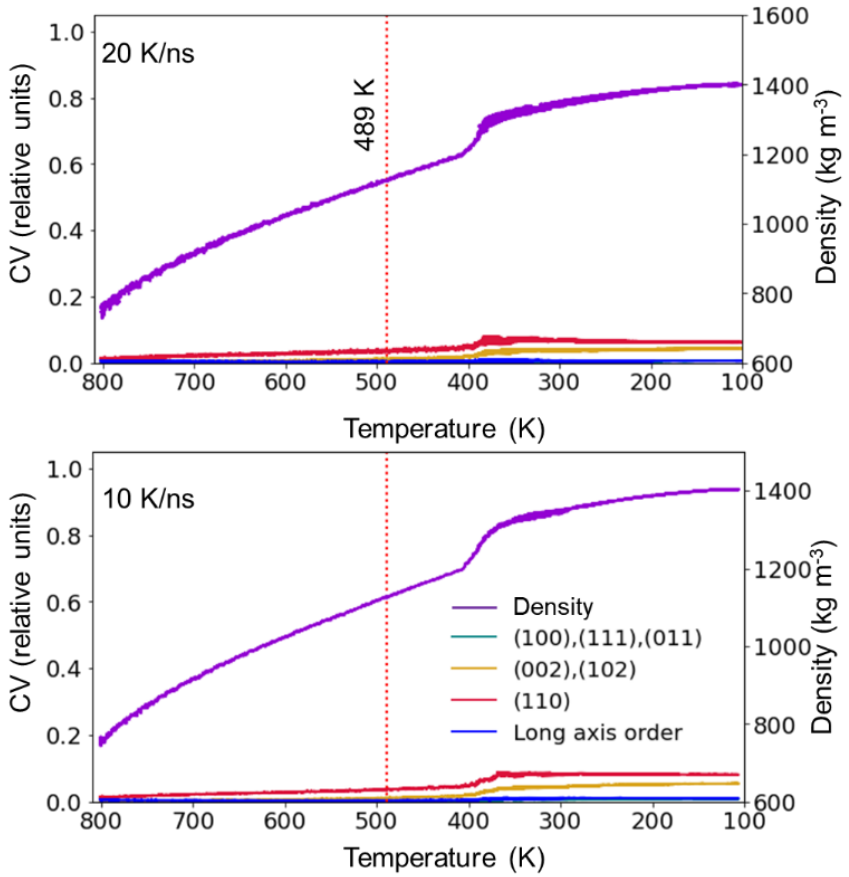

Figure 5.18 Density curves and collective variables (CV) corresponding to crystal planes versus temperature for BTBT for cooling simulations at either (top) 20 K/ns or (bottom) 10 K/ns rates.

We now move to the symmetrically octyl-substituted BTBT chromophore, which is 2,7-dioctylbenzo[b]benzo[4,5]thieno[2,3-d]thiophene (C8-BTBT-C8). The crystal structure reveals layered stacks of chromophores that give rise to efficient two-

dimensional charge transport.[16] RDF peaks for the BFDH crystallographic faces and bulk crystal structure are shown in Figure 5.19. From the RDF profiles, each crystallographic face is characterized as a function of the dominant intermolecular short-axis stacking types: edge-to-face at a COM distance of ~0.5 nm (see the teal RDF profile corresponding to (001), (110), and (111) faces), and edge-to-edge stacking at COM distance of ~0.6 nm (see the gold RDF profile corresponding to (011) face). The intermolecular long-axis stacking resides at a COM distance of ~3.0 nm (extracted from direct measurements through visualization tools).

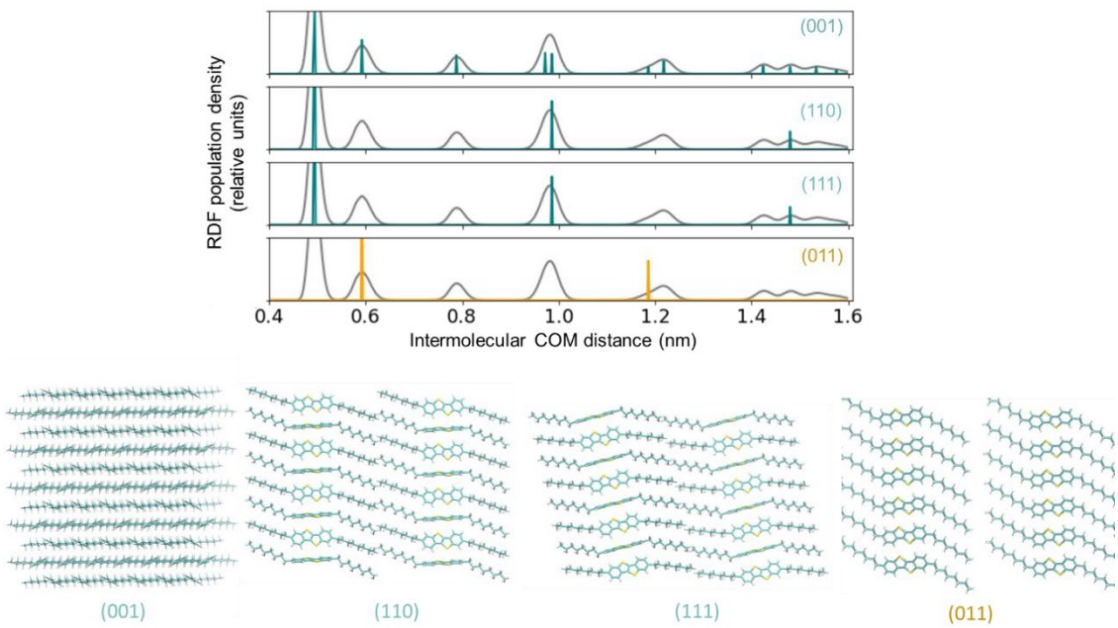

Figure 5.19 (top) Radial distribution function (RDF) plots for the bulk C8-BTBT-C8 crystal (grey lines) and for specific crystal planes as depicted by the teal and gold color peaks that are used to resolve the dominating intermolecular stacking types: Teal correspond to edge-to-face, gold represents edge-to-edge type intermolecular stacking (bottom) of the C8-BTBT-C8 crystal lattice planes.

Notable changes of the CV profiles are shown for the case of C8-BTBT-C8: Before melting, the C8-BTBT-C8 short-axis stacking is lost first, contributing to the density drop (Figure 5.20). A clear phase transition from solid to melt is then seen at ~450 K, where both the teal and gold CV curves drop significantly along with the density. The experimental melting is reported at ~399 K.[16] The edge-to-edge stacking of the (011) face (which corresponds to the gold CV curve) shows an apparent delay before losing its structure after melting compared to that of the CV curve for edge-to-face packing (shown by the teal curve). This suggests that the edge-to-edge stacked crystallinity is maintained quite well prior to melting, even after the edge-to-face short-axis stacking is completely lost. Interestingly, the long-axis order remains unchanged even longer, even after melting, (shown by the blue CV curve, that slowly loses its composition only after melting at ~450 K), indicating the presence of preserved long-axis order due to significantly stronger inter-alkyl chain interactions. Experimental data based on differential scanning calorimetry, X-ray scattering, dielectric spectroscopy, and rheological measurements of C8-BTBT-C8 report the existence of smectic liquid crystalline phase: Solid crystalline to smectic A ~110.1 C (~383 K), and Smectic A to isotropic liquid at ~126.4 C (~399 K).

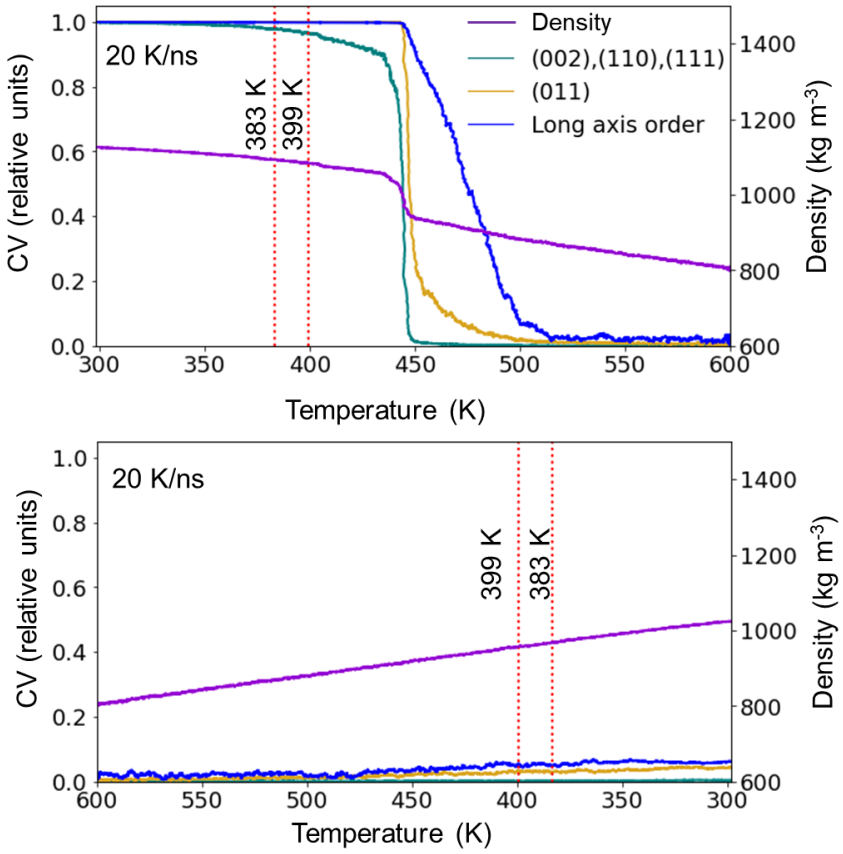

Figure 5.20 Density and CV versus temperature profiles for C8-BTBT-C8 along (top) heating from the solid to the melt and (bottom) cooling from the melt to the solid. The colors correspond to the density and dominant interaction types in terms of the intermolecular distances as determined by the RDF.

Through the trajectory visualizations, we observe that the delay region shown by both gold and blue CV indeed signify the existence of liquid crystalline type phases, where first a clear smectic phase with preserved long-axis order and some level of layer-wise periodicity that suddenly transforms into an isotropic liquid beyond 500 K (Figure 5.21).

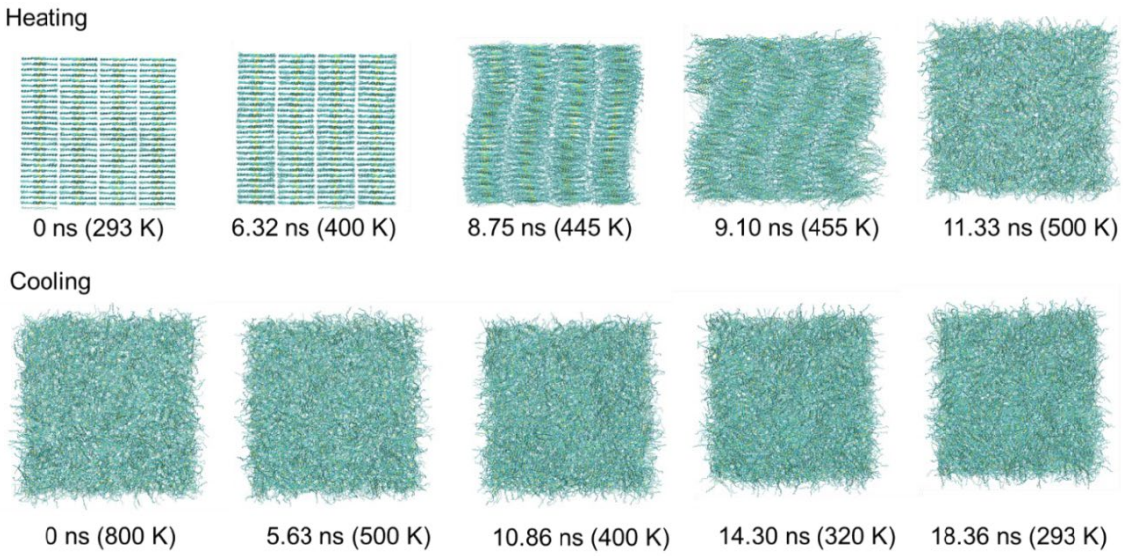

Figure 5.21 Trajectory visualizations as C8-BTBT-C8 (top) melts from the crystal to the liquid and (condenses) from the melt to the solid at 20 K/ns rate. The simulation times and corresponding temperatures are noted. The liquid crystalline smectic A phase is captured in the ~445K – 455 K region.

During cooling, we do not observe the return of the crystal morphology from the melt, rather an amorphous solid structure is recovered with no order/crystalline attributes (Figure 5.22). The density and CV curves confirm that the original crystallinity is not regained through both cooling rates (Figure 5.23). Visualizations indicate the molecules find themselves in trapped/entangled conformations during the cooling process that do not allow for rearrangement to assemble in crystalline order within the narrow timescales of the annealing process.

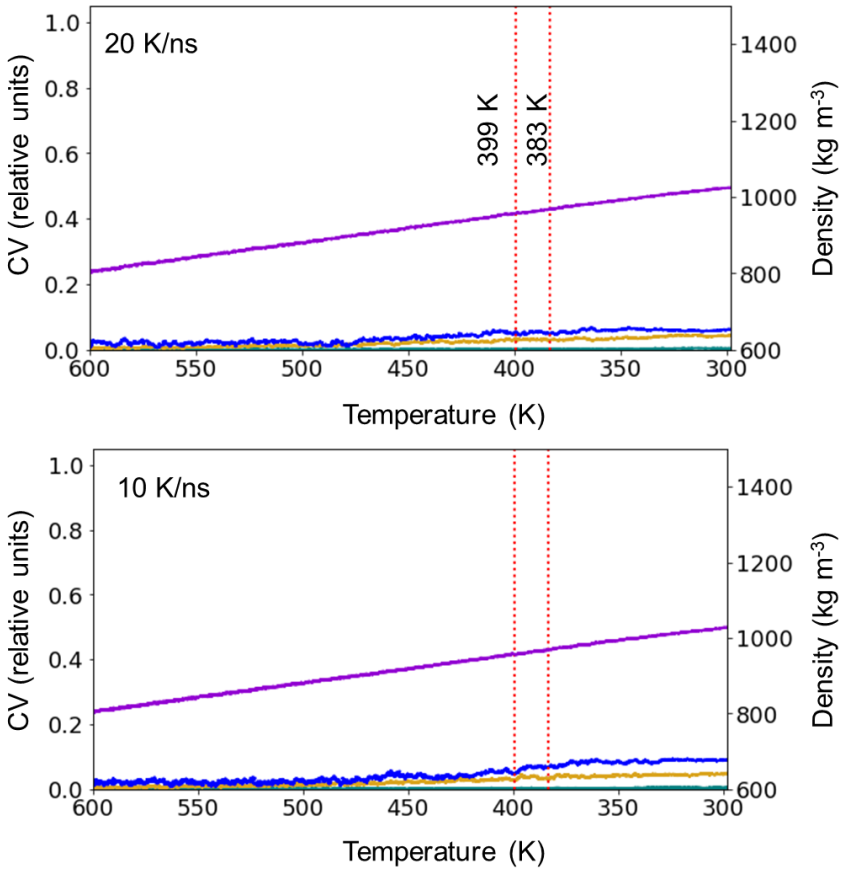

Figure 5.22 Density curves and collective variables (CV) corresponding to crystal planes versus temperature for C8-BTBT-C8 for cooling simulations at either (top) 20 K/ns or (bottom) 10 K/ns rates.

We now move to the mono octyl-substituted BTBT, which is 2-Octyl[1]benzothieno[3,2-b][1]benzothiophene (C8-BTBT) that has the asymmetrical C_{1h} symmetry. The crystal structure reveals double layers of lamellar stacks of chromophores sandwiched by the alkyl chain layers. Based on the RDF profiles, each crystallographic face is characterized as a function of the dominant intermolecular short-axis stacking types: edge-to-face stacked double-layered packing at a COM distance of ~0.5 nm (see the teal RDF profile corresponding to (100), (111), and (011) faces), edge-to-edge stacking at COM distance of ~0.58 nm (see the gold RDF profile corresponding to (002)

and (102) faces), and co-facial stacking at a COM distance of ~0.82 nm (see the red RDF profile corresponding to (110) face). The intermolecular long-axis stacking resides at a COM distance of ~1.17 nm (extracted through visualization tools). We note that the face-to-face stacking is absent in the symmetrically disubstituted C8-BTBT-C8 molecule (Figure 5.23).

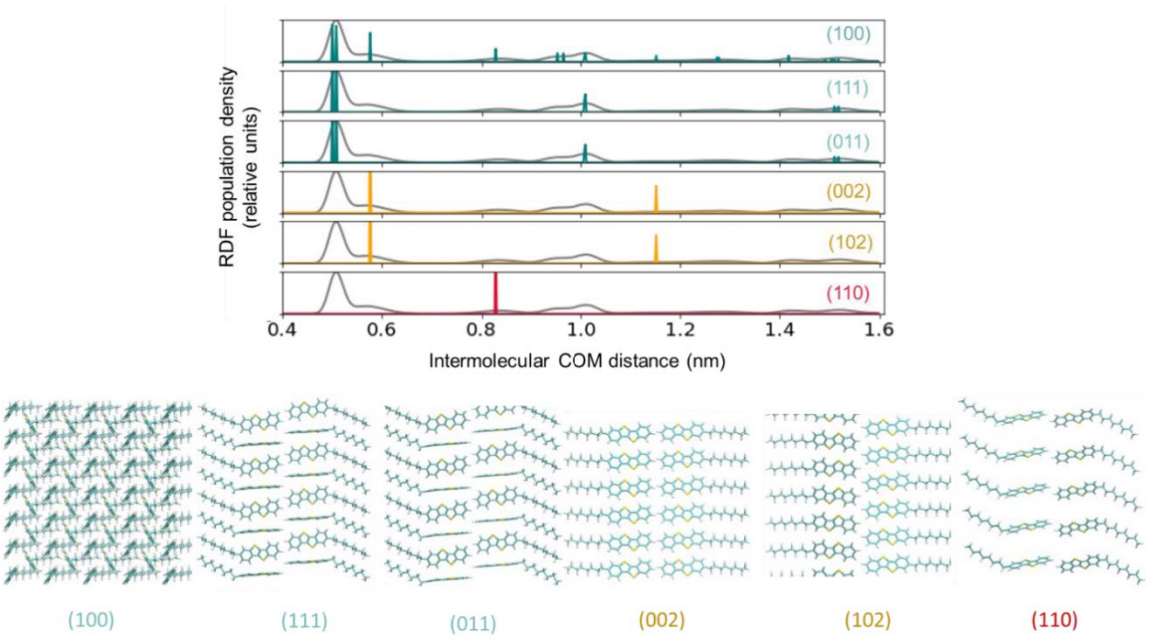

Figure 5.23 (top) Radial distribution function (RDF) plots for the bulk C8-BTBT crystal (grey lines) and for specific crystal planes as depicted by the teal, gold, and red color peaks. The dominating intermolecular stacking types in terms of the center of mass distance are identified by using the tallest peak(s) positions; teal represents edge-to-face intermolecular stacking, gold represents edge-to-edge intermolecular stacking, and red represents face-to-face stacking (bottom) of the C8-BTBT crystal lattice planes.

The melting and cooling curves show quite different behavior from one another, as observed for C8-BTBT-C8: A clear phase transition exists at ~510 K, where all CVs and density curves drop dramatically (Figure 5.24). Experimental melting is reported at ~392 K.[16] Here we note that all CV behave quite similarly throughout melting, with some indication of a solid-crystalline phase transition marked around 380 K, where a clear change associated with the rate at which all CV and density decrease. Note that experimental data also report a solid-crystalline phase transition (~55 C, or ~333 K) before melting to achieve an isotropic liquid (at ~ 114 C, or 392 K). Visualizations indicate that the crystalline I and crystalline II phases are similar, but the latter is associated with broader intermolecular spacing and lower edge-to-face packing order (Figure 5.25). This may result from the interaction energies of the chromophores and alkyl chains that are of the same order of magnitude that are disrupted simultaneously during heating.

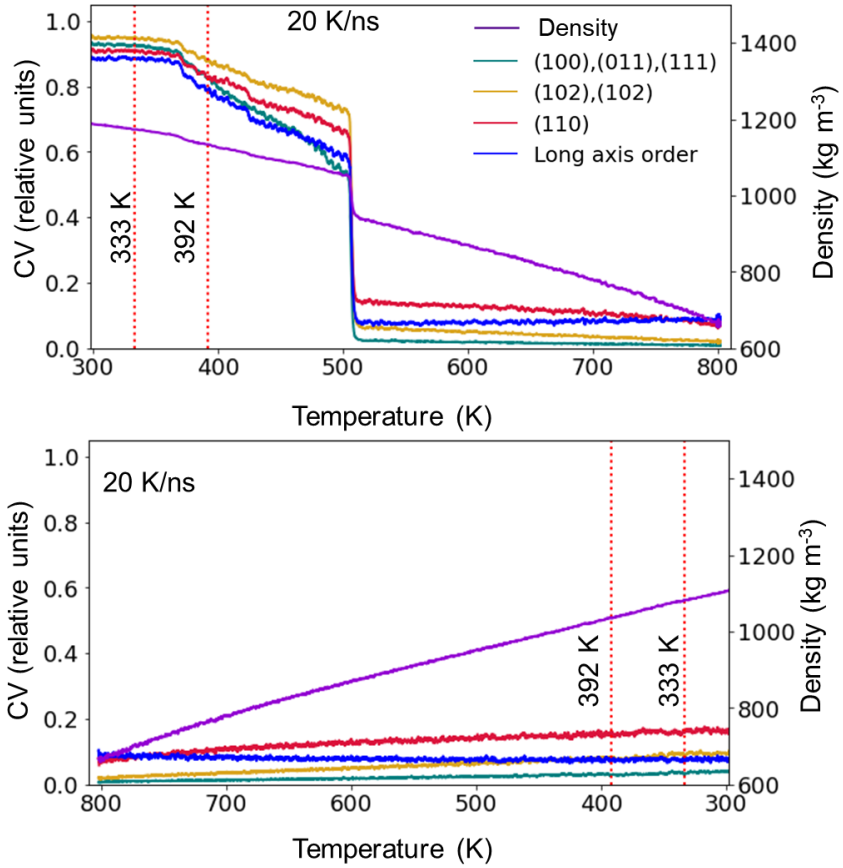

Figure 5.24 Density and CV versus temperature profiles for C8-BTBT along (top) heating from the solid to the melt and (bottom) cooling from the melt to the solid. The colors correspond to the density and dominant interaction types in terms of the intermolecular distances as determined by the RDF.

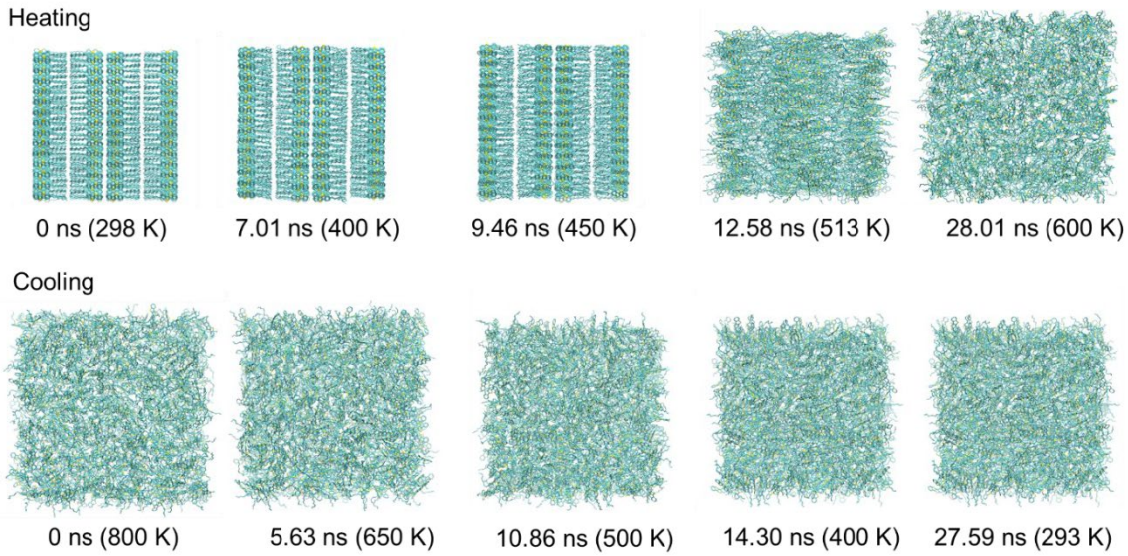

Figure 5.25 Trajectory visualizations as C8-BTBT (top) melts from the crystal to the liquid and (condenses) from the melt to the solid at 20 K/ns rate. The simulation times and corresponding temperatures are noted. The solid-crystalline phase is captured at ~400 K – 500 K region during melting.

During cooling from the melt, the long-axis order is further decreased, while all other CV show signs of a slight increase in magnitude but remain very low compared to that of the original crystal structure. The density and CV curves again confirm that original crystallinity is not regained through both cooling rates (Figure 5.24). Visualizations show that under both cooling rates, the molecules often find themselves in trapped positions (as observed for C8-BTBT-C8) during the cooling process that do not allow for rearrangement to assemble in crystalline order during the fast-annealing timescales (Figure 5.25).

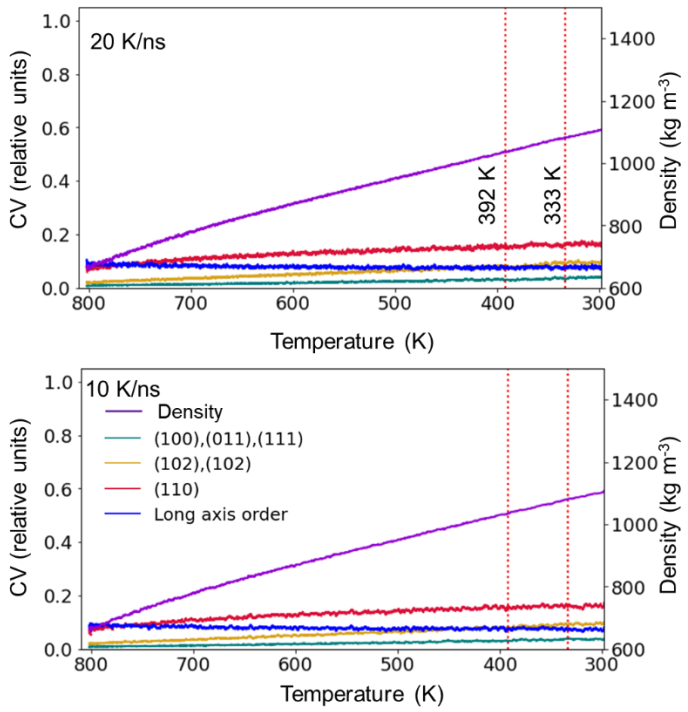

Figure 5.26 Density curves and collective variables (CV) corresponding to crystal planes versus temperature for C8-BTBT for cooling simulations at either (top) 20 K/ns or (bottom) 10 K/ns rates.

5.4 Conclusions

Through a systematic study of phase behavior of OSC derived from small molecules, observed under fast annealing simulations that promote kinetic contributions, we demonstrate how molecular order of different crystallographic faces belonging to the bulk crystal integrity contribute to melting and solidification processes. We further provide an initial test case of a semi-to-fully automated procedure for simulation of OSC small molecule crystals to investigate phase behaviors and demonstrate how collective variables can be carefully selected to identify different molecular stacking types present in the crystal bulk. The study reveals that for the crystal bulk with herringbone packing motif in general, the edge-to-face short-axis molecular stacking – the signature molecular

stacking integrity of herringbone conformation – can be easily lost (due to low interaction strength) during melting and can be harder to reform during recrystallization in the absence of other stacking types (i.e., co-facial and edge-to-edge) providing assistance. However, this observation appears to only hold true in this four membered fused-ring molecular series when the chromophore structures contain no more than one thiophene ring in the molecular structure: Incorporation of two thiophenes, either to the terminal ends (NDT) or to the center as fused thiophene ring system (BTBT), serve to impact negatively the ability regaining crystalline order upon cooling during the timescales and rates of cooling used for the simulations; this result suggests a higher degree of kinetic disorder is introduced due to the modification of the molecular chemistry. As revealed under faster (reverse) annealing rates, the S atoms lead to entrapment of the molecules in local non-equilibrium configurations that exacerbate the nucleation events required to achieve higher degrees of order and, eventually, the bulk crystal.

We also demonstrate how varied alkyl side chain substitution can impact phase behavior. For the case of dialkylated chromophore (C8-BTBT-C8), the alkyl chains establish strong inter-alkyl chain interactions to maintain long-axis order of the crystal bulk, which during melting, leads to the existence of liquid crystalline (smectic) phases by first disrupting the relatively weaker molecular short-axis interactions – a molecular feature that favors post-annealing (reheating and then cooling back) to improve molecular order in fabricated thin films. For the case of monoalkylated chromophore (C8-BTBT), however, the alkyl-chain interactions are not strong (or uniform) enough to facilitate sufficient long-axis order (and thereby any smectic phases). Therefore, during heating, the weaker inter-alkyl chain interactions that are of the same order of short-axis order

begin to lose composition simultaneously, resulting in solid-crystalline phase transformations from early in the simulations. Importantly, the experimentally reported solid-solid crystalline and liquid crystalline phases in alkylated BTBT variants were successfully captured in the simulations.[23]

CHAPTER 6. PERSPECTIVES

6.1 Synopsis and future considerations

OSC have earned a growing spotlight in both academia and industry as emerging materials systems that offer promising solutions for both current and future applications of optical and electronics technologies. However, the development of new OSC requires hard-and-fast materials design and processing strategies, which require fundamental understanding of structure–processing–function relationships. Unfortunately, the field faces challenges in this domain that arise from limitations associated with current experimental characterization techniques. The continued advance of computational tools and techniques offers effective means to provide these required insights and overcome experimental limitations. This dissertation reports computational techniques and analyses that provide dynamic, atomic-scale understanding that is requisite to formulate guidelines derived from first principles understanding to realize *a priori* morphology regulation protocols for processing OSC materials. Throughout the Chapters, we portray multiscale calculations carried out through techniques based on both quantum and classical mechanics approaches to bring about an in-depth atomic-scale foundation for thermodynamics and kinetic parameters control that will assist in the design of pathways of OSC morphology development through chromophore design and process optimization.

In Chapter 3, we explore the impacts of intramolecular noncovalent interactions in alternating donor-acceptor (*D-A)* type oligomers on the conformational structure and dynamics. We reveal how relatively weak noncovalent interactions, often considered to be responsible for conformational "locking", cannot offer such capacity especially during solution processing. Instead, we provide a rationale as to how the degree of delocalization

of the π-electron density across the rotatable bridging bonds among the *D* and *A* moieties may serves as a more important proxy in controlling rotational conformations thereby determine equilibrium structure, that in turn impact on the solution dynamics. Through classical dynamics simulations of concentrated solutions, we reveal critical dynamic insight related to oligomer aggregation/solvation: In addition to the intrinsic tendencies of thermodynamic-equilibrium conformational preference, driven by static interactions, the choice of solvent can lead to further impose variations to adopt conformations that either promote or prevent aggregation in solution. We highlight the importance of maintaining fine balance between the extremities of conformational variability vs. the rigidity in solution to optimize the solution processability while not disrupting the capacity to form aggregates at the solid state with consistent thin film structures. The results from this study provide an in-depth atomic-scale foundation for OSC morphology development through chromophore design and solvent optimization, assisted by design pathways using kinetic and thermodynamic control.

Fabrication of thin films with crystalline order is preferred feature of interest, targeted in advanced device fabrication strategies to accommodate efficient charge-carrier transport across active materials. In Chapter 4, we uncover atomic-scale insights pertaining to understanding crystallization mechanisms as a function of different solution environments, supersaturation levels, and temperatures to demonstrate how these process conditions can serve as tunable degrees of freedom to regulate crystallization of herringbone-based molecular crystals. By comparing crystallization under distinctively different solution environments, we reveal that the overall crystallization mechanism adopted by the organic molecules can be further varied by the non-ideal dynamic

behaviors of solution, in which solute-solvent interactions plays a dominant role. We show that weaker solute–solvent interactions promote phase separation that in turn speed up the crystallization process. However, driving forces for phase separation that are overly high can serve to negatively impact the assembly mechanisms, often due to kinetic entrapment of molecular conformations in unfavorable forms for crystallization. We then shed light to the impact of shape anisotropy associated with OSC crystallization, where faceted crystal growth is promoted. By comparing crystallization at different crystallographic faces, we explain how different nucleation and growth mechanisms are orchestrated in each growth front, directed by the anisotropic molecular shape aspect ratio, that not only determine the overall crystal morphology, but also the roughness evolution of the crystal surfaces, through the extremes between 3D island formation vs. smooth layer-by-layer growth. We further uncover the thermodynamic and kinetic factors associated with the surface nucleation and growth of the crystal as a function of temperature, that can be used as an additional proxy to alter assembly mechanisms to regulate crystallization. Overall, we provide detailed descriptions as to how these process variables allow one to gain fine control over important parameters including surface roughness, crystal domain size, and crystal shape, to develop precise process protocols to optimize crystallization in thin film fabrication.

We then extend our investigations to understand crystallization from the melt. In Chapter 5, we conduct a systematic study of phase behavior of OSC small molecules, utilizing high-throughput computational tools to fully automate the labor-intensive calculation procedures to demonstrate how different building block chemistries translate to the morphologies of herringbone-packed crystals with different crystallographic faces

that contribute to melting and cooling/recrystallization processes. For crystal OSC derived from fused four-ring systems (e.g., based on tetracene), we show that edge-to-face packed short-axis molecular stacking can be easily lost during melting and can be difficult to reform during recrystallization in the absence of other types molecular stacking being assembled first. For example, we show how co-facial and edge-to-edge stacking can serve to assist in acquiring crystalline order of the edge-to-face stacking that then increase the overall herringbone packing when regaining crystalline morphology of the melts during cooling. However, we note that this observation, although under fast annealing rates, appears to be valid only when the chromophore structures under investigation contain no more than one thiophene ring; incorporation of more can lead to exacerbation of the capacity of the melt to regain crystalline order upon cooling, as entrapment of molecules in local non-equilibrium (crystalline) configurations serve to delay nucleation of the material to achieve bulk crystalline properties. From the simulated annealing trajectories, we capture experimentally reported solid-solid crystalline and liquid crystalline phases. We also establish a fully automated classical MD procedure for the simulation of small-molecule OSC crystals to investigate the phase behavior between solid and melt. Through the insights generated by the simulations. we uncover atomic scale information for understanding relationships between temperature and the solid-state morphology to assist in formulating rational design strategies of OSC thin films with preferred long-range crystalline order and operational stability.

Throughout the studies in this thesis, we demonstrated how multiscale simulations can provide invaluable atomic-scale dynamic information to extend our current understanding to develop more accurate and descriptive models of structure-processing-

function protocols. We rationalize how quantum and classical mechanics techniques derived from generalized empirical data can be appropriately combined to study physicochemical phenomena in relevance to OSC morphology regulation to push through the challenges hindered by limited experimentational probing techniques. We incorporate and adopt state-of-the-art computational techniques to provide a dynamic perspective of intricate mechanisms behind crystallization and molecular assembly specific to shape anisotropic OSC. Simultaneously, we set initiative to fully automated high-throughput algorithms, derived from the community developed computational tools of different temporal scales and techniques to generate large scale, human-interpretable data that are required to investigate the vast chemical space of OSC. Based on the insights of our more-advanced calculations, we further develop models and provide new descriptions to derive protocols for materials discovery and characterization. Thus, we provide groundwork for the community to allow to adopt advanced analytical techniques including machine learning algorithms to improve accuracy of simulations through improved force fields and mitigated finite size limitations.

REFERENCES

Chapter 1: References

(1) Jester, T. L. Crystalline silicon manufacturing progress. *Progress in Photovoltaics: Research and Applications* 2002, *10* (2), 99-106.

(2) Despotou, E. 1.10 - Vision for Photovoltaics in the Future. In *Comprehensive Renewable Energy*, Sayigh, A. Ed.; Elsevier, 2012; pp 179-198.

(3) Zhang, Q.; Hu, W.; Sirringhaus, H.; Müllen, K. Recent Progress in Emerging Organic Semiconductors. *Advanced Materials* 2022, *34* (22), 2108701.

(4) Fratini, S.; Nikolka, M.; Salleo, A.; Schweicher, G.; Sirringhaus, H. Charge transport in high-mobility conjugated polymers and molecular semiconductors. *Nat Mater* 2020, *19* (5), 491-502.

(5) Liu, K.; Ouyang, B.; Guo, X.; Guo, Y.; Liu, Y. Advances in flexible organic field-effect transistors and their applications for flexible electronics. *npj Flexible Electronics* 2022, *6* (1).

(6) Chen, H.; Zhang, W.; Li, M.; He, G.; Guo, X. Interface Engineering in Organic Field-Effect Transistors: Principles, Applications, and Perspectives. *Chemical Reviews* 2020, *120* (5), 2879-2949.

(7) Yi, H. T.; Payne, M. M.; Anthony, J. E.; Podzorov, V. Ultra-flexible solution-processed organic field-effect transistors. *Nature Communications* 2012, *3* (1), 1259.

(8) Sudheendran Swayamprabha, S.; Dubey, D. K.; Shahnawaz; Yadav, R. A. K.; Nagar, M. R.; Sharma, A.; Tung, F.-C.; Jou, J.-H. Approaches for Long Lifetime Organic Light Emitting Diodes. *Advanced Science* 2021, *8* (1), 2002254.

(9) Brédas, J.-L.; Norton, J. E.; Cornil, J.; Coropceanu, V. Molecular Understanding of Organic Solar Cells: The Challenges. *Accounts of Chemical Research* 2009, *42* (11), 1691-1699.

(10) Fratini, S.; Nikolka, M.; Salleo, A.; Schweicher, G.; Sirringhaus, H. Charge transport in high-mobility conjugated polymers and molecular semiconductors. *Nature Materials* 2020, *19* (5), 491-502.

(11) Abdulrazzaq, O. A.; Saini, V.; Bourdo, S.; Dervishi, E.; Biris, A. S. Organic Solar Cells: A Review of Materials, Limitations, and Possibilities for Improvement. *Particulate Science and Technology* 2013, *31* (5), 427-442.

(12) Petty, A. J.; Ai, Q.; Sorli, J. C.; Haneef, H. F.; Purdum, G. E.; Boehm, A.; Granger, D. B.; Gu, K.; Rubinger, C. P. L.; Parkin, S. R.; et al. Computationally aided design of a high-performance organic semiconductor: the development of a universal crystal engineering core. *Chemical Science* 2019, *10* (45), 10543-10549.

(13) Almosni, S.; Delamarre, A.; Jehl, Z.; Suchet, D.; Cojocaru, L.; Giteau, M.; Behaghel, B.; Julian, A.; Ibrahim, C.; Tatry, L.; et al. Material challenges for solar cells in the twenty-first century: directions in emerging technologies. *Sci Technol Adv Mater* 2018, *19* (1), 336-369.

(14) An, Q.; Zhang, F.; Zhang, J.; Tang, W.; Deng, Z.; Hu, B. Versatile ternary organic solar cells: a critical review. *Energy & Environmental Science* 2016, *9* (2), 281-322.

(15) Wedler, S.; Bourdick, A.; Athanasopoulos, S.; Gekle, S.; Panzer, F.; McDowell, C.; Nguyen, T.-Q.; Bazan, G. C.; Köhler, A. What is the role of planarity and torsional freedom for aggregation in a π-conjugated donor–acceptor model oligomer? *Journal of Materials Chemistry C* 2020, *8* (14), 4944-4955.
(16) Quinn, J. T. E.; Zhu, J.; Li, X.; Wang, J.; Li, Y. Recent progress in the development of n-type organic semiconductors for organic field effect transistors. *Journal of Materials Chemistry C* 2017, *5* (34), 8654-8681.
(17) Usta, H.; Facchetti, A.; Marks, T. J. n-Channel Semiconductor Materials Design for Organic Complementary Circuits. *Accounts of Chemical Research* 2011, *44* (7), 501-510.
(18) Coropceanu, V.; Li, H.; Winget, P.; Zhu, L.; Brédas, J.-L. Electronic-Structure Theory of Organic Semiconductors: Charge-Transport Parameters and Metal/Organic Interfaces. *Annual Review of Materials Research* 2013, *43* (1), 63-87.
(19) Huang, Y.; Kramer, E. J.; Heeger, A. J.; Bazan, G. C. Bulk Heterojunction Solar Cells: Morphology and Performance Relationships. *Chemical Reviews* 2014, *114* (14), 7006-7043.
(20) Huang, C.-F.; Wu, S.-L.; Huang, Y.-F.; Chen, Y.-C.; Chang, S.-T.; Wu, T.-Y.; Wu, K.-Y.; Chuang, W.-T.; Wang, C.-L. Packing Principles for Donor–Acceptor Oligomers from Analysis of Single Crystals. *Chemistry of Materials* 2016, *28* (15), 5175-5190.
(21) McDowell, C.; Narayanaswamy, K.; Yadagiri, B.; Gayathri, T.; Seifrid, M.; Datt, R.; Ryno, Sean M.; Heifner, M. C.; Gupta, V.; Risko, C.; et al. Impact of rotamer diversity on the self-assembly of nearly isostructural molecular semiconductors. *Journal of Materials Chemistry A* 2018, *6* (2), 383-394.
(22) Purdum, G. E.; Chen, X.; Telesz, N.; Ryno, S. M.; Sengar, N.; Gessner, T.; Risko, C.; Clancy, P.; Weitz, R. T.; Loo, Y.-L. Solvent–Molecule Interactions Govern Crystal-Habit Selection in Naphthalene Tetracarboxylic Diimides. *Chemistry of Materials* 2019, *31* (23), 9691-9698.
(23) Lee, J. K.; Ma, W. L.; Brabec, C. J.; Yuen, J.; Moon, J. S.; Kim, J. Y.; Lee, K.; Bazan, G. C.; Heeger, A. J. Processing additives for improved efficiency from bulk heterojunction solar cells. *J Am Chem Soc* 2008, *130* (11), 3619-3623.
(24) Zhao, W.; Li, S.; Yao, H.; Zhang, S.; Zhang, Y.; Yang, B.; Hou, J. Molecular Optimization Enables over 13% Efficiency in Organic Solar Cells. *J. Am. Chem. Soc.* 2017, *139* (21), 7148-7151.
(25) Noriega, R.; Rivnay, J.; Vandewal, K.; Koch, F. P. V.; Stingelin, N.; Smith, P.; Toney, M. F.; Salleo, A. A general relationship between disorder, aggregation and charge transport in conjugated polymers. *Nature materials* 2013, *12* (11), 1038-1044.
(26) Rivnay, J.; Mannsfeld, S. C. B.; Miller, C. E.; Salleo, A.; Toney, M. F. Quantitative Determination of Organic Semiconductor Microstructure from the Molecular to Device Scale. *Chemical Reviews* 2012, *112* (10), 5488-5519.
(27) Wang, C.; Dong, H.; Jiang, L.; Hu, W. Organic semiconductor crystals. *Chemical Society Reviews* 2018, *47* (2), 422-500.
(28) Hollamby, M. J. Practical applications of small-angle neutron scattering. *PCCP* 2013, *15* (26), 10566-10579.

(29) Headen, T. F.; Boek, E. S.; Stellbrink, J.; Scheven, U. M. Small Angle Neutron Scattering (SANS and V-SANS) Study of Asphaltene Aggregates in Crude Oil. *Langmuir* 2009, *25* (1), 422-428.
(30) Seifrid, M. T.; Reddy, G. N. M.; Zhou, C.; Chmelka, B. F.; Bazan, G. C. Direct Observation of the Relationship between Molecular Topology and Bulk Morphology for a π-Conjugated Material. *Journal of the American Chemical Society* 2019, *141* (13), 5078-5082.
(31) van der Poll, T. S.; Zhugayevych, A.; Chertkov, E.; Bakus, R. C., 2nd; Coughlin, J. E.; Teat, S. J.; Bazan, G. C.; Tretiak, S. Polymorphism of Crystalline Molecular Donors for Solution-Processed Organic Photovoltaics. *The journal of physical chemistry letters* 2014, *5* (15), 2700-2704.
(32) Coughlin, J. E.; Zhugayevych, A.; Bakus, R. C.; Van Der Poll, T. S.; Welch, G. C.; Teat, S. J.; Bazan, G. C.; Tretiak, S. A Combined Experimental and Theoretical Study of Conformational Preferences of Molecular Semiconductors. *The Journal of Physical Chemistry C* 2014, *118* (29), 15610-15623.
(33) McDowell, C.; Abdelsamie, M.; Zhao, K.; Smilgies, D.-M.; Bazan, G. C.; Amassian, A. Synergistic Impact of Solvent and Polymer Additives on the Film Formation of Small Molecule Blend Films for Bulk Heterojunction Solar Cells. *Advanced Energy Materials* 2015, *5* (18), 1501121.
(34) Zhang, X.; Hudson, S. D.; DeLongchamp, D. M.; Gundlach, D. J.; Heeney, M.; McCulloch, I. In-Plane Liquid Crystalline Texture of High-Performance Thienothiophene Copolymer Thin Films. *Advanced Functional Materials* 2010, *20* (23), 4098-4106.
(35) van de Laar, T.; Hooiveld, E.; Higler, R.; van der Scheer, P.; Sprakel, J. Gel Trapping Enables Optical Spectroscopy of Single Solvated Conjugated Polymers in Equilibrium. *ACS Nano* 2019, *13* (11), 13185-13195.
(36) Kharandiuk, T.; Hussien, E. J.; Cameron, J.; Petrina, R.; Findlay, N. J.; Naumov, R.; Klooster, W. T.; Coles, S. J.; Ai, Q.; Goodlett, S.; et al. Noncovalent Close Contacts in Fluorinated Thiophene–Phenylene–Thiophene Conjugated Units: Understanding the Nature and Dominance of O···H versus S···F and O···F Interactions with Respect to the Control of Polymer Conformation. *Chemistry of Materials* 2019, *31* (17), 7070-7079.
(37) Variankaval, N.; Cote, A. S.; Doherty, M. F. From form to function: Crystallization of active pharmaceutical ingredients. *AIChE Journal* 2008, *54* (7), 1682-1688.
(38) Rietveld, I. B.; Céolin, R. Rotigotine: Unexpected Polymorphism with Predictable Overall Monotropic Behavior. *Journal of Pharmaceutical Sciences* 2015, *104* (12), 4117-4122.
(39) Yang, J.; Hu, C. T.; Zhu, X.; Zhu, Q.; Ward, M. D.; Kahr, B. DDT Polymorphism and the Lethality of Crystal Forms. *Angewandte Chemie International Edition* 2017, *56* (34), 10165-10169.
(40) Zhu, X.; Hu, C. T.; Erriah, B.; Vogt-Maranto, L.; Yang, J.; Yang, Y.; Qiu, M.; Fellah, N.; Tuckerman, M. E.; Ward, M. D.; et al. Imidacloprid Crystal Polymorphs for Disease Vector Control and Pollinator Protection. *Journal of the American Chemical Society* 2021, *143* (41), 17144-17152.

(41) Lee, A. Y.; Erdemir, D.; Myerson, A. S. Crystal Polymorphism in Chemical Process Development. *Annual Review of Chemical and Biomolecular Engineering* 2011, *2* (1), 259-280.
(42) Rimer, J. D.; An, Z.; Zhu, Z.; Lee, M. H.; Goldfarb, D. S.; Wesson, J. A.; Ward, M. D. Crystal Growth Inhibitors for the Prevention of l-Cystine Kidney Stones Through Molecular Design. *Science* 2010, *330* (6002), 337-341.
(43) Simone, E.; Klapwijk, A. R.; Wilson, C. C.; Nagy, Z. K. Investigation of the Evolution of Crystal Size and Shape during Temperature Cycling and in the Presence of a Polymeric Additive Using Combined Process Analytical Technologies. *Crystal Growth & Design* 2017, *17* (4), 1695-1706.
(44) Reyes-Martinez, M. A.; Crosby, A. J.; Briseno, A. L. Rubrene crystal field-effect mobility modulation via conducting channel wrinkling. *Nature Communications* 2015, *6* (1), 6948.
(45) Chen, H.; Zhang, W.; Ren, S.; Zhao, X.; Jiao, Y.; Wang, Y.; Stoddart, J. F.; Guo, X. Temperature-Triggered Supramolecular Assembly of Organic Semiconductors. *Advanced Materials* 2022, *34* (22), 2101487.
(46) Ling, H.; Liu, S.; Zheng, Z.; Yan, F. Organic flexible electronics. *Small Methods* 2018, *2* (10), 1800070.
(47) Bao, Z.; Chen, X. Flexible and stretchable devices. Wiley Online Library: 2016; Vol. 28, pp 4177-4179.
(48) Han, S. T.; Peng, H.; Sun, Q.; Venkatesh, S.; Chung, K. S.; Lau, S. C.; Zhou, Y.; Roy, V. An overview of the development of flexible sensors. *Advanced materials* 2017, *29* (33), 1700375.
(49) Huang, Y.; Tang, W.; Feng, L.; Chen, S.; Zhao, J.; Liu, Z.; Han, L.; Ouyang, B.; Guo, X. Printable low power organic transistor technology for customizable hybrid integration towards internet of everything. *IEEE Journal of the Electron Devices Society* 2020, *8*, 1219-1226.
(50) Evans, J. W.; Thiel, P. A.; Bartelt, M. C. Morphological evolution during epitaxial thin film growth: Formation of 2D islands and 3D mounds. *Surface Science Reports* 2006, *61* (1), 1-128.
(51) Sirringhaus, H. Reliability of Organic Field-Effect Transistors. *Advanced Materials* 2009, *21* (38), 3859-3873.
(52) Walters, D. M.; Richert, R.; Ediger, M. D. Thermal stability of vapor-deposited stable glasses of an organic semiconductor. *The Journal of Chemical Physics* 2015, *142* (13), 134504.
(53) Kaur, A. P.; Harris, K. C.; Attanayake, N. H.; Liang, Z.; Parkin, S. R.; Tang, M. H.; Odom, S. A. Quantifying Environmental Effects on the Solution and Solid-State Stability of a Phenothiazine Radical Cation. *Chemistry of Materials* 2020, *32* (7), 3007-3017.
(54) Attanayake, N. H.; Kaur, A. P.; Suduwella, T. M.; Elliott, C. F.; Parkin, S. R.; Odom, S. A. A stable, highly oxidizing radical cation. *New Journal of Chemistry* 2020, *44* (42), 18138-18148.
(55) Hasell, T.; Culshaw, J. L.; Chong, S. Y.; Schmidtmann, M.; Little, M. A.; Jelfs, K. E.; Pyzer-Knapp, E. O.; Shepherd, H.; Adams, D. J.; Day, G. M.; et al. Controlling the Crystallization of Porous Organic Cages: Molecular Analogs of

Isoreticular Frameworks Using Shape-Specific Directing Solvents. *Journal of the American Chemical Society* 2014, *136* (4), 1438-1448.

(56) Panda, M. K.; Runčevski, T.; Husain, A.; Dinnebier, R. E.; Naumov, P. Perpetually Self-Propelling Chiral Single Crystals. *Journal of the American Chemical Society* 2015, *137* (5), 1895-1902.

(57) Brédas, J. L.; Calbert, J. P.; Da Silva Filho, D. A.; Cornil, J. Organic semiconductors: A theoretical characterization of the basic parameters governing charge transport. *Proceedings of the National Academy of Sciences* 2002, *99* (9), 5804-5809.

(58) Wang, S.; Peng, L.; Sun, H.; Huang, W. The future of solution processing toward organic semiconductor devices: a substrate and integration perspective. *Journal of Materials Chemistry C* 2022.

(59) Diao, Y.; Shaw, L.; Bao, Z.; Mannsfeld, S. C. B. Morphology control strategies for solution-processed organic semiconductor thin films. *Energy & Environmental Science* 2014, *7* (7), 2145-2159.

(60) Salvalaglio, M.; Vetter, T.; Mazzotti, M.; Parrinello, M. Controlling and Predicting Crystal Shapes: The Case of Urea. *Angewandte Chemie International Edition* 2013, *52* (50), 13369-13372.

(61) Song, L.; Zhao, F.-Q.; Xu, S.-Y.; Ju, X.-H.; Ye, C.-C. Crystal Morphology Prediction and Anisotropic Evolution of 1,1-Diamino-2,2-dinitroethylene (FOX-7) by Temperature Tuning. *Scientific Reports* 2020, *10* (1).

(62) Dandekar, P.; Kuvadia, Z. B.; Doherty, M. F. Engineering Crystal Morphology. *Annual Review of Materials Research* 2013, *43* (1), 359-386.

(63) Sosso, G. C.; Chen, J.; Cox, S. J.; Fitzner, M.; Pedevilla, P.; Zen, A.; Michaelides, A. Crystal Nucleation in Liquids: Open Questions and Future Challenges in Molecular Dynamics Simulations. *Chemical Reviews* 2016, *116* (12), 7078-7116.

(64) Gibbs, J. W. *On the equilibrium of heterogenous substances*; Connecticut Academy of Arts and Sciences, 1874.

(65) Veringa, H. J. Part II of New Basic Theory of Gravity. *Journal of Modern Physics* 2016, *07* (16), 2266-2280.

(66) Kashchiev, D. Nucleation at time-dependent supersaturation. *Surface Science* 1970, *22* (2), 319-324.

(67) Laaksonen, A.; Napari, I. Breakdown of the Capillarity Approximation in Binary Nucleation: A Density Functional Study. *The Journal of Physical Chemistry B* 2001, *105* (47), 11678-11682.

(68) Gebauer, D.; Kellermeier, M.; Gale, J. D.; Bergström, L.; Cölfen, H. Pre-nucleation clusters as solute precursors in crystallisation. *Chem. Soc. Rev.* 2014, *43* (7), 2348-2371.

(69) Han, D.; Karmakar, T.; Bjelobrk, Z.; Gong, J.; Parrinello, M. Solvent-mediated morphology selection of the active pharmaceutical ingredient isoniazid: Experimental and simulation studies. *Chemical Engineering Science* 2019, *204*, 320-328.

(70) Thanh, N. T.; Maclean, N.; Mahiddine, S. Mechanisms of nucleation and growth of nanoparticles in solution. *Chem Rev* 2014, *114* (15), 7610-7630.

(71) Li, J.; Tilbury, C. J.; Joswiak, M. N.; Peters, B.; Doherty, M. F. Rate Expressions for Kink Attachment and Detachment During Crystal Growth. *Crystal Growth & Design* 2016, *16* (6), 3313-3322.
(72) Gates, D. J.; Westcott, M. Markov Models of Steady Crystal Growth. *The Annals of Applied Probability* 1993, *3* (2), 339-355.
(73) Li, J.; Tilbury, C. J.; Kim, S. H.; Doherty, M. F. A design aid for crystal growth engineering. *Progress in Materials Science* 2016, *82*, 1-38.
(74) Dull, J. T.; Chen, X.; Johnson, H. M.; Otani, M. C.; Schreiber, F.; Clancy, P.; Rand, B. P. A comprehensive picture of roughness evolution in organic crystalline growth: the role of molecular aspect ratio. *Materials Horizons* 2022.
(75) Sutton, C.; Marshall, M. S.; Sherrill, C. D.; Risko, C.; Brédas, J.-L. Rubrene: The Interplay between Intramolecular and Intermolecular Interactions Determines the Planarization of Its Tetracene Core in the Solid State. *Journal of the American Chemical Society* 2015, *137* (27), 8775-8782.
(76) Salvalaglio, M.; Mazzotti, M.; Parrinello, M. Urea homogeneous nucleation mechanism is solvent dependent. *Faraday Discussions* 2015, *179* (0), 291-307.
(77) Gibbs, J. W. *The Scientific Papers of J. Willard Gibbs*; 1961.
(78) Wulff, G. XXV. Zur Frage der Geschwindigkeit des Wachsthums und der Auflösung der Krystallflächen. *Zeitschrift für Kristallographie - Crystalline Materials 34*, 449 - 530.
(79) Herring, C. Some Theorems on the Free Energies of Crystal Surfaces. *Physical Review* 1951, *82* (1), 87-93.
(80) Abbona, F.; Aquilano, D. Morphology of Crystals Grown from Solutions. Springer Berlin Heidelberg, 2010; pp 53-92.
(81) Liu, G.; Chen, K.; Zhou, H.; Tian, J.; Pereira, C.; Ferreira, J. M. F. Fast Shape Evolution of TiN Microcrystals in Combustion Synthesis. *Crystal Growth & Design* 2006, *6* (10), 2404-2411.
(82) Jackson, K. A.; Uhlmann, D. R.; Hunt, J. D. On the nature of crystal growth from the melt. *Journal of Crystal Growth* 1967, *1* (1), 1-36.
(83) Donnay, J. D. H.; Harker, D. A new law of crystal morphology extending the Law of Bravais. *American Mineralogist* 1937, *22* (5), 446-467.
(84) Hartman, P.; Bennema, P. The attachment energy as a habit controlling factor: I. Theoretical considerations. *Journal of Crystal Growth* 1980, *49* (1), 145-156.
(85) Hartman, P.; Perdok, W. G. On the relations between structure and morphology of crystals. I. *Acta Crystallographica* 1955, *8* (1), 49-52.
(86) Davey, R. J.; Black, S. N.; Logan, D.; Maginn, S. J.; Fairbrother, J. E.; Grant, D. J. W. Structural and kinetic features of crystal growth inhibition: adipic acid growing in the presence of n-alkanoic acids. *Journal of the Chemical Society, Faraday Transactions* 1992, *88* (23), 3461-3466.

Chapter 2: References

(1) Steinhauser, M.; Hiermaier, S. A Review of Computational Methods in Materials Science: Examples from Shock-Wave and Polymer Physics. *International Journal of Molecular Sciences* 2009, *10* (12), 5135-5216.

(2) Yost, S. R.; Wang, L.-P.; Van Voorhis, T. Molecular Insight Into the Energy Levels at the Organic Donor/Acceptor Interface: A Quantum Mechanics/Molecular Mechanics Study. *The Journal of Physical Chemistry C* 2011, *115* (29), 14431-14436.

(3) Berendsen, H. J. C.; Postma, J. P. M.; Gunsteren, W. F. v.; DiNola, A.; Haak, J. R. Molecular dynamics with coupling to an external bath. *The Journal of Chemical Physics* 1984, *81* (8), 3684-3690.

(4) Schneider, R.; Sharma, A. R.; Rai, A. Introduction to Molecular Dynamics. Springer Berlin Heidelberg, 2008; pp 3-40.

(5) Vollmayr-Lee, K. Introduction to molecular dynamics simulations. *American Journal of Physics* 2020, *88* (5), 401-422.

(6) Verlet, L. Computer "Experiments" on Classical Fluids. I. Thermodynamical Properties of Lennard-Jones Molecules. *Physical Review* 1967, *159* (1), 98-103.

(7) Baer, M. Born-Oppenheimer Approach: Diabatization and Topological Matrix. In *Beyond Born–Oppenheimer*, 2006; pp 26-57.

(8) Jorgensen, W. L.; Maxwell, D. S.; Tirado-Rives, J. Development and Testing of the OPLS All-Atom Force Field on Conformational Energetics and Properties of Organic Liquids. *Journal of the American Chemical Society* 1996, *118* (45), 11225-11236.

(9) Wang, J.; Wolf, R. M.; Caldwell, J. W.; Kollman, P. A.; Case, D. A. Development and testing of a general amber force field. *J Comput Chem* 2004, *25* (9), 1157-1174.

(10) Marenich, A. V.; Jerome, S. V.; Cramer, C. J.; Truhlar, D. G. Charge Model 5: An Extension of Hirshfeld Population Analysis for the Accurate Description of Molecular Interactions in Gaseous and Condensed Phases. *Journal of Chemical Theory and Computation* 2012, *8* (2), 527-541.

(11) Duan, Y.; Wu, C.; Chowdhury, S.; Lee, M. C.; Xiong, G.; Zhang, W.; Yang, R.; Cieplak, P.; Luo, R.; Lee, T.; et al. A point-charge force field for molecular mechanics simulations of proteins based on condensed-phase quantum mechanical calculations. *Journal of Computational Chemistry* 2003, *24* (16), 1999-2012.

(12) Metropolis, N.; Rosenbluth, A. W.; Rosenbluth, M. N.; Teller, A. H.; Teller, E. Equation of State Calculations by Fast Computing Machines. *The Journal of Chemical Physics* 1953, *21* (6), 1087-1092.

(13) Parrinello, M.; Rahman, A. Polymorphic transitions in single crystals: A new molecular dynamics method. *Journal of Applied Physics* 1981, *52* (12), 7182-7190.

(14) Perego, C.; Salvalaglio, M.; Parrinello, M. Molecular dynamics simulations of solutions at constant chemical potential. *The Journal of Chemical Physics* 2015, *142* (14), 144113.

(15) Willard, G. J. *Elementary principles in statistical mechanics : developed with especial reference to the rational foundation of thermodynamics*; New York : C. Scribner, 1902.
(16) Torrie, G. M.; Valleau, J. P. Nonphysical sampling distributions in Monte Carlo free-energy estimation: Umbrella sampling. *Journal of Computational Physics* 1977, *23* (2), 187-199.
(17) Hansen, J.-P.; McDonald, I. *Theory of Simple Liquids*; Elsevier, 1990.
(18) Kumar, S.; Rosenberg, J. M.; Bouzida, D.; Swendsen, R. H.; Kollman, P. A. THE weighted histogram analysis method for free-energy calculations on biomolecules. I. The method. *Journal of Computational Chemistry* 1992, *13* (8), 1011-1021.
(19) Berendsen, H. J. C.; van der Spoel, D.; van Drunen, R. GROMACS: A message-passing parallel molecular dynamics implementation. *Computer Physics Communications* 1995, *91* (1), 43-56.
(20) Van Der Spoel, D.; Lindahl, E.; Hess, B.; Groenhof, G.; Mark, A. E.; Berendsen, H. J. GROMACS: fast, flexible, and free. *J Comput Chem* 2005, *26* (16), 1701-1718.
(21) Promoting transparency and reproducibility in enhanced molecular simulations. *Nature Methods* 2019, *16* (8), 670-673.
(22) Levine, I. N. *Quantum Chemistry*; Prentice-Hall, Inc., 2000.
(23) Cohen-Tannoudji, C.; Diu, B.; Laloë, F. *Quantum Mechanics*; John Wiley and Sons, 1977.
(24) Szabo, A.; Ostlund, N. S. *Modern Quantum Chemistry: Introduction to Advanced Electronic Structure Theory*; Dover Publications, Inc., 1989.
(25) Jensen, F. *Introduction to Computational Chemistry*; John Wiley and Sons, Ltd., 1999.
(26) Cramer, C. J. *Essentials of Computational Chemistry: Theories and Models*; John Wiley and Sons, Ltd., 2004.
(27) Koch, W.; Holthausen, M. C. *A Chemist's Guide to Density Functional Theory*; Wiley-VCH, 2001.
(28) Hohenberg, P.; Kohn, W. Inhomogeneous Electron Gas. *Physical Review* 1964, *136* (3B), B864-B871.
(29) Becke, A. D. Density-functional exchange-energy approximation with correct asymptotic behavior. *Physical Review A* 1988, *38* (6), 3098-3100.
(30) Becke, A. D. A new mixing of Hartree–Fock and local density-functional theories. *The Journal of Chemical Physics* 1993, *98* (2), 1372-1377.
(31) Perdew, J. P. Density-functional approximation for the correlation energy of the inhomogeneous electron gas. *Physical Review B* 1986, *33* (12), 8822-8824.
(32) Burke, K.; Perdew, J. P.; Wang, Y. *Derivation of a Generalized Gradient Approximation: The PW91 Density Functional*; Springer Science+Business Media, 1998.
(33) Lee, C.; Yang, W.; Parr, R. G. Development of the Colle-Salvetti correlation-energy formula into a functional of the electron density. *Phys Rev B Condens Matter* 1988, *37* (2), 785-789.
(34) Armiento, R.; Mattsson, A. E. Functional designed to include surface effects in self-consistent density functional theory. *Physical Review B* 2005, *72* (8), 085108.

(35) Saglam, Z.; Saglam, M. Spin Dependent Selection Rules for Photonic Transitions in Hydrogen-Like Atoms. *Journal of Modern Physics* 2011, *02* (08), 787-791.
(36) Vosko, S. H.; Wilk, L.; Nusair, M. Accurate spin-dependent electron liquid correlation energies for local spin density calculations: a critical analysis. *Canadian Journal of Physics* 1980, *59*, 1200.
(37) Stephens, P. J.; Devlin, F. J.; Chabalowski, C. F.; Frisch, M. J. Ab Initio Calculation of Vibrational Absorption and Circular Dichroism Spectra Using Density Functional Force Fields. *The Journal of Physical Chemistry* 1994, *98* (45), 11623-11627.
(38) Iikura, H.; Tsuneda, T.; Yanai, T.; Hirao, K. A long-range correction scheme for generalized-gradient-approximation exchange functionals. *The Journal of Chemical Physics* 2001, *115* (8), 3540-3544.
(39) Toulouse, J.; Colonna, F.; Savin, A. Long-range--short-range separation of the electron-electron interaction in density-functional theory. *Physical Review A* 2004, *70* (6), 062505.
(40) Yanai, T.; Tew, D. P.; Handy, N. C. A new hybrid exchange–correlation functional using the Coulomb-attenuating method (CAM-B3LYP). *Chemical Physics Letters* 2004, *393* (1), 51-57.
(41) Brémond, É.; Pérez-Jiménez, Á. J.; Sancho-García, J. C.; Adamo, C. Range-separated hybrid density functionals made simple. *The Journal of Chemical Physics* 2019, *150* (20), 201102.
(42) Chai, J.-D.; Head-Gordon, M. Long-range corrected hybrid density functionals with damped atom–atom dispersion corrections. *Physical Chemistry Chemical Physics* 2008, *10* (44), 6615.
(43) Tomasi, J.; Mennucci, B.; Cammi, R. Quantum Mechanical Continuum Solvation Models. *Chemical Reviews* 2005, *105* (8), 2999-3094.
(44) Connolly, M. L. Solvent-Accessible Surfaces of Proteins and Nucleic Acids. *Science* 1983, *221* (4612), 709-713.
(45) Butt, H.-J.; Graf, K.; Kappl, M. *Physics and Chemistry of Interfaces*; Wiley-VCH, 2006.
(46) Spackman, M. A. The Quantum Theory of Atoms in Molecules. From Solid State to DNA and Drug Design. Edited by Chérif F. Matta and Russell J. Boyd. *Angewandte Chemie* 2007, *46*, 6766-6767.
(47) Matta, C. F., Boyd R. J. *The quantum theory of atoms in molecules*; WILLEY-VCH, 2007.
(48) Johnson, E. R.; Keinan, S.; Mori-Sánchez, P.; Contreras-García, J.; Cohen, A. J.; Yang, W. Revealing Noncovalent Interactions. *Journal of the American Chemical Society* 2010, *132* (18), 6498-6506.
(49) Lu, T.; Chen, Q. Interaction Region Indicator: A Simple Real Space Function Clearly Revealing Both Chemical Bonds and Weak Interactions. *Chemistry–Methods* 2021, *1* (5), 231-239.
(50) *Gaussian 16 Rev. C.01*; Wallingford, CT, 2016.
(51) Lu, T.; Chen, F. Multiwfn: A multifunctional wavefunction analyzer. *Journal of Computational Chemistry* 2012, *33* (5), 580-592.

Chapter 3: References

(1) Huang, C. F.; Wu, S. L.; Huang, Y. F.; Chen, Y. C.; Chang, S. T.; Wu, T. Y.; Wu, K. Y.; Chuang, W. T.; Wang, C. L. Packing Principles for Donor–Acceptor Oligomers from Analysis of Single Crystals. *Chemistry of Materials* 2016, *28* (15), 5175-5190.

(2) Huang, H.; Yang, L.; Facchetti, A.; Marks, T. J. Organic and Polymeric Semiconductors Enhanced by Noncovalent Conformational Locks. *Chemical Reviews* 2017, *117* (15), 10291-10318.

(3) Anthony, J. E.; Brooks, J. S.; Eaton, D. L.; Parkin, S. R. Functionalized Pentacene: Improved Electronic Properties from Control of Solid-State Order. *Journal of the American Chemical Society* 2001, *123* (38), 9482-9483.

(4) Bronstein, H.; Nielsen, C. B.; Schroeder, B. C.; McCulloch, I. The role of chemical design in the performance of organic semiconductors. *Nature Reviews Chemistry* 2020, *4* (2), 66-77.

(5) Coropceanu, V.; Cornil, J.; Da Silva Filho, D. A.; Olivier, Y.; Silbey, R.; Brédas, J.-L. Charge Transport in Organic Semiconductors. *Chemical Reviews* 2007, *107* (4), 926-952.

(6) Coropceanu, V.; Li, H.; Winget, P.; Zhu, L.; Brédas, J.-L. Electronic-Structure Theory of Organic Semiconductors: Charge-Transport Parameters and Metal/Organic Interfaces. *Annual Review of Materials Research* 2013, *43* (1), 63-87.

(7) Lee, J. H.; Seo, Y.; Park, Y. D.; Anthony, J. E.; Kwak, D. H.; Lim, J. A.; Ko, S.; Jang, H. W.; Cho, K.; Lee, W. H. Effect of Crystallization Modes in TIPS-pentacene/Insulating Polymer Blends on the Gas Sensing Properties of Organic Field-Effect Transistors. *Scientific Reports* 2019, *9* (1), 21.

(8) Liu, X.; Burgers, M. A.; Hsu, B. B. Y.; Coughlin, J. E.; Perez, L. A.; Heeger, A. J.; Bazan, G. C. Molecular orientation within thin films of isomorphic molecular semiconductors. *RSC Advances* 2015, *5* (108), 89144-89148, 10.1039/C5RA19606J.

(9) McDowell, C.; Narayanaswamy, K.; Yadagiri, B.; Gayathri, T.; Seifrid, M.; Datt, R.; Ryno, Sean M.; Heifner, M. C.; Gupta, V.; Risko, C.; et al. Impact of rotamer diversity on the self-assembly of nearly isostructural molecular semiconductors. *Journal of Materials Chemistry A* 2018, *6* (2), 383-394, 10.1039/C7TA09972J.

(10) Zhao, W.; Li, S.; Yao, H.; Zhang, S.; Zhang, Y.; Yang, B.; Hou, J. Molecular Optimization Enables over 13% Efficiency in Organic Solar Cells. *J Am Chem Soc* 2017, *139* (21), 7148-7151.

(11) Wang, C.; Dong, H.; Jiang, L.; Hu, W. Organic semiconductor crystals. *Chemical Society Reviews* 2018, *47* (2), 422-500, 10.1039/C7CS00490G.

(12) Guo, C.; Wang, J.; Li, J.; Wang, Z.; Tang, S. Kinetic Pathways and Mechanisms of Two-Step Nucleation in Crystallization. *The Journal of Physical Chemistry Letters* 2016, *7* (24), 5008-5014.

(13) Baklar, M. A.; Koch, F.; Kumar, A.; Domingo, E. B.; Campoy-Quiles, M.; Feldman, K.; Yu, L.; Wobkenberg, P.; Ball, J.; Wilson, R. M.; et al. Solid-state processing of organic semiconductors. *Advanced materials (Deerfield Beach, Fla.)* 2010, *22* (35), 3942-3947.

(14) Nakajima, Y.; Takei, T.; Tsuzuki, T.; Suzuki, M.; Fukagawa, H.; Yamamoto, T.; Tokito, S. Fabrication of 5.8-in. OTFT-driven flexible color AMOLED display using dual protection scheme for organic semiconductor patterning. *Journal of the Society for Information Display* 2009, *17* (8), 629-634.

(15) Niazi, M. R.; Li, R.; Qiang Li, E.; Kirmani, A. R.; Abdelsamie, M.; Wang, Q.; Pan, W.; Payne, M. M.; Anthony, J. E.; Smilgies, D.-M.; et al. Solution-printed organic semiconductor blends exhibiting transport properties on par with single crystals. *Nature Communications* 2015, *6* (1), 8598.

(16) Peet, J.; Kim, J. Y.; Coates, N. E.; Ma, W. L.; Moses, D.; Heeger, A. J.; Bazan, G. C. Efficiency enhancement in low-bandgap polymer solar cells by processing with alkane dithiols. *Nature materials* 2007, *6* (7), 497-500.

(17) Peet, J.; Soci, C.; Coffin, R. C.; Nguyen, T. Q.; Mikhailovsky, A.; Moses, D.; Bazan, G. C. Method for increasing the photoconductive response in conjugated polymer/fullerene composites. *Applied Physics Letters* 2006, *89* (25), 252105.

(18) Do, K.; Saleem, Q.; Ravva, M. K.; Cruciani, F.; Kan, Z.; Wolf, J.; Hansen, M. R.; Beaujuge, P. M.; Brédas, J.-L. Impact of Fluorine Substituents on π-Conjugated Polymer Main-Chain Conformations, Packing, and Electronic Couplings. *Advanced Materials* 2016, *28* (37), 8197-8205.

(19) Kang, H.; Lee, W.; Oh, J.; Kim, T.; Lee, C.; Kim, B. J. From Fullerene–Polymer to All-Polymer Solar Cells: The Importance of Molecular Packing, Orientation, and Morphology Control. *Accounts of Chemical Research* 2016, *49* (11), 2424-2434.

(20) Kharandiuk, T.; Hussien, E. J.; Cameron, J.; Petrina, R.; Findlay, N. J.; Naumov, R.; Klooster, W. T.; Coles, S. J.; Ai, Q.; Goodlett, S.; et al. Noncovalent Close Contacts in Fluorinated Thiophene–Phenylene–Thiophene Conjugated Units: Understanding the Nature and Dominance of O⋯H versus S⋯F and O⋯F Interactions with Respect to the Control of Polymer Conformation. *Chemistry of Materials* 2019, *31* (17), 7070-7079.

(21) *Gaussian 16 Rev. C.01*; Wallingford, CT, 2016. (accessed.

(22) Pascual-ahuir, J. L.; Silla, E.; Tuñon, I. GEPOL: An improved description of molecular surfaces. III. A new algorithm for the computation of a solvent-excluding surface. *Journal of Computational Chemistry* 1994, *15* (10), 1127-1138.

(23) Lu, T.; Chen, F. Multiwfn: A multifunctional wavefunction analyzer. *Journal of Computational Chemistry* 2012, *33* (5), 580-592.

(24) Lu, T.; Chen, F. Quantitative analysis of molecular surface based on improved Marching Tetrahedra algorithm. *Journal of Molecular Graphics and Modelling* 2012, *38*, 314-323.

(25) Johnson, E. R.; Keinan, S.; Mori-Sánchez, P.; Contreras-García, J.; Cohen, A. J.; Yang, W. Revealing Noncovalent Interactions. *Journal of the American Chemical Society* 2010, *132* (18), 6498-6506.

(26) Berendsen, H. J. C.; van der Spoel, D.; van Drunen, R. GROMACS: A message-passing parallel molecular dynamics implementation. *Computer Physics Communications* 1995, *91* (1), 43-56.

(27) Wang, J.; Wolf, R. M.; Caldwell, J. W.; Kollman, P. A.; Case, D. A. Development and testing of a general amber force field. *Journal of Computational Chemistry* 2004, *25* (9), 1157-1174.
(28) Jorgensen, W. L.; Tirado-Rives, J. The OPLS [optimized potentials for liquid simulations] potential functions for proteins, energy minimizations for crystals of cyclic peptides and crambin. *Journal of the American Chemical Society* 1988, *110* (6), 1657-1666.
(29) Berendsen, H. J. C.; Postma, J. P. M.; van Gunsteren, W. F.; DiNola, A.; Haak, J. R. Molecular dynamics with coupling to an external bath. *The Journal of Chemical Physics* 1984, *81* (8), 3684-3690.
(30) Parrinello, M.; Rahman, A. Polymorphic transitions in single crystals: A new molecular dynamics method. *Journal of Applied Physics* 1981, *52* (12), 7182-7190.
(31) Lemkul, J. *Umbrella Simulations*. 2015. http://www.bevanlab.biochem.vt.edu/Pages/Personal/justin/gmx-tutorials/umbrella/05_pull.html (accessed 2019-09-17).
(32) Hub, J. S.; de Groot, B. L.; van der Spoel, D. g_wham—A Free Weighted Histogram Analysis Implementation Including Robust Error and Autocorrelation Estimates. *Journal of Chemical Theory and Computation* 2010, *6* (12), 3713-3720.
(33) Kumar, S.; Rosenberg, J. M.; Bouzida, D.; Swendsen, R. H.; Kollman, P. A. THE weighted histogram analysis method for free-energy calculations on biomolecules. I. The method. *Journal of Computational Chemistry* 1992, *13* (8), 1011-1021.
(34) *Pandas plotting*. Github, https://github.com/pandas-dev/pandas/blob/v0.25.0/pandas/plotting/_core.py#L1127-L1233 (accessed 2019 2019-09-19).
(35) Battersby, S. News Feature: The solar cell of the future. *Proc Natl Acad Sci U S A* 2019, *116* (1), 7-10.
(36) Conlen, M. *Kernel Density Estimation*. https://mathisonian.github.io/kde/ (accessed 2019-09-19).
(37) McKinney, W. *Data structures for statistical computing in python*; Proceedings of the 9th Python Science Conference, 2010.
(38) Palusiak, M.; Krygowski, T. M. Application of AIM Parameters at Ring Critical Points for Estimation of π-Electron Delocalization in Six-Membered Aromatic and Quasi-Aromatic Rings. *Chemistry - A European Journal* 2007, *13* (28), 7996-8006.
(39) Lopes, T. O.; Machado, D. F. S.; Risko, C.; Brédas, J.-L.; de Oliveira, H. C. B. Bond Ellipticity Alternation: An Accurate Descriptor of the Nonlinear Optical Properties of π-Conjugated Chromophores. *The Journal of Physical Chemistry Letters* 2018, *9* (6), 1377-1383.
(40) Che, Y.; Perepichka, D. F. Quantifying Planarity in the Design of Organic Electronic Materials. *Angew Chem Int Ed Engl* 2021, *60* (3), 1364-1373.
(41) Coughlin, J. E.; Zhugayevych, A.; Bakus, R. C.; Van Der Poll, T. S.; Welch, G. C.; Teat, S. J.; Bazan, G. C.; Tretiak, S. A Combined Experimental and

Theoretical Study of Conformational Preferences of Molecular Semiconductors. *The Journal of Physical Chemistry C* 2014, *118* (29), 15610-15623.

(42) Coughlin, J. E.; Henson, Z. B.; Welch, G. C.; Bazan, G. C. Design and Synthesis of Molecular Donors for Solution-Processed High-Efficiency Organic Solar Cells. *Accounts of Chemical Research* 2014, *47* (1), 257-270.

(43) McDowell, C.; Abdelsamie, M.; Zhao, K.; Smilgies, D.-M.; Bazan, G. C.; Amassian, A. Synergistic Impact of Solvent and Polymer Additives on the Film Formation of Small Molecule Blend Films for Bulk Heterojunction Solar Cells. *Advanced Energy Materials* 2015, *5* (18), 1501121.

(44) Kim, Y. J.; Ahn, S.; Wang, D. H.; Park, C. E. A Mechanistic Understanding of a Binary Additive System to Synergistically Boost Efficiency in All-Polymer Solar Cells. *Scientific Reports* 2015, *5* (1), 18024.

(45) Perez, L. A.; Chou, K. W.; Love, J. A.; van der Poll, T. S.; Smilgies, D.-M.; Nguyen, T.-Q.; Kramer, E. J.; Amassian, A.; Bazan, G. C. Solvent Additive Effects on Small Molecule Crystallization in Bulk Heterojunction Solar Cells Probed During Spin Casting. *Advanced Materials* 2013, *25* (44), 6380-6384.

(46) Wedler, S.; Bourdick, A.; Athanasopoulos, S.; Gekle, S.; Panzer, F.; McDowell, C.; Nguyen, T. Q.; Bazan, G. C.; Köhler, A. What is the role of planarity and torsional freedom for aggregation in a π-conjugated donor–acceptor model oligomer? *Journal of Materials Chemistry C* 2020, *8* (14), 4944-4955, 10.1039/D0TC00217H.

(47) Chen, J.; Shao, M.; Xiao, K.; Rondinone, A. J.; Loo, Y.-L.; Kent, P. R. C.; Sumpter, B. G.; Li, D.; Keum, J. K.; Diemer, P. J.; et al. Solvent-type-dependent polymorphism and charge transport in a long fused-ring organic semiconductor. *Nanoscale* 2014, *6* (1), 449-456.

(1) Szilágyi, B.; Nagy, Z. K. Aspect Ratio Distribution and Chord Length Distribution Driven Modeling of Crystallization of Two-Dimensional Crystals for Real-Time Model-Based Applications. *Crystal Growth & Design* 2018, *18* (9), 5311-5321.

(2) Guthrie, S.; Huelsenbeck, L.; Salahi, A.; Varhue, W.; Smith, N.; Yu, X.; Yoon, L. U.; Choi, J. J.; Swami, N.; Giri, G. Crystallization of high aspect ratio HKUST-1 thin films in nanoconfined channels for selective small molecule uptake. *Nanoscale Advances* 2019, *1* (8), 2946-2952, 10.1039/C9NA00254E.

(3) Dull, J.; Chen, X.; Johnson, H.; Otani, M. C.; Schreiber, F.; Clancy, P.; Rand, B. P. A comprehensive picture of roughness evolution in organic crystalline growth: The role of molecular aspect ratio. *Materials Horizons* 2022.

(4) Alkan, M.; Yavuz, I. Intrinsic charge-mobility in benzothieno[3,2-b][1]benzothiophene (BTBT) organic semiconductors is enhanced with long alkyl side-chains. *Physical Chemistry Chemical Physics* 2018, *20* (23), 15970-15979.

(5) Yao, Z.-F.; Wang, J.-Y.; Pei, J. Control of π–π Stacking via Crystal Engineering in Organic Conjugated Small Molecule Crystals. *Crystal Growth & Design* 2018, *18* (1), 7-15.

(6) Dandekar, P.; Kuvadia, Z. B.; Doherty, M. F. Engineering Crystal Morphology. *Annual Review of Materials Research* 2013, *43* (1), 359-386.

(7) Snyder, R. C.; Doherty, M. F. Faceted crystal shape evolution during dissolution or growth. *AIChE Journal* 2007, *53* (5), 1337-1348.

(8) Song, L.; Zhao, F.-Q.; Xu, S.-Y.; Ju, X.-H.; Ye, C.-C. Crystal Morphology Prediction and Anisotropic Evolution of 1,1-Diamino-2,2-dinitroethylene (FOX-7) by Temperature Tuning. *Scientific Reports* 2020, *10* (1).

(9) Salvalaglio, M.; Vetter, T.; Giberti, F.; Mazzotti, M.; Parrinello, M. Uncovering Molecular Details of Urea Crystal Growth in the Presence of Additives. *Journal of the American Chemical Society* 2012, *134* (41), 17221-17233.

(10) Salvalaglio, M.; Vetter, T.; Mazzotti, M.; Parrinello, M. Controlling and Predicting Crystal Shapes: The Case of Urea. *Angewandte Chemie International Edition* 2013, *52* (50), 13369-13372.

(11) Salvalaglio, M.; Mazzotti, M.; Parrinello, M. Urea homogeneous nucleation mechanism is solvent dependent. *Faraday Discussions* 2015, *179* (0), 291-307, 10.1039/C4FD00235K.

(12) Shinamura, S.; Miyazaki, E.; Takimiya, K. Synthesis, Properties, Crystal Structures, and Semiconductor Characteristics of Naphtho[1,2-b:5,6-b′]dithiophene and -diselenophene Derivatives. *The Journal of Organic Chemistry* 2010, *75* (4), 1228-1234.

(13) Perego, C.; Salvalaglio, M.; Parrinello, M. Molecular dynamics simulations of solutions at constant chemical potential. *The Journal of Chemical Physics* 2015, *142* (14), 144113.

(14) Han, D.; Karmakar, T.; Bjelobrk, Z.; Gong, J.; Parrinello, M. Solvent-mediated morphology selection of the active pharmaceutical ingredient isoniazid: Experimental and simulation studies. *Chemical Engineering Science* 2019, *204*, 320-328.

(15) Bjelobrk, Z.; Piaggi, P. M.; Weber, T.; Karmakar, T.; Mazzotti, M.; Parrinello, M. Naphthalene crystal shape prediction from molecular dynamics simulations. *CrystEngComm* 2019, *21* (21), 3280-3288.
(16) Donnay, J. D. H.; Harker, D. A new law of crystal morphology extending the Law of Bravais. *American Mineralogist* 1937, *22* (5), 446-467.
(17) Macrae, C. F.; Sovago, I.; Cottrell, S. J.; Galek, P. T. A.; McCabe, P.; Pidcock, E.; Platings, M.; Shields, G. P.; Stevens, J. S.; Towler, M.; et al. Mercury 4.0: from visualization to analysis, design and prediction. *Journal of Applied Crystallography* 2020, *53* (1), 226-235.
(18) Van Der Spoel, D.; Lindahl, E.; Hess, B.; Groenhof, G.; Mark, A. E.; Berendsen, H. J. GROMACS: fast, flexible, and free. *J Comput Chem* 2005, *26* (16), 1701-1718.
(19) Abraham, M. J.; Murtola, T.; Schulz, R.; Páll, S.; Smith, J. C.; Hess, B.; Lindahl, E. GROMACS: High performance molecular simulations through multi-level parallelism from laptops to supercomputers. *SoftwareX* 2015, *1-2*, 19-25.
(20) Promoting transparency and reproducibility in enhanced molecular simulations. *Nature Methods* 2019, *16* (8), 670-673.
(21) Tribello, G. A.; Bonomi, M.; Branduardi, D.; Camilloni, C.; Bussi, G. PLUMED 2: New feathers for an old bird. *Computer Physics Communications* 2014, *185* (2), 604-613.
(22) Bonomi, M.; Branduardi, D.; Bussi, G.; Camilloni, C.; Provasi, D.; Raiteri, P.; Donadio, D.; Marinelli, F.; Pietrucci, F.; Broglia, R. A.; et al. PLUMED: A portable plugin for free-energy calculations with molecular dynamics. *Computer Physics Communications* 2009, *180* (10), 1961-1972.
(23) Jorgensen, W. L.; Tirado-Rives, J. The OPLS [optimized potentials for liquid simulations] potential functions for proteins, energy minimizations for crystals of cyclic peptides and crambin. *Journal of the American Chemical Society* 1988, *110* (6), 1657-1666.
(24) Grimme, S. Semiempirical GGA-type density functional constructed with a long-range dispersion correction. *Journal of Computational Chemistry* 2006, *27* (15), 1787-1799.
(25) Hehre, W. J.; Ditchfield, R.; Pople, J. A. Self Consistent Molecular Orbital Methods. XII. Further Extensions of Gaussian-Type Basis Sets for Use in Molecular Orbital Studies of Organic Molecules. *The Journal of Chemical Physics* 1972, *56* (5), 2257-2261.
(26) Hariharan, P. C.; Pople, J. A. The influence of polarization functions on molecular orbital hydrogenation energies. *Theoretica chimica acta* 1973, *28* (3), 213-222.
(27) Marenich, A. V.; Jerome, S. V.; Cramer, C. J.; Truhlar, D. G. Charge Model 5: An Extension of Hirshfeld Population Analysis for the Accurate Description of Molecular Interactions in Gaseous and Condensed Phases. *Journal of Chemical Theory and Computation* 2012, *8* (2), 527-541.
(28) *Gaussian 16 Rev. C.01*; Wallingford, CT, 2016.
(29) Berendsen, H. J. C.; Postma, J. P. M.; Gunsteren, W. F. v.; DiNola, A.; Haak, J. R. Molecular dynamics with coupling to an external bath. *The Journal of Chemical Physics* 1984, *81* (8), 3684-3690.

(30) Parrinello, M.; Rahman, A. Polymorphic transitions in single crystals: A new molecular dynamics method. *Journal of Applied Physics* 1981, *52* (12), 7182-7190.

(31) Hess, B.; Bekker, H.; Berendsen, H. J. C.; Fraaije, J. G. E. M. LINCS: A linear constraint solver for molecular simulations. *Journal of Computational Chemistry* 1997, *18* (12), 1463-1472.

(32) Bonomi, M.; Bussi, G.; Camilloni, C.; Tribello, G. A.; Banáš, P.; Barducci, A.; Bernetti, M.; Bolhuis, P. G.; Bottaro, S.; Branduardi, D.; et al. Promoting transparency and reproducibility in enhanced molecular simulations. *Nature Methods* 2019, *16* (8), 670-673.

(33) Tribello, G. A.; Giberti, F.; Sosso, G. C.; Salvalaglio, M.; Parrinello, M. Analyzing and Driving Cluster Formation in Atomistic Simulations. *Journal of Chemical Theory and Computation* 2017, *13* (3), 1317-1327.

(34) Derrien, T. L.; Lauritzen, A. E.; Kaienburg, P.; Hardigree, J. F. M.; Nicklin, C.; Riede, M. In Situ Observations of the Growth Mode of Vacuum-Deposited α-Sexithiophene. *The Journal of Physical Chemistry C* 2020, *124* (22), 11863-11869.

(35) Vasseur, K.; Rolin, C.; Vandezande, S.; Temst, K.; Froyen, L.; Heremans, P. A Growth and Morphology Study of Organic Vapor Phase Deposited Perylene Diimide Thin Films for Transistor Applications. *The Journal of Physical Chemistry C* 2010, *114* (6), 2730-2737.

(36) Evans, J. W.; Thiel, P. A.; Bartelt, M. C. Morphological evolution during epitaxial thin film growth: Formation of 2D islands and 3D mounds. *Surface Science Reports* 2006, *61* (1), 1-128.

(37) Lorenz, M.; Wei, H.; Jung, F.; Hohenberger, S.; Hochmuth, H.; Grundmann, M.; Patzig, C.; Selle, S.; Höche, T. Two-dimensional Frank–van-der-Merwe growth of functional oxide and nitride thin film superlattices by pulsed laser deposition. *Journal of Materials Research* 2017, *32* (21), 3936-3946.

Chapter 5: References

(1) Zhang, Q.; Hu, W.; Sirringhaus, H.; Müllen, K. Recent Progress in Emerging Organic Semiconductors. *Advanced Materials* 2022, *34* (22), 2108701.

(2) Fratini, S.; Nikolka, M.; Salleo, A.; Schweicher, G.; Sirringhaus, H. Charge transport in high-mobility conjugated polymers and molecular semiconductors. *Nature Materials* 2020, *19* (5), 491-502.

(3) Sosso, G. C.; Chen, J.; Cox, S. J.; Fitzner, M.; Pedevilla, P.; Zen, A.; Michaelides, A. Crystal Nucleation in Liquids: Open Questions and Future Challenges in Molecular Dynamics Simulations. *Chemical Reviews* 2016, *116* (12), 7078-7116.

(4) Root, S. E.; Savagatrup, S.; Printz, A. D.; Rodriquez, D.; Lipomi, D. J. Mechanical Properties of Organic Semiconductors for Stretchable, Highly Flexible, and Mechanically Robust Electronics. *Chemical Reviews* 2017, *117* (9), 6467-6499.

(5) Diao, Y.; Shaw, L.; Bao, Z.; Mannsfeld, S. C. B. Morphology control strategies for solution-processed organic semiconductor thin films. *Energy & Environmental Science* 2014, *7* (7), 2145-2159, 10.1039/C4EE00688G.

(6) Dandekar, P.; Kuvadia, Z. B.; Doherty, M. F. Engineering Crystal Morphology. *Annual Review of Materials Research* 2013, *43* (1), 359-386.

(7) Ryno, S. M.; Noruzi, R.; Karunasena, C.; Pokuri, B. S. S.; Li, S.; Ganapathysubramanian, B.; Risko, C. Following the crystal growth of anthradithiophenes through atomistic molecular dynamics simulations and graph characterization. *Molecular Systems Design & Engineering* 2022, 10.1039/D1ME00157D.

(8) Li, S.; Ryno, S. M.; Risko, C. Exploring thermal transitions in anthradithiophene-based organic semiconductors to reveal structure-packing relationships. *Journal of Materials Chemistry C* 2018, *6* (40), 10924-10934.

(9) Huang, Y.; Gong, X.; Meng, Y.; Wang, Z.; Chen, X.; Li, J.; Ji, D.; Wei, Z.; Li, L.; Hu, W. Effectively modulating thermal activated charge transport in organic semiconductors by precise potential barrier engineering. *Nature Communications* 2021, *12* (1).

(10) Chen, H.; Zhang, W.; Ren, S.; Zhao, X.; Jiao, Y.; Wang, Y.; Stoddart, J. F.; Guo, X. Temperature-Triggered Supramolecular Assembly of Organic Semiconductors. *Advanced Materials* 2022, *34* (22), 2101487.

(11) Walters, D. M.; Richert, R.; Ediger, M. D. Thermal stability of vapor-deposited stable glasses of an organic semiconductor. *The Journal of Chemical Physics* 2015, *142* (13), 134504.

(12) Fulem, M.; Laštovka, V.; Straka, M.; Růžička, K.; Shaw, J. M. Heat Capacities of Tetracene and Pentacene. *Journal of Chemical & Engineering Data* 2008, *53* (9), 2175-2181.

(13) Valiyev, F.; Hu, W.-S.; Chen, H.-Y.; Kuo, M.-Y.; Chao, I.; Tao, Y.-T. Synthesis and Characterization of Anthra[2,3-b]thiophene and Tetraceno[2,3-b]thiophenes for Organic Field-Effect Transistor Applications. *Chemistry of Materials* 2007, *19* (12), 3018-3026.

(14) Shinamura, S.; Miyazaki, E.; Takimiya, K. Synthesis, Properties, Crystal Structures, and Semiconductor Characteristics of Naphtho[1,2-b:5,6-

b′]dithiophene and -diselenophene Derivatives. *The Journal of Organic Chemistry* 2010, *75* (4), 1228-1234.

(15) Saito, M.; Osaka, I.; Miyazaki, E.; Takimiya, K.; Kuwabara, H.; Ikeda, M. One-step synthesis of [1]benzothieno[3,2-b][1]benzothiophene from o-chlorobenzaldehyde. *Tetrahedron Letters* 2011, *52* (2), 285-288.

(16) Grigoriadis, C.; Niebel, C.; Ruzié, C.; Geerts, Y. H.; Floudas, G. Order, Viscoelastic, and Dielectric Properties of Symmetric and Asymmetric Alkyl[1]benzothieno[3,2-b][1]benzothiophenes. *The Journal of Physical Chemistry B* 2014, *118* (5), 1443-1451.

(17) Abraham, M. J.; Murtola, T.; Schulz, R.; Páll, S.; Smith, J. C.; Hess, B.; Lindahl, E. GROMACS: High performance molecular simulations through multi-level parallelism from laptops to supercomputers. *SoftwareX* 2015, *1-2*, 19-25.

(18) Van Der Spoel, D.; Lindahl, E.; Hess, B.; Groenhof, G.; Mark, A. E.; Berendsen, H. J. GROMACS: fast, flexible, and free. *J Comput Chem* 2005, *26* (16), 1701-1718.

(19) Irrgang, M. E.; Davis, C.; Kasson, P. M. gmxapi: A GROMACS-native Python interface for molecular dynamics with ensemble and plugin support. *PLOS Computational Biology* 2022, *18* (2), e1009835.

(20) Bonomi, M.; Branduardi, D.; Bussi, G.; Camilloni, C.; Provasi, D.; Raiteri, P.; Donadio, D.; Marinelli, F.; Pietrucci, F.; Broglia, R. A.; et al. PLUMED: A portable plugin for free-energy calculations with molecular dynamics. *Computer Physics Communications* 2009, *180* (10), 1961-1972.

(21) Tribello, G. A.; Bonomi, M.; Branduardi, D.; Camilloni, C.; Bussi, G. PLUMED 2: New feathers for an old bird. *Computer Physics Communications* 2014, *185* (2), 604-613.

(22) Bernardi, A.; Faller, R.; Reith, D.; Kirschner, K. N. ACPYPE update for nonuniform 1–4 scale factors: Conversion of the GLYCAM06 force field from AMBER to GROMACS. *SoftwareX* 2019, *10*, 100241.

(23) Wang, J.; Wolf, R. M.; Caldwell, J. W.; Kollman, P. A.; Case, D. A. Development and testing of a general amber force field. *Journal of Computational Chemistry* 2004, *25* (9), 1157-1174.

(24) Hariharan, P. C.; Pople, J. A. The influence of polarization functions on molecular orbital hydrogenation energies. *Theoretica chimica acta* 1973, *28* (3), 213-222.

(25) Hehre, W. J.; Ditchfield, R.; Pople, J. A. Self—Consistent Molecular Orbital Methods. XII. Further Extensions of Gaussian—Type Basis Sets for Use in Molecular Orbital Studies of Organic Molecules. *The Journal of Chemical Physics* 1972, *56* (5), 2257-2261.

(26) Marenich, A. V.; Jerome, S. V.; Cramer, C. J.; Truhlar, D. G. Charge Model 5: An Extension of Hirshfeld Population Analysis for the Accurate Description of Molecular Interactions in Gaseous and Condensed Phases. *Journal of Chemical Theory and Computation* 2012, *8* (2), 527-541.

(27) *Gaussian 16 Rev. C.01*; Wallingford, CT, 2016. (accessed.

(28) Ai, Q.; Bhat, V.; Ryno, S. M.; Jarolimek, K.; Sornberger, P.; Smith, A.; Haley, M. M.; Anthony, J. E.; Risko, C. OCELOT: An infrastructure for data-driven research to discover and design crystalline organic semiconductors. *The Journal of Chemical Physics* 2021, *154* (17), 174705.

(29) Berendsen, H. J. C.; Postma, J. P. M.; Gunsteren, W. F. v.; DiNola, A.; Haak, J. R. Molecular dynamics with coupling to an external bath. *The Journal of Chemical Physics* 1984, *81* (8), 3684-3690.
(30) Parrinello, M.; Rahman, A. Polymorphic transitions in single crystals: A new molecular dynamics method. *Journal of Applied Physics* 1981, *52* (12), 7182-7190.
(31) Hess, B.; Bekker, H.; Berendsen, H. J. C.; Fraaije, J. G. E. M. LINCS: A linear constraint solver for molecular simulations. *Journal of Computational Chemistry* 1997, *18* (12), 1463-1472.
(32) Macrae, C. F.; Sovago, I.; Cottrell, S. J.; Galek, P. T. A.; McCabe, P.; Pidcock, E.; Platings, M.; Shields, G. P.; Stevens, J. S.; Towler, M.; et al. Mercury 4.0: from visualization to analysis, design and prediction. *Journal of Applied Crystallography* 2020, *53* (1), 226-235.
(33) John, S.; Justin, G.; Paul, G.; Klaus, S. A System for Interactive Molecular Dynamics Simulation. In 2001.
(34) William, H.; Andrew, D.; Klaus, S. VMD -- Visual Molecular Dynamics. *Journal of Molecular Graphics* 1996, *14*, 33-38.

VITA

Name

Chamikara D. Karunasena

Place of birth

Kandy, Sri Lanka

Education

BSc. University of Peradeniya, 2017

PhD. University of Kentucky, Lexington, 2022

Publications

1. Karunasena, C., Li, S., Heifner, M. C., Ryno, S. M., & Risko, C. (2021). Reconsidering the Roles of Noncovalent Intramolecular "Locks" in π-Conjugated Molecules. Chemistry of Materials, 33(23), 9139-9151. https://doi.org/10.1021/acs.chemmater.1c02335

2. Ryno, S. M., Noruzi, R., Karunasena, C., Pokuri, B. S. S., Li, S., Ganapathysubramanian, B., & Risko, C. (2022). Following the Crystal Growth of Anthradithiophenes through Atomistic Molecular Dynamics Simulations and Graph Characterization. Molecular Systems Design & Engineering, online, DOI: 10.1039/d1me00157d

3. Pandeya, A., Yang, L., Alegun, O., Karunasena, C., Risko, C., Li, Z., & Wei, Y. (2021). Biotinylation as a Tool to Enhance the Uptake of Small Molecules in Gram-Negative Bacteria. PLOS ONE, 16(11), e0260023. https://doi.org/10.1371/journal.pone.0260023

4. Karunasena, C., Bjelobrk, Z., Mazzotti, M., Parrinello, M., & Risko, C (2022). Crystal growth of herringbone packed molecular crystals from solution (2022), Submitted.

5. Karunasena, C., Li, S., Ryno, S., & Risko, C., Thermal Transitions of Herringbone-packed Organic Semiconductors: Influence of Chemical Modifications on Melting and Solidification (2022), Submitted.

6. Karunasena, C., Pokuri, B. S. S., Wodo, O., Ganapathysubramanian, B., & Risko, C., Towards machine-enabled models to design the morphologies of organic semiconductors. (2022), In preparation.